Comparison of Random Vibration Theory and Time Series Seismic Site Response Analyses

Albert R. Kottke and Ellen M. Rathje

May 12, 2010

Contents

Contents **1**

List of Figures **3**

List of Tables **9**

1 Introduction **10**

2 Site Response Methods **12**
2.1 Introduction . . . 12
2.2 Equivalent-Linear Method . . . 13
2.3 Nonlinear Method . . . 15
2.4 Input Motion Specification . . . 18
2.5 Linear Elastic Simplification . . . 22

3 Site Profiles Analyzed **23**
3.1 Introduction . . . 23
3.2 Turkey Flat Site . . . 23
3.3 Sylmar County Hospital Site . . . 25
3.4 Calvert Cliffs Site . . . 30

4 Input Ground Motion Characterization **37**
4.1 Introduction . . . 37
4.2 Stochastically Simulated Ground Motions . . . 38
4.3 Recorded Ground Motions . . . 41
4.3.1 Ground Motion Selection . . . 41
4.3.2 Maximum Usable Frequency . . . 47
4.4 Spectrally Matched Ground Motions . . . 52
4.5 Response Spectrum Compatible Motion for RVT . . . 57

5 Comparison of Equivalent-Linear Methods **62**
5.1 Introduction . . . 62
5.2 Comparison Using Stochastic Input Motions . . . 63
5.3 Comparisons Using Scaled Time Series . . . 85

5.4 Comparisons Using Spectrally Matched Time Series 96
5.5 Summary 108

6 Comparison of Equivalent-Linear and Nonlinear Methods 111
6.1 Introduction 111
6.2 Linear Elastic Analysis 112
6.3 Analyses for Low-Intensity Input Motions 118
6.4 Analyses for Moderate- to High-Intensity Input Motions 125
6.5 Summary 134

7 Conclusion 136
7.1 Summary 136
7.2 Recommendations for Future Work 138

Bibliography 139

A Input Files 144
A.1 `SMSIM` Parameter File 144

B Scaled Time Series 147

C Spectrally-Matched Time Series 163

List of Figures

2.1 The typical nonlinear shear stress (τ) versus shear strain (γ) response of soil under cyclic loading results. 14
2.2 Shear modulus reduction and damping curves that characterize the nonlinear response of soil. 14
2.3 The fit of an MKZ nonlinear curve to nonlinear curves computed with the Darendeli (2001) model. 17
2.4 Suites of recorded motions scaled and spectrally matched to fit a target response spectrum. 20

3.1 The shear-wave velocity profile of the Turkey Flat site (Real, 1988). . . 25
3.2 The shear-wave velocity profile of the SCH site (Chang, 1996). 27
3.3 The Darendeli (2001) and MKZ curves for the SCH site. 29
3.4 The shear-wave velocity profile of the CC site (UniStar Nuclear Services, 2007). 32
3.5 The Darendeli (2001) and MKZ curves for the CC site (soil types 1 to 3). 34
3.6 The Darendeli (2001) and MKZ curves for the CC site (soil types 4 to 6). 35
3.7 The Darendeli (2001) and MKZ curves for the CC site (soil types 7 to 9). 36

4.1 The stochastic FAS computed with seismological theory using the parameters listed in Table 4.1. 39
4.2 A FAS of a single simulated ground motion, along with the average of 100 stochastic simulations and the target FAS 40
4.3 The acceleration-time series of a single simulated ground motion. 40
4.4 The response spectrum of a single simulated ground motion, along with the median of 100 stochastic simulations and the response spectrum computed with RVT. 41
4.5 The target acceleration response spectrum computed using the Boore and Atkinson (2008) ground motion prediction equation. 42
4.6 The response spectra of the fifteen ground motions scaled to the target response spectrum. 44
4.7 The FAS of the fifteen ground motions scaled to the target response spectrum. 46

4.8 The median response spectrum of the fifteen scaled motions and an RVT motion defined by the root-mean-square FAS of the scaled motions and a duration of 4.83 seconds. 46
4.9 Distribution of the low-pass frequency used in the processing of motions in the NGA database. 48
4.10 The effect of truncation on the `CHICHI06-TCU076-E` motion on the response spectrum and spectral ratio computed for the Sylmar County Hospital site. 51
4.11 The effect of truncation on the suite of input ground motions used in this study. 52
4.12 The response spectrum for the scaled, scaled prior to spectral matching, and spectrally matched versions of the `NORTHR-WON185` ground motion, along with the target response spectrum. 54
4.13 The acceleration-, velocity-, and displacement-time series for the scaled and spectrally matched versions of the `NORTHR-WON185` ground motion. . 55
4.14 The fifteen ground motions spectrally matched and truncated at 25 Hz. 56
4.15 The standard deviation of the stochastically simulated, scaled, and spectrally matched ground motion suites. 56
4.16 A response spectrum compatible RVT motion computed for a seismological theory derived target response spectrum, along with the comparison of the associated FAS 61
4.17 A response spectrum compatible RVT motion computed from a GMPE derived target response spectrum. 61

5.1 The input Fourier amplitude and response spectra for the stochastic input motions. 64
5.2 The relative difference of the input response spectrum for the stochastic input motions. 65
5.3 The response spectrum, spectral ratio, and relative difference for the Turkey Flat site computed with LE site response using simulated time series and an RVT motion defined by seismological theory. 66
5.4 The response spectrum, spectral ratio, and relative difference for the SCH site computed with LE site response using simulated time series and an RVT motion defined by seismological theory. 67
5.5 The response spectrum, spectral ratio, and relative difference for the CC site computed with LE site response using simulated time series and an RVT motion defined by seismological theory. 68
5.6 The linear-elastic transfer functions for the three sites used in this study. 70
5.7 The input FAS for the time series with the largest and smallest spectral ratios for the SCH site, along with the input FAS of the RVT analysis and the LE transfer function. 71
5.8 The input FAS for the time series with the largest and smallest spectral ratios for the CC site, along with the input FAS of the RVT analysis and the LE transfer function. 72

5.9 Sensitivity of the relative difference of the spectral ratio at the site frequency and at a frequency of 0.01 seconds to various site characteristics. 74
5.10 The response spectrum, spectral ratio, and relative difference for the SCH computed with EQL site response using simulated time series and an RVT motion defined by seismological theory (input PGA of 0.17 g). . 76
5.11 The response spectrum, spectral ratio, and relative difference for the SCH computed with EQL site response using simulated time series and an RVT motion defined by seismological theory (input PGA of 0.40 g). . 77
5.12 The relative difference of the spectral ratio of the SCH site computed using simulated time series and an RVT motion defined by seismological theory. 78
5.13 The maximum strain profiles for the SCH site computed using simulated time series and an RVT motion defined by seismological theory. 80
5.14 The spectral ratio and maximum strain profiles for selected motions propagated through the SCH site with an input PGA of 0.40 g. 81
5.15 Histograms of the spectral ratio at the site frequency of the RVT analysis for the SCH site. 82
5.16 The relative difference of the spectral ratio of the CC site computed using simulated time series and an RVT motion defined by seismological theory. 83
5.17 The maximum strain profiles for the CC site computed using simulated time series and an RVT motion defined by seismological theory. 84
5.18 The input Fourier amplitude and response spectra for the scaled input motions, as well as FAS and response spectrum compatible RVT motions. 87
5.19 The relative difference of the input response spectra for the FAS and response spectrum compatible RVT motions. 88
5.20 The response spectrum, spectral ratio, and relative difference for the SCH site computed with LE site response using scaled time series, as well as FAS and response spectrum compatible RVT motions. 89
5.21 The spectral ratios for the SCH site computed with EQL site response using scaled time series, as well as FAS and response spectrum compatible RVT motions. 91
5.22 The maximum strain profiles for the SCH site computed using scaled time series and a response spectrum compatible RVT motion. 92
5.23 The relative difference of the spectral ratio of the SCH and CC sites computed using scaled time series and a response spectrum compatible RVT motion. 94
5.24 The maximum strain profiles for the CC site computed using scaled time series and a response spectrum compatible RVT motion. 95
5.25 The input Fourier amplitude and response spectra for the spectrally-matched time series and a response spectrum compatible RVT motion. . 97
5.26 The relative difference of the input response spectra computed using a response spectrum compatible RVT motion. 98

5.27 The response spectrum, spectral ratio, and relative difference for the SCH site computed with LE site response using spectrally-matched time series and a response spectrum compatible RVT motion. 99
5.28 The response spectrum, spectral ratio, and relative difference for the SCH site computed with EQL site response using spectrally-matched time series and a response spectrum compatible RVT motion (input PGA of 0.13 g). 100
5.29 The response spectrum, spectral ratio, and relative difference for the SCH site computed with EQL site response using spectrally-matched time series and a response spectrum compatible RVT motion (input PGA of 0.40 g). 101
5.30 The maximum strain profiles for the SCH site computed using spectrally-matched time series and a response spectrum compatible RVT motion. . 102
5.31 The relative difference of the spectral ratio of the SCH site computed using spectrally-matched time series and a response spectrum compatible RVT motion. 103
5.32 The response spectrum, spectral ratio, and relative difference for the CC site computed with EQL site response using spectrally-matched time series and a response spectrum compatible RVT motion (input PGA of 0.13 g). 105
5.33 The maximum strain profiles for the CC site computed using spectrally-matched time series and a response spectrum compatible RVT motion. . 106
5.34 The relative difference of the spectral ratio of the CC site computed using spectrally-matched time series and a response spectrum compatible RVT motion. 107
5.35 The computed spectral ratios for the SCH and CC sites at an input intensity of 0.40 g. 110

6.1 Variation of damping ratio with frequency for the full Rayleigh damping formulation. 114
6.2 Spectral ratio of the SCH and CC sites using linear-elastic time domain and frequency domain methods. 115
6.3 Amplitude of the transfer function computed for the SCH and CC sites using LE time-domain (TD) and frequency-domain (FD) methods. . . . 117
6.4 The spectral ratio and relative difference for the SCH site computed with time domain and frequency domain methods using the spectrally-matched ground motions. 120
6.5 The spectral ratio and relative difference for the CC site computed with time domain and frequency domain methods using the spectrally-matched ground motions. 121
6.6 Amplitude and phase of the transfer functions computed by the EQL and nonlinear methods for the SCH site (input PGA of 0.01 g). 123
6.7 Amplitude and phase of the transfer functions computed by the EQL and nonlinear methods for the CC site (input PGA of 0.01 g). 124

6.8 The spectral ratio and relative difference for the SCH site computed with nonlinear and EQL methods using the spectrally-matched ground motions (input PGA of 0.13 g). 126
6.9 Amplitude and phase of the transfer functions computed by the EQL and nonlinear methods for SCH (input PGA of 0.13 g). 127
6.10 The effect of smooth phase on the surface response spectrum for the SCH site. 129
6.11 The spectral ratio and relative difference for the SCH site computed with nonlinear and EQL methods using the spectrally-matched ground motions (input PGA of 0.40 g). 130
6.12 The maximum strain profile for the SCH site computed with the nonlinear and EQL methods. 131
6.13 The spectral ratio and relative difference for the CC site computed with nonlinear and EQL methods using the spectrally-matched ground motions. 133
6.14 The relative difference of the spectral ratio of the SCH and CC sites computed with nonlinear and EQL methods using the spectrally-matched ground motions. 135

B.1 The `CHICHI06-TCU076-E` time series scaled by 0.79. 148
B.2 The `ITALY-A-AUL270` time series scaled by 1.55. 149
B.3 The `ITALY-A-BAG00` time series scaled by 0.62. 150
B.4 The `ITALY-A-STU270` time series scaled by 0.25. 151
B.5 The `ITALY-B-AUL270` time series scaled by 4.19. 152
B.6 The `KOZANI-KOZ--L` time series scaled by 0.73. 153
B.7 The `LOMAP-G01000` time series scaled by 0.33. 154
B.8 The `LOMAP-GIL067` time series scaled by 0.32. 155
B.9 The `MORGAN-GIL337` time series scaled by 2.01. 156
B.10 The `NORTHR-H12180` time series scaled by 0.66. 157
B.11 The `NORTHR-HOW330` time series scaled by 0.83. 158
B.12 The `NORTHR-LV1000` time series scaled by 1.30. 159
B.13 The `NORTHR-LV3090` time series scaled by 1.24. 160
B.14 The `NORTHR-WON185` time series scaled by 0.76. 161
B.15 The `VICT-CPE045` time series scaled by 0.21. 162

C.1 The spectrally-matched `CHICHI06-TCU076-E` time series. 164
C.2 The spectrally-matched `ITALY-A-AUL270` time series. 165
C.3 The spectrally-matched `ITALY-A-BAG000` time series. 166
C.4 The spectrally-matched `ITALY-A-STU270` time series. 167
C.5 The spectrally-matched `ITALY-B-AUL270` time series. 168
C.6 The spectrally-matched `KOZANI-KOZ--L` time series. 169
C.7 The spectrally-matched `LOMAP-G01000` time series. 170
C.8 The spectrally-matched `LOMAP-GIL067` time series. 171
C.9 The spectrally-matched `MORGAN-GIL337` time series. 172
C.10 The spectrally-matched `NORTHR-H12180` time series. 173

C.11 The spectrally-matched NORTHR-HOW330 time series. 174
C.12 The spectrally-matched NORTHR-LV1000 time series. 175
C.13 The spectrally-matched NORTHR-LV3090 time series. 176
C.14 The spectrally-matched NORTHR-WON185 time series. 177
C.15 The spectrally-matched VICT-CPE045 time series. 178

List of Tables

3.1 The shear-wave velocity profile for the Turkey Flat site (Real, 1988). . . 24
3.2 The shear-wave velocity profile for the SCH site (Chang, 1996). 26
3.3 The soil types and model parameters of the SCH site profile. 28
3.4 The shear-wave velocity profile for the CC site (UniStar Nuclear Services, 2007). 31
3.5 The soil types and model parameters of the CC site profile. 33

4.1 The selected input parameters used by `SMSIM` for the calculation of the Fourier amplitude spectrum shown in Figure 4.1. 38
4.2 The parameters used to define the ground motion library for consideration by the selection algorithm. 42
4.3 The earthquake events and number of records used in the library of ground motions. 44
4.4 The ground motions and their properties for the suite shown in Figure 4.6. 45
4.5 The high-pass and low-pass frequencies of the suite of motions, as well as the recorded time step. 49
4.6 Parameters for the Abrahamson and Silva (1996) empirical duration model. 59

5.1 Site properties used in the sensitivity analysis. 73

Chapter 1

Introduction

Local soil conditions influence the characteristics of earthquake ground shaking and these effects must be taken into account when specifying ground shaking levels for seismic design. These effects are quantified via site response analysis, which involves the propagation of earthquake motions from the base rock through the overlying soil layers to the ground surface. Site response analysis provides surface acceleration-time series, surface acceleration response spectra, and/or spectral amplification factors based on the dynamic response of the local soil conditions.

Site response analyses are used to specify the site-specific ground motion response spectrum (GMRS) used in the seismic design and evaluation of nuclear power plants, as outlined in NUREG/CR-6728 (McGuire et al., 2001), NUREG/CR-6769 (McGuire et al., 2002), and Regulatory Guide 1.208 (NRC, 2007). In most cases, one-dimensional (1D) site response analysis is performed to assess the effect of soil conditions on ground shaking because vertically-propagating, horizontally-polarized shear waves dominate the earthquake ground motion wave field. The input motion specification, the 1D wave propagation, and the model for soil response may vary between different site response techniques. The most common techniques for site response analysis are equivalent-linear (EQL) analysis using the time series approach, EQL analysis using the random vibration

theory (RVT) approach, or fully nonlinear analysis using the time series approach. These three techniques are explicitly cited in NUREG/CR-6728 and Regulatory Guide 1.208 as appropriate techniques for site response analysis. However, the dynamic responses computed via these techniques can vary considerably due to inherent differences in the numerical approaches (time series vs. RVT), differences in how the nonlinear soil response is modeled (EQL vs. nonlinear), and differences in the specification of the input rock motion (time series vs. Fourier amplitude spectrum). This report presents a comprehensive comparison of these different site response techniques over a range of site conditions (i.e., shallow soil to very deep soil) and over a range of input intensities that induce different levels of nonlinearity.

The following report consists of seven chapters. Chapter 2 introduces the equivalent-linear and nonlinear site response methods, as well as the random vibration theory approach to site response. Chapter 3 then presents the characteristics and nonlinear properties of the three sites used in this study. In Chapter 4, the input motions used in the analyses found in this report are presented. This discussion includes the characterization of the stochastically-simulated time series, scaled time series and spectrally-matched time series, as well as response spectrum compatible motion for random vibration theory. Chapter 5 presents a comparison of the equivalent-linear method using time series and random vibration theory approaches. Chapter 6 compares the equivalent-linear and nonlinear methods using a suite of spectrally-match time series. Chapter 7 presents a summary of the findings of this report and provides recommendations for future studies.

Chapter 2

Site Response Methods

2.1 Introduction

Site response analysis numerically propagates shear waves from the base rock through the overlying layers of soil to the ground surface. One-dimensional site response analysis is commonly performed and requires the following information: (1) the shear-wave velocity profile of the site, (2) the nonlinear stress-strain response of the soil, and (3) an input rock motion. The shear-wave velocity profile represents the small-strain stiffness of the soil and is required for all types of site response analysis. The nonlinear response of the soil can be characterized either through the EQL approach or through the fully nonlinear approach. Traditionally, all site response methods have required the specification of an acceleration-time series as the input rock motion, and a suite of motions is commonly used to develop a statistically stable estimate of the response due to motion-to-motion variability. Alternatively, RVT can be applied to EQL analysis, such that only an Fourier amplitude spectrum (FAS) is required as input and the selection of input motions is avoided. The details regarding the different approaches to site response analysis (EQL vs. nonlinear) and the different methods of input motion specification (time series vs. RVT) are discussed in the following chapter.

2.2 Equivalent-Linear Method

Equivalent-linear (EQL) site response analysis uses one-dimensional, linear-elastic wave propagation through layered media to model the dynamic response of the soil deposit. The method incorporates soil nonlinearity through the use of strain-compatible soil properties for each soil layer. The typical nonlinear shear stress (τ) versus shear strain (γ) response of soil under cyclic loading results in a hysteresis loop (Figure 2.1). The hysteresis loop for a given level of shear strain can be characterized by a secant shear modulus (G) and a damping ratio (D) that is related to the size of the loop. Generally, as the shear strain increases, G decreases and D increases. The variations of shear modulus and damping ratio with shear strain are prescribed through modulus reduction (G/G_{max}) and damping (D) curves (Figure 2.2), in which G_{max} is the shear modulus at small strains. G_{max} can be related to shear-wave velocity (V_s) through the mass density (ρ) of the soil ($G_{max} = \rho V_s^2$).

The key to the EQL approach is the selection of soil properties (G and D) for each soil layer that are consistent with the level of shear strain induced by the input rock motion. Development of strain-compatible properties requires an iterative approach in which the strains are computed, the properties are revised based on the strains, and revised strains are computed based on the updated properties. These iterations continue until the properties assigned to each layer in the wave-propagation analysis are consistent with the strains generated in each layer. The strain level used to select the strain-compatible properties is not the peak time domain shear strain, but rather an effective shear strain (γ_{eff}) that typically is about 65% of the peak value.

Another important aspect of EQL site response analysis is that it is performed in the frequency domain using transfer functions. The input time series is first converted to the frequency domain using the Fast Fourier Transform (FFT), and the wave propagation calculations are simply performed by multiplying the complex-valued Fourier amplitudes

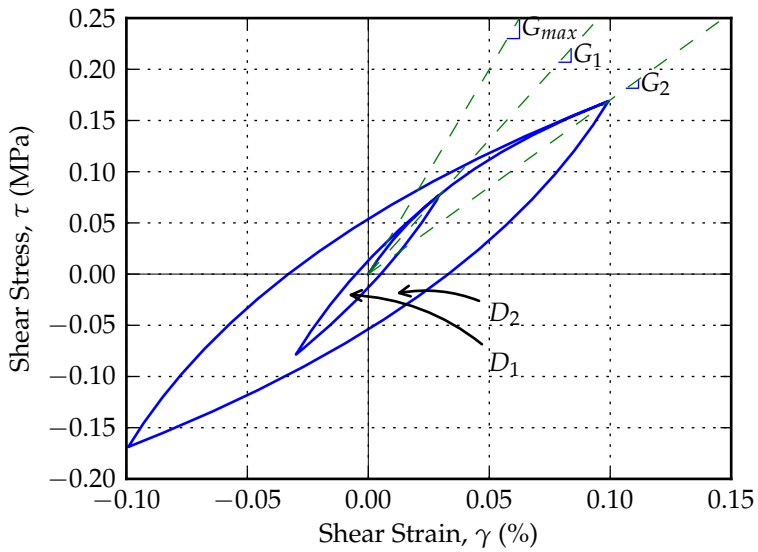

Figure 2.1: The typical nonlinear shear stress (τ) versus shear strain (γ) response of soil under cyclic loading results.

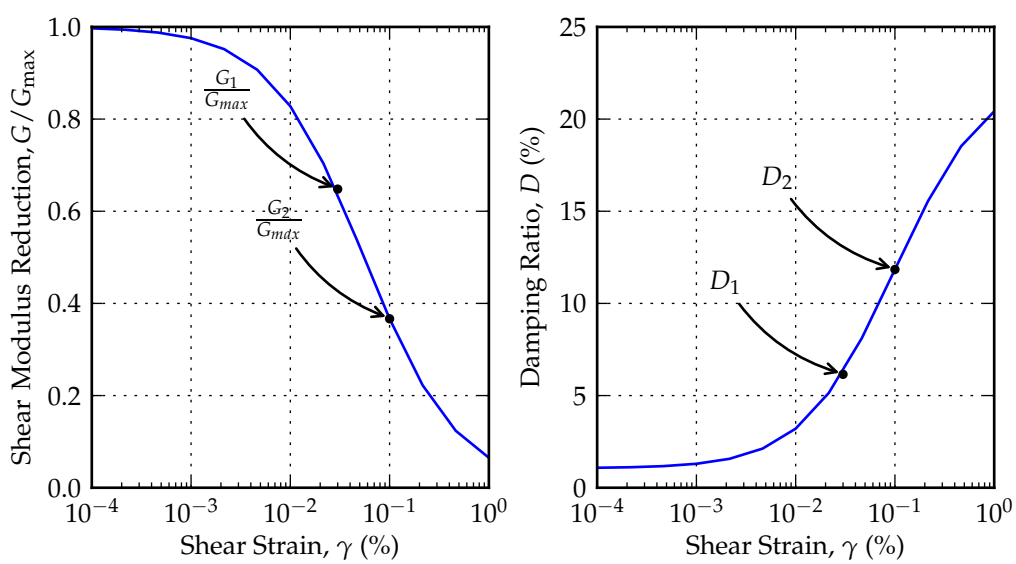

Figure 2.2: Shear modulus reduction and damping curves that characterize the nonlinear response of soil.

of the input motion by the complex-valued transfer function. The time series at the ground surface is obtained through application of an inverse FFT. The calculation is generally limited to frequencies less than a maximum frequency which is governed by the time step, filter characteristics, and engineering interest. Frequencies higher than the maximum frequency interest are truncated or defined to be zero. A more thorough discussion of the maximum frequency is presented in Section 4.3.2.

This approach has been used since the 1970s when the program `SHAKE` was introduced by Schnabel et al. (1972), and has been used by most EQL site response programs subsequently developed (e.g., `SHAKE91`, Idriss and Sun 1993; `Shake2000`, Ordónez 2002; `Strata`, Kottke and Rathje 2008b). The use of frequency domain computations makes EQL analysis a very efficient technique for site response calculations. For this study, the program `Strata` (Kottke and Rathje, 2008b) was used for all EQL analyses. The program `SHAKE91` was used to validate the equivalent-linear site response portion of `Strata`, and the program `SMSIM` was used to validate the random vibration theory portion.

2.3 Nonlinear Method

Nonlinear site response analysis computes the dynamic response of a 1D soil column consisting of lumped masses and nonlinear shear springs subjected to an input rock motion. Nonlinear analysis incorporates the fully nonlinear shear stress versus shear strain response of the soil (e.g. Figure 2.1) in the time domain and does not incorporate strain-compatible properties. Stewart et al. (2008) provides a complete review of various nonlinear models and discusses the calibration of nonlinear methods to the equivalent-liner method and recordings from borehole arrays.

The nonlinear approach relies on a backbone shear stress-shear strain curve and unloading/reloading rules (i.e., Masing rules) to define the hysteretic response of the

soil under cyclic loading. A common backbone curve is the MKZ model (Matasović and Vucetic, 1993), which is a modified hyperbola defined as:

$$\tau = \frac{G_{max} \cdot \gamma}{1 + \alpha \left(\frac{\gamma}{\gamma_r}\right)^s} \tag{2.1}$$

This curve requires three fitting parameters: α, γ_r, and s, in addition to G_{max} (which is defined for each layer based on the shear-wave velocity profile). The Masing rules use the backbone curve to generate the unload/reload response under cyclic loading, and these hysteresis loops represent the modeled levels of damping. Additional viscous damping ($D_{\min}$) is required to model energy dissipation at very small strains where hysteretic damping is essentially zero and not representative of soil.

Most laboratory tests provide information regarding the nonlinear properties of soil in the form of modulus reduction and damping curves (Figure 2.2) rather than shear-stress shear-strain curves. To relate a nonlinear stress-strain model to measured modulus reduction and damping curves, a nonlinear backbone curve and its associated hysteresis loops at different strain levels are converted into equivalent G/G_{max} and D curves. The nonlinear fitting parameters are selected such that the equivalent modulus reduction and damping curves from the nonlinear model match those specified for the soil. Figure 2.3 shows a comparison of modulus reduction and damping curves from the empirical model of Darendeli (2001) with those from the MKZ model. The MKZ parameters were selected based on a least-sum-square-of-error fit to the Darendeli (2001) curves over the entire strain range. While the MKZ curves show favorable agreement at smaller strains, they deviate from the empirical curves at larger strains. In particular, the MKZ damping curve produces much larger damping at larger strains. This issue is common with nonlinear models and is caused by the shape of the modified hyperbolic stress-strain curve at large strains and the use of the Masing rules to generate the hysteresis loops.

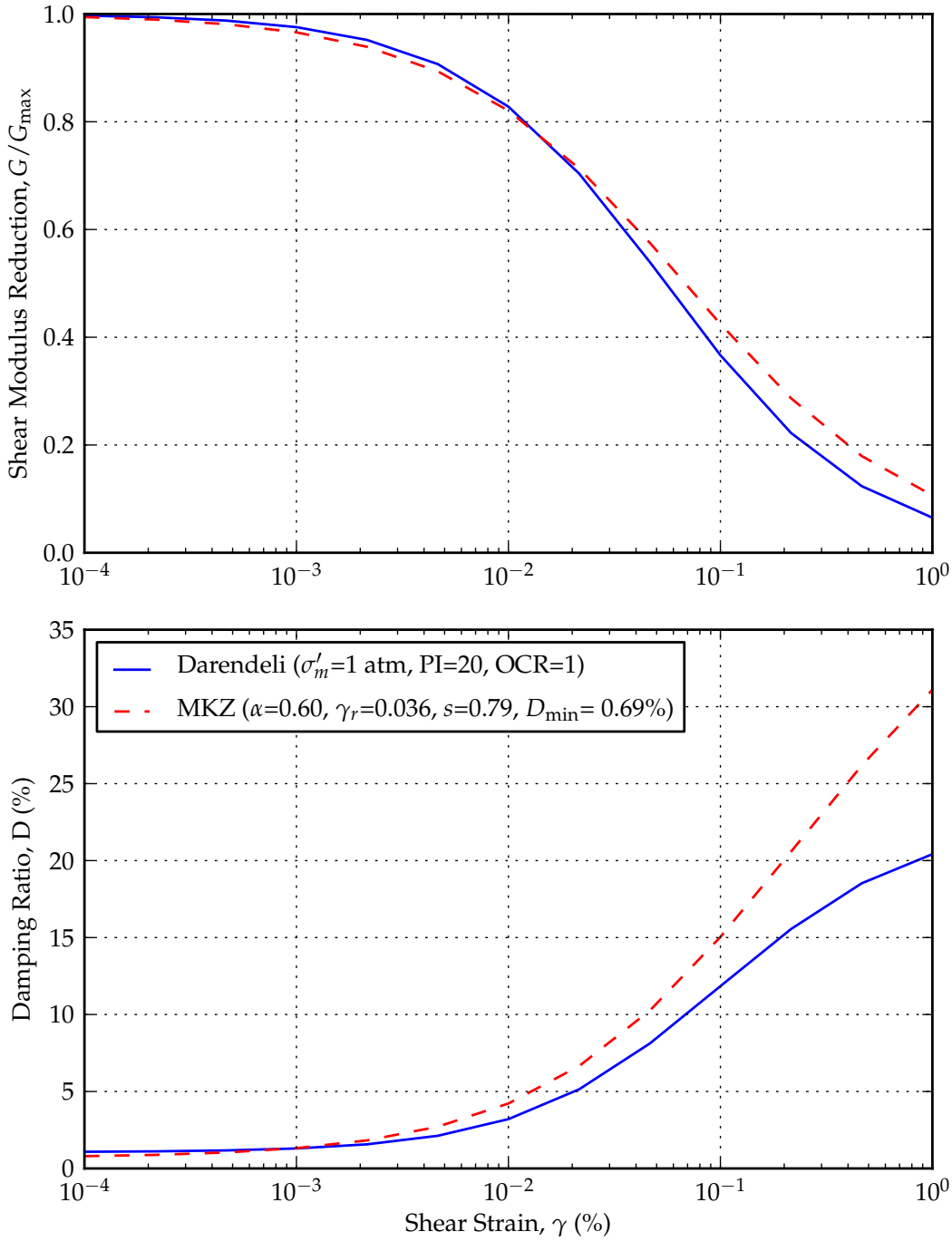

Figure 2.3: The fit of an MKZ nonlinear curve to nonlinear curves computed with the Darendeli (2001) model.

For this study, the nonlinear site response program `DeepSoil` (Hashash, 2002; Hashash and Park, 2001) was used. `DeepSoil` incorporates the MKZ backbone model, and viscous damping is incorporated via the Rayleigh damping formulation. Rayleigh damping is frequency dependent, and thus the target viscous damping is achieved only at specified target frequencies. The target frequencies were generally specified as the first mode natural frequency (f_s) and five times the first mode natural frequency ($5 \cdot f_s$), as recommended by Stewart et al. (2008). Additionally, frequency-independent Rayleigh damping (Phillips and Hashash, 2009) was also investigated. The MKZ model parameters were selected to best fit both the specified modulus reduction and damping curves for each layer.

2.4 Input Motion Specification

Equivalent-linear and nonlinear wave propagation analysis requires specification of an input rock motion. For EQL analysis, this input acceleration-time series is converted to the frequency domain using the FFT, the resulting FAS is multiplied by the transfer function that represents wave propagation to the ground surface, and the FAS at the surface is converted to an acceleration-time series using the inverse FFT. Nonlinear analysis solves the differential equations of motion in the time domain using numerical time stepping methods, and the properties of the system vary with each time step to incorporate the nonlinear response of the soil. Here, the input time series is used as the forcing function for the time stepping method.

Commonly, a suite of input motions is used to capture the motion-to-motion variability present in earthquake ground motions for similar events. A suite is required because the detailed characteristics of each input motion influence the induced dynamic response. A suite of recorded motions can be linearly scaled to match, on average, a target acceleration response spectrum (Figure 2.4). In this case, the median response

spectrum of the suite matches the target response spectrum at all frequencies, but none of the individual motions matches the target spectrum at all frequencies. Alternatively, recorded motions can be modified through spectral matching such that each motion matches the target spectrum across all frequencies (Figure 2.4). None of these motions has a response spectrum that is representative of a motion that could be recorded during an earthquake, but each matches the target spectrum at all frequencies.

To avoid selection, scaling, and matching of input acceleration time histories, the random vibration theory (RVT) approach can be used. In this case, the input motion is characterized solely by the amplitude of the FAS and the ground motion duration (T_{gm}). Because only the amplitudes of the FAS are known, without the associated phase angles, the specified FAS cannot be converted into an acceleration-time series. However, the FAS can be used to calculate time domain parameters of motion such as PGA and spectral acceleration (S_a). These values are obtained from the FAS using Parseval's Theorem and extreme value statistics. A review of these RVT procedures are given below, but more detailed information can be found in Boore (2003), Rathje and Kottke (2008), and Silva et al. (1996).

The root-mean-square acceleration (a_{rms}) can be computed from the FAS using Parseval's Theorem and the root-mean-squared duration (T_{rms}) using.:

$$a_{rms} = \sqrt{\frac{2}{T_{rms}} \int_0^\infty |A(f)|^2 \, \mathrm{d}f} = \sqrt{\frac{m_0}{T_{rms}}} \tag{2.2}$$

where $A(f)$ is the Fourier amplitude at frequency f, and m_0 is the zero-th moment of the FAS. The root-mean-squared duration is equal to the ground motion duration (T_gm) when computing the PGA, but requires an oscillator correction for computing the spectral acceleration (Boore and Joyner, 1984). The k-th spectral moment of the FAS is defined by:

$$m_k = 2 \int_0^\infty (2\pi f)^k |A(f)|^2 \, \mathrm{d}f \tag{2.3}$$

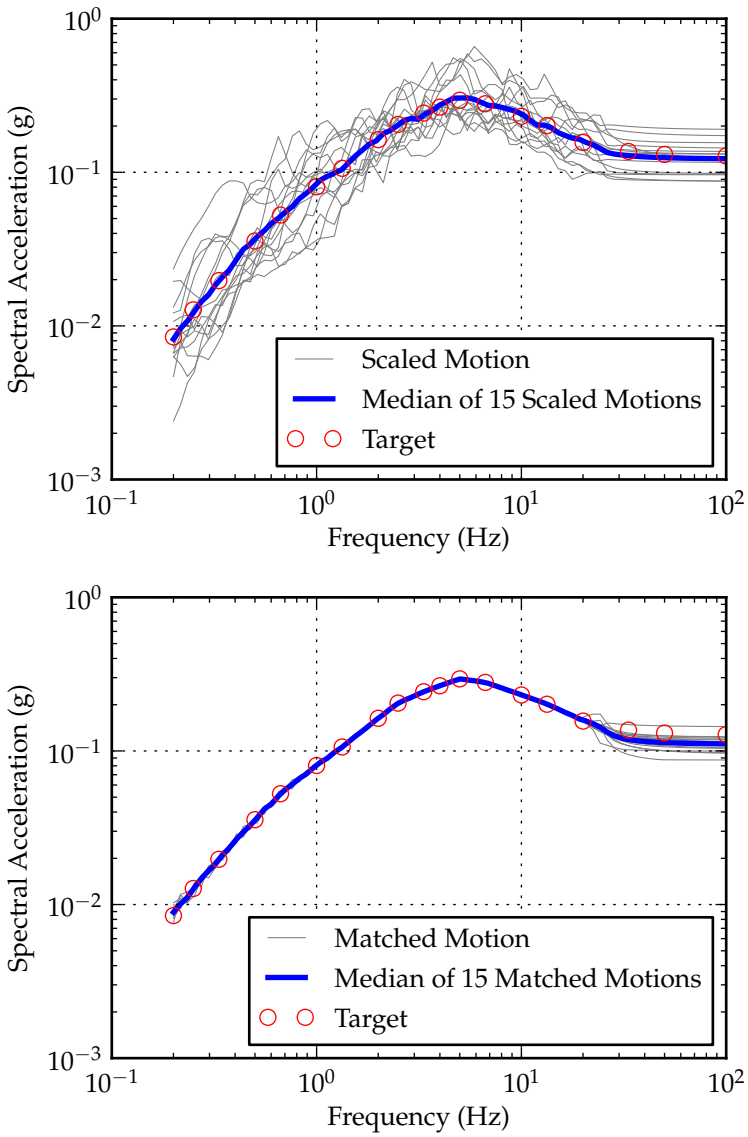

Figure 2.4: Suites of recorded motions scaled and spectrally matched to fit a target response spectrum.

To compute the peak acceleration (i.e., PGA), a_{rms} is multiplied by a peak factor (pf). Cartwright and Longuet-Higgins (1956) proposed the pf be defined as:

$$pf = \frac{a_{max}}{a_{rms}} = \sqrt{2} \int_0^{\infty} 1 - \left(1 - \xi \exp(-z^2)\right)^{N_e} \, \mathrm{d}z \tag{2.4}$$

where ξ is the bandwidth and N_e is the number of extrema. Equation (2.4) was proposed by Cartwright and Longuet-Higgins (1956). The parameters in equation (2.4) are estimated from the moments of the FAS and the ground motion duration (T_{gm}) using:

$$\xi = \sqrt{\frac{m_2^2}{m_0 m_4}} \tag{2.5}$$

and

$$N_e = \frac{T_{\mathrm{gm}}}{\pi} \sqrt{\frac{m_4}{m_2}} \tag{2.6}$$

To generate response spectral values, the FAS is multiplied by the transfer function for a single-degree-of-freedom oscillator before computation of a_{rms}, the spectral moments, and the peak factor.

Given that the input motion for RVT is specified by an FAS with no ability to reconstruct a time series, the RVT approach can only be applied to EQL site response analysis. In the RVT approach, the input rock FAS is specified and multiplied by the amplitude of the transfer function that represents wave propagation for the site. The surface FAS is converted to a surface response spectrum using the RVT methodology outlined above. The RVT response spectrum represents the average response spectrum at the surface, and thus provides in one analysis the same information as the average from a suite of input motions from time-series analysis. There are several ways in which the input FAS can be specified for RVT analysis. Seismological theory can be used to generate an FAS based on earthquake magnitude, source-to-site distance, and additional seismological parameters, or an FAS can be generated that is consistent with a target

input rock acceleration response spectrum or an FAS from a suite of time series. These different methods are discussed and compared in Chapter 4.

2.5 Linear Elastic Simplification

In both equivalent-linear and nonlinear methods, the strain dependence of the properties can obscure the differences of various approaches and methods. In this report, strain-independent linear-elastic (LE) analyses are used as an initial point of comparison. In the equivalent-linear method, the linear-elastic simplification is achieved by using the maximum shear-modulus value and a fixed value for the damping ratio. Whereas in the nonlinear method, the linear elastic simplification is made by defining the exponent term (s) in equation (2.1) to be zero and damping ratio is defined solely by the viscous damping (D_{min}) value. The linear-elastic simplification is made to facilitate the identification and explanation of differences not associated with discrepancies strain level. However, in comparing the actual differences it is important that the differences in computed strain level are considered.

Chapter 3

Site Profiles Analyzed

3.1 Introduction

Three sites were analyzed as part of this study to compare the different site response methods. The sites range from shallow to deep, and were selected to investigate a range of fundamental site frequencies and regional characteristics. The characteristics of these sites as well as their characterization for site response analysis are discussed in this chapter.

3.2 Turkey Flat Site

The Turkey Flat site is located in the central California Coast Range near the town of Parkfield, California. The site consists generally of 20 meters of coarse-grained alluvium over bedrock. The site characteristics presented in Table 3.1 were proposed by Real et al. (2006) and are plotted in Figure 3.1. No nonlinear curves for the soil are presented because the site will only be used in LE analyses that require only a prescribed damping. The natural frequency of a site (f_s) can be estimated as the

quarter-wavelength frequency, using:

$$f_s = \frac{\overline{V_s}}{4H} \tag{3.1}$$

where H is the depth to bedrock and $\overline{V_s}$ is the time-averaged shear-wave velocity defined by:

$$\overline{V_s} = \frac{\sum_i h_i}{\sum_i h_i / V_{s,i}} \tag{3.2}$$

where h_i and $V_{s,i}$ are the thickness and shear-wave velocity, respectively, of layer i. Using equation (3.1) the site frequency for Turkey Flat is estimated to be 4.76 Hz.

Depth (m)	**Thickness** (m)	**Soil Type**	$\mathbf{V_s}$ (m/s)	$\gamma_\mathbf{t}$ (kN/m^3)	**Damping** (%)
0	2.4	Alluvium	135	18	5
2.4	5.2	Alluvium	460	18	5
7.6	13.7	Alluvium	610	18	5
21.3	∞	Bedrock	1340	22	1

Table 3.1: The shear-wave velocity profile for the Turkey Flat site (Real, 1988).

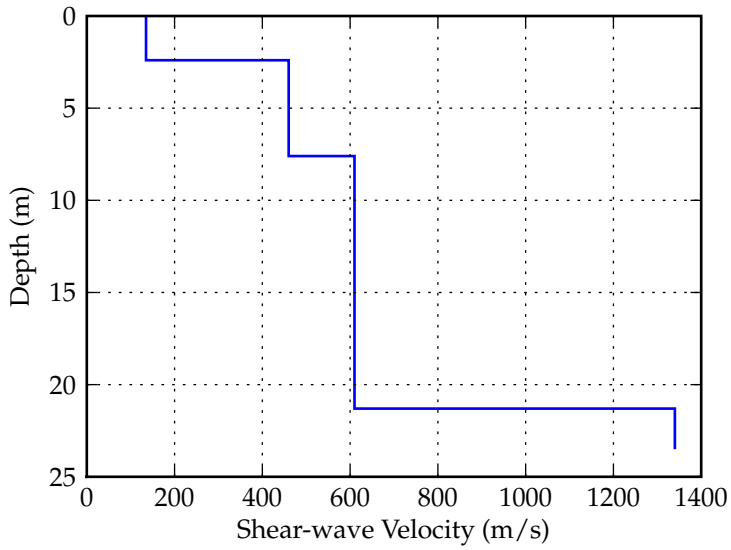

Figure 3.1: The shear-wave velocity profile of the Turkey Flat site (Real, 1988).

3.3 Sylmar County Hospital Site

The Sylmar County Hospital Parking Lot (SCH) site is located in the San Fernando Valley of Southern California and consists of 90 meters of alluvium over rock. The site characteristics used in this study are based on the measurement made by Gibbs et al. (1999), but modified to reduce the potential for large strains in the low-velocity surface layer. The site characteristics used in analysis are presented in Table 3.2 and in Figure 3.2. The quarter-wavelength site frequency is 1.16 Hz. The nonlinear soil properties were modeled with four different nonlinear curves to capture the influence of confining stress on nonlinear soil response. The empirical model of Darendeli (2001) was used and the plasticity index, over-consolidation ratio, and mean confining pressures used in the model for each of the soil types are presented in Table 3.3. Not shown are the number of cycles and excitation frequency used in the model, which were assumed to be 10 and 1 Hz, respectively. Figure 3.2 shows a comparison of the nonlinear curves computed with the Darendeli (2001) model and the fit of the MKZ model to the curves.

There is generally good agreement between the curves, except that the MKZ damping curves are higher at strains greater than about 0.1%. The resulting MKZ parameters are listed in Table 3.3. The bedrock layer was assumed to have a damping ratio of 1%.

Depth (m)	**Thickness** (m)	**Soil Type**	$\mathbf{V_s}$ (m/s)
0	6	Alluvium (0.36 atm)	250
6	25	Alluvium (2.2 atm)	300
31	30	Alluvium (5.6 atm)	460
61	30	Alluvium (7.7 atm)	700
91	∞	Bedrock	760

Table 3.2: The shear-wave velocity profile for the SCH site (Chang, 1996).

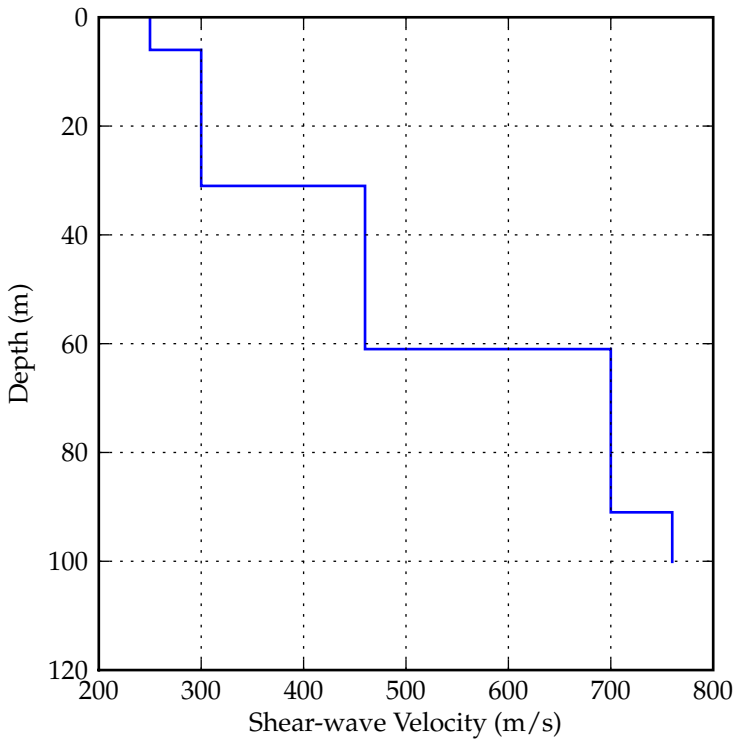

Figure 3.2: The shear-wave velocity profile of the SCH site (Chang, 1996).

Soil Type	Unit Wt. (kN/m^3)	Darendeli Parameters $\sigma'_{\mathbf{m}}$ (atm)	PI	OCR	MKZ Parameters α	$\gamma_{\mathbf{r}}$ (%)	s	$\mathbf{D}_{\mathrm{min}}$ (%)
Alluvium (0.36 atm)	18	0.36	0	1.0	1.237	3.25E-02	0.772	0.438
Alluvium (2.2 atm)	18	2.2	0	1.0	0.856	5.10E-02	0.816	0.388
Alluvium (5.6 atm)	19	5.6	0	1.0	0.605	5.18E-02	0.837	0.336
Alluvium (7.7 atm)	22	7.7	0	1.0	0.515	4.97E-02	0.844	0.317
Bedrock	22	–	–	–	–	–	–	–

Table 3.3: The soil types and model parameters of the SCH site profile.

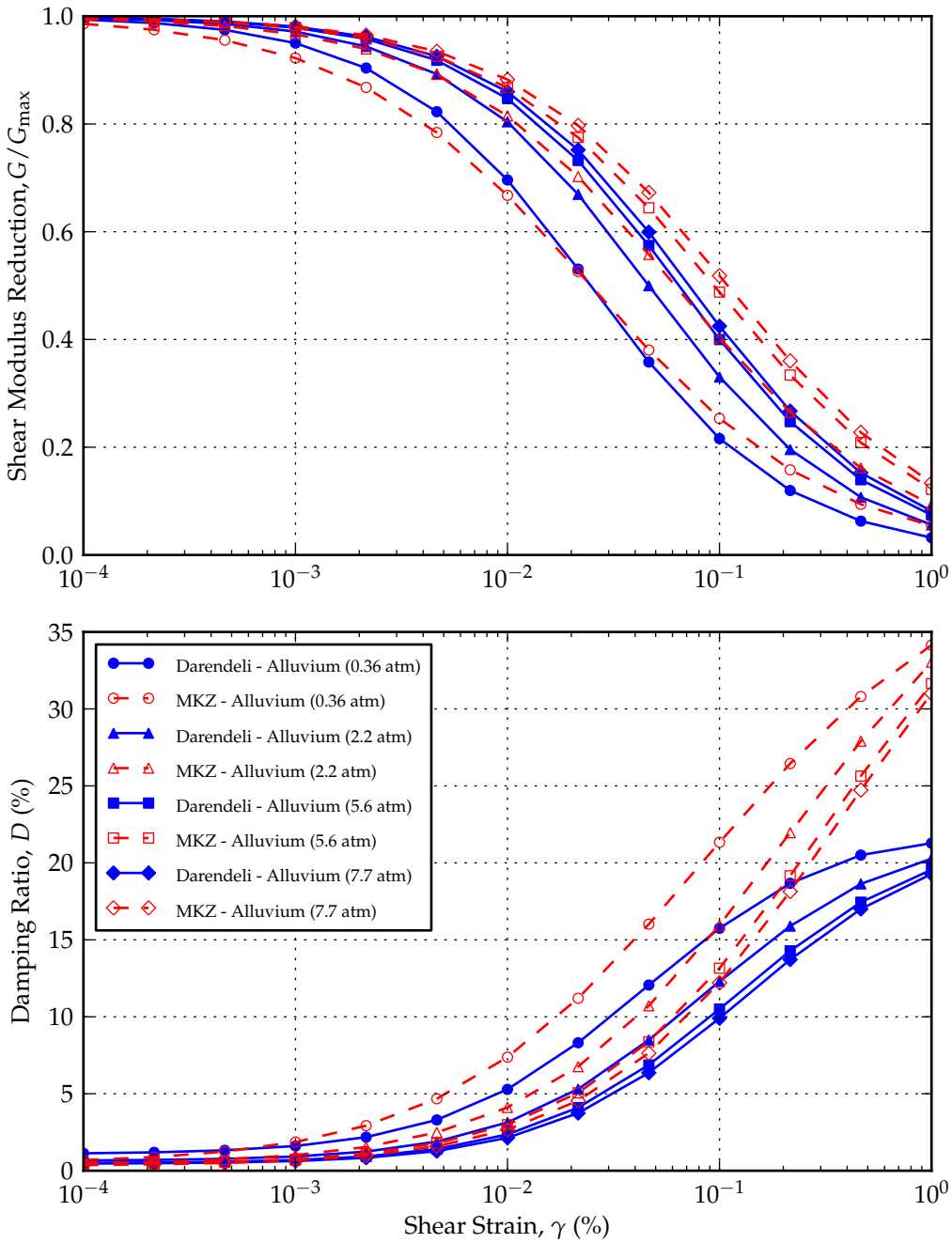

Figure 3.3: The Darendeli (2001) and MKZ curves for the SCH site.

3.4 Calvert Cliffs Site

The Calvert Cliffs (CC) site is located in Maryland on the coast of Chesapeake Bay. The site consists of alternating layers of sand and clay/silt to a depth of over 750 meters (UniStar Nuclear Services, 2007). The site was modeled using the site characteristics reported in UniStar Nuclear Services (2007), presented in Table 3.4 and Figure 3.4. The site frequency was estimated to be 0.21 Hz based on the quarter-wavelength method.

The nonlinear properties of the soil types were modeled using Darendeli (2001), as opposed to the generic EPRI curves used in UniStar Nuclear Services (2007), because the Darendeli (2001) models captures both the stress dependence and variation in soil type (i.e., plasticity index). The UniStar Nuclear Services (2007) report provided the soil properties required for the Darendeli (2001) model for the top five layers (i.e., Terrance Sand, Chesapeake Clay/Silt (1), Chesapeake Cemented Sand, Chesapeake Clay/Silt (2), and Nanjemoy Sand). The soil properties for the remaining four soil types (i.e., Nanjemoy Clay/Silt, Aquia-Brightseat Sand, Patapsco Sand, and Patuxent/Arundel Clay) were estimated based on the nonlinear curves used in the UniStar Nuclear Services (2007) report. Between the Patuxent/Arundel Clay and the granite bedrock exists a nine meter zone of weathered bedrock which was assumed to behave in a linear-elastic manner (i.e., strain independent properties) with a damping ratio of 0.50%. The bedrock was assumed to have a damping of 0.30%. The information regarding the nonlinear model for each of the soil types is summarized in Table 3.5 with the nonlinear curves for the Darendeli (2001) model and for the MKZ model plotted in Figures 3.5, 3.6, and 3.7. As with the SCH site, the number of cycles and excitation frequency were assumed to be 10 and 1 Hz, respectively. Again, the MKZ damping curves deviate from the Darendeli (2001) curves at larger strains.

Depth (m)	**Thickness** (m)	**Soil Type**	$\mathbf{V_s}$ (m/s)
0.0	2.4	Terrace Sand	241
2.4	5.2	Terrace Sand	335
7.6	4.6	Chesapeake Clay/Silt (1)	335
12.2	4.6	Chesapeake Cemented Sand	442
16.8	4.6	Chesapeake Cemented Sand	549
21.3	4.6	Chesapeake Cemented Sand	344
25.9	4.6	Chesapeake Cemented Sand	530
30.5	10.7	Chesapeake Clay/Silt (2)	381
41.1	45.7	Chesapeake Clay/Silt (2)	381
86.9	6.1	Nanjemoy Sand	546
93.0	3.0	Nanjemoy Sand	710
96.0	12.2	Nanjemoy Sand	619
108	13.7	Nanjemoy Sand	588
122	30.5	Nanjemoy Clay/Silt	671
152	39.9	Aquia-Brightseat Sand	671
192	138	Patapsco Sand	671
331	152	Patapsco Sand	710
483	44.5	Patapsco Sand	777
528	108	Patuxent/Arundel Clay	777
636	136	Patuxent/Arundel Clay	853
772	3	Weathered Granite	1524
775	3	Weathered Granite	2134
778	∞	Bedrock	2804

Table 3.4: The shear-wave velocity profile for the CC site (UniStar Nuclear Services, 2007).

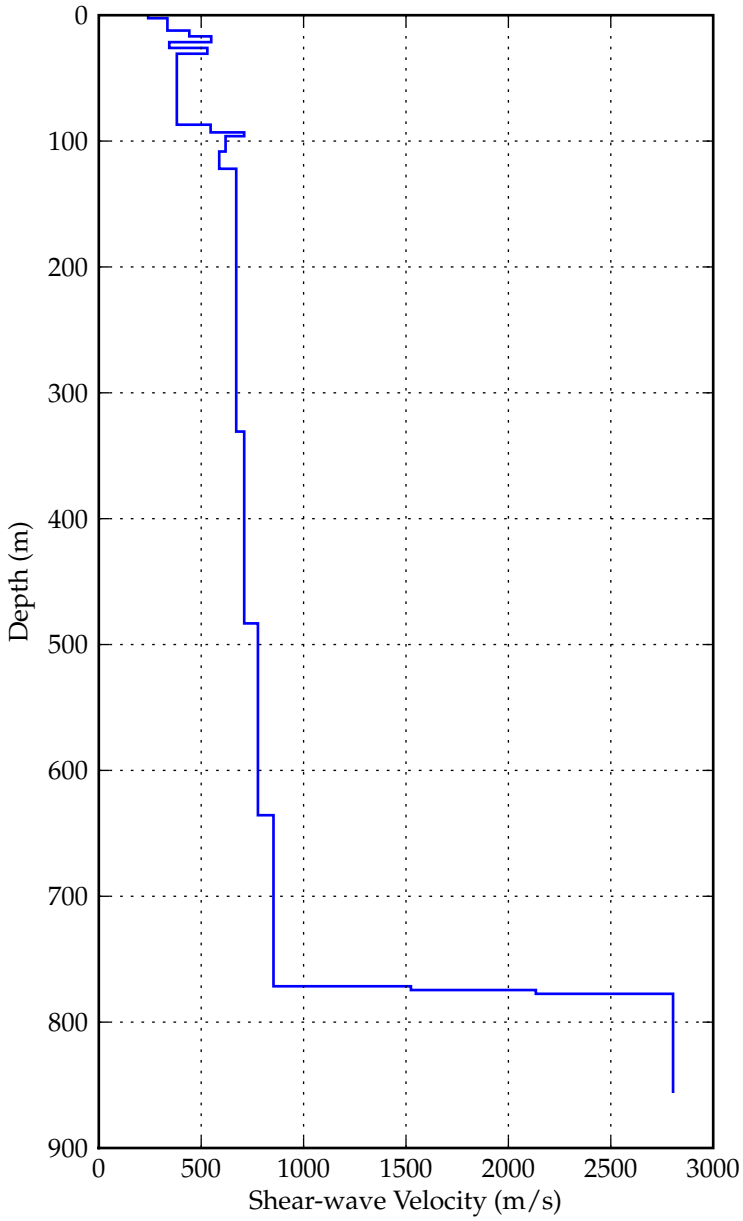

Figure 3.4: The shear-wave velocity profile of the CC site (UniStar Nuclear Services, 2007).

Soil Type	Unit Wt. (kN/m^3)	Darendeli Parameters σ'_m (atm)	PI	OCR	MKZ Parameters α	γ_r (%)	s	D_{min} (%)
Terrace Sand	18.85	0.57	0	4.0	1.067	3.45E-02	0.784	0.437
Chesapeake Clay/Silt (1)	18.07	1.22	35	4.0	0.320	3.20E-02	0.802	0.858
Chesapeake Cemented Sand	18.85	2.51	20	3.0	0.358	3.64E-02	0.821	0.595
Chesapeake Clay/Silt (2)	17.28	4.25	45	3.0	0.235	4.60E-02	0.833	0.731
Nanjemoy Sand	18.85	6.90	30	3.0	0.223	4.24E-02	0.846	0.550
Nanjemoy Clay/Silt†	17.28	8.94	45	3.0	0.168	4.48E-02	0.852	0.613
Aquia-Brightseat Sand†	20.42	11.1	20	3.0	0.178	3.28E-02	0.857	0.431
Patapsco Sand†	20.42	25.6	20	2.0	0.196	5.03E-02	0.874	0.354
Patuxent/Arundel Clay†	19.64	39.4	50	2.0	0.092	4.38E-02	0.887	0.450
Weathered Granite‡	22.00	–	–	–	0.0	1.	1.	0.500
Bedrock	25.13	–	–	–				

† Plasticity index and over-consolidation ratio estimated.
‡ Assumed to be linear-elastic with a damping of 0.50%.

Table 3.5: The soil types and model parameters of the CC site profile.

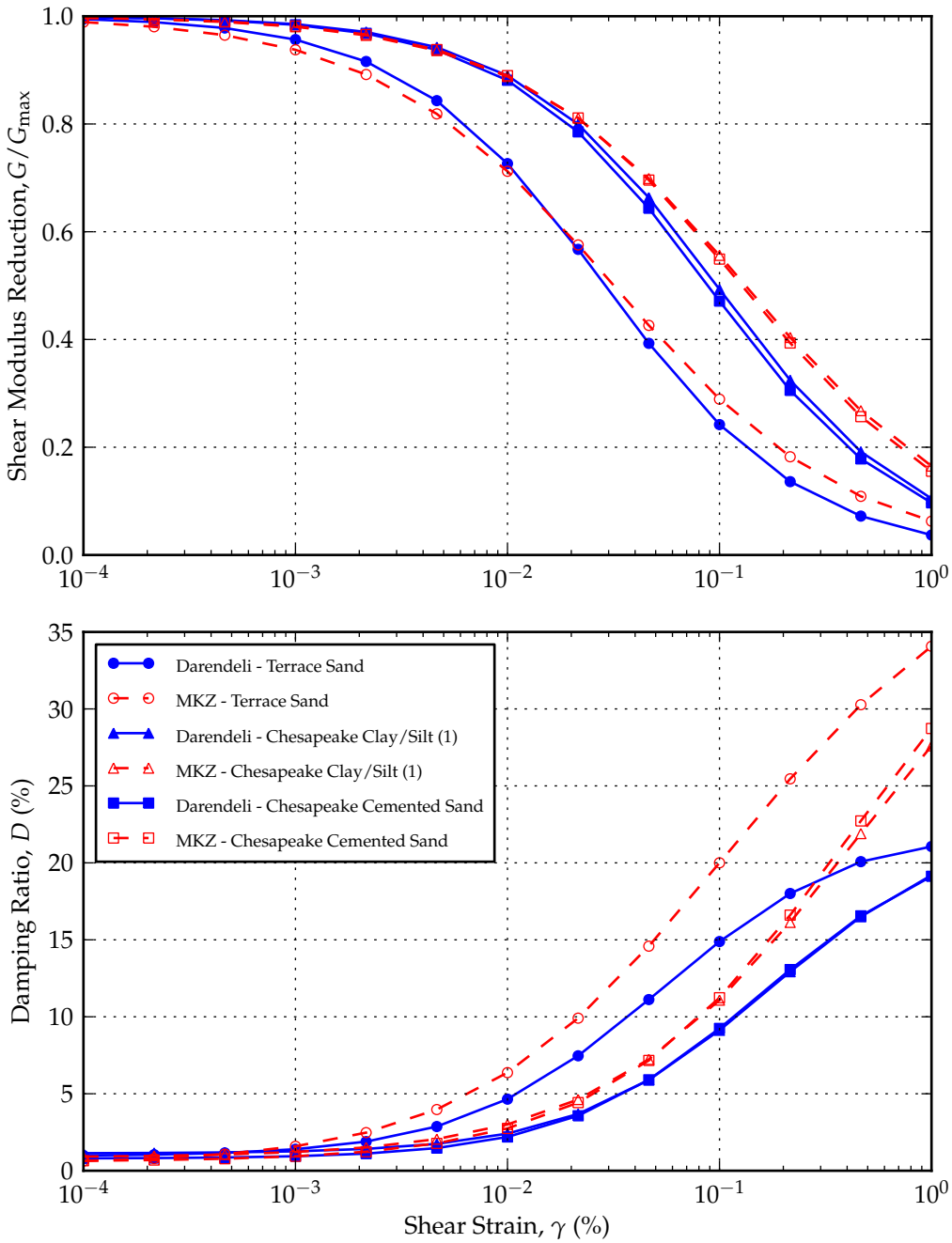

Figure 3.5: The Darendeli (2001) and MKZ curves for the CC site (soil types 1 to 3).

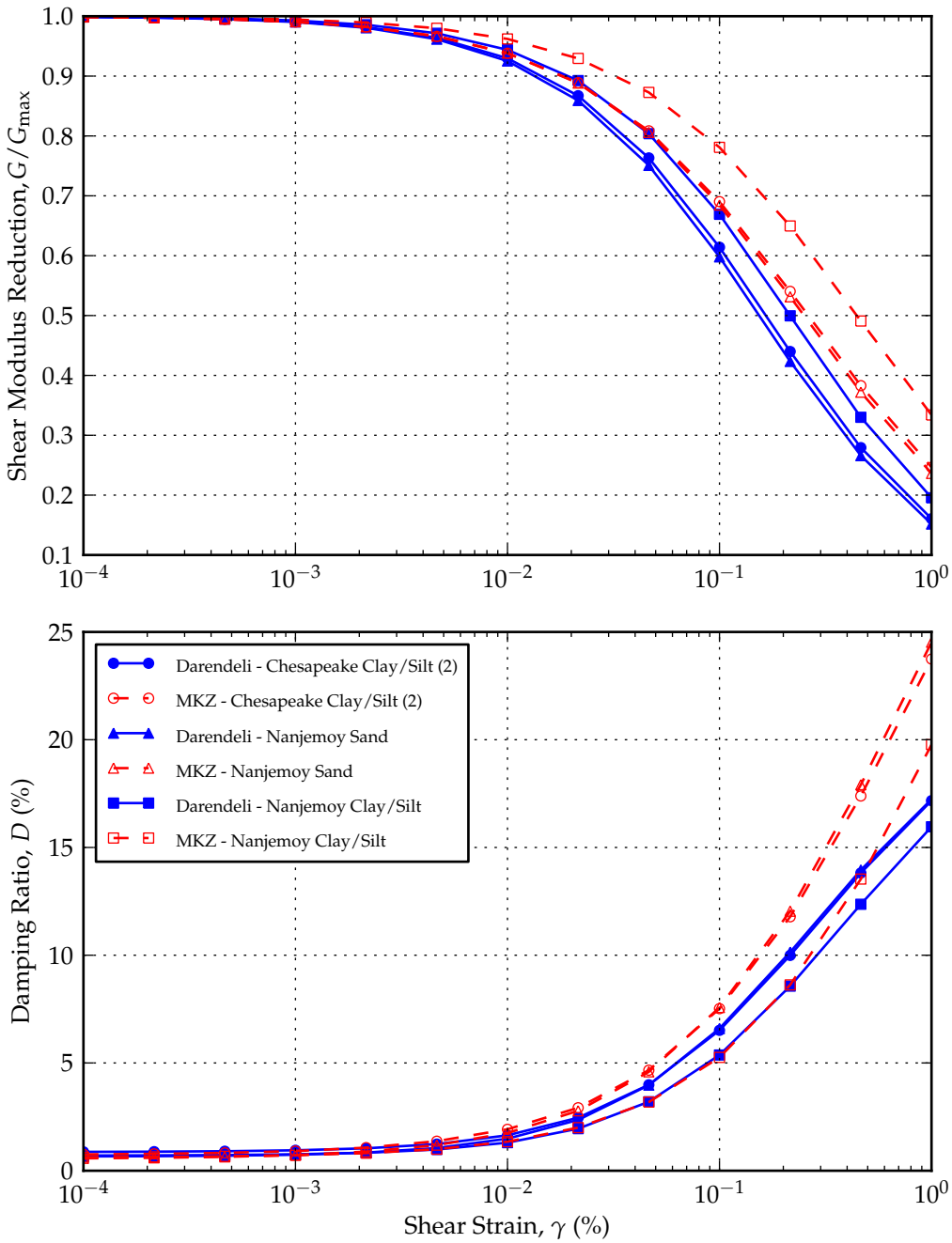

Figure 3.6: The Darendeli (2001) and MKZ curves for the CC site (soil types 4 to 6).

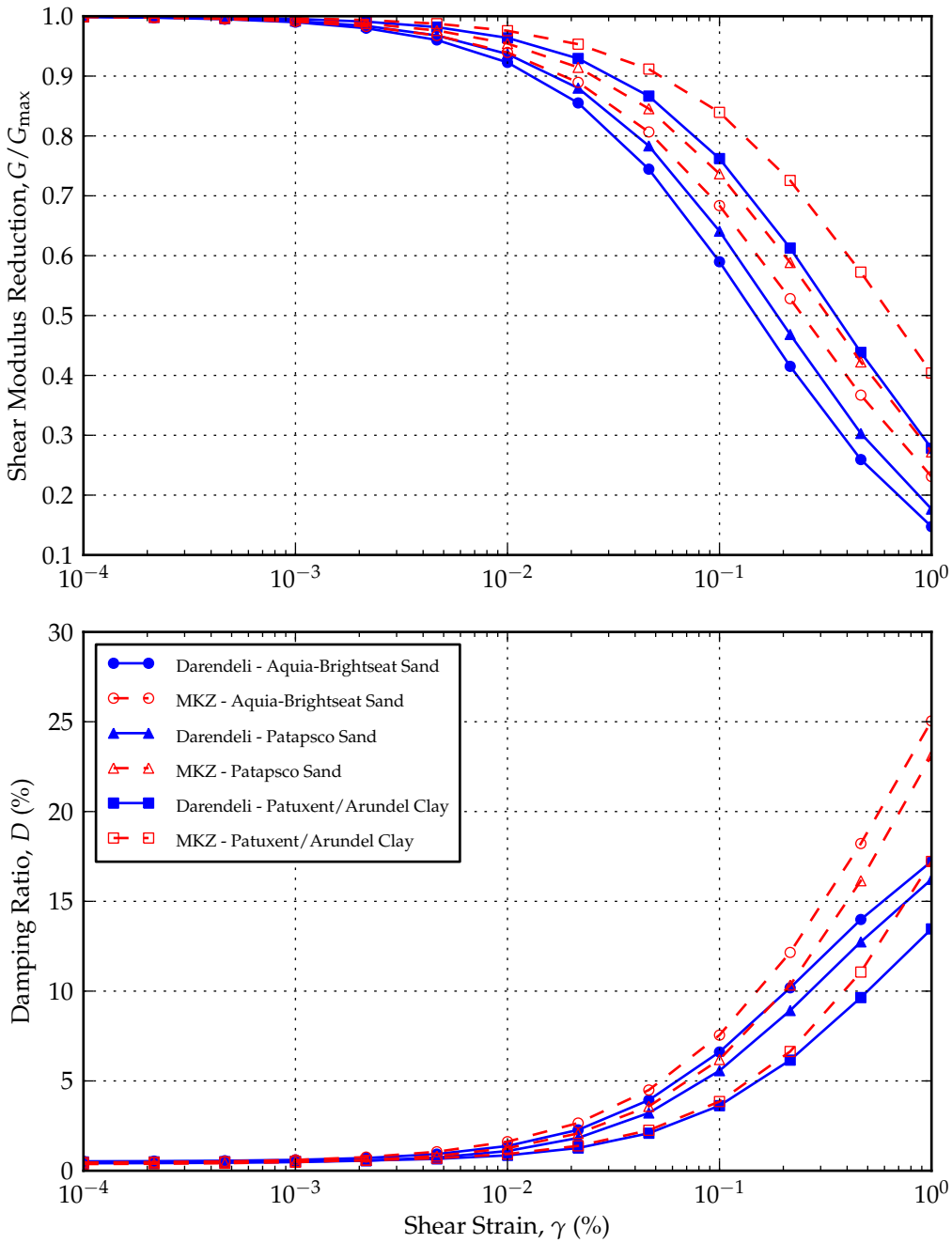

Figure 3.7: The Darendeli (2001) and MKZ curves for the CC site (soil types 7 to 9).

Chapter 4

Input Ground Motion Characterization

4.1 Introduction

Three separate suites of input ground motions were generated for the site response analyses for a hypothetical magnitude 6.5 earthquake at a distance of 20 km. The first suite consisted of numerically simulated time series generated via seismological simulations using a theoretical FAS and stochastic simulation methods using `SMSIM` (Boore, 2003). The second suite consisted of recorded motions selected and scaled to fit a response spectrum from a ground motion prediction equation. The third suite was generated by spectral matching the selected motions to fit the response spectrum from the ground motion prediction equation. The consistency of each of the suites of time series with the input required for RVT analysis (i.e., the Fourier amplitude spectra and response spectra) is also considered.

4.2 Stochastically Simulated Ground Motions

Stochastic simulation of ground motions is commonly used to generate time series in situations where there is a lack of recorded motions, such as for large events or in less tectonically active areas. The stochastic method generates a FAS based on seismological models that incorporate the effects of the source, path, and site (Boore, 2003). In the context of seismological models, the site effect represents the changes in shear-wave velocity from the depth of the fault rupture to the bedrock at the site. To generate the simulated time series, the FAS is used to modify a windowed time series of white noise (Boore, 2003). Stochastically simulated motions were used in this study because they could be most directly compared with RVT site response analyses that use a seismological FAS as input.

The FAS for a magnitude 6.5 earthquake at a distance of 20 km was computed using the program `SMSIM` (Boore, 2005). The parameters characterizing the effects of the source, path, and site represent typical values for shallow crustal events in Western North America as given by Boore (2005). The key parameters are presented in Table 4.1 and the complete input `SMSIM` file is attached in Appendix A.1. The Fourier amplitude spectrum generated from these parameters for a magnitude (M_w) 6.5 event at a distance (R) of 20 km is shown in Figure 4.1.

One-hundred time series were generated with `SMSIM` from the FAS in Figure 4.1. Figure 4.2 shows the Fourier amplitude spectrum of a single simulated motion and its

Parameter	**Value**
Source spectrum	Brune ω-squared, point source
Stress drop, $\Delta\sigma$ (bar)	80
Site diminution, κ (sec)	0.03
Density, ρ (g/cm^3)	2.8
Shear-wave velocity of crust (km/sec)	3.6

Table 4.1: The selected input parameters used by `SMSIM` for the calculation of the Fourier amplitude spectrum shown in Figure 4.1.

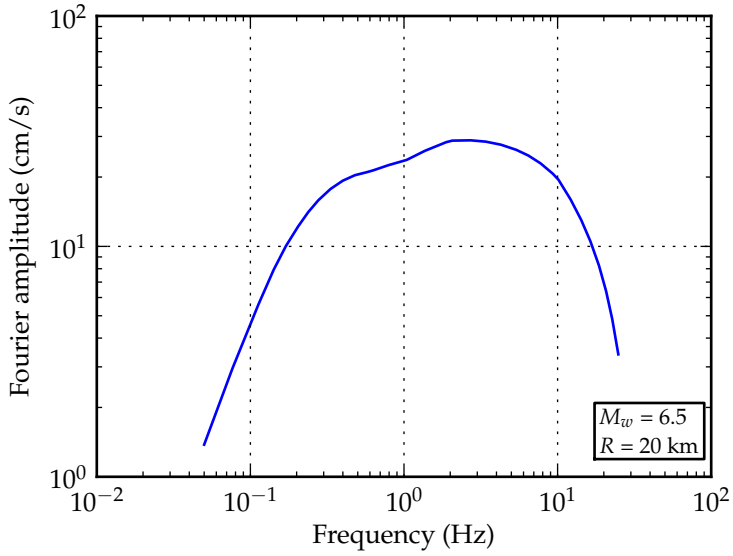

Figure 4.1: The stochastic FAS computed with seismological theory using the parameters listed in Table 4.1.

corresponding time series is shown in Figure 4.3. Figure 4.2 also shows the mean of 100 simulations and the stochastic seismological spectrum. A single motion cannot match the stochastic FAS, but the average FAS over a suite of motions will match the stochastic FAS. The average response spectrum for the 100 simulated motions is shown in Figure 4.4 along with the response spectrum of a single simulated motion. For comparison, the FAS in Figure 4.1 was used with RVT and a duration (T_{gm}) of 6.8 seconds to compute a response spectrum. This spectrum is also shown in Figure 4.4 and demonstrates excellent agreement with the median of the simulated time series. This result indicates that RVT can provide a response spectrum consistent with a stochastic suite of time series based on the same FAS.

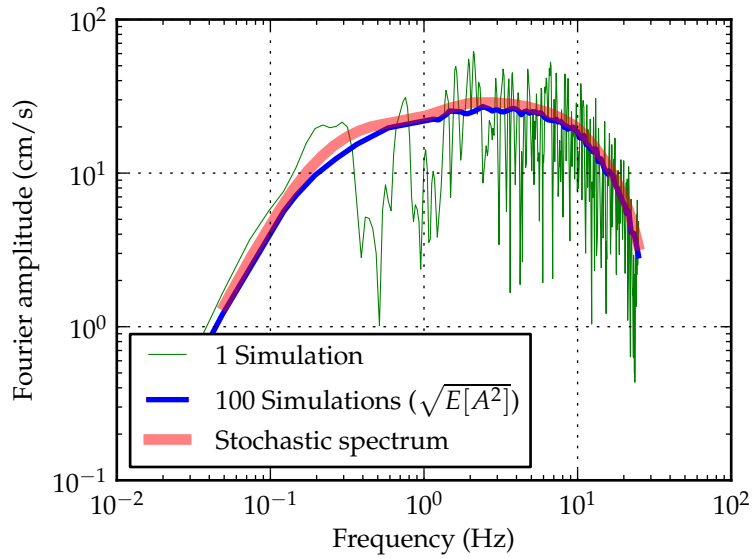

Figure 4.2: A FAS of a single simulated ground motion, along with the average of 100 stochastic simulations and the target FAS

.

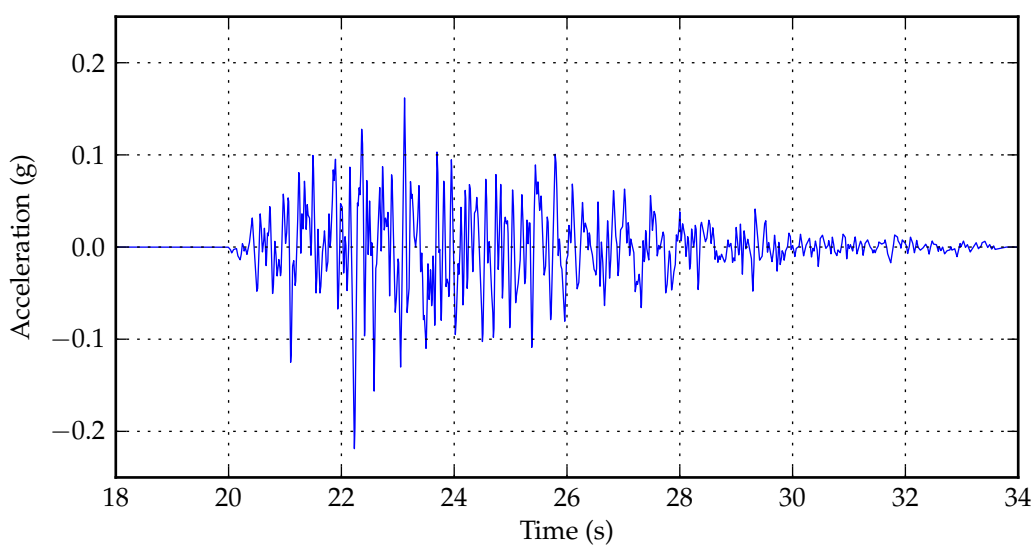

Figure 4.3: The acceleration-time series of a single simulated ground motion.

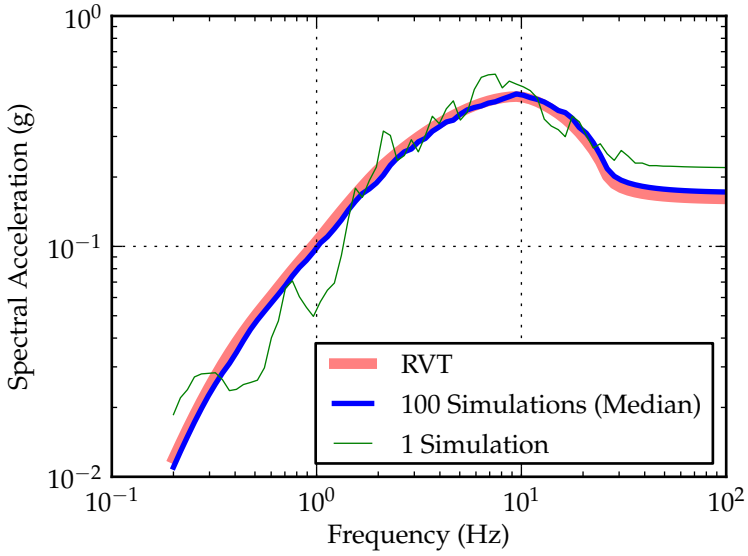

Figure 4.4: The response spectrum of a single simulated ground motion, along with the median of 100 stochastic simulations and the response spectrum computed with RVT.

4.3 Recorded Ground Motions

Empirical ground motion prediction equations can be used to specify a target acceleration response spectrum for use in selecting and scaling recorded time series. The target response spectrum used in this study was from the Boore and Atkinson (2008) ground motion prediction equation. The target response spectrum for the magnitude (M_w) 6.5 at a distance (R) of 20 km scenario event is shown in Figure 4.5 and a suite of fifteen motions was selected to match this target.

4.3.1 Ground Motion Selection

The recorded motions were selected and scaled using the framework of Kottke and Rathje (2008a). A catalog of potential motions was selected from the Next Generation Attenuation (NGA) database (`http://peer.berkeley.edu/nga/`) using the parameters presented in Table 4.2. These parameters (magnitude range, distance range, faulting

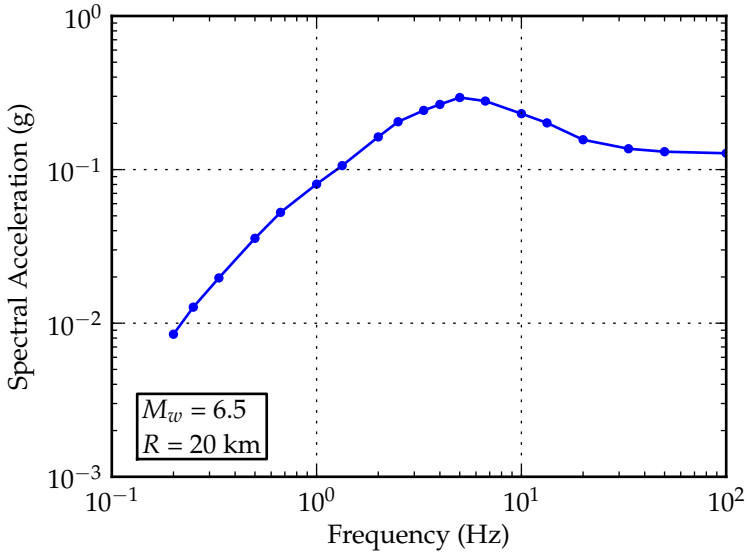

Figure 4.5: The target acceleration response spectrum computed using the Boore and Atkinson (2008) ground motion prediction equation.

mechanism, and rock site conditions) are specified to represent the scenario event but are expanded such that a variety of motions are present in the catalog. The search resulted in a total of 105 ground motions from 14 events, as summarized in Table 4.3.

The Kottke and Rathje (2008a) procedure generates a number of potential suites through a combination of trial and error, and iteration. The top suites that best matched the target response spectrum were saved and from these suites one suite was selected. The suite of motions was scaled to match the target response spectrum and

Parameter	**Values**
Magnitude (M_w)	6.1 to 6.94
Distance	5 to 40 km
Fault Type	Strike-Slip, Reverse, and Normal
$V_{s,30}$	600 to 2500 m/s
GeoMatrix 1 Class	A, B, and I

Table 4.2: The parameters used to define the ground motion library for consideration by the selection algorithm.

minimize the variation within the suite. The scaled response spectra for the final suite of fifteen ground motions selected to fit the scenario event are shown in Figure 4.6 and the motions are listed in Table 4.4. The acceleration-, velocity-, and displacement-time series, as well as the acceleration response spectra, for all selected ground motions are included in Appendix B. The median of the suite shows excellent agreement with the target response spectrum (Figure 4.6) with a root-mean-square error of 0.031 and a maximum error of 7.4%. Nonetheless, within the suite each motion varies significantly from the median.

The FAS of the scaled ground motions are shown in Figure 4.7 and an FAS for use with RVT was developed by calculating the average squared Fourier amplitudes (Boore, 2003). The average of the squared Fourier amplitudes are used because RVT uses squared Fourier amplitudes in the calculations (see equation (2.3)). The median duration between the 5% and 75% of the maximum Arias intensity was calculated to be 4.83 seconds for the suite of ground motions. Using this duration as T_{gm} with the average FAS, the expected response spectrum was computed using RVT is shown in Figure 4.8. The response spectrum computed with RVT fits well at frequencies above about 10 Hz, but slightly over predicts spectral accelerations at lower frequencies.

Event	Magnitude	Fault Type	No. of Records
San Fernando	6.61	Reverse	6
Imperial Valley	6.53	Strike-Slip	2
Victoria, Mexico	6.33	Strike-Slip	2
Irpinia, Italy	6.9	Normal	10
Irpinia, Italy	6.2	Normal	10
Coalinga, 1983	6.36	Reverse	3
Morgan Hill	6.19	Strike-Slip	6
Loma Prieta	6.93	Reverse-oblique	16
Northridge	6.69	Reverse	26
Kobe, Japan	6.9	Strike-Slip	2
Kozani, Greece	6.4	Normal	2
Chi-Chi, Taiwan (3)	6.2	Reverse	8
Chi-Chi, Taiwan (4)	6.2	Strike-Slip	2
Chi-Chi, Taiwan (5)	6.2	Reverse	2
Chi-Chi, Taiwan (6)	6.3	Reverse	8

Table 4.3: The earthquake events and number of records used in the library of ground motions.

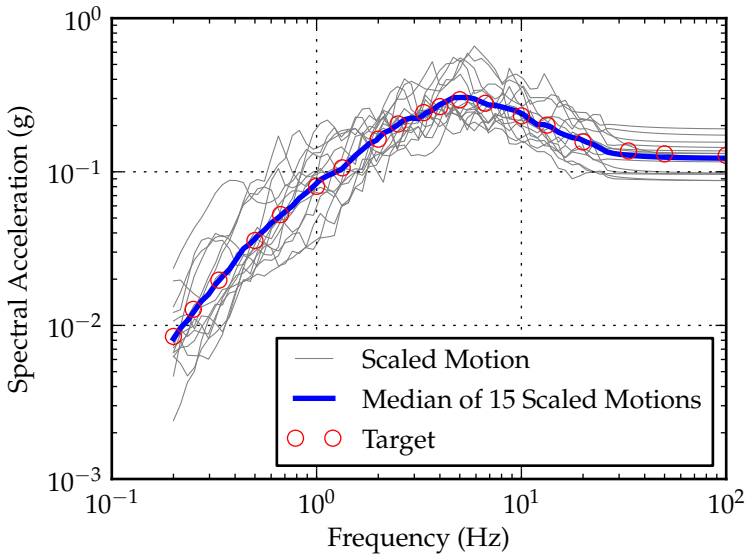

Figure 4.6: The response spectra of the fifteen ground motions scaled to the target response spectrum.

Filename	**Scale**	**PGA†** (g)	**PGV†** (cm/sec)	**PGD†** (cm)	$\mathbf{D_{5-75}}$ (sec)	$\mathbf{D_{5-95}}$ (sec)	**Details**
CHICHI06-TCU076-E	0.79	0.10	8.99	3.91	7.60	12.48	Chi-Chi Aftershock 09/25/99, 23:52, TCU076, E
ITALY-A-AUL270	1.55	0.10	9.46	5.71	13.11	19.21	Irpinia, 11/23/80, 19:34:54, Auletta, 270
ITALY-A-BAG000	0.62	0.09	13.74	5.77	5.26	19.51	Irpinia, 11/23/80, 19:34, Bagnoli Irpino, 000
ITALY-A-STU270	0.25	0.09	12.73	7.87	6.23	15.22	Irpinia, 11/23/80, 19:34:54, Sturno, 270
ITALY-B-AUL270	4.19	0.10	9.70	3.52	7.89	17.80	Irpinia, 11/23/80, 19:35:04, Auletta, 270
KOZANI-KOZ–L	0.73	0.16	6.83	1.21	2.49	6.44	Kozani, 05/13/95, 08:47, Kozani, L
LOMAP-G01000	0.33	0.14	10.41	2.09	2.00	6.53	Loma Prieta, 10/18/89, 00:05, Gilroy Array #1, 000
LOMAP-GIL067	0.32	0.11	9.18	2.04	1.57	5.00	Loma Prieta, 10/18/89, 00:05, Gilroy Gavilan Coll, 067
MORGAN-GIL337	2.01	0.19	5.77	1.90	4.70	8.18	Morgan Hill, 04/24/84, 04:24, Gilroy Gavilan Coll, 337
NORTHR-H12180	0.66	0.17	5.88	2.73	5.40	9.81	Northridge, 1/17/94, 12:31, Lake Hughes #12A, 180
NORTHR-HOW330	0.83	0.14	7.01	1.50	5.06	7.99	Northridge, 1/17/94, 12:31, Burbank - Howard, 330
NORTHR-LV1000	1.30	0.12	10.10	2.11	5.42	12.42	Northridge, 1/17/94, 12:31, Leona Valley #1, 000
NORTHR-LV3090	1.24	0.13	10.02	2.15	5.80	13.60	Northridge, 1/17/94, 12:31, Leona Valley #3, 090
NORTHR-WON185	0.76	0.13	8.97	2.11	5.12	6.67	Northridge, 1/17/94, 12:31, LA - Wonderland, 185
VICT-CPE045	0.21	0.13	6.75	2.80	4.41	8.57	Victoria, Mexico, 06/09/80, 03:28, Cerro Prieto, 045

† Scaled values

Table 4.4: The ground motions and their properties for the suite shown in Figure 4.6.

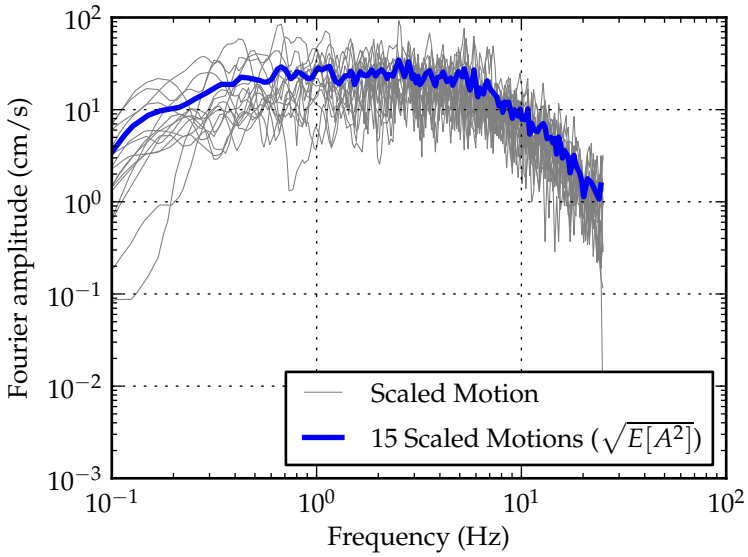

Figure 4.7: The FAS of the fifteen ground motions scaled to the target response spectrum.

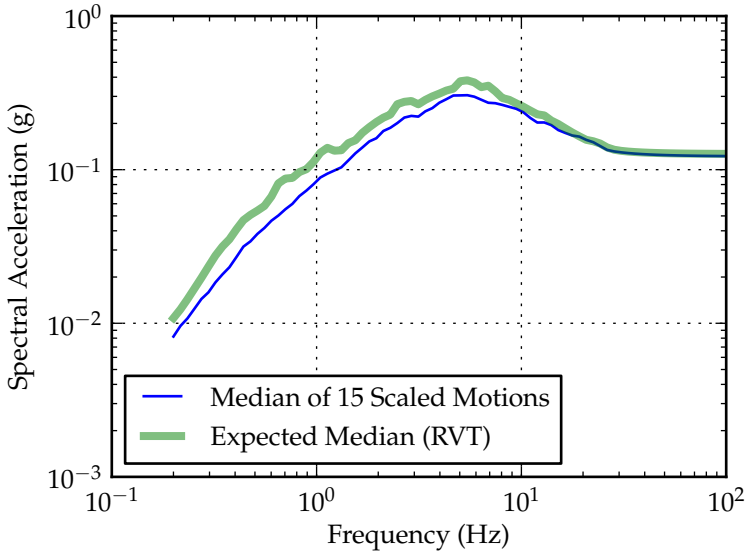

Figure 4.8: The median response spectrum of the fifteen scaled motions and an RVT motion defined by the root-mean-square FAS of the scaled motions and a duration of 4.83 seconds.

4.3.2 Maximum Usable Frequency

In defining the maximum frequency used in site response analysis, it is necessary to consider the frequency content of the input time series, the numerical model used for the site response analysis, and the frequencies of engineering interest in the design/evaluation process.

The maximum frequency captured by a time series is known as the Nyquist frequency (f_{Nyq}) and is related to the time step (Δt) by:

$$f_{\mathrm{Nyq}} = \frac{1}{2 \cdot \Delta t} \tag{4.1}$$

However, the Nyquist frequency does not typically represent the maximum usable frequency in a time series because ground motion processing involves removing the high-frequency noise using a low-pass filter. A low-pass filter is described by a low-pass filter frequency (f_{LP}) which is defined as the frequency at which the filter response is $\frac{1}{\sqrt{2}}$ (≈ 0.707) of the maximum response. The NGA time series database contains motions with f_{LP} ranging from 4 to 90 Hz, but f_{LP} for the majority of records ranges between 20 and 40 Hz, as shown in Figure 4.9. While an f_{LP} of 30 Hz may be appropriate for time series recorded in the Western US, a higher f_{LP} would be required for a time series recorded in the Central or Eastern US where the properties of the bedrock result in significant earthquake motion at higher frequencies. Abrahamson and Silva (1997) defined the maximum usable frequency as $0.80 \cdot f_{\mathrm{LP}}$. For example, a motion processed using an f_{LP} of 30 Hz would have a maximum usable frequency of 24 Hz. Frequencies above the maximum usable frequency are significantly affected by the filter response, and therefore do not represent earthquake motions and are inappropriate for consideration in an engineering analysis.

The time step and filter characteristics of the suite of selected input motions used in this study are presented in Table 4.5. The f_{LP} of the selected motions ranges between 23

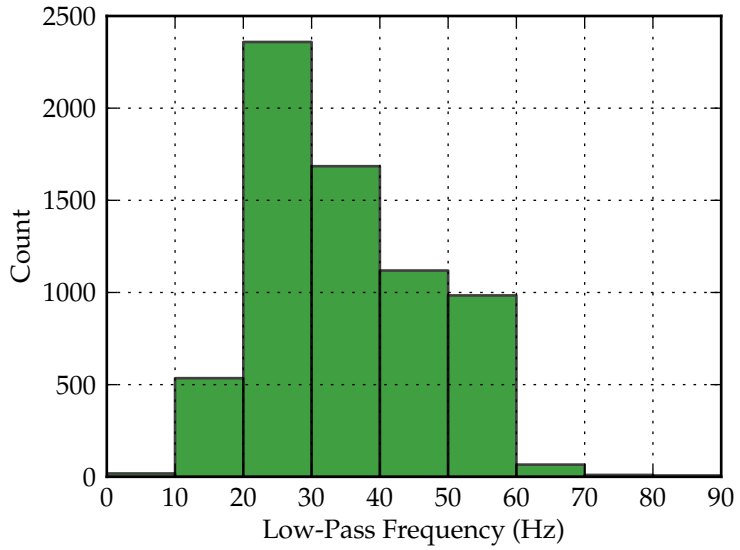

Figure 4.9: Distribution of the low-pass frequency used in the processing of motions in the NGA database.

to 62.5 Hz. Of the fifteen records, nine of the records have maximum usable frequencies less than 24 Hz ($f_{\mathrm{LP}} < 30$ Hz). For these nine motions, it would be inappropriate to consider frequencies higher than 24 Hz in the site response analysis because these high frequencies have already been modified through the processing of the time series. Furthermore, it is important that the maximum frequency be consistent between analyses performed with different motions. For this reason, it was decided to universally truncate all motions at used in this study 25 Hz. Again, it is important to acknowledge that this maximum frequency would not be appropriate for: (1) seismological conditions in the Central and Eastern US with more high frequency motion, and (2) structures (buildings and/or sites) where the dynamic response above 25 Hz is important in the design process.

The truncation of the motions was achieved by defining the Fourier amplitudes above 25 Hz to be zero. The abrupt truncation of the motion is only appropriate when the amplitude of the motion above the truncation frequency is relatively insignificant.

Filename	**Time Step** (sec)	**High Pass†** (Hz)	**Low Pass†** (Hz)
CHICHI06-TCU076-E	0.005	0.12	50.0
ITALY-A-AUL270	0.0029	0.10	30.0
ITALY-A-BAG000	0.0029	0.10	35.0
ITALY-A-STU270	0.0024	0.08	30.0
ITALY-B-AUL270	0.0029	0.30	23.0
KOZANI-KOZ–L	0.005	0.20	25.0
LOMAP-G01000	0.005	0.20	50.0
LOMAP-GIL067	0.005	0.20	45.0
MORGAN-GIL337	0.005	0.10	30.0
NORTHR-H12180	0.01	0.12	46.0
NORTHR-HOW330	0.01	0.10	30.0
NORTHR-LV1000	0.02	0.20	23.0
NORTHR-LV3090	0.02	0.20	23.0
NORTHR-WON185	0.01	0.10	30.0
VICT-CPE045	0.01	0.20	62.5

† Defined by the frequency at which the filter response is $\frac{1}{\sqrt{2}}$ (or ≈ 0.707) of the maximum response.

Table 4.5: The high-pass and low-pass frequencies of the suite of motions, as well as the recorded time step.

Thus, the effect of this truncation is most influential to records with f_{LP} greater than 25 Hz. To demonstrate the impact of the truncation on the input motion and the site response results, the `CHICHI06-TCU076-E` motion ($f_{\mathrm{Nyq}} = 100$ Hz and $f_{\mathrm{LP}} = 50$ Hz) is truncated at 25 and 50 Hz and then propagated through the Sylmar County Hospital site (see Section 3.3). Figure 4.10 shows the surface response spectra, spectral ratios, and bedrock response spectra for the motion truncated at 25 and 50 Hz, as well as the original recording with a maximum frequency of 100 Hz. The truncation at 50 Hz only slightly influences the bedrock response spectrum because of the minimal energy in the time series at frequencies above 50 Hz. However, when the motion is truncated at 25 Hz the effect on the bedrock motion is more pronounced with reduced spectral accelerations at frequencies above 20 Hz. At the surface of the site, all three motions produce nearly identical response spectra (Figure 4.10). Truncation does not affect the computed surface response because the site does not amplify the high frequencies, instead the site acts as a low-pass filter and attenuates the high-frequency content of the time series. However, the computed spectral ratio between 25 and 50 Hz is affected by truncation due to the high frequency content in the input motion. These results indicate that truncating records below f_{LP} affects the bedrock response spectrum, but does not affect the response spectrum computed at the surface for this site.

Considering the fifteen scaled motions selected for this study, only two motions (`CHICHI06-TCU076-E` and `VICT-CPE045`) have considerable earthquake motion at frequencies greater than 25 Hz (Figure 4.11). As shown in Figure 4.10, the removal of this high-frequency motion does not affect the computed surface response, although it does affect the high-frequency spectral ratios. Nonetheless, only two motions out of fifteen show this effect and therefore the median response from this suite should be minimally affected by truncation.

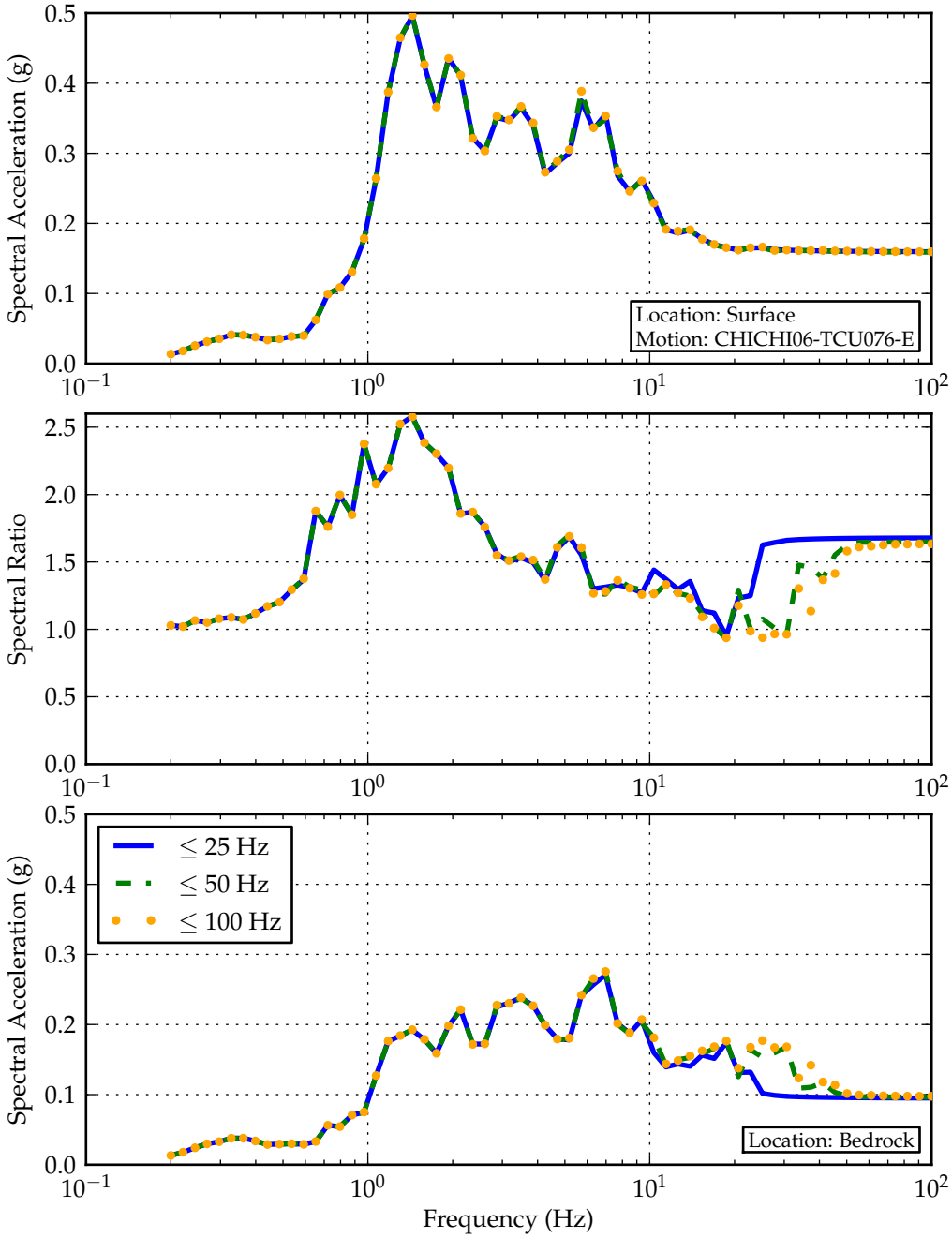

Figure 4.10: The effect of truncation on the `CHICHI06-TCU076-E` motion on the response spectrum and spectral ratio computed for the Sylmar County Hospital site.

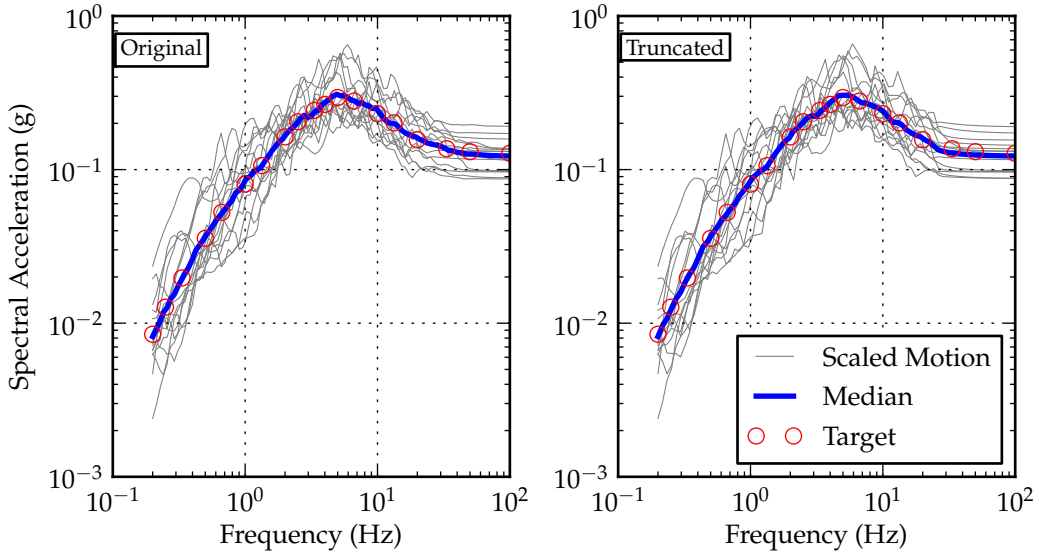

Figure 4.11: The effect of truncation on the suite of input ground motions used in this study.

4.4 Spectrally Matched Ground Motions

Spectral matching modifies the frequency content of a time series to improve the fit of the time series to a target response spectrum. Using the suite of fifteen motions selected in the previous section, the program `RSPMatch` (Abrahamson, 1992; Hancock, 2006) was used to spectrally match each record to the target response spectrum.

The spectral matching procedure is illustrated by matching the `NORTHR-WON185` motion to the target response spectrum from Figure 4.5. The frequency spacing in the target response spectrum was increased to 60 points equally spaced in log space from 0.2 to 25 Hz. Prior to modifying the time series, it was scaled to best fit (defined by the least sum of squared errors) the target response spectrum at frequencies between 0.2 and 1 Hz to reduce the required modifications to the record at low frequencies (Hancock, 2006). Figure 4.12 shows the original scaled response spectrum and the spectrally matched response spectrum along with the target response spectrum. As expected,

the spectrally matched time series shows excellent agreement with the target response spectrum over the range in matched frequencies (0.2 to 25 Hz) while maintaining some of the time domain characteristics of the original recording as shown in Figure 4.13.

`RSPMatch` superimposes wavelets on the time series that adjust the amplitudes of the oscillator responses to fit the target response spectrum at each frequency. The procedure requires that the time step of the motion be reduced to allow for the creation of the wavelets at the highest target frequencies. The time step of the time series is adjusted such that the number of samples per second is ten times greater than the maximum frequency (e.g., to spectrally match to 25 Hz requires 250 samples per second, or a time step of 0.004 seconds). The increased time step is required to create the zero-displacement wavelets used in adjusting the time series. These higher frequencies are then removed by the truncation at a maximum frequency 25 Hz prior to being used in the site response analyses.

The suite of fifteen spectrally matched motions was developed by applying a similar technique to each of the remaining motions. The individual response spectra for the spectrally matched time series matched and then truncated to 25 Hz, along with the median and target response spectra, are shown in Figure 4.14. The acceleration-, velocity-, and displacement-time series, as well as the acceleration response spectra, for all spectrally-matched ground motions are included in Appendix C. These spectrally-matched motions demonstrate excellent agreement with the target response spectrum over frequencies from 0.2 to 25 Hz. By adjusting each motion in the suite to fit the target response spectrum, the standard deviation of the suite of spectrally matched motions is greatly reduced compared to the suite of stochastically simulated or scaled ground motions, shown in Figure 4.15.

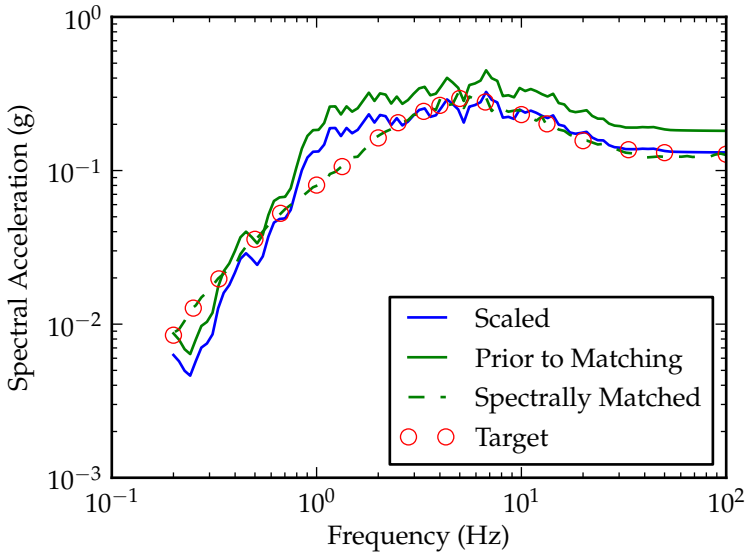

Figure 4.12: The response spectrum for the scaled, scaled prior to spectral matching, and spectrally matched versions of the `NORTHR-WON185` ground motion, along with the target response spectrum.

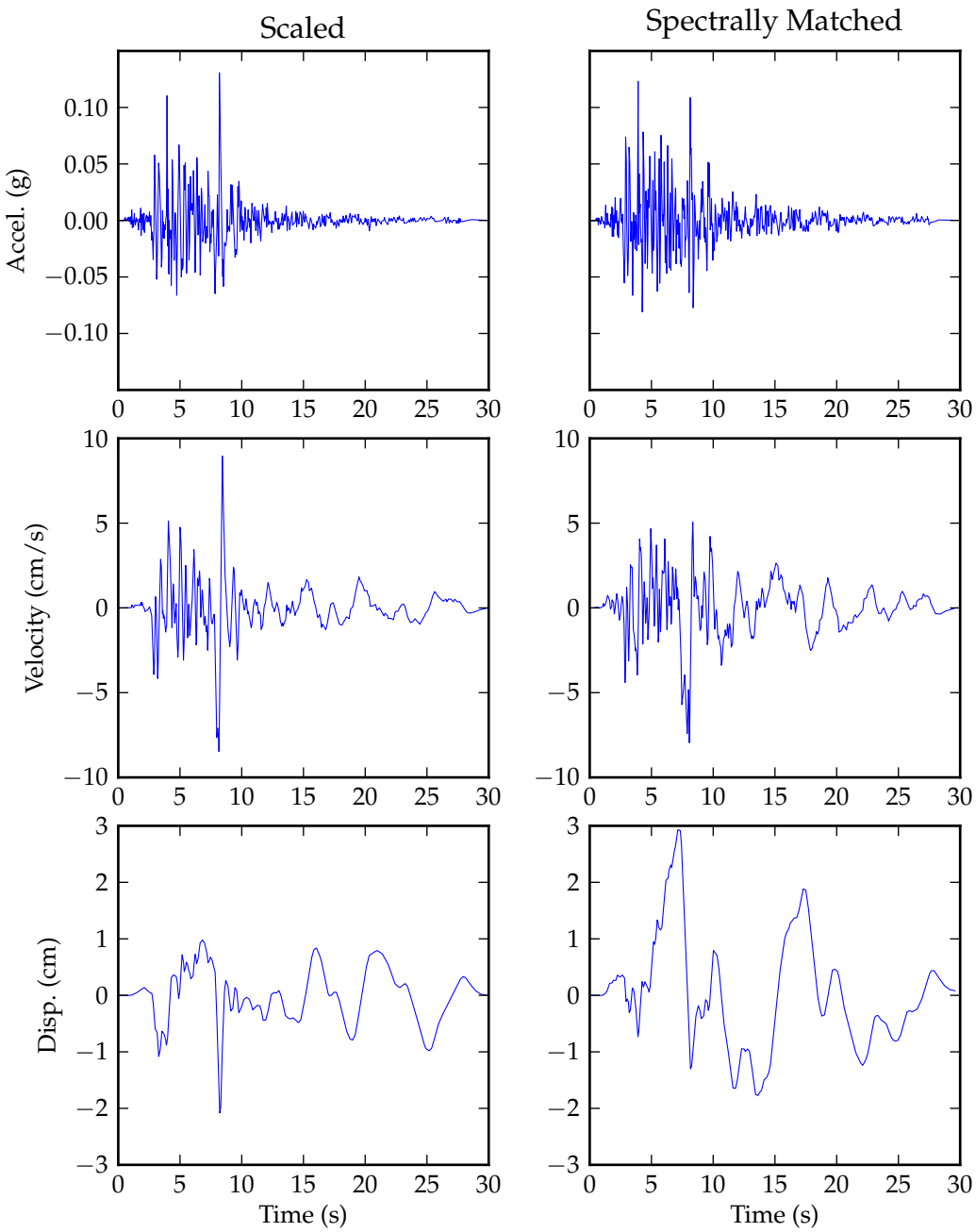

Figure 4.13: The acceleration-, velocity-, and displacement-time series for the scaled and spectrally matched versions of the `NORTHR-WON185` ground motion.

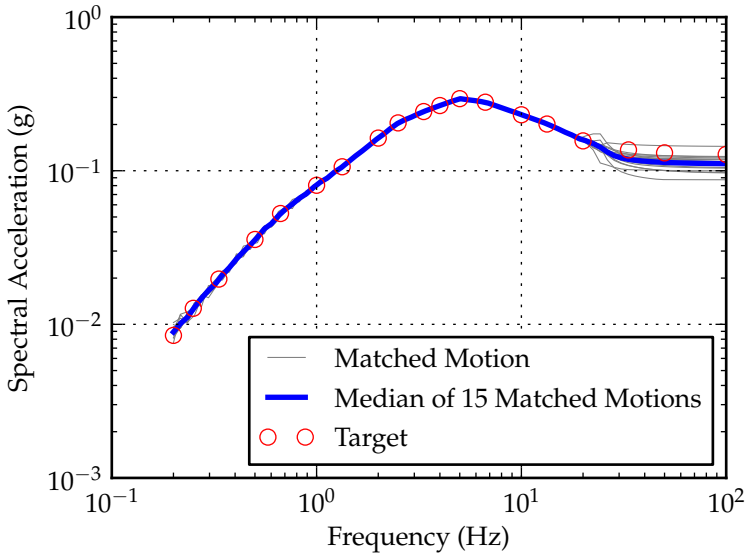

Figure 4.14: The fifteen ground motions spectrally matched and truncated at 25 Hz.

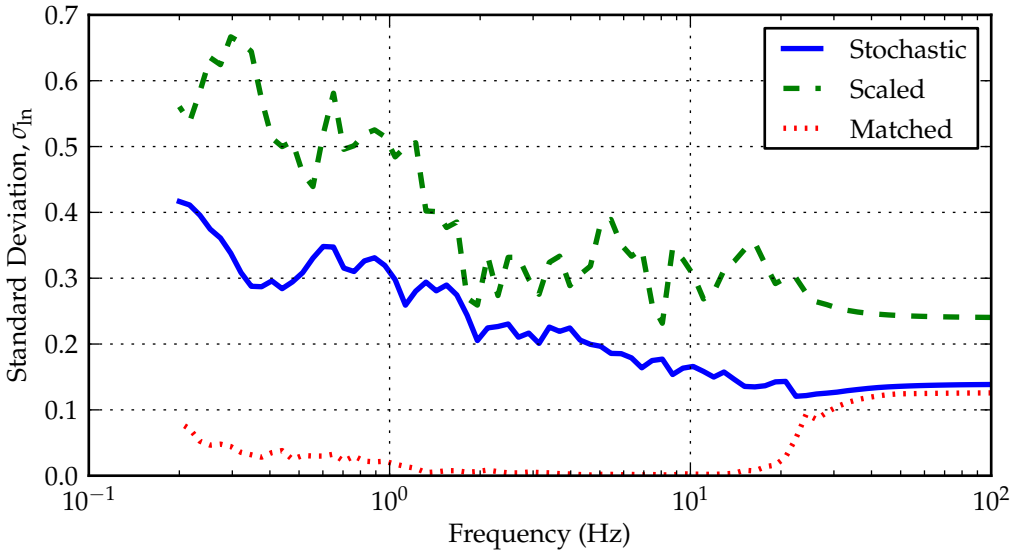

Figure 4.15: The standard deviation of the stochastically simulated, scaled, and spectrally matched ground motion suites.

4.5 Response Spectrum Compatible Motion for RVT

An acceleration response spectrum computed with a ground motion prediction equation provides the frequency content information required for an RVT analysis. However, as the response spectrum retains no information regarding the duration of the ground motion, RVT analyses require an independent estimate of the duration. With the response spectrum and duration, an FAS can be derived for input into an RVT site response analysis. However, it must be noted that this relationship between the response spectrum and FAS is not unique because the phase information is not available and the RVT calculation invokes an independent assessment of duration.

In the procedure proposed by Gasparini and Vanmarcke (1976) and described in Rathje and Kottke (2008), the initial estimate of the Fourier amplitude (A) is computed from the spectral acceleration at $f = f_n$ using:

$$|A(f_n)|^2 \approx \frac{1}{f_n\left(\frac{\pi}{4D} - 1\right)}\left(\frac{T_{rms}}{2} \cdot \frac{S_{a,target}(f_n)^2}{pf^2} - \int_0^{f_n} |A(f)|^2 \, \mathrm{d}f\right) \tag{4.2}$$

where f_n and D are the natural frequency and damping ratio, respectively, of the oscillator at the frequency of interest; $S_a(f_n)$ is the spectral acceleration at the oscillator frequency f_n; T_{rms} is the root-mean-square duration (see Section 2.4); pf is the peak factor; and $A(f)$ represents the Fourier amplitudes as a function of f. The peak factor is initially assumed to be 2.5 for all frequencies which is within the typical range of 2 to 3.5. Equation (4.2) is applied starting at low frequencies of the target response spectrum, where the influence of higher frequencies in the integral in (4.2) can be ignored, and it is then incrementally applied to higher frequencies. The resulting FAS generally shows good agreement with the target response spectrum, but the fit can be further improved by correcting the FAS based on the misfit between the target response spectral values ($S_{a,target}$) and the values calculated from the FAS with RVT ($S_{a,calc}$).

The correction between the target and calculated response spectra relies on the

properties of the single-degree-of-freedom acceleration transfer function. For an oscillator with light damping, the peak is narrow and tall which strongly connects the amplitude of $|A(f)|$ to S_a at the same frequency. Using this connection, an iterative correction is defined as:

$$|A(f)|_{i+1} = \frac{S_{a,target}(f)}{S_{a,calc}(f)}|A(f)|_i \tag{4.3}$$

The frequency-dependent correction is applied to the FAS at each frequency, and then a new response spectrum is calculated. After less than ten iterations, the misfit between the target and calculated response spectra typically reaches a minimum.

A response spectrum provides no information regarding the duration of the event, therefore an independent of estimate of the duration is required. Abrahamson and Silva (1996) proposed an empirical duration model that is presented here for completeness. The model defines the duration based on normalized Arias intensity. First, relating source and site characteristics to the duration between a normalized Arias intensity of 0.05 and 0.75 ($D_{0.05-0.75}$). Then, $D_{0.05-0.75}$ is generalized for any duration defined by a final normalized Arias intensity ($D_{0.05-I}$). The empirical model is defined as:

$$\ln D_{0.05-I} = \ln\left(\frac{\left(\frac{\Delta\sigma(M)}{10^{1.5M+16.05}}\right)^{-1/3}}{4.9\cdot 10^6\beta} + Sc_1 + c_2\max(r-r_c,0)\right) + \ln\left(\frac{D_{0.05-I}}{D_{0.05-0.75}}\right) \tag{4.4}$$

where $\Delta\sigma(M)$ is the stress drop as a function of magnitude (M), β is the shear-wave velocity at the source, S is a dummy variable for soil conditions (1 for soil or 0 for rock), and , and r is the distance. In equation (4.4), $\Delta\sigma(M)$ is defined as:

$$\Delta\sigma(M) = \exp\left(b_1 + b_2\left(M-6\right)\right) \tag{4.5}$$

and $\frac{D_{0.05-I}}{D_{0.05-0.75}}$ is defined as:

$$\ln\left(\frac{D_{0.05-I}}{D_{0.05-0.75}}\right) = a_1 + a_2 \ln\left(\frac{I-0.05}{1-I}\right) + a_3 \left(\ln\left(\frac{I-0.05}{1-I}\right)\right)^2 \tag{4.6}$$

The coefficients for use in equations (4.4), (4.5), and (4.6) are presented in Table 4.6. In a random vibration theory analysis, $D_{0.05-0.75}$ is used as the duration, as previous studies have shown that this value is similar to the source duration from seismological models.

To evaluate this procedure, a target response spectrum was generated from an FAS specified from seismological theory (Figure 4.16). Using this target response spectrum and the procedure described above, an FAS was calculated that is compatible with the target response spectrum (Figure 4.16). The FAS was then used to generate a response spectrum. The results show very good agreement between the target and calculated response spectra over the range in frequencies of shown (0.2 to 100 Hz). Agreement between the seismological FAS and the FAS derived from the response spectrum is good over the frequency range defined by the response spectrum (greater than 0.2 Hz). At frequencies less than 0.2 Hz, discrepancies between the seismological FAS and the FAS derived from the response spectrum are present due to a lack of information regarding low frequency energy in the target response spectrum.

Coefficient	**Horizontal**	**Vertical**
a_1	-0.532	-0.466
a_2	0.552	0.540
a_3	-0.0262	-0.0537
b_1	5.204	4.61
b_2	0.851	1.536
c_1	0.805	1.076
c_2	0.063	0.107
r_c (km)	10	10
β (km/s)	3.2	3.2

Table 4.6: Parameters for the Abrahamson and Silva (1996) empirical duration model.

Using a target response spectrum from the Boore and Atkinson (2008) ground motion prediction equation, a response spectrum compatible FAS was calculated (Figure 4.17). The duration of the RVT motion was estimated to be 4.55 seconds using the empirical Abrahamson and Silva (1996) relationship for duration. In this example, the compatible response spectrum does not match the target response spectrum well at low frequencies. At natural frequency of 100 Hz, the error relative to the target is -17.2%. The misfit at frequencies higher than 5 Hz cannot be reduced without increasing the misfit at lower frequencies, or creating an FAS with uncharacteristic high frequency attenuation (i.e., the FAS curls up at high frequencies). This inability for RVT to generate a seismologically plausible FAS that fits an empirical ground motion prediction equation at short frequencies indicates that the shape of the empirical response spectrum at short frequencies is inconsistent with seismological theory.

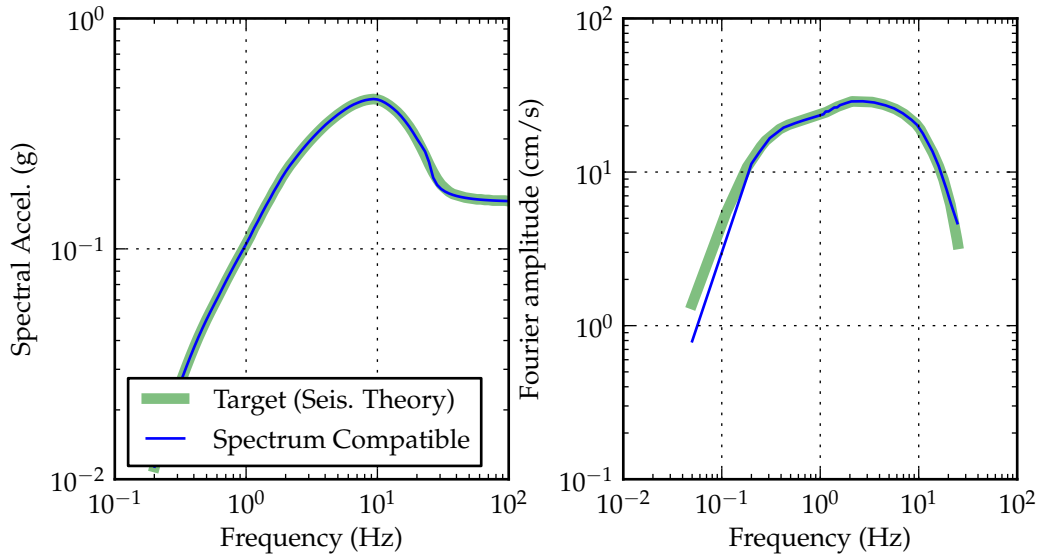

Figure 4.16: A response spectrum compatible RVT motion computed for a seismological theory derived target response spectrum, along with the comparison of the associated FAS

.

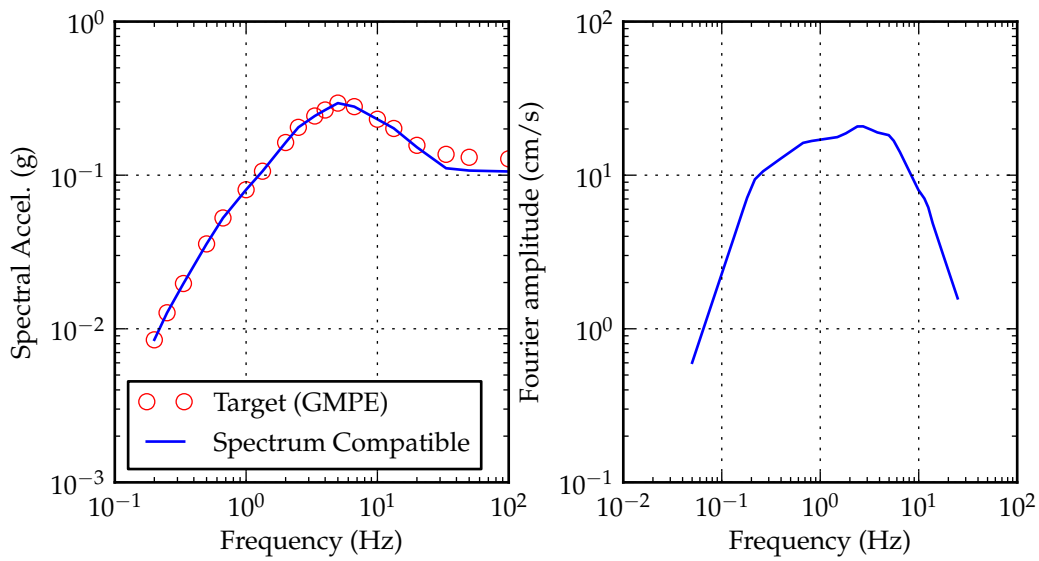

Figure 4.17: A response spectrum compatible RVT motion computed from a GMPE derived target response spectrum.

Chapter 5

Comparison of Equivalent-Linear Methods

5.1 Introduction

The different approaches of equivalent-linear (EQL) analysis (time series and RVT) are compared in this chapter using the different input motion characterizations discussed in Chapter 4. Comparisons will focus on the median spectral accelerations (S_a) and the median spectral ratios ($SR = S_{a,\text{soil}}/S_{a,\text{rock}}$) predicted from a suite of time series and the values predicted by RVT. Comparisons will be made through calculation of the difference of RVT relative to time-series analysis. The relative difference of the spectral acceleration (δ_{S_a}) is defined as:

$$\delta_{S_a} = \frac{S_{a,RVT} - \tilde{S}_{a,TS}}{\tilde{S}_{a,TS}} \tag{5.1}$$

where $\tilde{S}_{a,TS}$ is the median spectral acceleration of the time series simulations and $S_{a,RVT}$ is the spectral acceleration computed with RVT. Similarly, the relative difference of the

spectral ratio for RVT (δ_{SR}) is defined as:

$$\delta_{SR} = \frac{SR_{RVT} - \widetilde{SR}_{TS}}{\widetilde{SR}_{TS}} \tag{5.2}$$

where $\widetilde{SR}_{TS}$ is the median spectral ratio of the time series simulations, and SR_{RVT} is the spectral ratio computed with RVT.

5.2 Comparison Using Stochastic Input Motions

The consistency between an FAS derived from seismological theory and stochastically generated time series (Section 4.2) makes for an ideal situation in comparing RVT and time series based site response analysis. The input motions for the time series and RVT analyses are in general agreement when visualized as an FAS and as an acceleration response spectrum (Figure 5.1). Figure 5.2 shows the relative difference of the RVT input motion relative to the median of the time series simulations. In general, the RVT motion is within 10% of the median of the time series with a tendency for over prediction of the spectral accelerations at low frequencies and under prediction of spectral accelerations at high frequencies.

The stochastically simulated motions are propagated through the Turkey Flat, Sylmar County Hospital, and Calvert Cliffs sites; first assuming the response of the soil is linear-elastic (LE) with 5% damping. The results of the Turkey Flat site for the time series and RVT analyses are shown in Figure 5.3. The results show good agreement between the surface response spectrum computed with RVT and the median from time series analyses. Nonetheless, the relative difference in the surface response spectrum is as large as 10% and it tends to be dominated by the relative differences of the input motions (Figure 5.2). By examining the relative difference of the spectral ratio, the differences caused by the site response calculation can be separated from differences in the input motions.

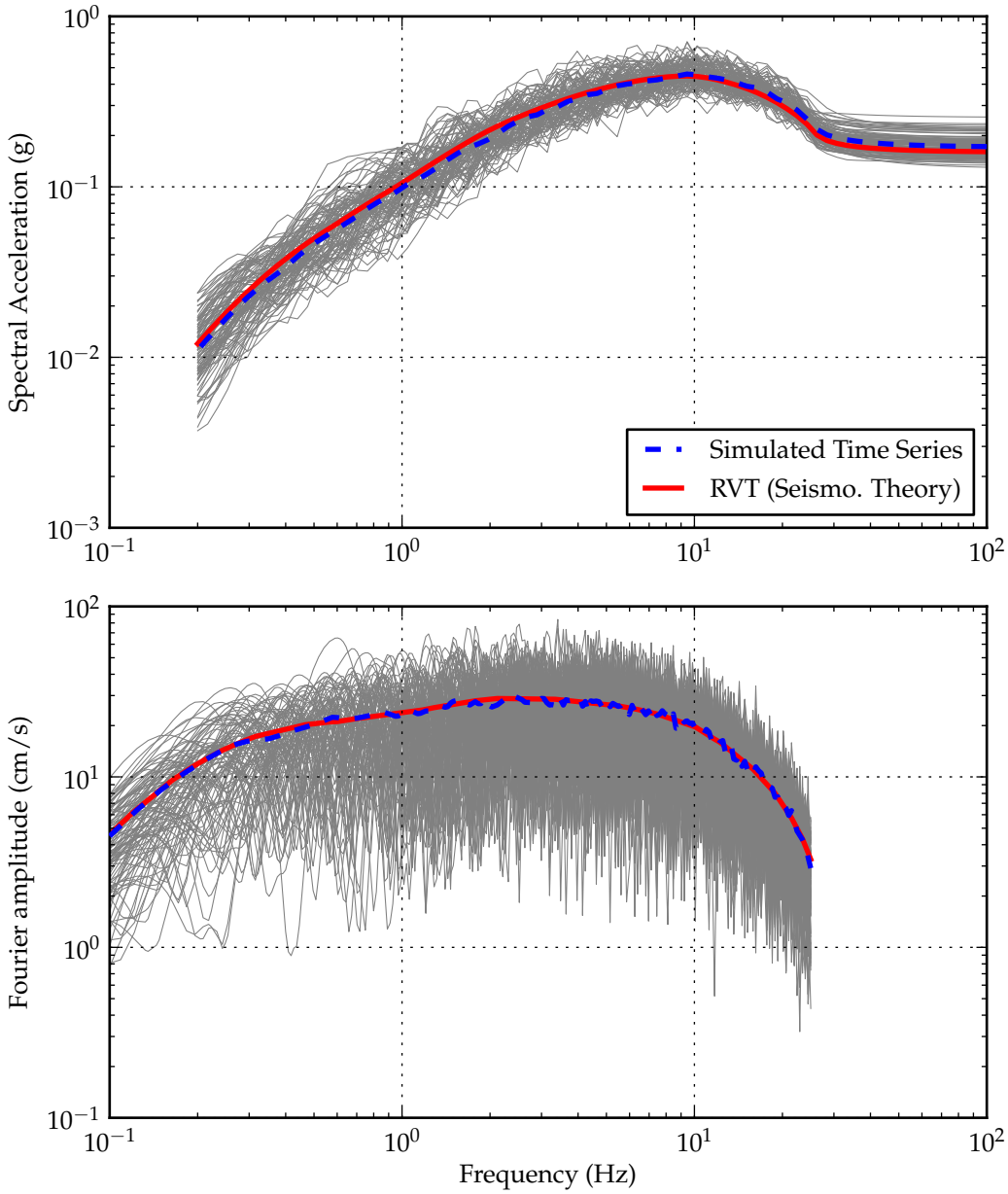

Figure 5.1: The input Fourier amplitude and response spectra for the stochastic input motions.

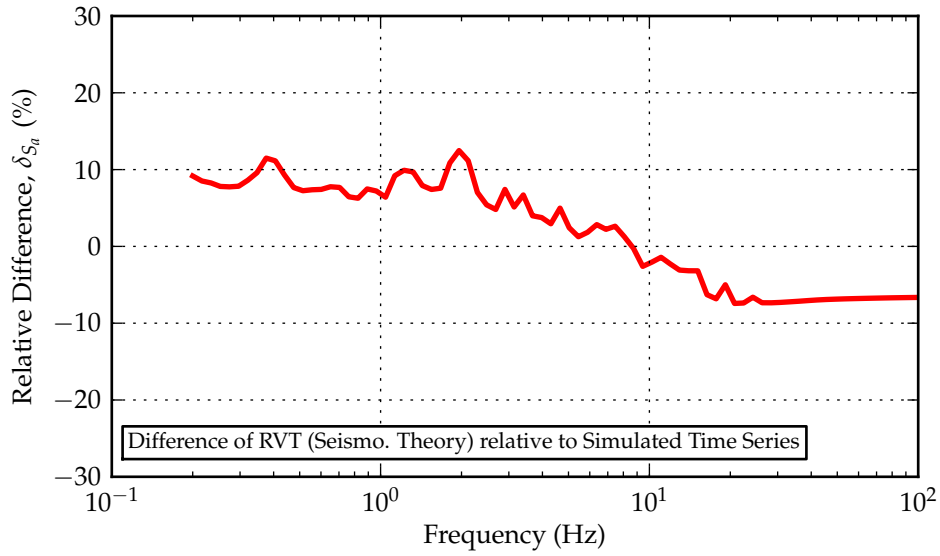

Figure 5.2: The relative difference of the input response spectrum for the stochastic input motions.

The relative difference of the spectral ratio (δ_{SR}) between the RVT and median time series motions is less than 5% at most frequencies, with the largest differences ($\approx$ 8%) at frequencies of strong amplification (7.69 and 14.29 Hz). Similar results are observed in the response calculated for the SCH site (Figure 5.4) with the maximum relative difference of approximately 6% occurring at the site frequency (1.67 Hz). In the response of the CC site, shown in Figure 5.5, the RVT analysis is again relatively high at the site frequency (0.25 Hz), but the relative difference of 25% is more significant than for the other two sites. In addition to being relatively high at the site frequency, the relative difference of RVT for the CC site is -12% at a frequency of 0.48 Hz. The spectral ratios for the CC site indicate a tendency for the RVT analysis to exaggerate the influence of the site and produce a response with higher peaks and lower troughs.

The results of the LE analyses indicate that the difference of RVT site response analysis relative to time-series analysis is dependent on the site characteristics. The site characteristics are reflected in the site transfer function used in the wave propagation

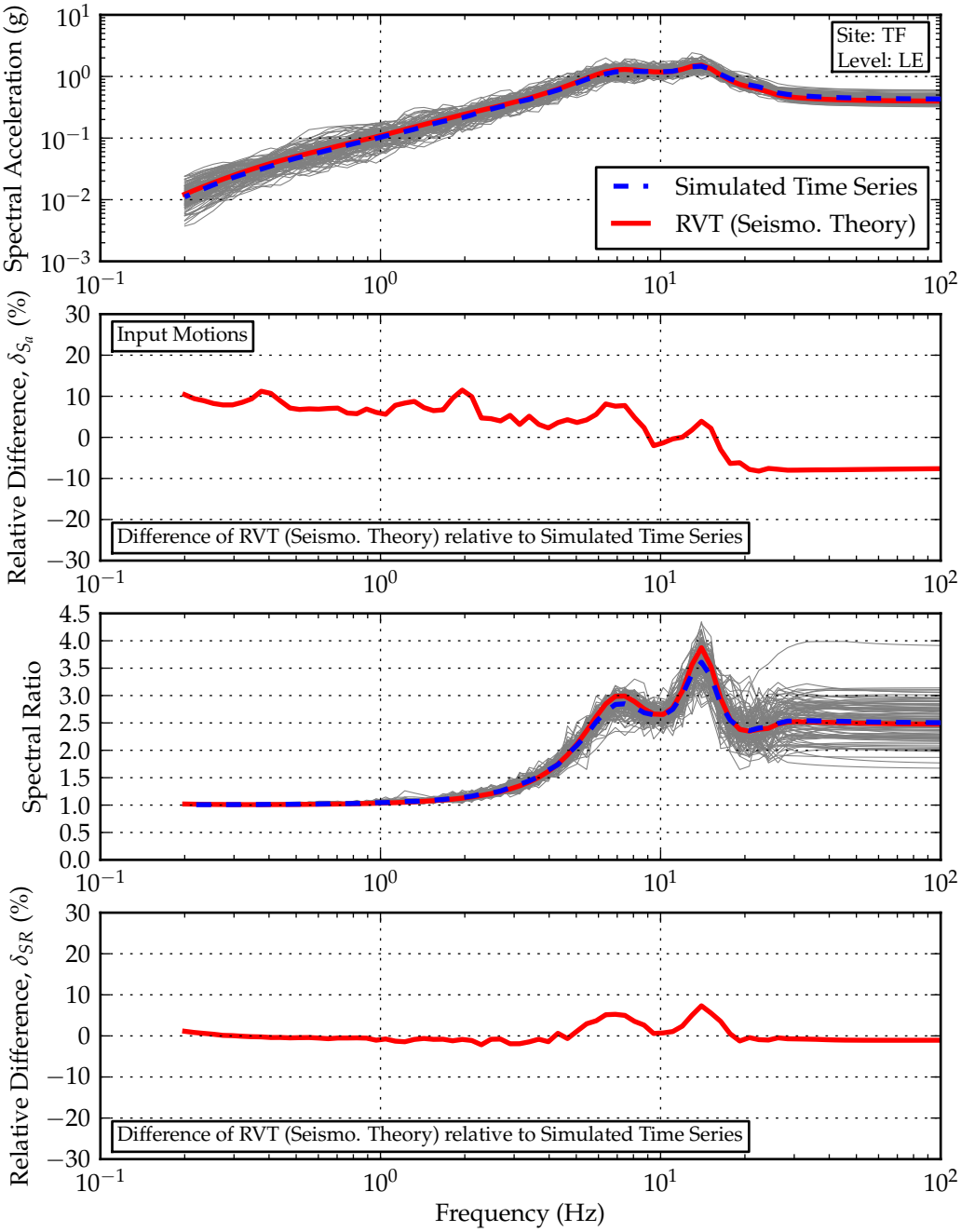

Figure 5.3: The response spectrum, spectral ratio, and relative difference for the Turkey Flat site computed with LE site response using simulated time series and an RVT motion defined by seismological theory.

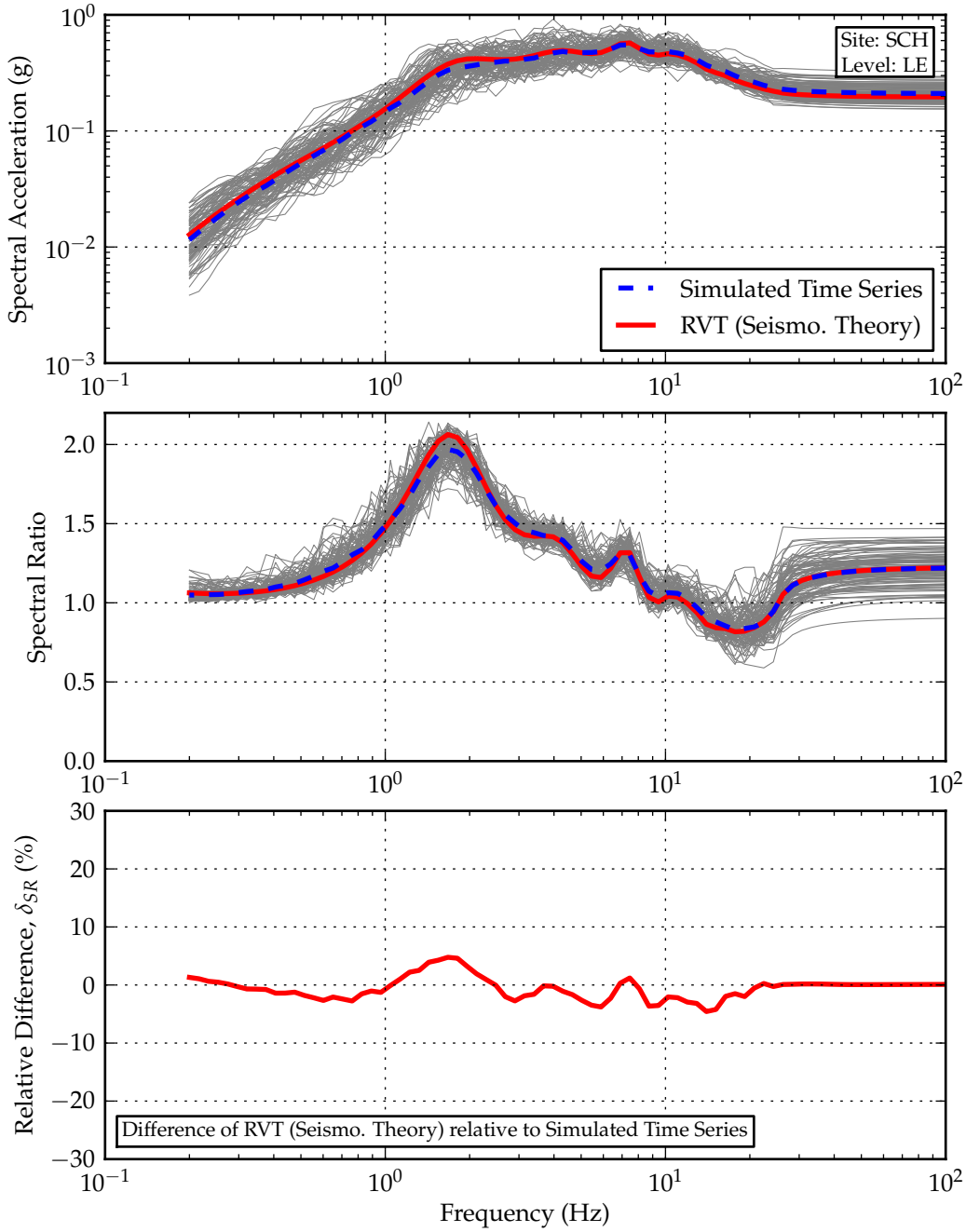

Figure 5.4: The response spectrum, spectral ratio, and relative difference for the SCH site computed with LE site response using simulated time series and an RVT motion defined by seismological theory.

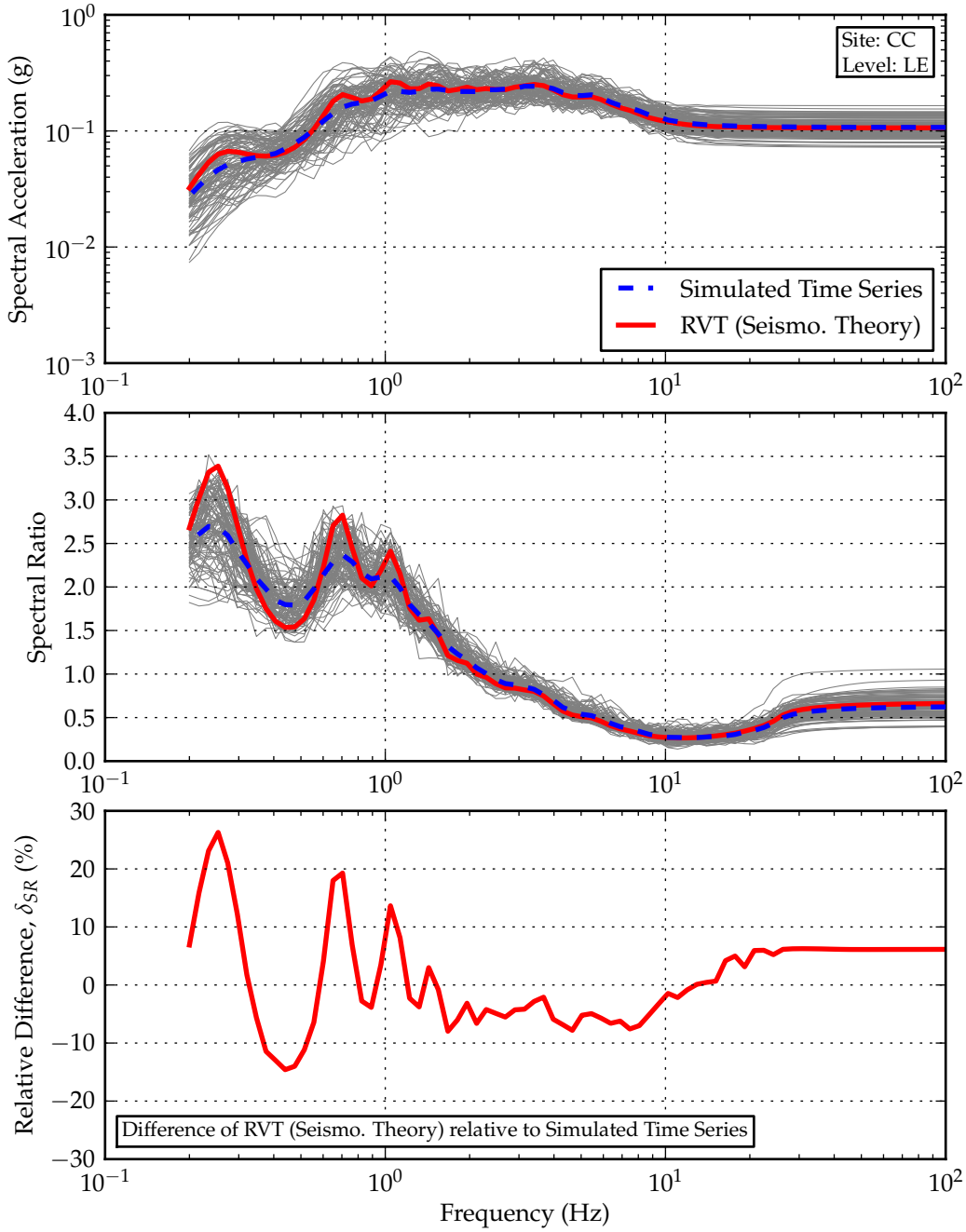

Figure 5.5: The response spectrum, spectral ratio, and relative difference for the CC site computed with LE site response using simulated time series and an RVT motion defined by seismological theory.

analysis. The LE transfer functions for the three sites are shown in Figure 5.6 and these transfer functions represent what was used for both the time series and the RVT analyses. Figure 5.6 shows that the transfer function of the Turkey Flat site has a strong narrow peak at 14 Hz; the SCH site has a less strong, but wide, peak at 1.7 Hz; and the CC site has several strong, narrow peaks at frequencies below 1 Hz and its largest peak is at 0.23 Hz. Differences in the spectral ratios computed by RVT and time-series analysis are a result of differences in the shape of the FAS of the simulated time series and of the RVT input motion relative to these transfer functions.

Figure 5.7 shows the input FAS for the time series with the largest and smallest spectral ratios at a frequency of 1.7 Hz (the approximate site frequency) for the SCH site. Also shown is the input FAS for the RVT analysis. The time series with the smallest spectral ratio ($SR(1.67Hz) = 1.72$) shows a deficiency in motion at or near the frequency of the peak in the transfer function, while the time series with the largest spectral ratio ($SR(1.67Hz) = 2.13$) contains enhanced amplitudes around the same frequency. Additionally, the time series FAS display peaks and valleys within the frequency range of the peak of the transfer function. On the other hand, the RVT input motion contains no peaks and valleys in its FAS and varies smoothly. Because RVT varies smoothly and does not have any valleys or peaks within the width of the peak of the transfer function, it propagates the full strength of the transfer function to the surface and predicts a larger spectral ratio. As all time series motions will have some irregularities in the FAS across the peak in the transfer function, the median spectral ratio from a suite of time-series analyses will never be as large as calculated by RVT.

The effect of the smooth RVT input motion is magnified when the peak in the transfer function is multiplied by only a small number of frequencies of the input time series. The frequency increment at which the FAS is defined is constant for a given time series, and therefore the effect is magnified when the natural frequency of the site is low. Additionally, the effect will be magnified when the width of the transfer function

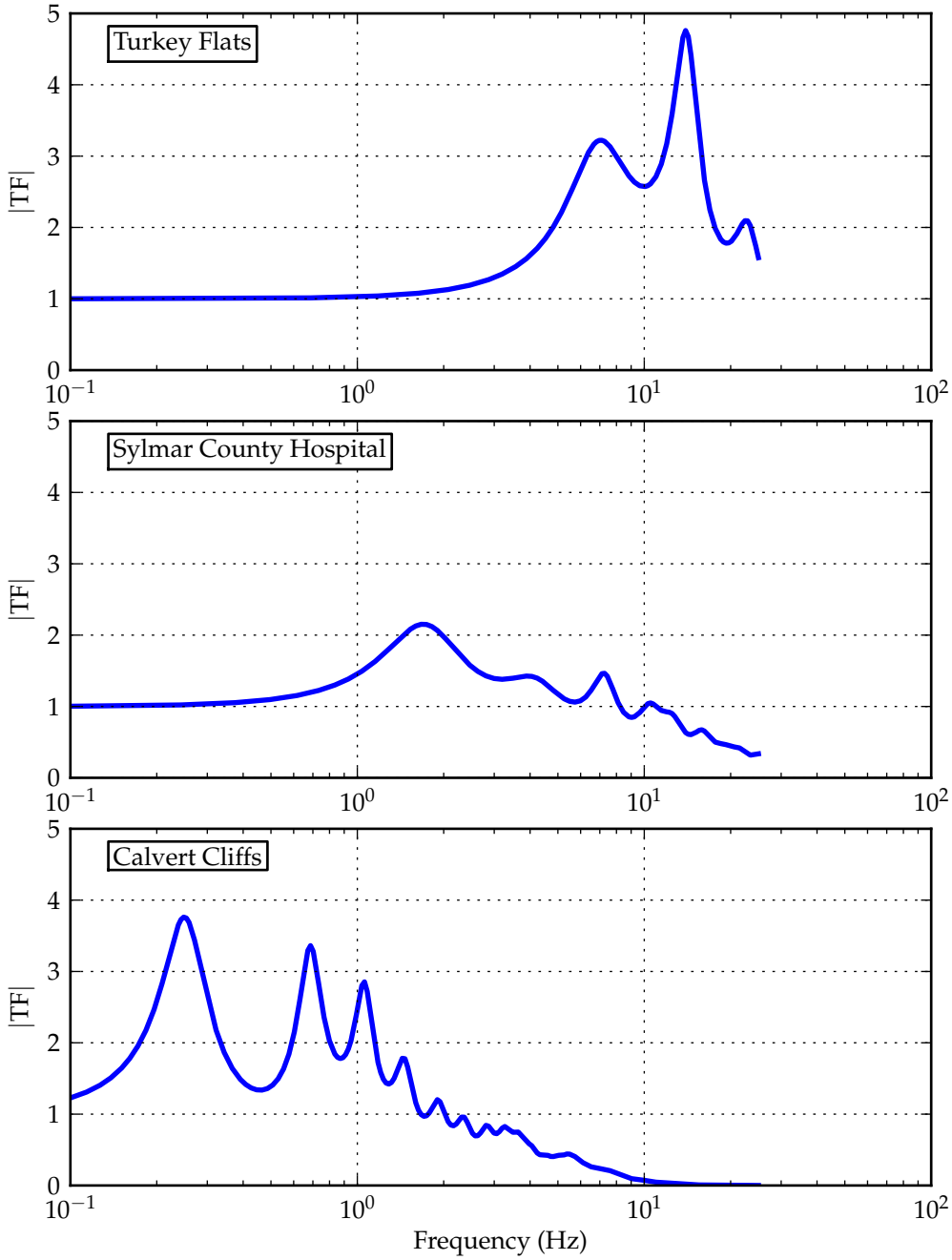

Figure 5.6: The linear-elastic transfer functions for the three sites used in this study.

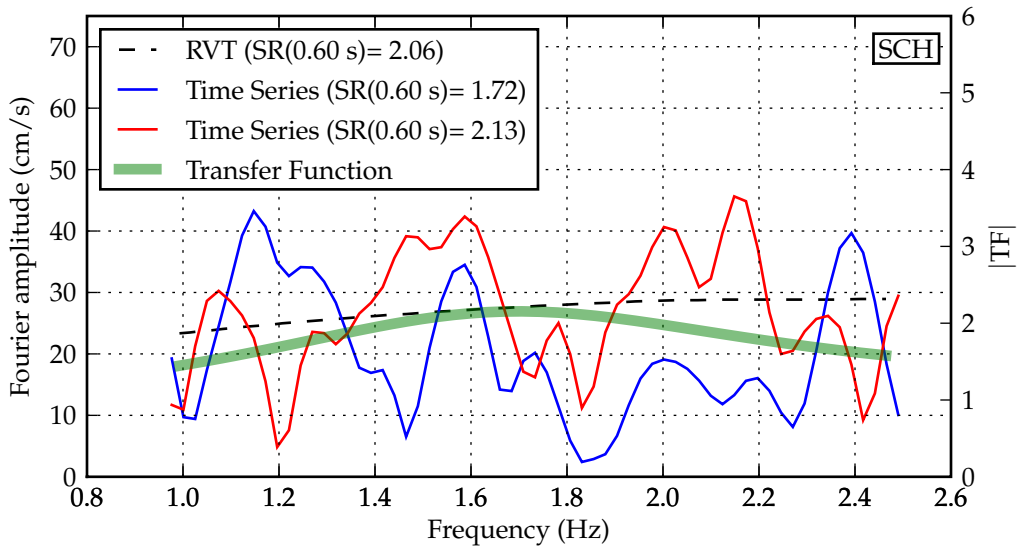

Figure 5.7: The input FAS for the time series with the largest and smallest spectral ratios for the SCH site, along with the input FAS of the RVT analysis and the LE transfer function.

is very narrow, or there is significant amplification by the site.

For the CC site, the input FAS for the time series with the largest and smallest spectral ratios at a frequency of 0.25 Hz (the approximate site frequency) are shown in Figure 5.8 along with the LE transfer function and the input FAS for RVT. The first mode amplification for the CC site, shown in Figure 5.8, occurs at a lower frequency and over a narrower frequency range than the first mode amplification for the SCH site, thus there is more difference between the spectral ratios from the time series analysis and RVT for the CC site (approximately 25% relative difference, see Figure 5.5). Additionally, there is more variability in the spectral ratios at the site frequency within the time series analysis for CC site, with the maximum spectral ratio being 81% larger than the minimum spectral ratio. For SCH site, the maximum spectral ratio is only 23% larger than the minimum spectral ratio.

Understanding the disparity in the relative difference computed for the SCH and

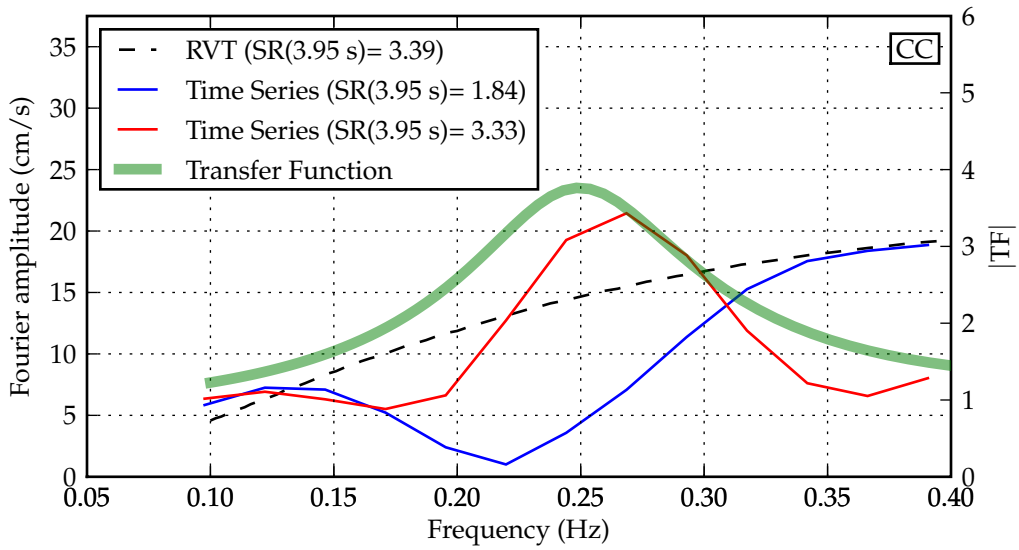

Figure 5.8: The input FAS for the time series with the largest and smallest spectral ratios for the CC site, along with the input FAS of the RVT analysis and the LE transfer function.

CC sites is complicated by the significant differences in site characteristics. A sensitivity analysis was performed on a fictitious sites to identity which site characteristics (i.e., site frequency, soil damping, bedrock V_s) most influence the differences in time series and RVT analyses. The site characteristics used in the sensitivity analysis are presented in Table 5.1. A constant shear-wave velocity of 400 m/s was used but the thickness was varied such that the site frequency ranged from 0.31 to 10 Hz. Soil damping ratios of 1 and 5% were considered, as well as bedrock shear-wave velocities of 1000 and 3000 m/s. Using linear-elastic analysis, the median spectral ratio was computed from the stochastic input motions using the time series and RVT approaches. The relative difference of the RVT spectral ratio at the site frequency for each site is shown in Figure 5.9, as well as the relative difference at 100 Hz. As the site frequency increases, the relative difference at the site frequency increases because the peak in the transfer function is affecting fewer points in the time series. More important than the natural frequency of

the site is the shear-wave velocity of the bedrock ($V_{s,rock}$), with the relative difference increasing by a factor of two when using very hard rock ($V_{s,rock} = 3000$ m/s) versus soft rock ($V_{s,rock} = 1000$ m/s). The increase in the bedrock shear-wave velocity increases the impedance contrast at the site, which increases the height in the transfer function. This increase in the peak height magnifies the differences caused by the different FAS shapes for the time series and RVT motions. The damping of the soil, which influences somewhat the width and height of the transfer functions, seems to have little influence over the relative difference. The relative difference of the spectral ratio at 0.01 seconds is generally less influenced by changes in properties (Figure 5.9), but the trend of increasing relative difference with increasing site frequency can still be observed.

Equivalent-linear analyses were performed to investigate how the relative difference changes with input intensity and induced strain level. The input motions were propagated through the Sylmar County Hospital site at two different intensity levels. The lower intensity level is the expected PGA predicted for the scenario event from seismological theory (PGA of 0.17 g, Figure 5.1). For the higher intensity level, all of the input motions were increased by a factor 2.35, increasing the median input PGA to 0.40 g. Figure 5.10 shows the site response results for both the RVT and time-series analysis for a median input PGA of 0.17 g. In general, the results show good agreement between the time series and RVT analyses. However, the relative difference in the RVT

Layer	**Property**	**Value(s)**
Soil	Thickness (m)	10, 32, 100, 316
	Shear-wave Velocity (m/s)	400
	Unit Weight (kN/m^3)	18
	Damping (%)	1, 5
Bedrock	Shear-wave Velocity (m/s)	1000, 3000
	Unit Weight (kN/m^3)	22
	Damping (%)	1

Table 5.1: Site properties used in the sensitivity analysis.

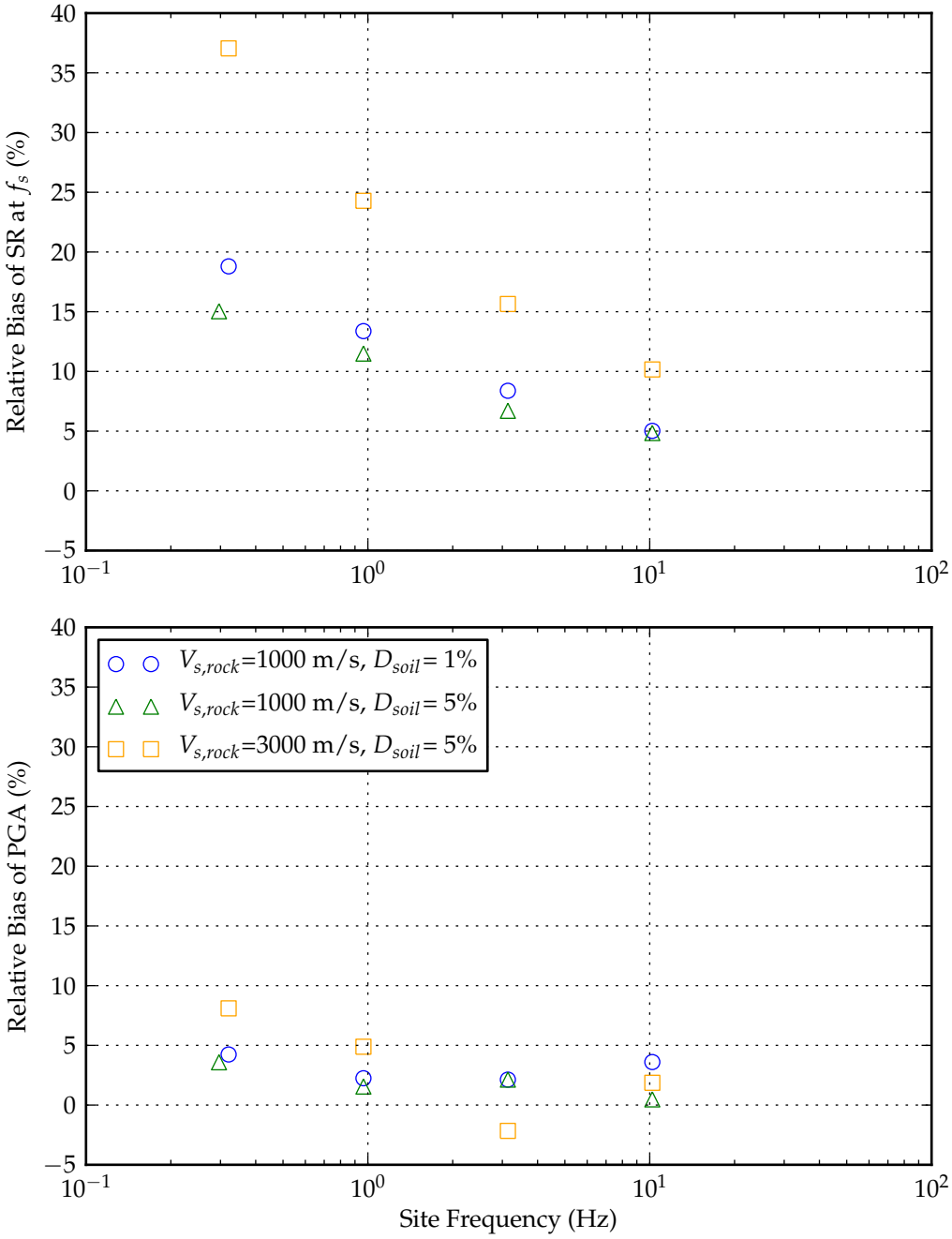

Figure 5.9: Sensitivity of the relative difference of the spectral ratio at the site frequency and at a frequency of 0.01 seconds to various site characteristics.

analysis has increased compared to the LE analysis (Figure 5.4), with the maximum relative difference at the site frequency now approaching 10%. At frequencies with no site amplification (i.e., troughs in the transfer function, such as at 0.11, 0.21, and 0.40 seconds), there is a consistent under prediction of the spectral ratio. These trends are even stronger when the intensity of the input motions increase to 0.40 g (Figure 5.11), where the relative difference at the site frequency exceeds 10%. Figure 5.12 summarizes the relative difference in the spectral ratios computed at the SCH site for the three sets of analyses performed. These data show that as the intensity of the input motion increases, the relative difference at the site frequency increases and it shifts to lower frequencies due to the increase in the site frequency associated with softening of the site.

To explain the increase in the relative difference with increase in intensity level, it is important to understand how the median response from the time series analyses are influenced by the different strain levels induced by each individual motion. The maximum strain profiles for the input intensities of 0.17 g and 0.40 g intensity level events are shown in Figure 5.13. These profiles indicate that the strain computed by the RVT analysis is very similar to the median strain in the time series analysis. However, the maximum strain profiles fail to capture the connection between the maximum strain and the computed spectral ratios for individual motions. Consider the two stochastic motions shown in Figure 5.14. Motion #68 tends to strain the site less than the median, which makes the peak in the spectral ratio occur at a higher frequency (i.e., stiffer site). Motion #7 induces strains in the site larger than the median, causing the peak in the spectral ratio to be shifted towards lower frequencies. At the frequency of approximately 1.11 Hz (approximately the average degraded site frequency), these two motions both have spectral ratios less than the median of all of the motions, and thus motions that strain a site more than or less than the median produce smaller spectral ratios at the average site frequency. Motions that induce strains similar to the median response

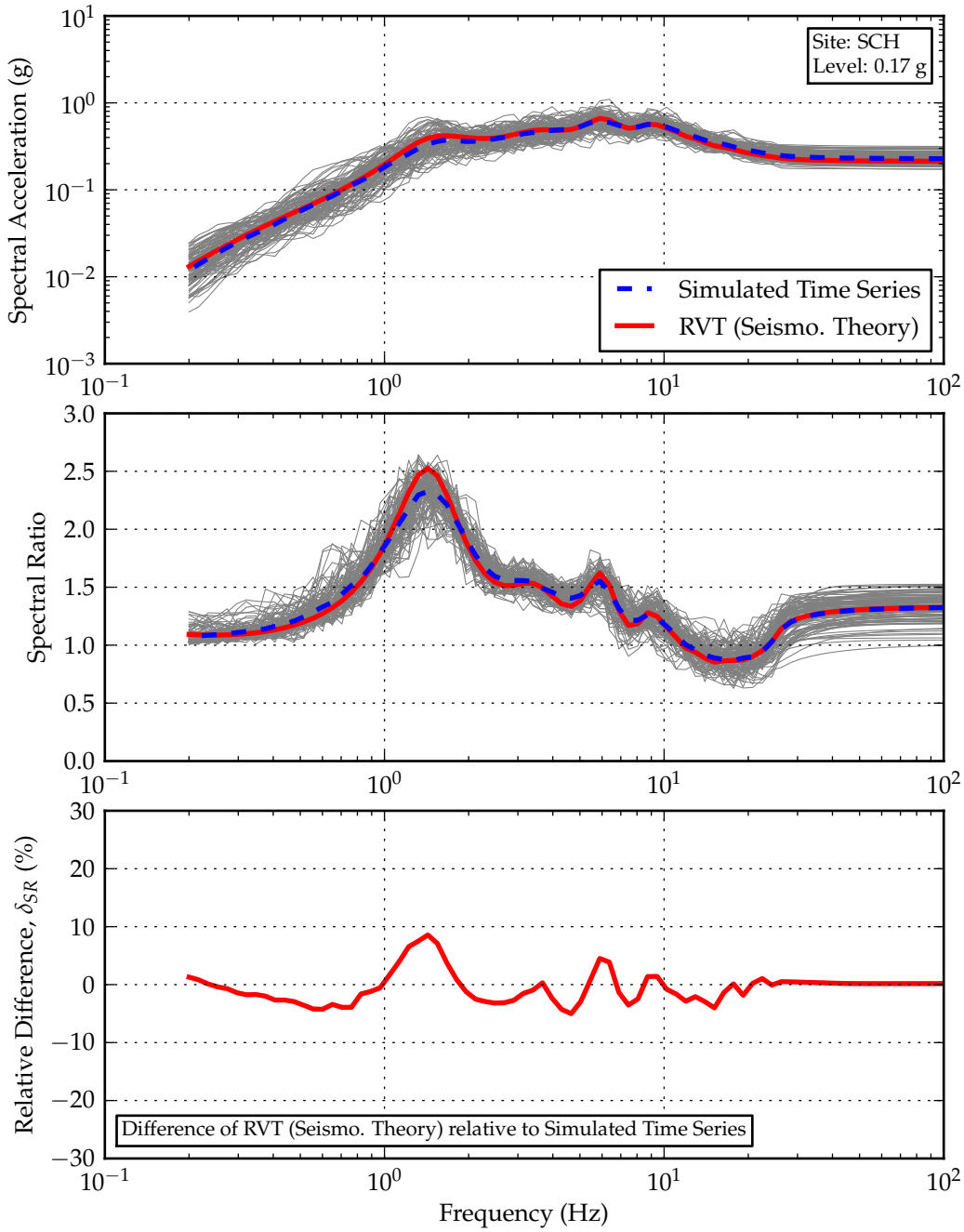

Figure 5.10: The response spectrum, spectral ratio, and relative difference for the SCH computed with EQL site response using simulated time series and an RVT motion defined by seismological theory (input PGA of 0.17 g).

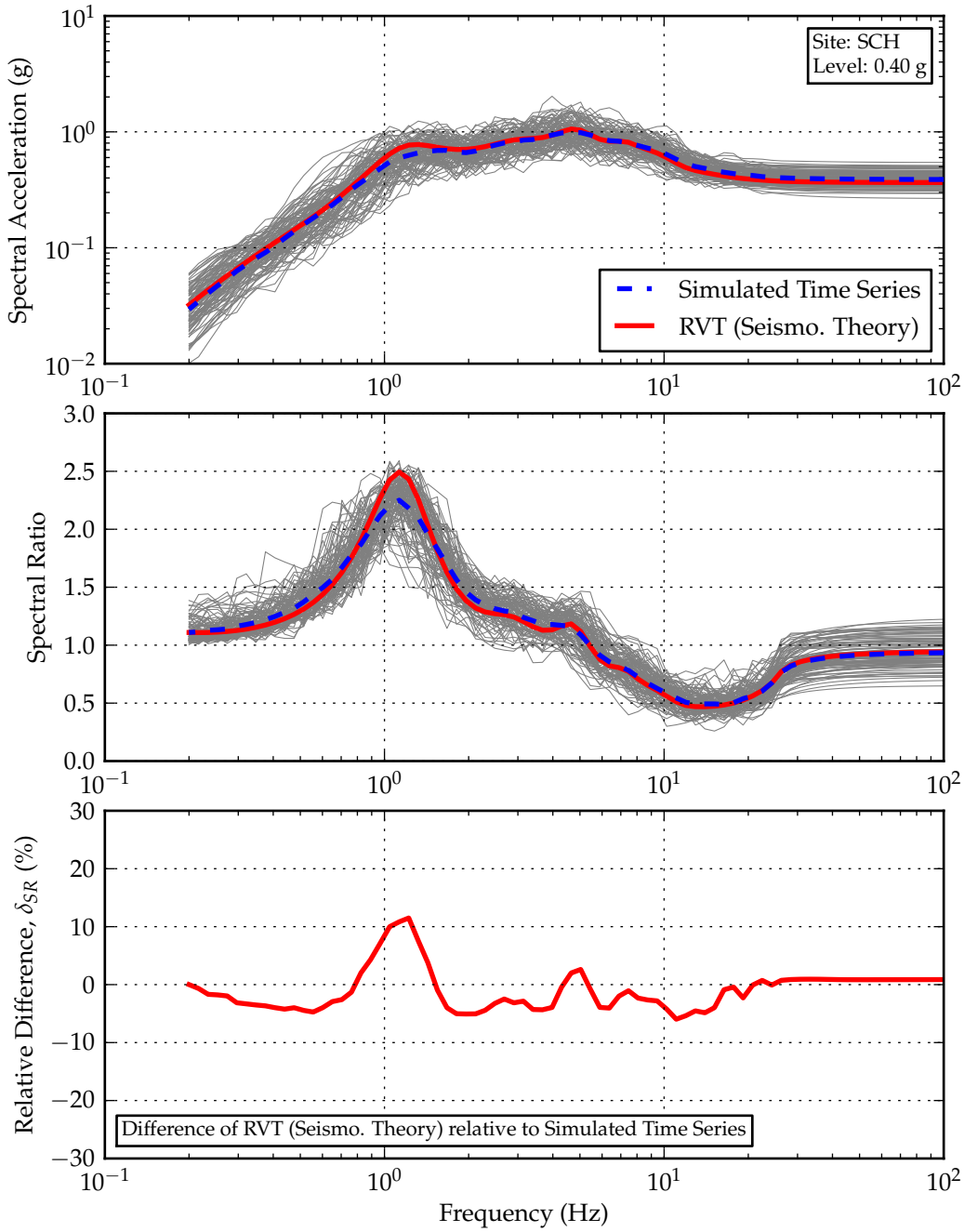

Figure 5.11: The response spectrum, spectral ratio, and relative difference for the SCH computed with EQL site response using simulated time series and an RVT motion defined by seismological theory (input PGA of 0.40 g).

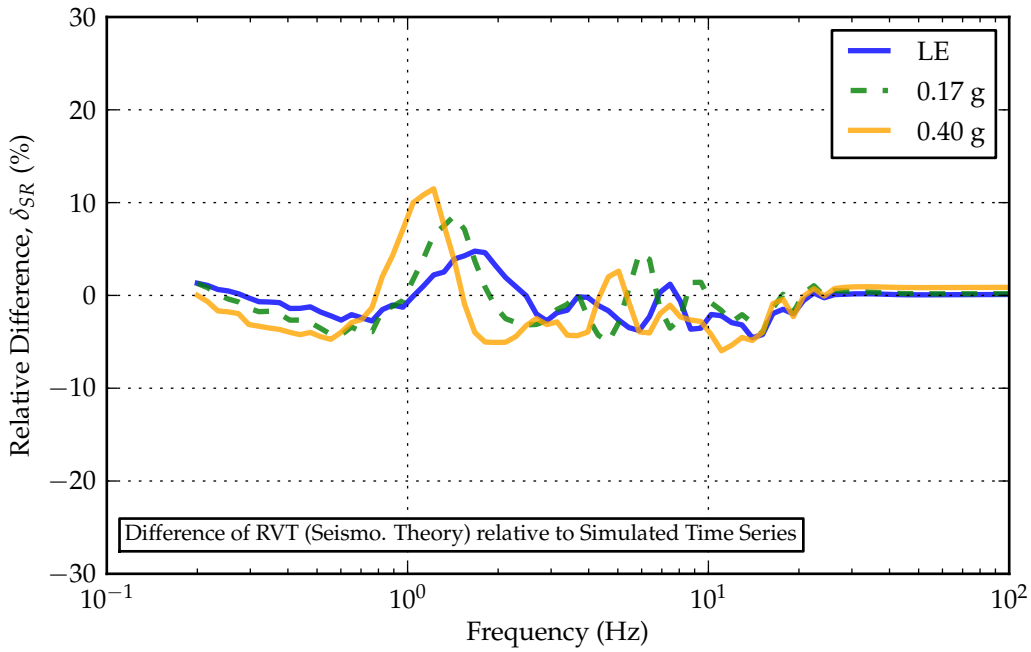

Figure 5.12: The relative difference of the spectral ratio of the SCH site computed using simulated time series and an RVT motion defined by seismological theory.

have the largest spectral ratio at the average site frequency. When all of the motions within the suite are averaged together, the effect of these differences is to pull down the average spectral response at the site frequency. At frequencies away from the peak spectral ratio, the motions #68 and #7 balance each other out (i.e., one is larger than the median and the other is smaller) such that the median of the time-series analyses is similar to RVT.

The strain effect is further illustrated by comparing histograms of the spectral ratios at the site frequency for each set of analyses (Figure 5.15). For the LE analysis, the histogram is quite narrow with a small skew to smaller values and the median from the suite of time-series analysis is larger than the value from RVT analysis. This difference is caused predominantly by the spectral shape effects discussed. For the EQL analyses, the median spectral ratios from the time series analysis increase relative to the linear-elastic analyses, but the histograms widen and become more skewed to smaller spectral ratios due to the fact that motions with relatively larger and relatively smaller shear strains both result in smaller spectral ratios at the site frequency. The skewness reduces the median from the time-series analysis, causing enhanced differences between time-series and RVT analyses.

The relative difference of the EQL RVT analysis and the EQL time-series analysis for the CC site (Figure 5.16) shows slightly different trends than were observed for the SCH site. The low site frequency of approximately 0.25 Hz along with high bedrock shear-wave velocity of this Eastern US site (Figure 3.4) accentuates the positive bias of the RVT spectral ratio at frequencies associated with peaks in the transfer function. This positive bias is as large as 25%. Additionally, the relative difference becomes increasingly negative at high frequencies and becomes increasingly negative as the input intensity increases. Unlike SCH, for CC the strains induced by the RVT analysis are larger than for the time-series analysis (Figure 5.17). The larger strains lead to more damping and reduced spectral ratios at higher frequencies for the RVT analysis.

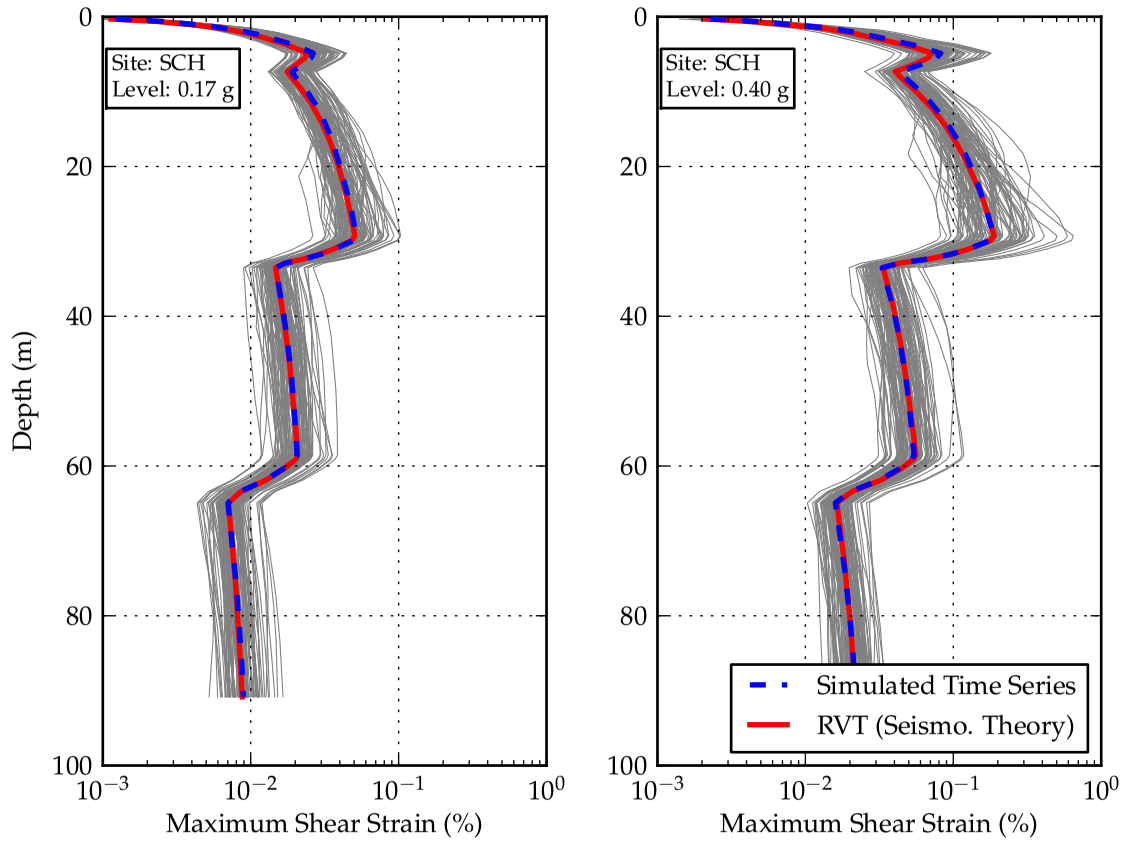

Figure 5.13: The maximum strain profiles for the SCH site computed using simulated time series and an RVT motion defined by seismological theory.

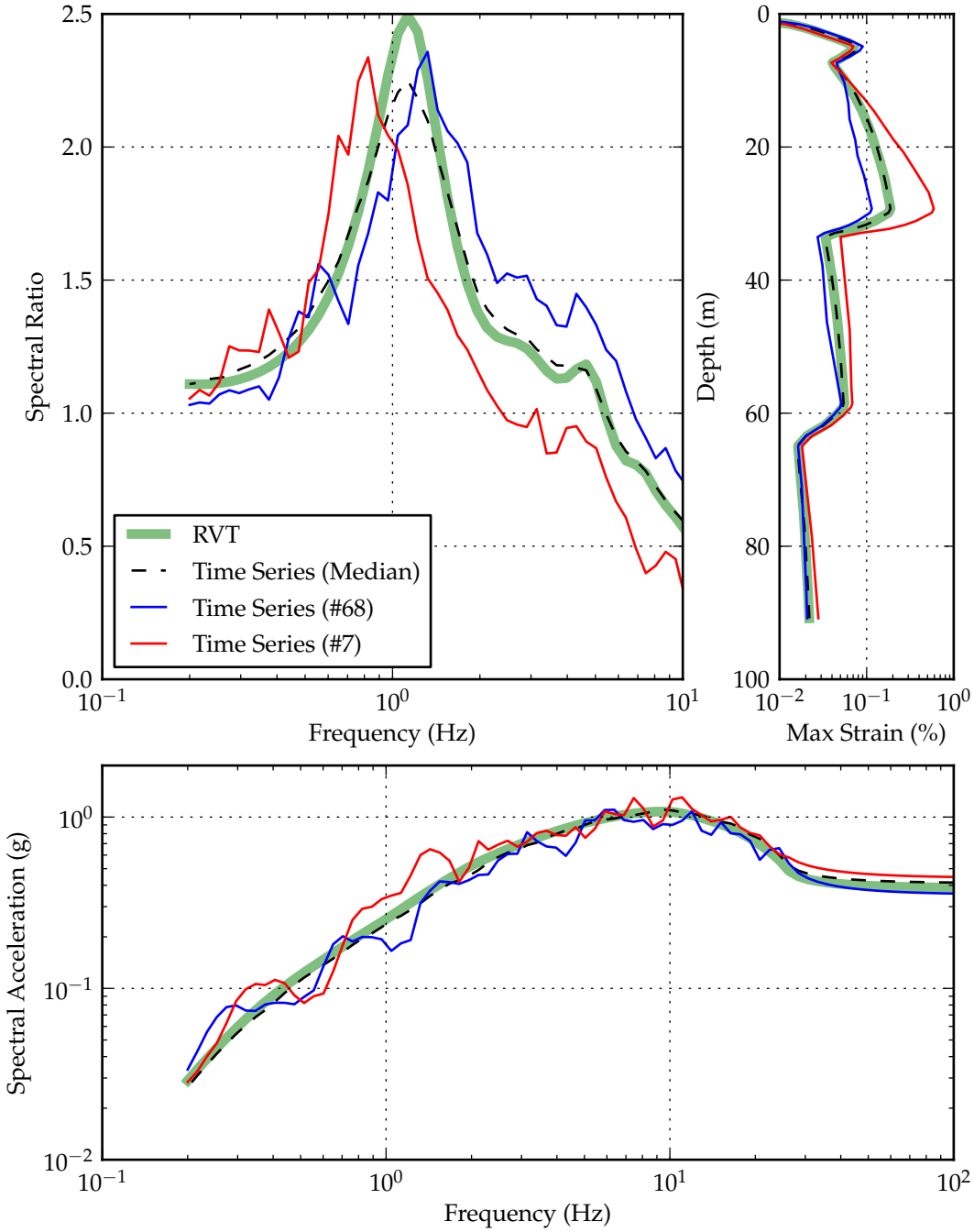

Figure 5.14: The spectral ratio and maximum strain profiles for selected motions propagated through the SCH site with an input PGA of 0.40 g.

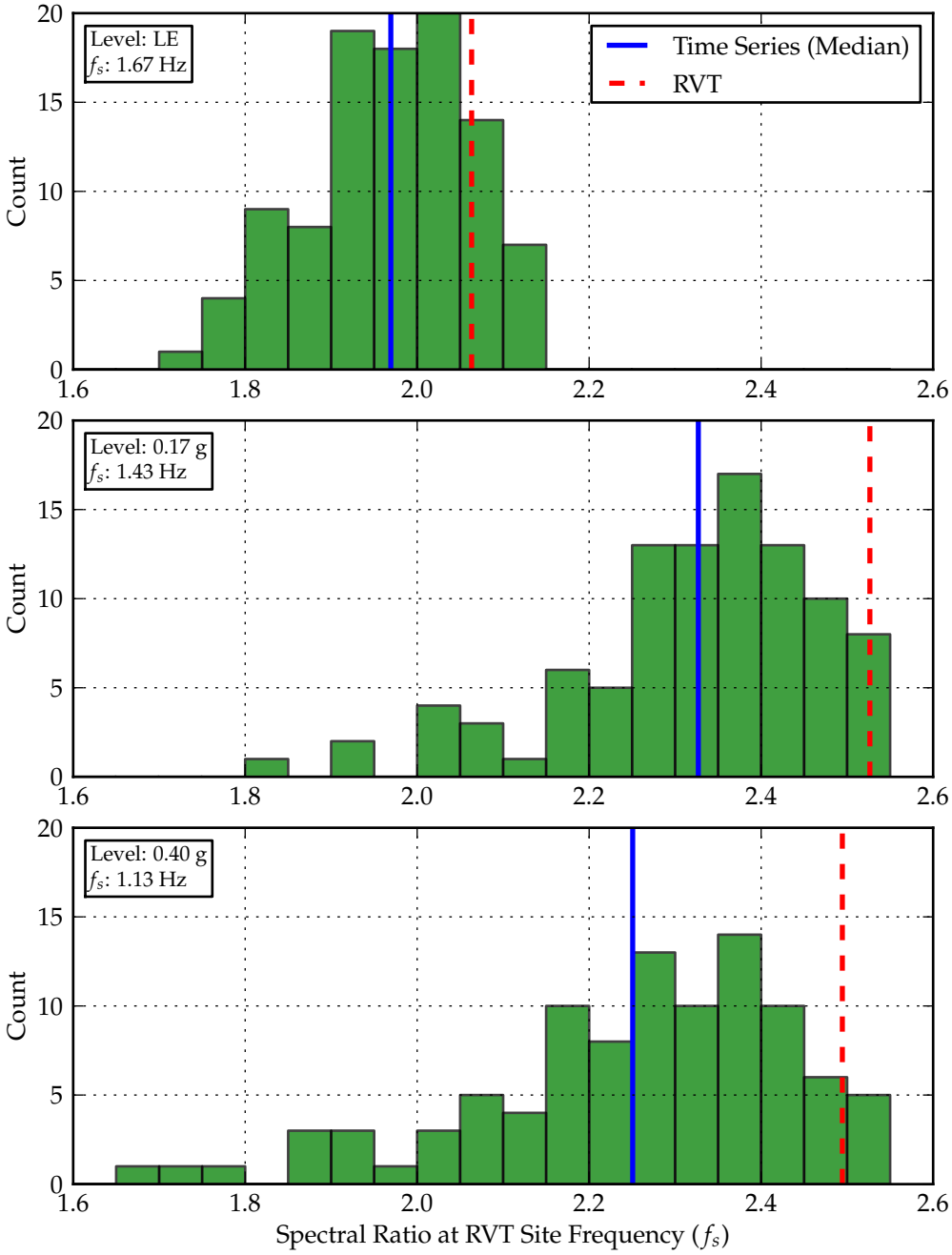

Figure 5.15: Histograms of the spectral ratio at the site frequency of the RVT analysis for the SCH site.

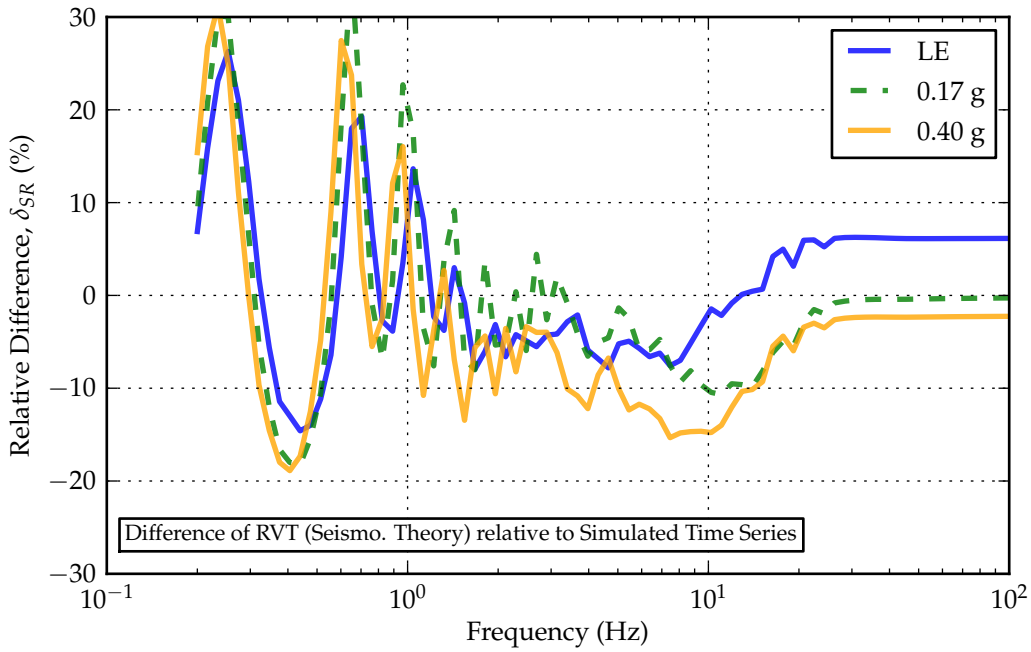

Figure 5.16: The relative difference of the spectral ratio of the CC site computed using simulated time series and an RVT motion defined by seismological theory.

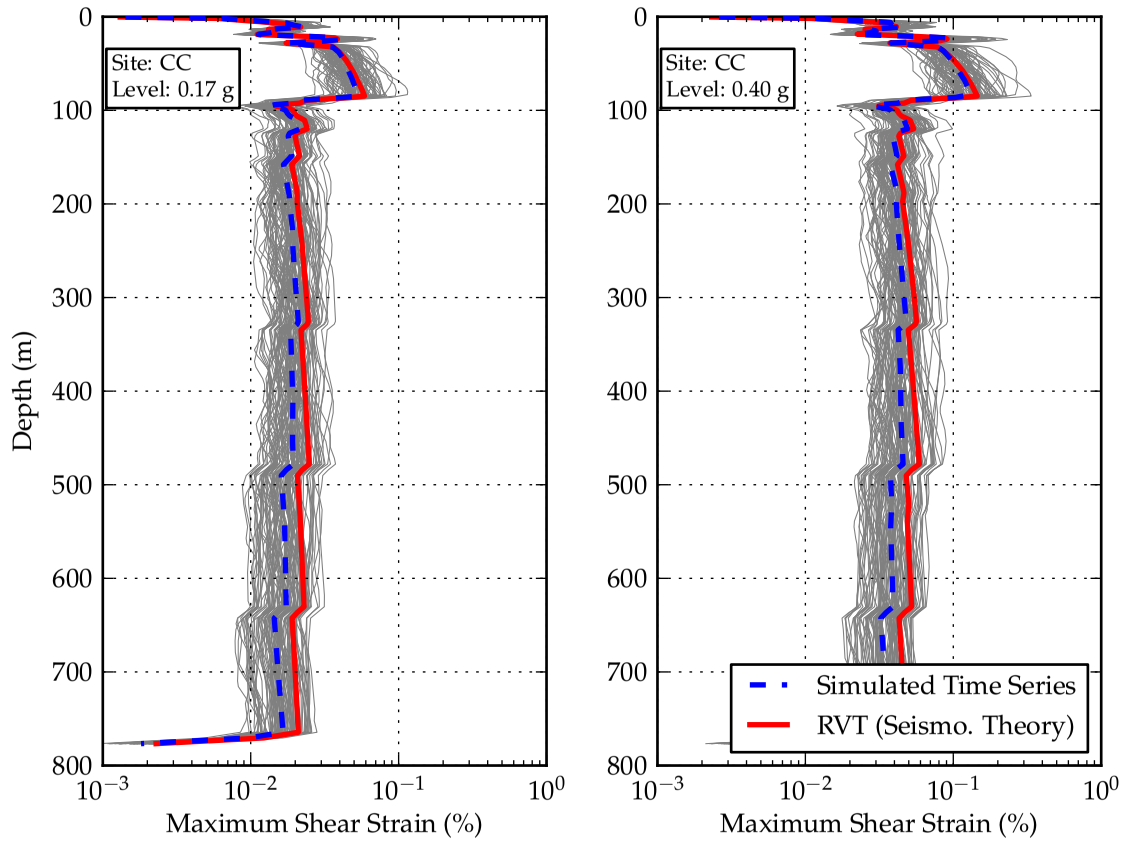

Figure 5.17: The maximum strain profiles for the CC site computed using simulated time series and an RVT motion defined by seismological theory.

To summarize, the difference in the site response computed using RVT analysis is affected by the characteristics of both the site and the input motions. The smooth shape of the RVT input FAS is more sensitive to the site transfer function than the irregular FAS of a time series, which results in larger amplification at the frequencies associated with peaks in the transfer function and less amplification at frequencies associated with troughs in the transfer function for RVT analyses. These differences are more significant for sites with low natural frequencies because the site amplification transfer function tends to be narrower and the number of points in the FAS affected by the amplification is smaller. Also important is the amplitude of the transfer function which increases for sites with large bedrock shear-wave velocity velocities or other strong velocity contrasts. The relative difference of RVT at the site frequency increases with increasing intensity because the RVT analysis does not take into account how individual motions strain a site differently (e.g. Figure 5.14). Finally, sites that have a large, positive bias at the site frequency for RVT analysis may induce larger strains that lead to negative bias for RVT at high frequencies.

5.3 Comparisons Using Scaled Time Series

The previous section focused on comparing RVT and time-series analyses using stochastically simulated input motions. However, most engineering practice uses recorded motions as input into site response analysis. Therefore, the suite of fifteen recorded ground motions discussed in Section 4.3 was used in a set of analyses to compare time-series and RVT methods and confirm the differences observed for simulated input motions. The scaled input motions have a median PGA of 0.13 g and are shown in Figure 5.18. These motions were also scaled to a median of 0.40 g and used as input. To develop the input RVT motion for comparison to a scaled suite of time series, one may derive a FAS compatible with the median response spectrum of the input time

series (called a response spectrum compatible input motion) or one may directly use the average FAS of the input time series (called an FAS compatible input motion). The response spectrum computed for the response spectrum compatible RVT input motion is within 5 to 10% of the median response spectrum of the scaled time series for frequencies less than 25 Hz (Figure 5.19) but under predicts the PGA (S_a at 100 Hz) by more than 10%. The response spectrum computed by the FAS compatible RVT input motion matches the target PGA but it is 10 to 60% larger than the median of the time series at frequencies lower than 10 Hz. The observed difference is frequency dependent and increases with increasing frequency. This observed trend is similar to what was observed for the stochastically simulated time series (Figure 5.2) although here the difference is much larger.

The observed differences between the response spectrum and FAS compatible RVT input motions is significant as it indicates a disconnect between the response spectra and FAS of recorded motions and RVT. As was previously shown, the stochastically simulated motions agreed with the RVT input motion in terms of both the FAS and the response spectrum (Figure 5.1) with a relative difference in the response spectrum ranging from -10 to 10%. However, when recorded motions are used it is nearly impossible to fit both the input response spectrum and the input FAS simultaneously. Even when using the average FAS of the input motions, the input response spectrum computed by RVT is 10 to 60% larger than the median response spectrum of the suite of scaled time series. As random phase angle is assumed in both the generation of stochastically simulated time series and RVT, it may play a role in the observed differences. However, characterization of the differences in the phase angle between stochastically simulated time series and recorded time series is beyond the scope of this report. The shape of the FAS derived from the response spectrum is different from the FAS of the input time series in terms of the relative amplitudes at high and low frequencies. These differences in the FAS shape are important because the differences in shape affect the response of the site.

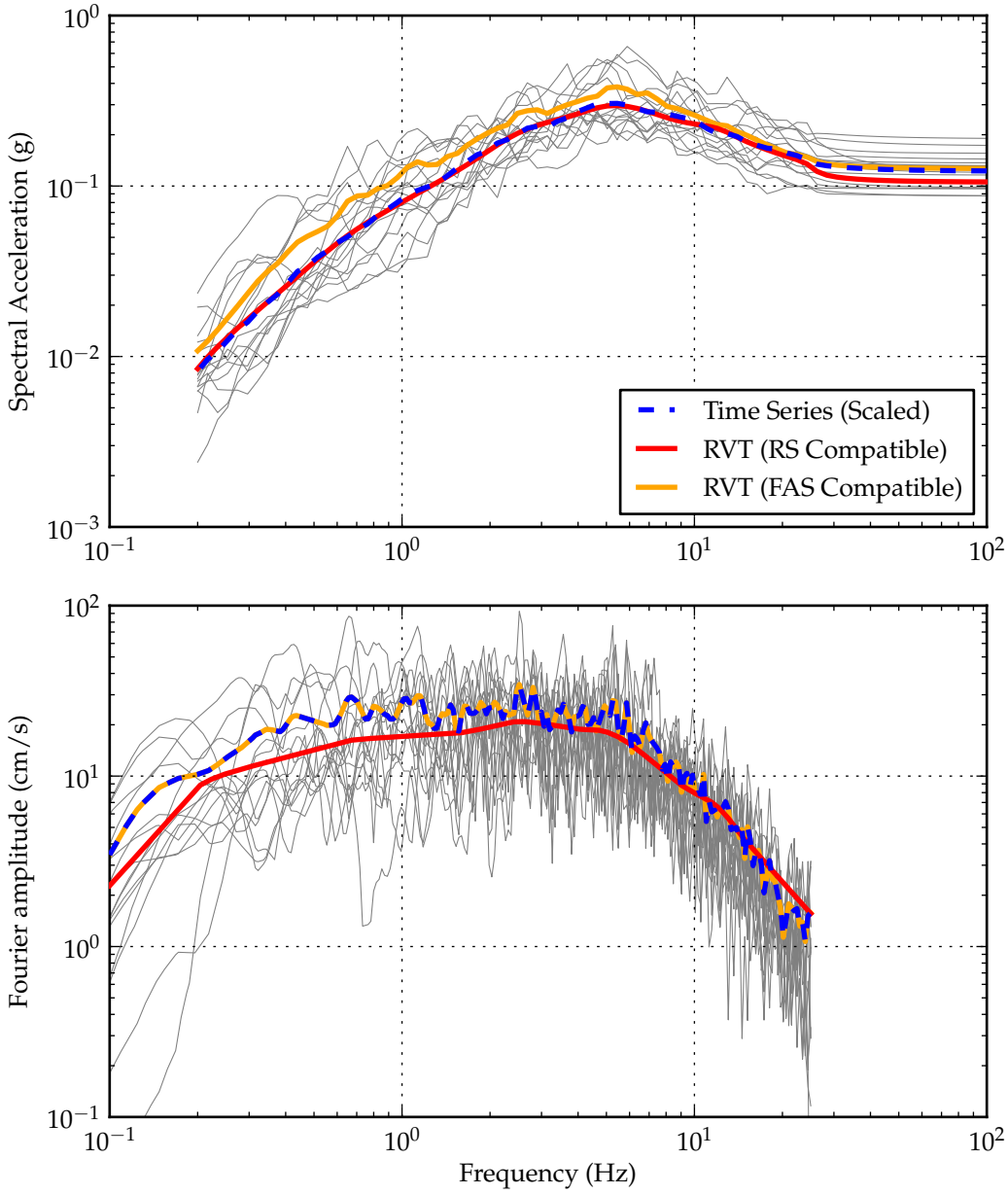

Figure 5.18: The input Fourier amplitude and response spectra for the scaled input motions, as well as FAS and response spectrum compatible RVT motions.

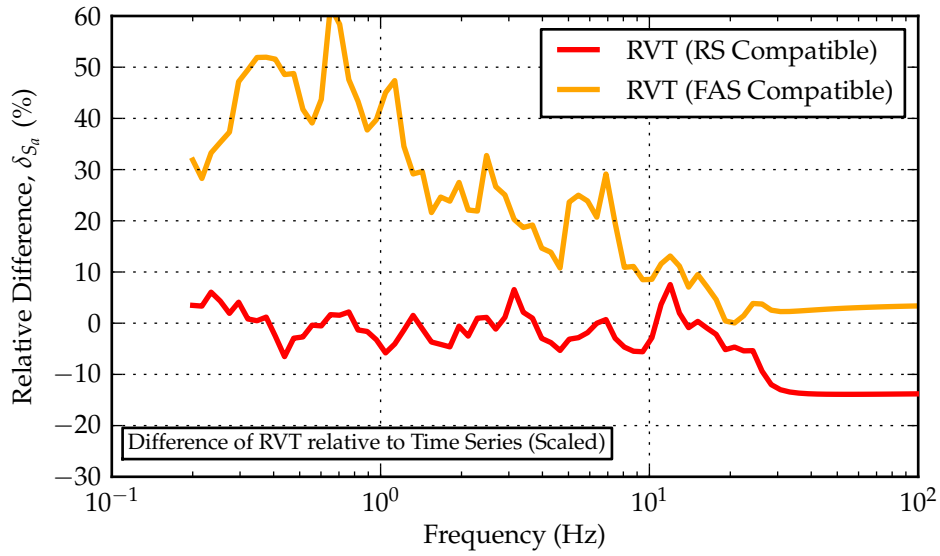

Figure 5.19: The relative difference of the input response spectra for the FAS and response spectrum compatible RVT motions.

The linear-elastic response of the SCH site for these three different input motions is shown in Figure 5.20 and these results are similar to those shown previously for the stochastically simulated input motions (Figure 5.4). A large positive bias in the RVT spectral ratio occurs at the site frequency, although the relative difference is slightly larger than the relative difference observed for the stochastically simulated input motions (8% versus 5%). There is a difference in the spectral ratios computed by the two different RVT methods at low frequencies as a result of differences in the shapes of the input FAS, as discussed previously (Figure 5.18).

The EQL spectral ratios computed for the SCH site for 0.13 and 0.40 g are shown in Figure 5.21. The RVT analysis with a response spectrum compatible input motion generally maintains a difference less than 10 to 15%, whereas the RVT analysis with the FAS compatible input motion produces large, negative bias (-20 to -30%) at frequencies between 1.43 and 14.3 Hz. The significant difference between responses computed by the two RVT motions is a result of differences in strains generated by the different

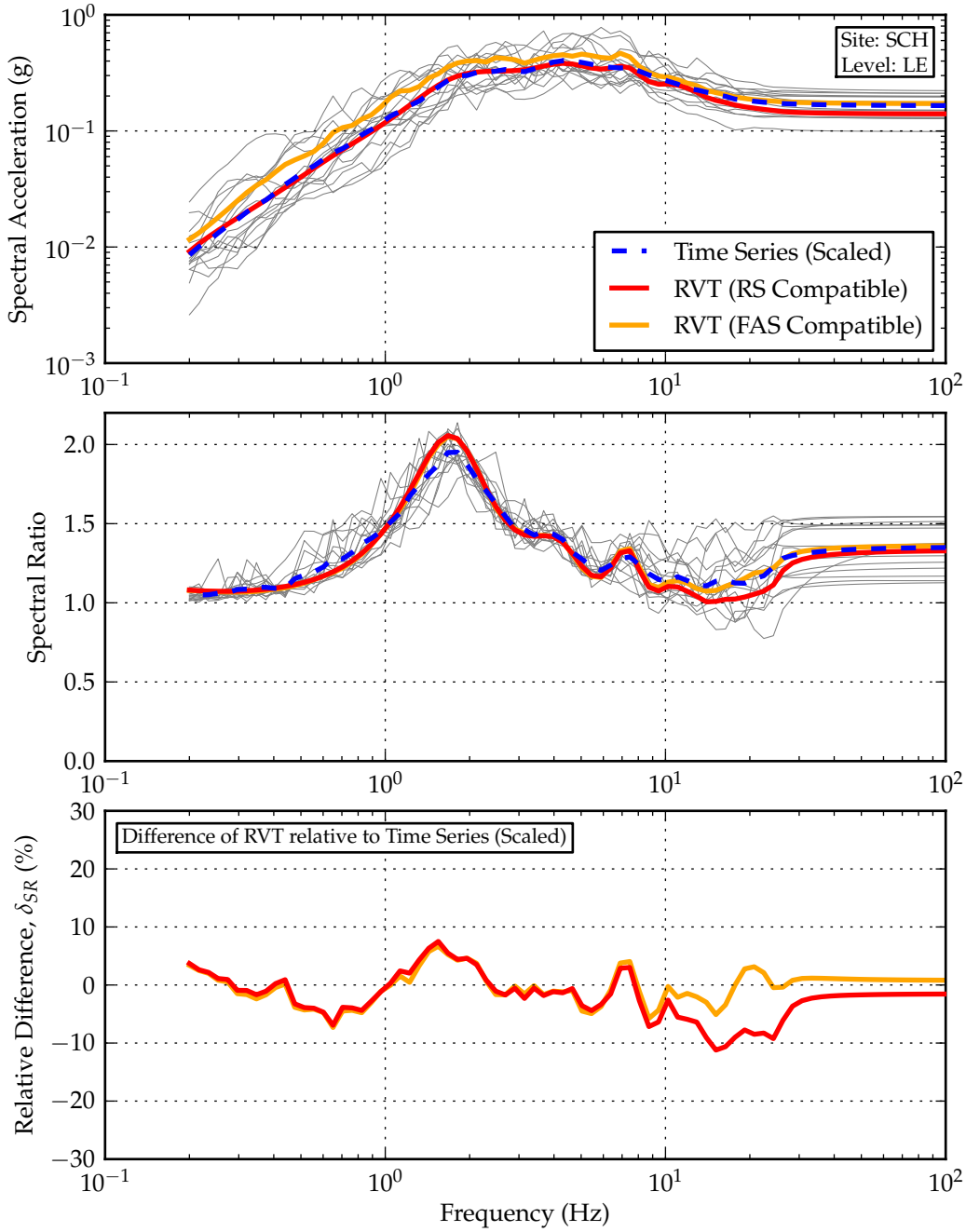

Figure 5.20: The response spectrum, spectral ratio, and relative difference for the SCH site computed with LE site response using scaled time series, as well as FAS and response spectrum compatible RVT motions.

input motions (Figure 5.22). The maximum strain predicted by the response spectrum compatible RVT motion agrees better with the time-series analysis than the FAS compatible RVT input motion at both intensities, and thus the response spectrum compatible motion yields more comparable results with time-series analysis. The improved performance of the response spectrum compatible motion is due to the fact that the FAS was developed to match the target input response spectrum for the specified duration. The FAS compatible RVT input motion is developed from the average FAS alone without ensuring that the FAS and the specified duration generate a response spectrum similar to the target response spectrum.

Using the response spectrum compatible RVT motion, the relative difference of the median spectral ratio was computed for the SCH and CC sites for input intensities of 0.13 and 0.40 g (Figure 5.23). For the SCH site, as the input intensity increases there is an increase in relative difference at the site frequency, as was observed with the stochastically simulated motions. However, the peak RVT difference of 15% in Figure 5.23 is larger than the peak RVT difference of about 10% observed for the stochastically simulated motions (Figure 5.12). This increase in RVT relative difference for the scaled motions is caused by a reduction in the median spectral ratio predicted by time-series analysis due to differences in the strains induced by individual time series. The data in Figure 5.23 also show increasingly negative relative difference for RVT at frequencies less than 0.1 seconds due to differences in FAS shape. The characteristics of the CC site result in greater amplification by the RVT analysis and a large positive bias at the site frequency at all intensity levels ($\approx$ 25% at 0.40 g, Figure 5.23). Additionally, there is a negative relative bias at frequencies higher than about 1.67 Hz, and this difference is also significant for linear-elastic analysis. This increasingly negative bias for RVT is due to the RVT analysis predicting larger strains (Figure 5.24).

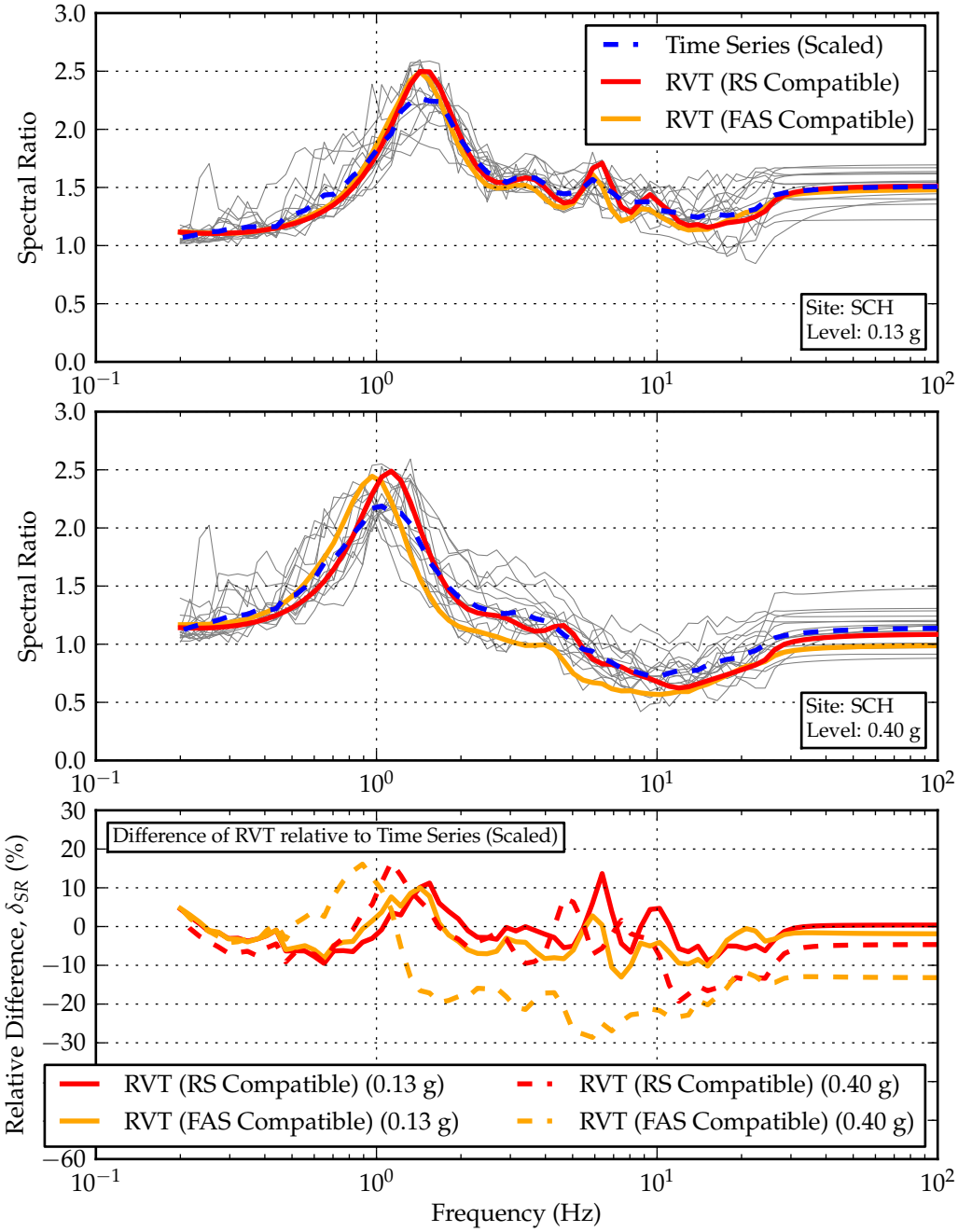

Figure 5.21: The spectral ratios for the SCH site computed with EQL site response using scaled time series, as well as FAS and response spectrum compatible RVT motions.

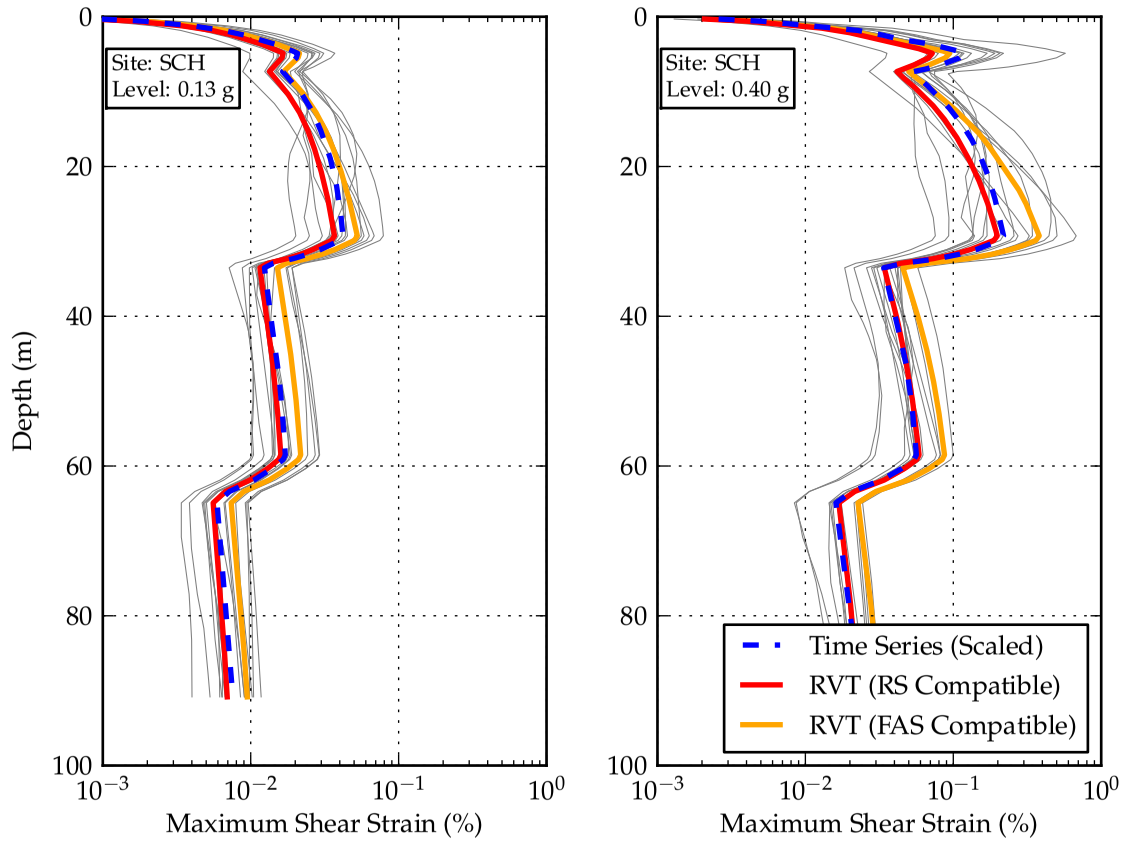

Figure 5.22: The maximum strain profiles for the SCH site computed using scaled time series and a response spectrum compatible RVT motion.

To summarize, the difference of RVT analysis assessed using scaled motions was similar to that assessment using stochastically simulated motions. It is recommended that a response spectrum compatible RVT input motion be developed for use in RVT analysis.

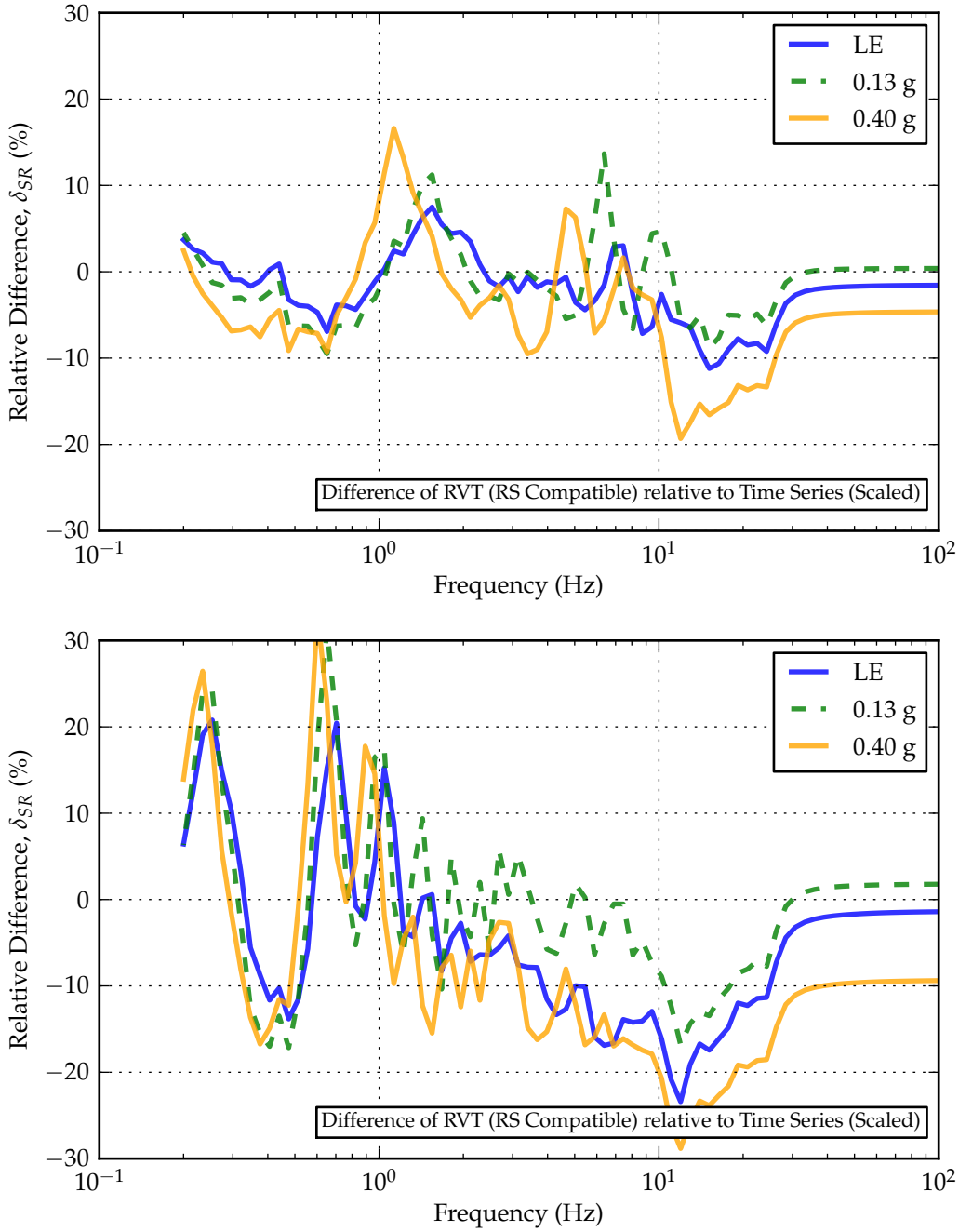

Figure 5.23: The relative difference of the spectral ratio of the SCH and CC sites computed using scaled time series and a response spectrum compatible RVT motion.

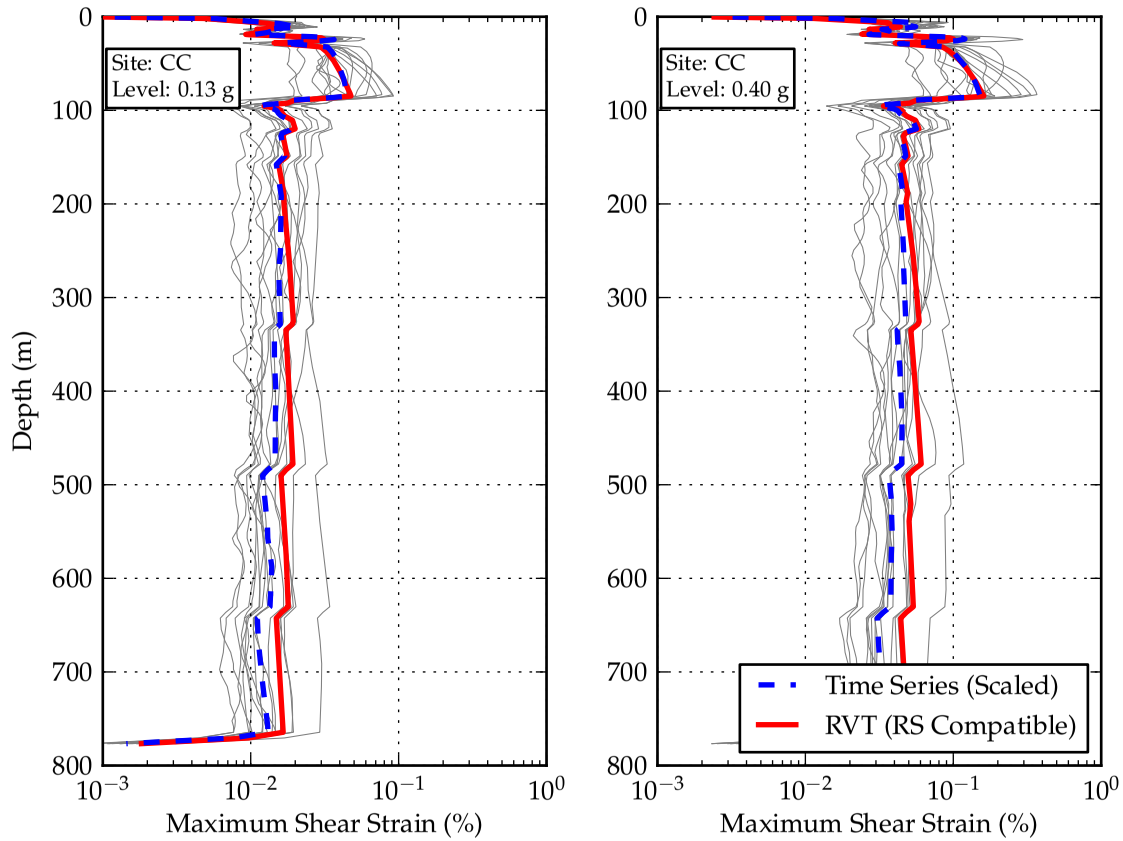

Figure 5.24: The maximum strain profiles for the CC site computed using scaled time series and a response spectrum compatible RVT motion.

5.4 Comparisons Using Spectrally Matched Time Series

The time-series analysis from the previous section involved a suite of input motions with significant motion-to-motion variability. For the time series analyses, this variability causes the site to strain and respond differently to each motion and results in a reduced median amplification at the site frequency, as previously shown in Figure 5.14. Spectrally matched motions display excellent agreement with the target response spectrum with very little variability, thus should provide results more similar to RVT analysis. The fifteen spectrally-matched input time series along with the response spectrum compatible input motion for RVT are shown in Figure 5.25. Generally, both the RVT response spectrum and FAS match the time series values, unlike the recorded time series which fit to either the FAS or the response spectrum. The variability in the time series at frequencies greater than 25 Hz is a result of the spectral matching only being performed up to 25 Hz. The difference of the RVT input response spectrum relative to the median of the time series is shown in Figure 5.26 and is less than 10% over the entire frequency range. The maximum relative difference of approximately 10% occurs at a frequency of 25 Hz and corresponds to the cutoff frequency used in the site response analysis (see Section 4.5).

The LE response of the SCH site for RVT and time-series analyses is shown in Figure 5.27. The results show excellent agreement between the response computed with the spectrally-matched time series and the RVT input motion, with the maximum difference of approximately 5% occurring at the site frequency (1.67 Hz). The EQL response of the site at 0.13 g is shown in Figure 5.28. There is generally less than 5% difference between the time series and RVT analysis, except at the site frequency frequency (1.49 Hz) and at a higher mode of vibration (7.69 Hz) where the relative difference is about 10%. Figure 5.29 shows the EQL response for an input motion intensity of 0.40 g. At this input intensity, differences between the spectrally-matched time

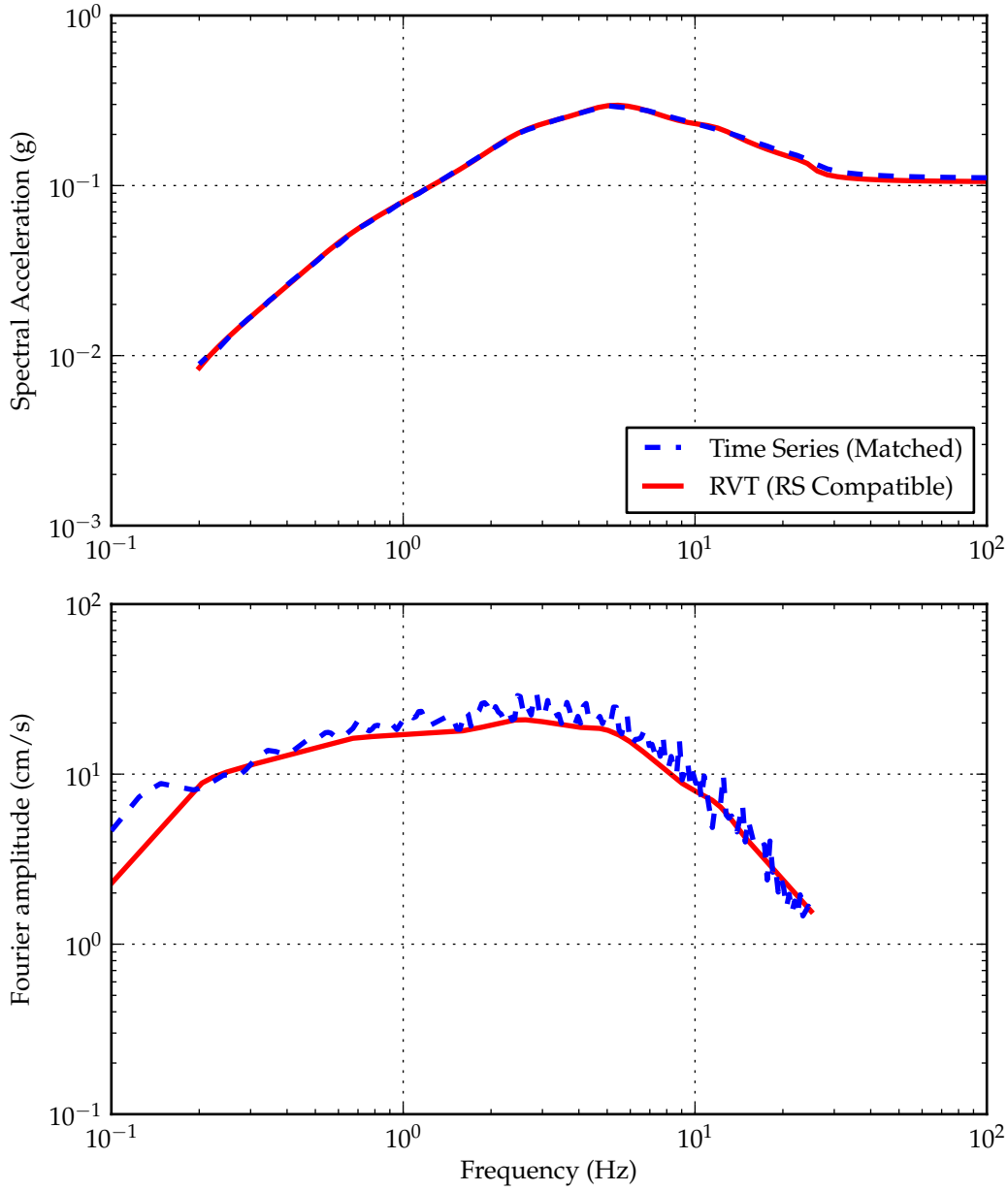

Figure 5.25: The input Fourier amplitude and response spectra for the spectrally-matched time series and a response spectrum compatible RVT motion.

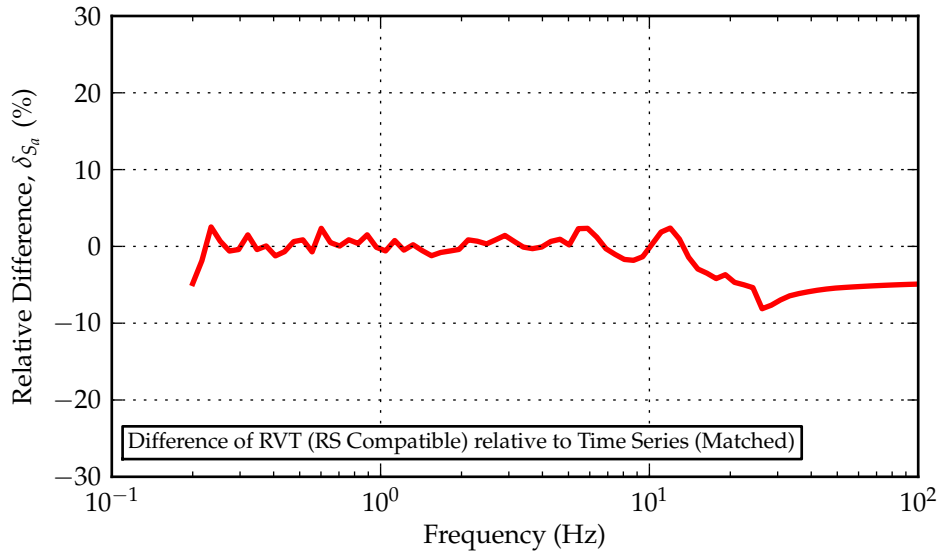

Figure 5.26: The relative difference of the input response spectra computed using a response spectrum compatible RVT motion.

series and RVT motion are more pronounced. The relative difference is approximately 8% at the site frequency (1.11 Hz), and approximately -5% to -9% at higher frequencies (1.42 to 25 Hz). The consistent negative bias of the RVT approach is again a result of larger strains computed by the RVT analysis (Figure 5.30). These larger strains are a result of increased sensitivity of the smooth RVT input to the site amplification. Figure 5.31 shows the relative difference for all analyses for the SCH site and illustrates the connection between increasing input motion intensity and increasing positive RVT bias at the site frequency and increasing negative RVT difference at higher frequencies. However, the relative difference of the RVT spectral ratio is never greater than 9% for this set of analyses. Using scaled input motions, the RVT difference was as large as 15 to 20% (Figure 5.23).

The EQL response of the CC site for RVT and time-series analyses is shown in Figure 5.32 for an 0.13 g input intensity. In general, the agreement between the time series and RVT analyses is good with the relative difference less than 10% for most

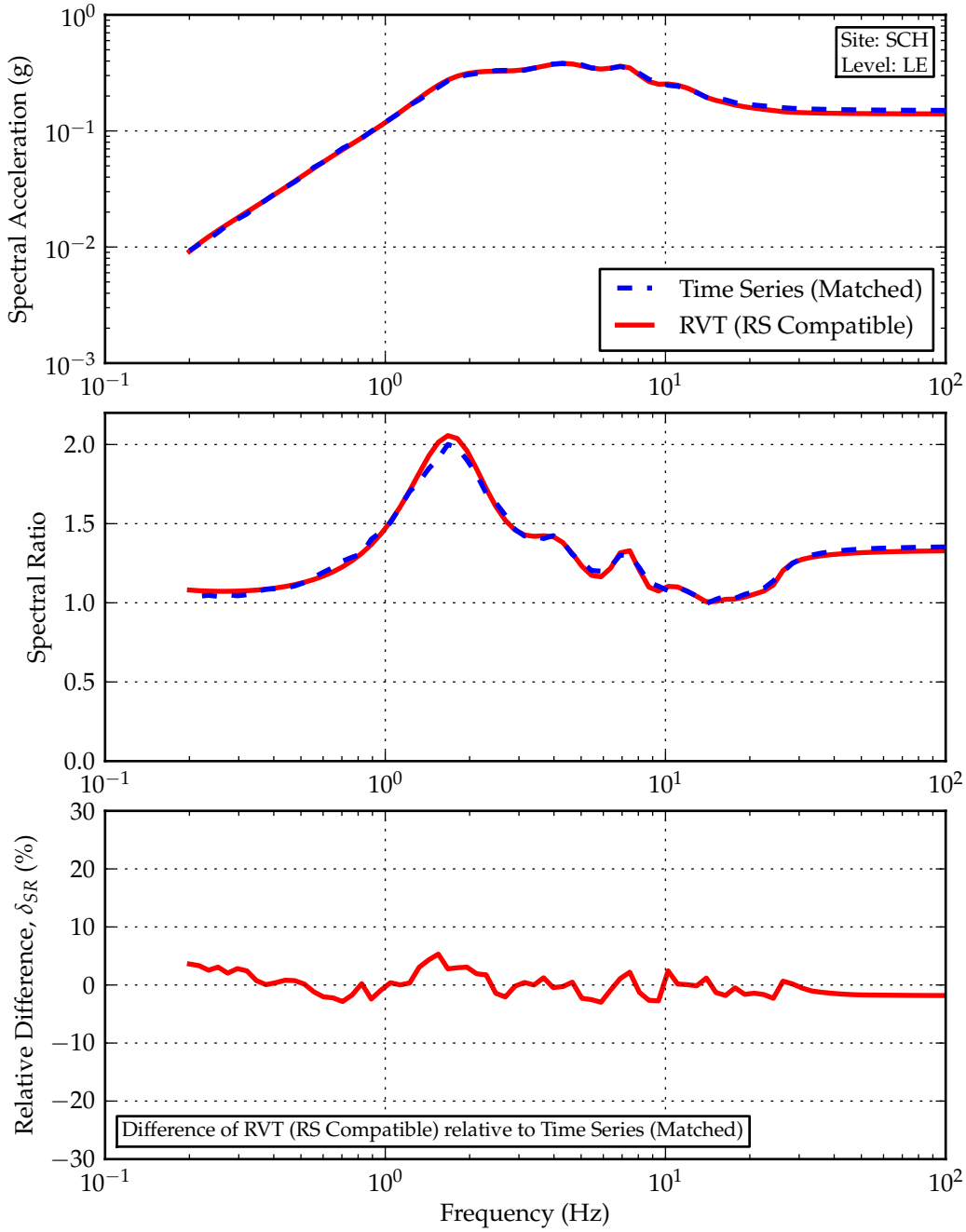

Figure 5.27: The response spectrum, spectral ratio, and relative difference for the SCH site computed with LE site response using spectrally-matched time series and a response spectrum compatible RVT motion.

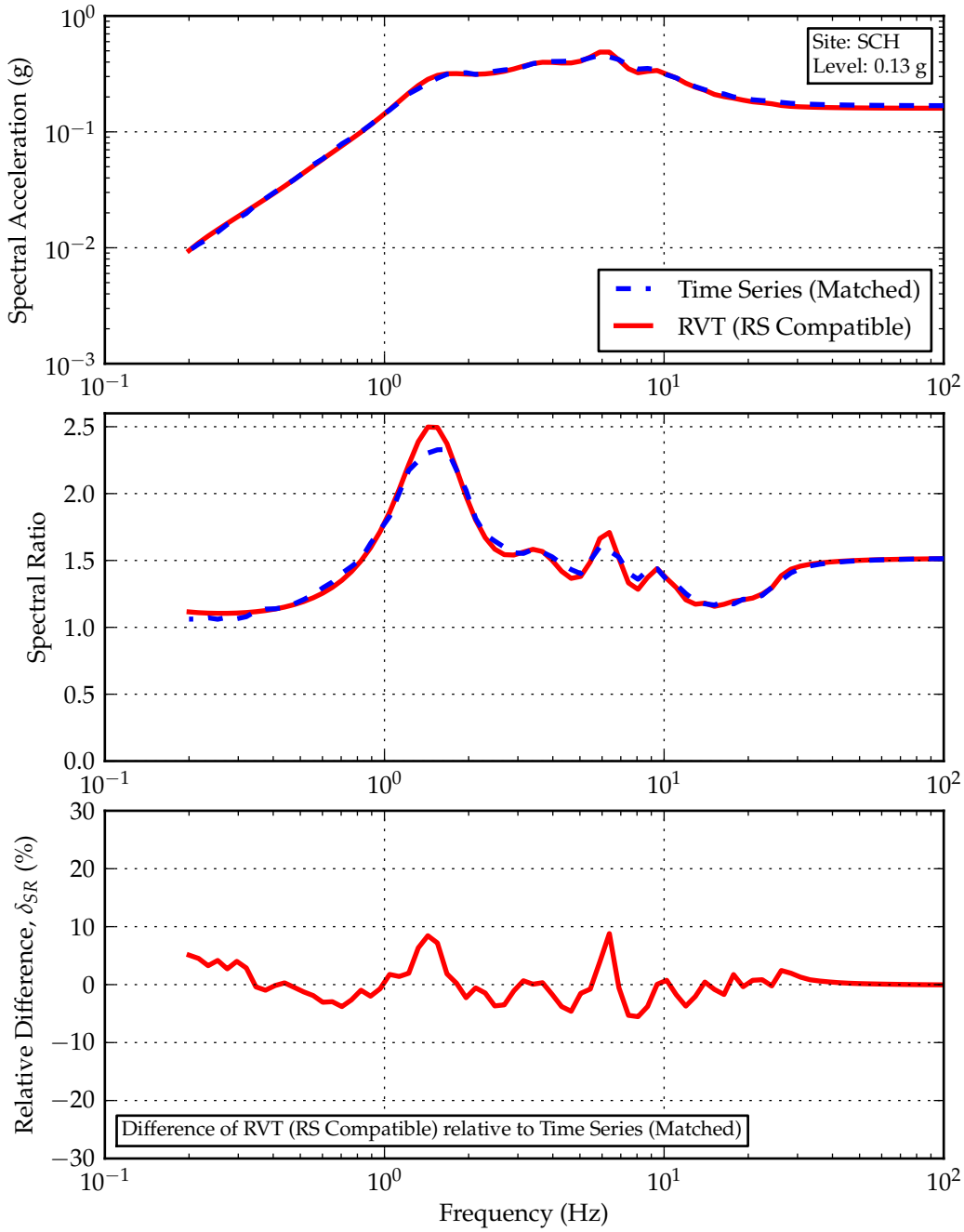

Figure 5.28: The response spectrum, spectral ratio, and relative difference for the SCH site computed with EQL site response using spectrally-matched time series and a response spectrum compatible RVT motion (input PGA of 0.13 g).

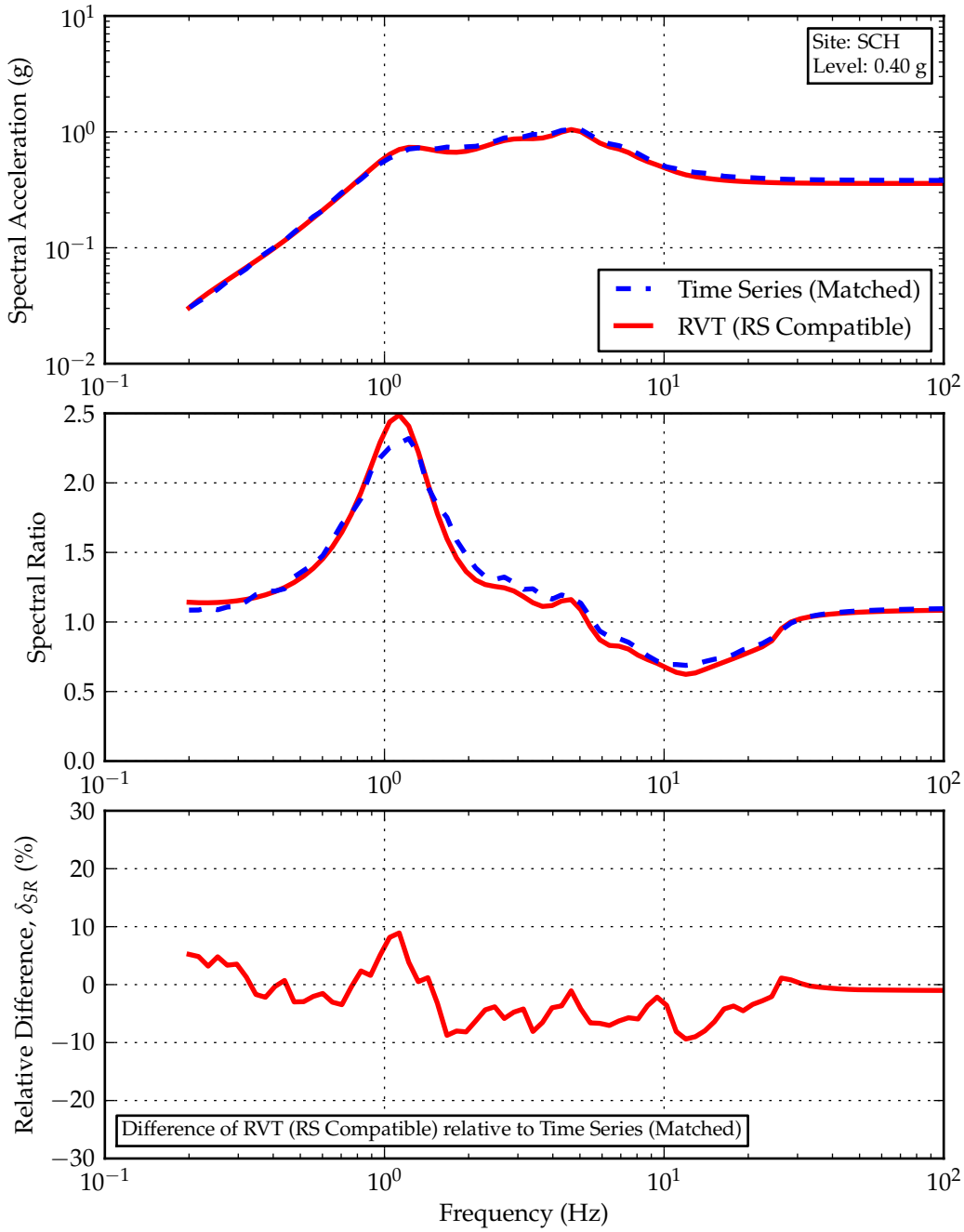

Figure 5.29: The response spectrum, spectral ratio, and relative difference for the SCH site computed with EQL site response using spectrally-matched time series and a response spectrum compatible RVT motion (input PGA of 0.40 g).

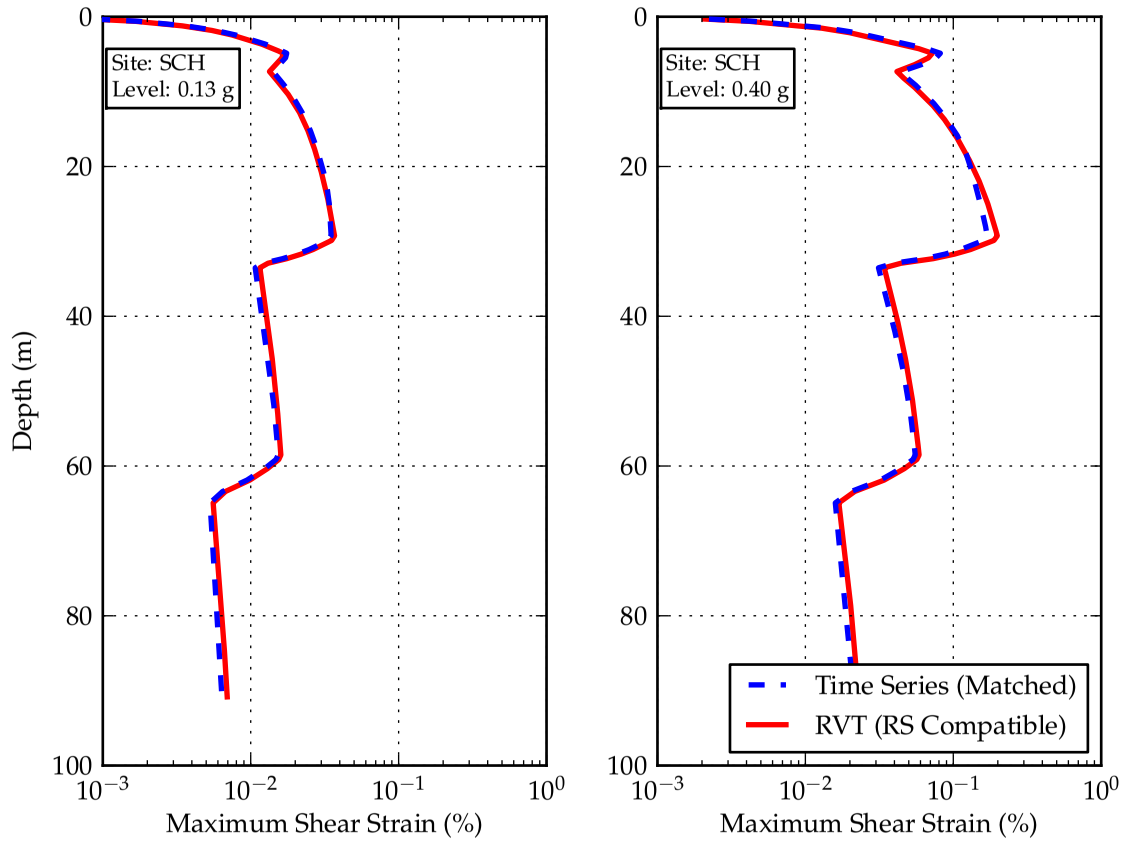

Figure 5.30: The maximum strain profiles for the SCH site computed using spectrally-matched time series and a response spectrum compatible RVT motion.

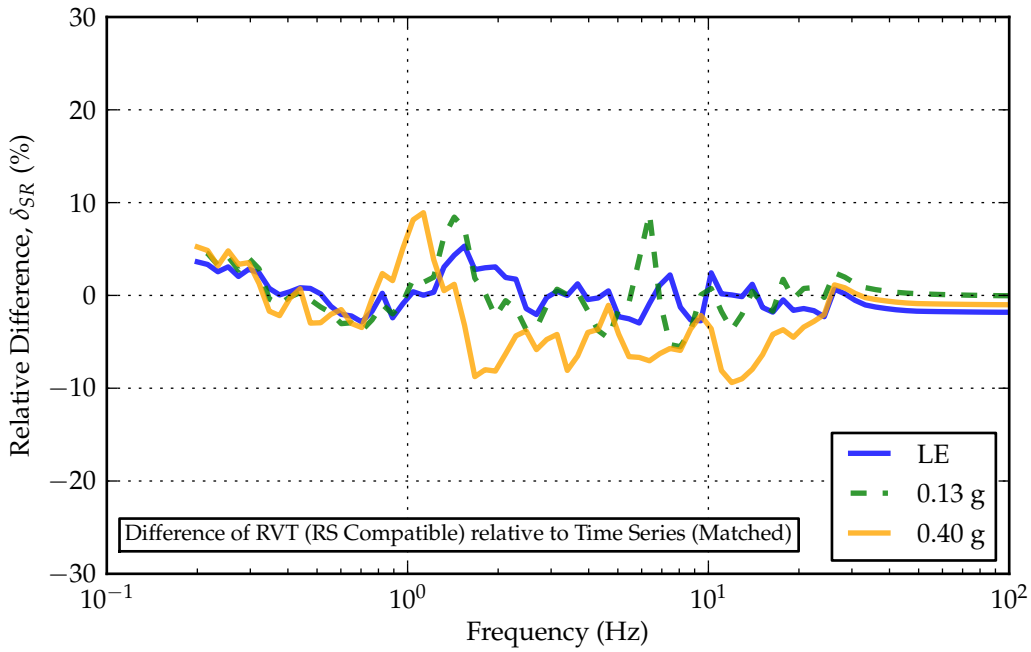

Figure 5.31: The relative difference of the spectral ratio of the SCH site computed using spectrally-matched time series and a response spectrum compatible RVT motion.

frequencies, except in two key regions. The first region is at low frequencies where the smooth input FAS used in RVT produces more amplification than the time-series analysis, and thus the RVT results are positively biased. The second region is around 0.1 Hz where there is a relative difference of -10%, which is associated with over-damping caused by the larger strains predicted by the RVT analysis (Figure 5.33). The RVT difference for CC and the 0.40 g input intensity is shown in Figure 5.34 along with the RVT difference for the other analyses already discussed. As with the previous results from SCH, as the intensity of the input motion increases the positive bias at the site frequency increases and the negative bias at high frequencies increases. Additionally, the RVT difference for the spectrally matched input motions (Figure 5.34) is somewhat smaller than for scaled input motions (Figure 5.23)

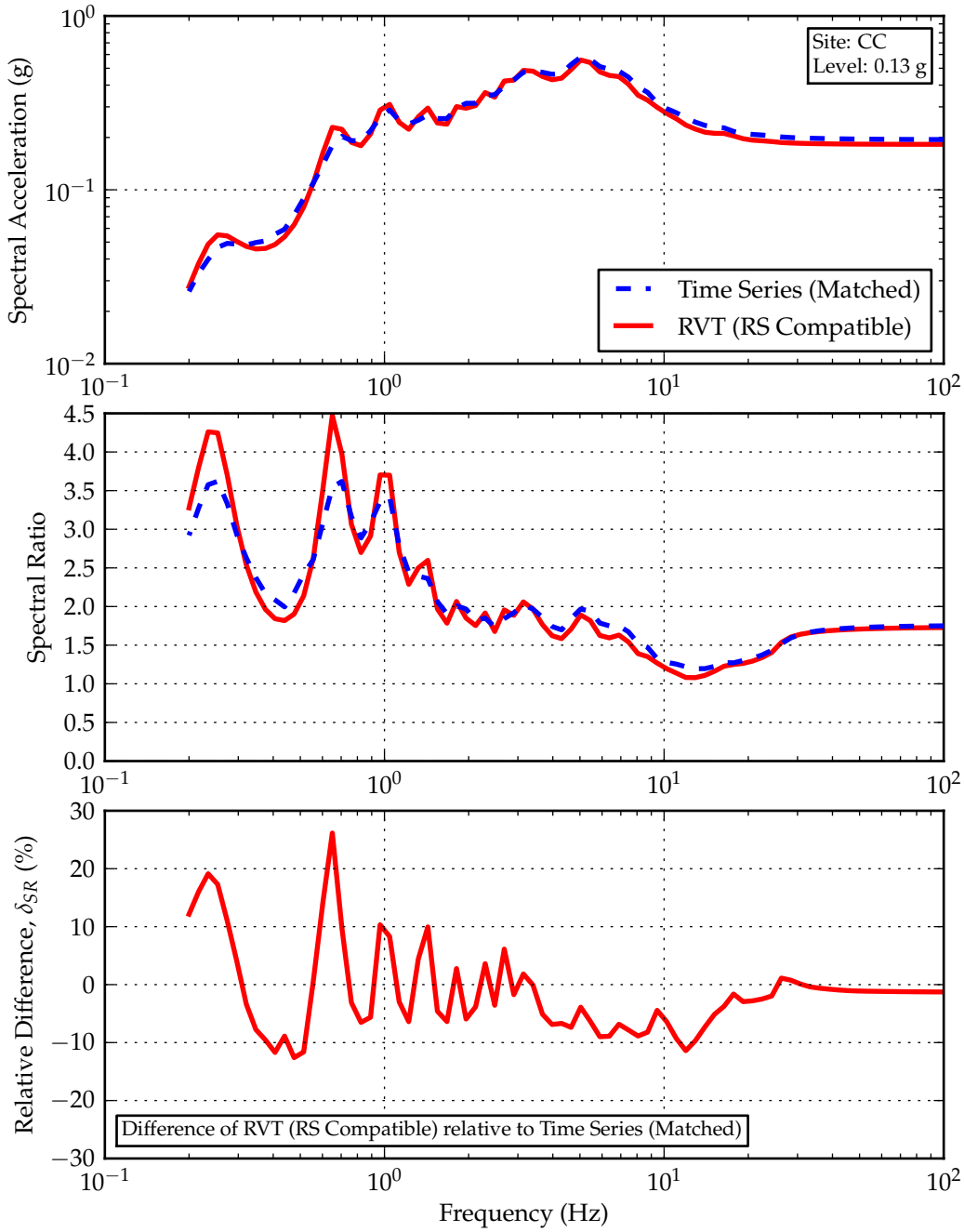

Figure 5.32: The response spectrum, spectral ratio, and relative difference for the CC site computed with EQL site response using spectrally-matched time series and a response spectrum compatible RVT motion (input PGA of 0.13 g).

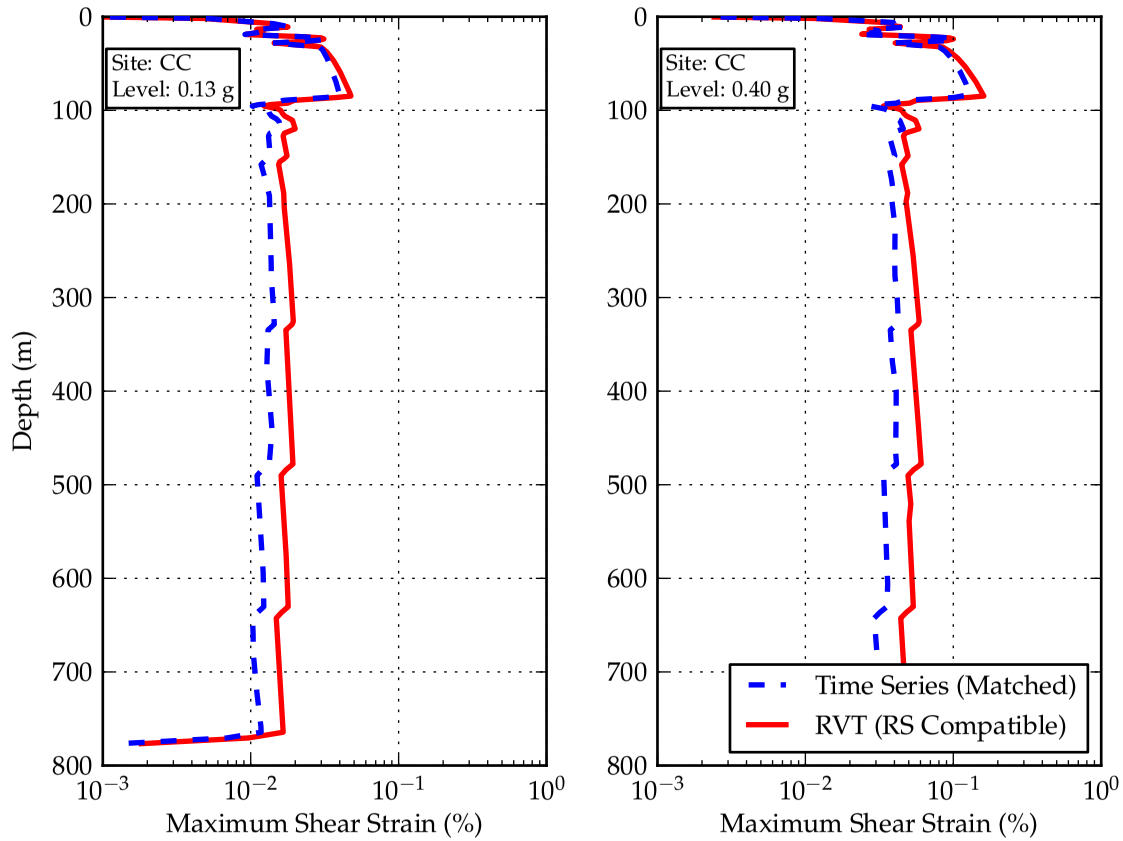

Figure 5.33: The maximum strain profiles for the CC site computed using spectrally-matched time series and a response spectrum compatible RVT motion.

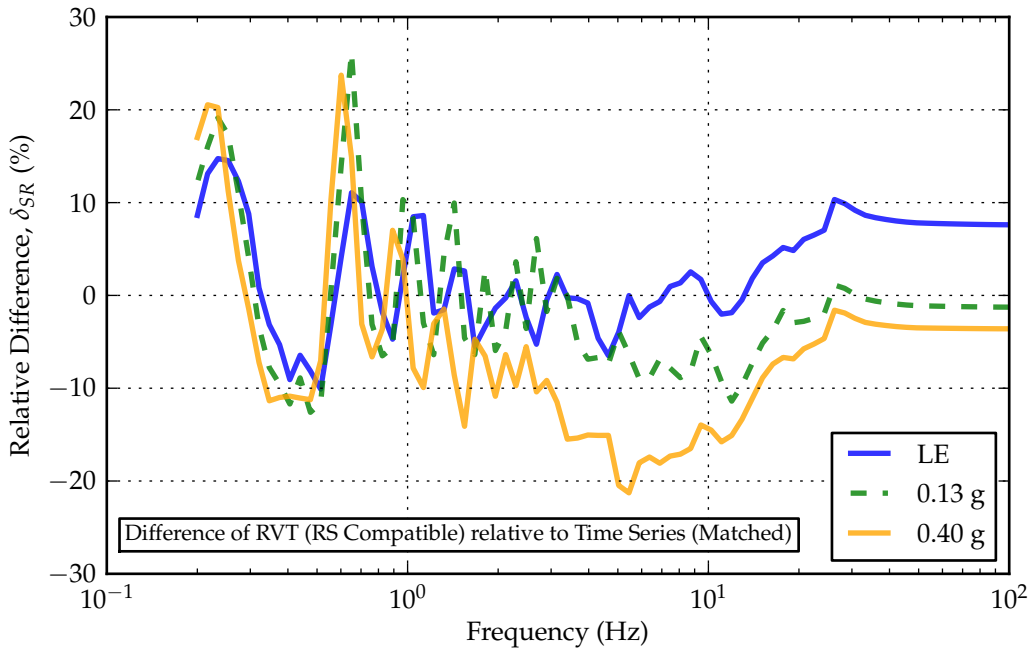

Figure 5.34: The relative difference of the spectral ratio of the CC site computed using spectrally-matched time series and a response spectrum compatible RVT motion.

5.5 Summary

This section has shown that the surface response spectrum and associated spectral ratios computed using the RVT approach may be noticeably different than the median response computed from a suite of input motions. Figure 5.35 summarizes these differences for the different input motion characterizations used and the two site analyzed. The smooth shape of the input FAS used in RVT analyses produces higher peaks and lower troughs in the spectral ratio and results in a consistent positive difference at the site frequency and first few modes, as shown in Figure 5.35. The positive bias of RVT is influenced most by site frequency and the shear-wave velocity of the bedrock. Lower site frequencies and larger bedrock velocities result in larger relative differences for RVT analysis, with relative differences as large as 30%. As the input intensity increases, the positive bias at the site frequency for RVT analysis generally increases, but the difference becomes negative at high frequencies. The negative bias (i.e., under prediction) at high frequencies is caused by RVT predicting larger strains and associated damping than the time-series analysis.

The time-series analyses performed using different suites of input motions demonstrated the influence of ground motion selection on the results from site response analysis. While each of the suites of input motions predicted responses that peaked at the same frequency, the median spectral ratio at the site frequency was largest for the spectrally matched motions and smallest for the scaled motions (Figure 5.35). The differences in the median spectral ratio are due to differences in the motion-to-motion variability within each suite of input motions. The suite of scaled ground motions had the greatest variability and produced the smallest median spectral ratio at the site frequency. Additionally, the results in Figure 5.35 show that the stochastically simulated input motions produced the smallest spectral ratios at high frequencies (i.e., above 10 Hz). This result is due to the FAS shape for the stochastically simulated input

motions, which has relatively greater high-frequency content. This effect also influenced the high-frequency spectral ratios for the response spectrum compatible RVT analysis and for the spectrally matched TS analysis.

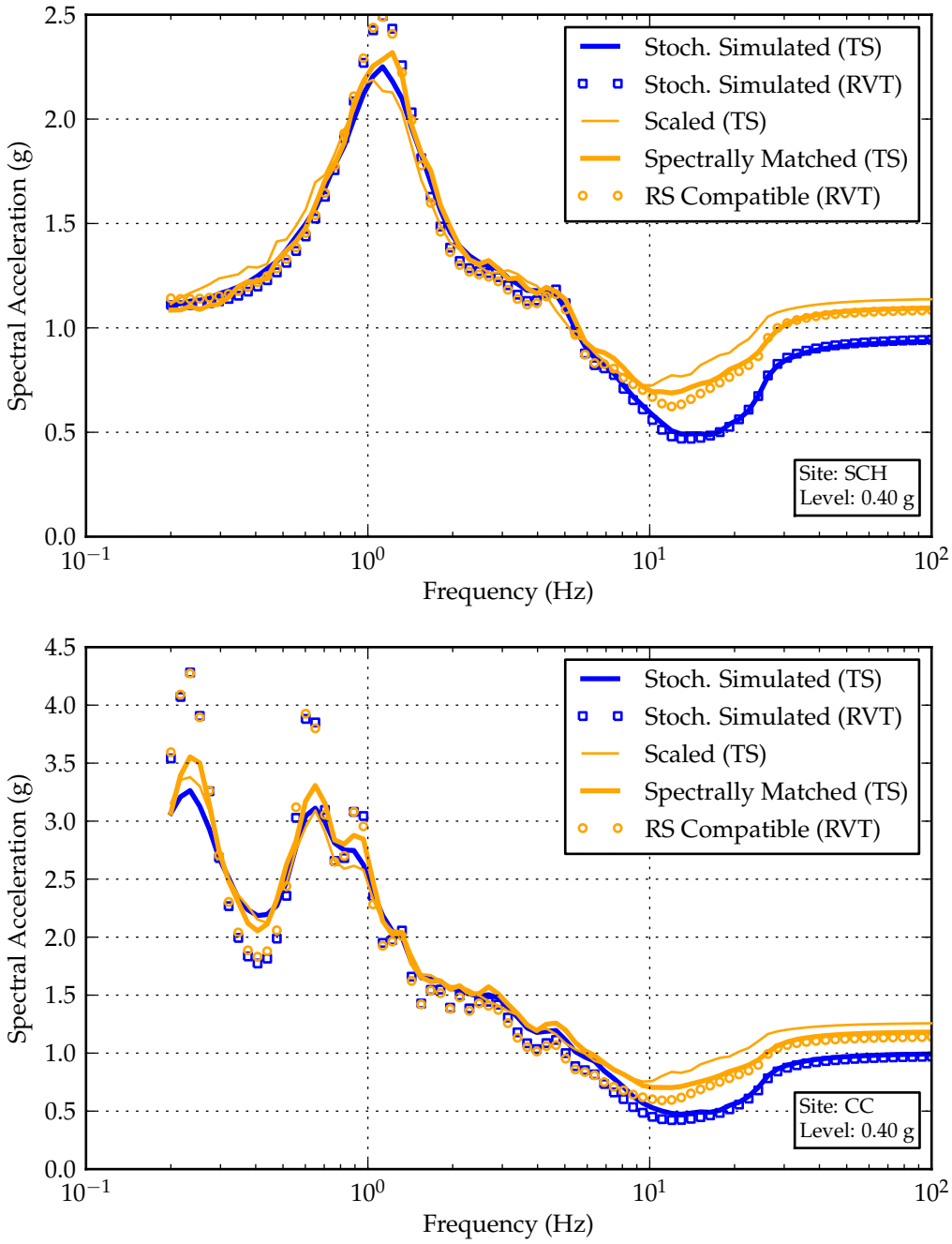

Figure 5.35: The computed spectral ratios for the SCH and CC sites at an input intensity of 0.40 g.

Chapter 6

Comparison of Equivalent-Linear and Nonlinear Methods

6.1 Introduction

Nonlinear site response analysis propagates the input ground motion through the soil deposit in the time domain and varies the soil properties with time. This approach allows for more realistic modeling of the nonlinear response of the soil. The nonlinear method is believed to provide more realistic site response results especially for high-intensity input motions. In this section, the equivalent-linear (EQL) method is compared to the nonlinear method using the suite of spectrally matched motions described in Section 4.4. Analyses are performed for linear-elastic conditions, as well as for nonlinear conditions with low-, moderate-, and high-intensity input motions. To maintain similarity between the nonlinear and equivalent-linear analyses, each time series used as input in the nonlinear analysis is truncated at 25 Hz. This filtering mimics the truncation performed in the equivalent-linear analysis.

6.2 Linear Elastic Analysis

A suite of linear-elastic analyses was performed to evaluate the influence of performing site response analysis in the time domain, which is used in nonlinear analysis, and performing site response analysis in the frequency domain, which is used in EQL analysis. The key differences in these two approaches are the treatment of damping and the numerical methods used to solve the equations of motion.

The nonlinear method incorporates damping in two ways: through a small-strain viscous damping matrix and through the nonlinear, cyclic stress-strain response. The viscous damping represents the damping at small strains (D_{min}), while the nonlinear, stress-strain response represents the hysteretic damping at larger strains. The majority of the damping for moderate to high levels of ground shaking comes from the nonlinear stress-strain response, while the viscous damping is more critical at lower intensities. The viscous damping has been traditionally modeled using the full Rayleigh damping formulation (Rayleigh and Lindsay, 1945), which generates the damping matrix ($\mathbf{C}$) as a linear combination of the initial stiffness ($\mathbf{K}$) and mass ($\mathbf{M}$) matrices:

$$\mathbf{C} = a_0\mathbf{K} + a_1\mathbf{M} \tag{6.1}$$

This formulation results in frequency-dependent viscous damping (e.g., Chopra (2007)). The coefficients a_0 and a_1 are selected to tune the viscous damping ratio to a target damping ratio at two frequencies. Stewart et al. (2008) recommends that Rayleigh damping be fit to the target damping at the natural frequency of the site (f_s) and five times the natural frequency of the site ($5f_s$). Using this guideline, the frequency-dependent viscous damping is computed for both the SCH and CC sites (Figure 6.1). For the SCH site, the Rayleigh damping ratio is within a factor of 2.0 of the target value between about 0.40 and 15 Hz. Considering that the target D_{min} value is typically around 1% and that the equivalent viscous damping due to the nonlinear soil response

may be well above 10%, this error should no not significantly impact site response results for the damping levels induced by moderate to high intensity levels of shaking. For the CC site, the Rayleigh damping ratio may be as much as 5 to 20 times larger than the target value at frequencies above 6.5 Hz. These large levels of damping at high frequencies are caused by fitting the Rayleigh damping to the very small natural frequency ($f_s = 0.21$ Hz) of the CC site. This level of excessive damping will lead to under prediction of high-frequency response from nonlinear analysis for sites with low natural frequencies like CC. Phillips and Hashash (2009) offer a potential solution to the problem of frequency-dependent damping by proposing a method that allows for frequency-independent Rayleigh damping.

To illustrate the influence of the Rayleigh damping model on site response results, linear-elastic (LE) site response analyses are conducted for both the SCH and CC sites. Results from time-domain analyses are compared with results from frequency-domain wave propagation, which rigorously solves the one-dimensional wave equation with frequency-independent damping. Figure 6.2 shows the computed median spectral ratio for the suite of spectrally-matched input motions using: (1) the frequency domain (FD) method, (2) the time domain (TD) method using Rayleigh damping tuned at f_s and $5f_s$, and (3) the TD method using the frequency-independent damping formulation. Compared to the frequency-domain results, the time-domain results with Rayleigh damping underestimate the spectral ratio at frequencies greater than 10 Hz for SCH. The underestimation is on the order of 10 to 25%. The frequency-independent damping improves the agreement, but only slightly (5 to 15% under prediction). For CC, the time-domain results start to deviate from the FD results at about 1.67 Hz when the viscous damping is tuned to f_s and $5f_s$ and the underestimation is as large as 50 to 75%. This reduction is caused by the large levels of Rayleigh damping at moderate to high frequencies (Figure 6.1). The results in Figure 6.2 for the CC site also include the response when tuning the Rayleigh damping to $3.3f_s$ (0.7 Hz) and $16.5f_s$ (3.5 Hz).

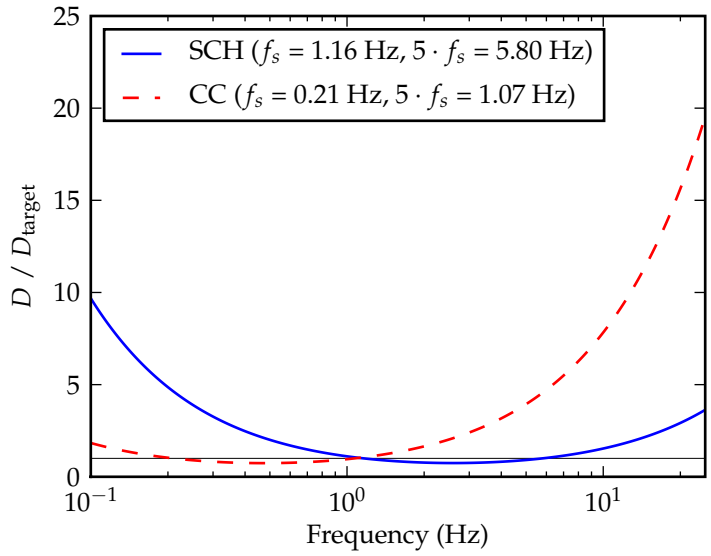

Figure 6.1: Variation of damping ratio with frequency for the full Rayleigh damping formulation.

By increasing the tuning frequencies, the over-damping at high frequencies is reduced, but then the amplification at the site frequency (0.25 Hz) becomes over damped. The frequency-independent Rayleigh damping formulation applied to the CC site results in agreement that is similar to the SCH site, with approximately 5 to 15% underestimation relative to the frequency domain method at frequencies higher than 3.3 Hz.

Another difference between time-domain and frequency-domain analyses is the numerical methods used to solve the dynamic equations of motion. The frequency-domain method uses a closed form solution for the one-dimensional wave equation such that no numerical approximation is required to compute the response. Time-domain analysis requires a time stepping method that solves the differential equation of motion incrementally between time steps, and this numerical method introduces some computational error.

`DeepSoil` uses the Newmark β method with $\beta = \frac{1}{4}$ to solve the differential equation of motion. The model assumes that the acceleration within a time step is a constant,

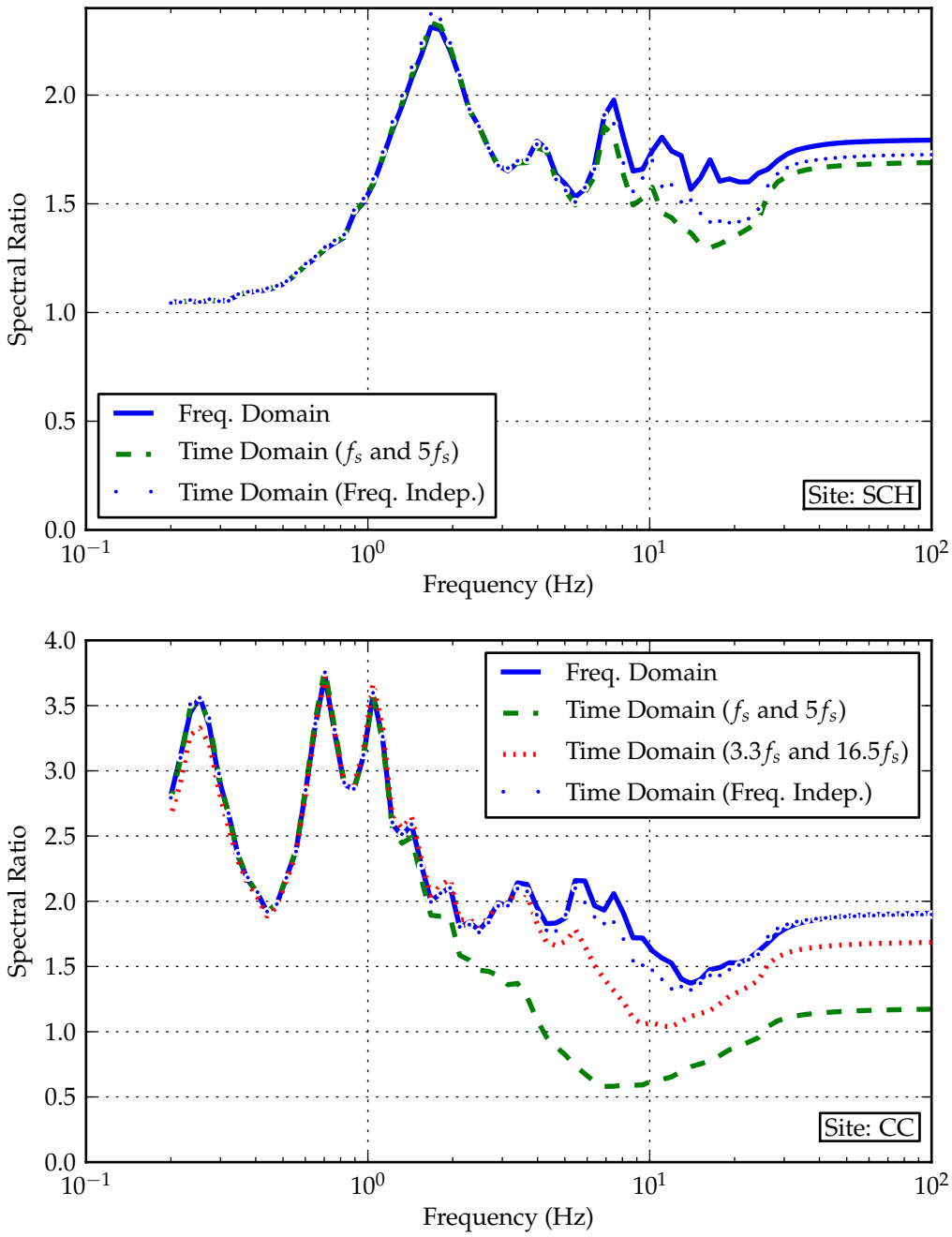

Figure 6.2: Spectral ratio of the SCH and CC sites using linear-elastic time domain and frequency domain methods.

average value. This time stepping method is unconditionally stable (Chopra, 2007), which is advantageous for multi-degree-of-freedom systems. However, numerical errors are also introduced that cause frequency elongation and amplitude decay (Chopra, 2007).

To illustrate these errors, the linear-elastic results (with frequency-independent damping) are considered. The site response results are presented as the ratio of the FAS of the surface motion to the FAS of the input motion, which represents the equivalent transfer function for the site. Figure 6.3 shows the amplitude of the SCH and CC transfer functions for the closed form solution in the frequency domain and for three different motions used in the linear-elastic, time-domain analysis. The time step (Δt) for the three input motions vary from 0.005 to 0.02 seconds. For the time-domain analyses, the peaks at high frequencies shift towards lower frequencies, which represents frequency shortening, and the amplitudes of the peaks decrease, which represents amplitude decay. The frequency shortening and amplitude decay for SCH becomes noticeable at about 10 Hz and significant at about 15 Hz. The frequency shortening and amplitude decay are more significant for motions with larger Δt. Because of the depth of the CC site, the character of the transfer function is different than SCH, with are many modes (i.e., peaks) at low frequencies (Figure 6.3). Nonetheless, frequency shortening and amplitude decay are again noticeable at frequencies greater than about 10 to 15 Hz, and they are more significant for motions with larger Δt.

The frequency elongation and amplitude decay observed in Figure 6.3 directly influence the spectral ratios at high frequencies. For both the SCH and CC sites, the spectral ratios from the time domain analysis with frequency-independent damping are 5 to 15% smaller than the frequency domain results at frequencies above 10 Hz, and this result is caused by the frequency shortening and amplitude decay observed at frequencies above 10 Hz in Figure 6.3.

The results from linear-elastic analysis illustrate two important effects that cause an

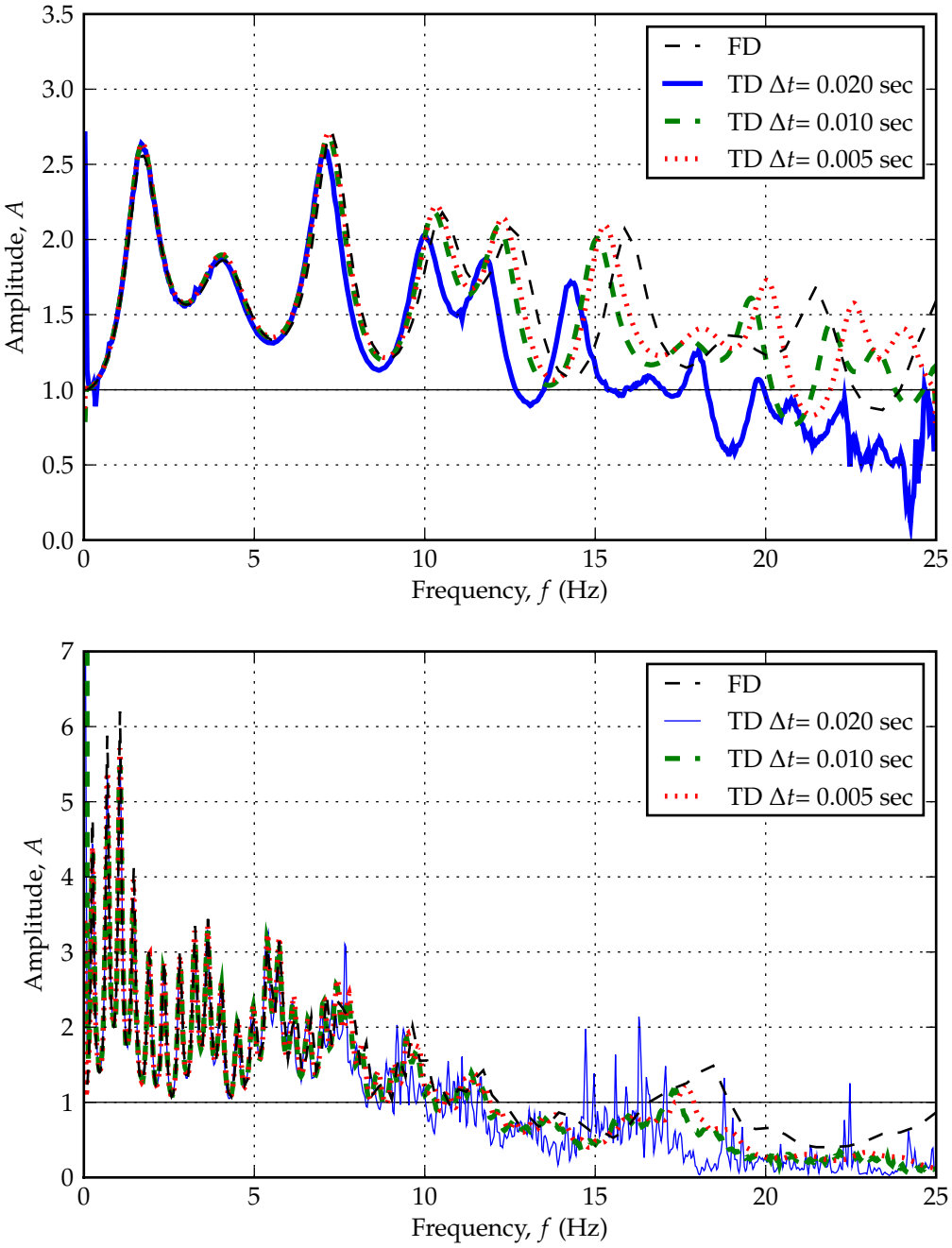

Figure 6.3: Amplitude of the transfer function computed for the SCH and CC sites using LE time-domain (TD) and frequency-domain (FD) methods.

underestimation of the site response at high frequencies for time domain methods. First, frequency-dependent viscous damping tuned to f_s and $5f_s$ in time domain analysis can significantly underestimate the site response at frequencies greater than $5 \cdot f_s$. The issue is most critical for low frequency sites, because the over-damped frequencies are in the range of engineering interest. The frequency-independent Rayleigh damping formulation of Phillips and Hashash (2009) can reduce this underestimation, but at the expense of computational effort. Additionally, numerical errors introduced by the time-stepping integration used in time-domain analysis influence the site response at frequencies greater than about 10 Hz. For linear-elastic analysis, the errors associated with the time-stepping integration are pronounced because the modes above 10 Hz contribute significantly to the response. For fully nonlinear analysis, these errors should not be significant because the modes at frequencies greater than 10 Hz no longer contribute significantly to the response.

6.3 Analyses for Low-Intensity Input Motions

It is generally believed that nonlinear and EQL analysis provide similar estimates of site response at low-intensity levels because the induced strains are small and the equivalent-linear assumption is valid at these strain levels. However, the previous section showed that even under linear-elastic conditions the frequency-domain approach (used in the EQL analysis) and the time-domain approach (used in the nonlinear analysis) do not provide similar results. To investigate the differences between nonlinear and EQL analysis at low-intensity levels, analyses were performed using the suite of spectrally-matched input motions scaled to a median PGA of 0.01 g.

The spectral ratio and relative difference between nonlinear and EQL analysis are shown in Figure 6.4 for the SCH site. The linear-elastic results with frequency-independent damping are shown for comparison. In general, these low-intensity motions

show a result similar to the linear-elastic results (i.e., nonlinear analysis under predicts the response at high frequencies relative to EQL analyses). However, the nonlinear results at low-intensity show more under prediction than the linear-elastic analysis at frequencies higher than 20 Hz. Between 7 and 20 Hz, the nonlinear results at low-intensity and the LE results are similar. The results for CC are shown in Figure 6.5 and the trends are similar. At frequencies above about 17 Hz, the nonlinear results at low-intensity show more under prediction than the LE results. Interestingly, at frequencies between 3 and 17 Hz the nonlinear results at low-intensity show less under prediction than the LE results.

To investigate these results, let us consider the equivalent transfer functions for the sites. The transfer function is complex valued, and computed from the Fourier Amplitudes of the surface and input motions using:

$$TF(f) = \frac{a_{\text{surf}}(f) + \imath b_{\text{surf}}(f)}{a_{\text{in}}(f) + \imath b_{\text{in}}(f)} = a(f) + \imath b(f) \tag{6.2}$$

The previous section only considered the amplitude of the transfer function ($A(f) = \sqrt{a(f)^2 + b(f)^2}$); this section will also consider the phase of the transfer function ($\phi(f) = \arctan[b(f)/a(f)]$). The amplitude and phase of the equivalent transfer functions derived from nonlinear and EQL analysis for the `KOZANI-KOZ--L` motion and the SCH site are shown in Figure 6.6. The results from linear elastic TD analysis are also shown for comparison. At low frequencies (less than 10 Hz), the amplitude and phase of the transfer functions are similar for the nonlinear, EQL, and linear-elastic analyses. The saw-tooth pattern for the phase represents the variation in phase as one moves from one mode to another. At higher frequencies (greater than 15 to 20 Hz), the nonlinear method predicts larger amplitudes and the phase becomes more irregular or incoherent. The phase remains smooth at all frequencies for the EQL analysis, and is also smooth for the linear-elastic analysis in the time domain (Figure 6.6).

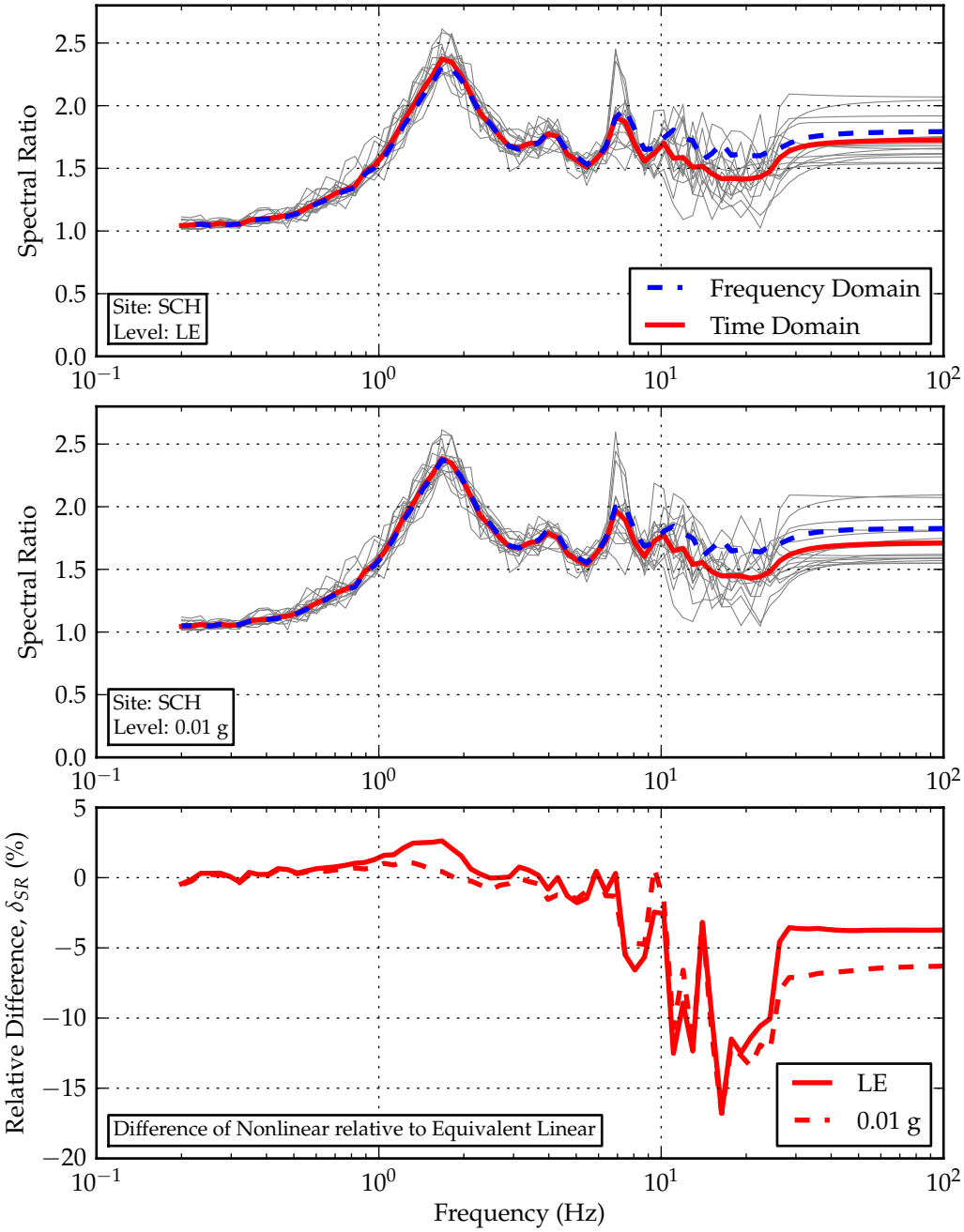

Figure 6.4: The spectral ratio and relative difference for the SCH site computed with time domain and frequency domain methods using the spectrally-matched ground motions.

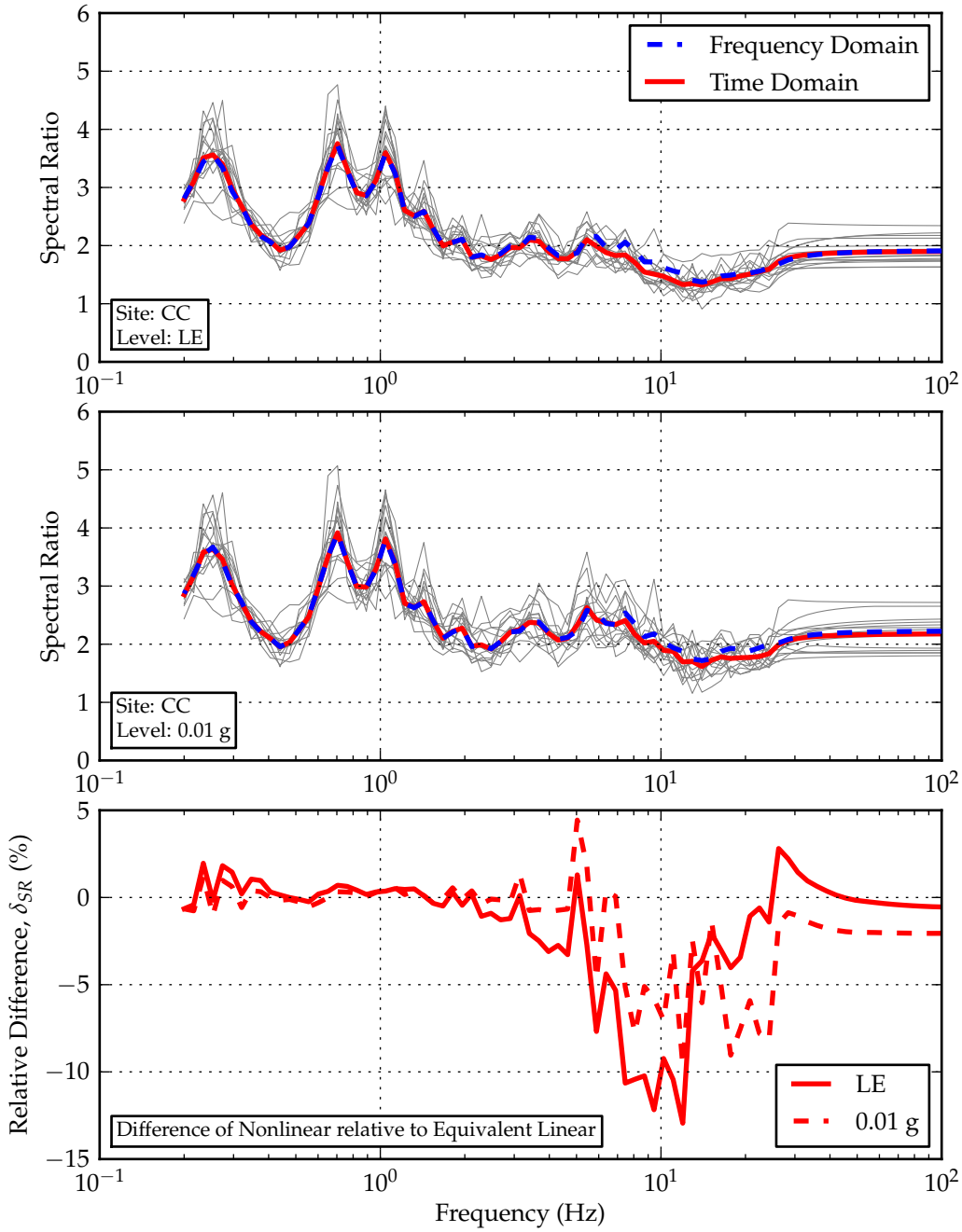

Figure 6.5: The spectral ratio and relative difference for the CC site computed with time domain and frequency domain methods using the spectrally-matched ground motions.

The phase incoherence at high frequencies, as well as the large peaks in the amplitude of the transfer function at high frequencies, is the result of the soil properties changing with time in nonlinear analysis, in particular the instantaneous change in stiffness that occurs upon load reversal. These effects are present in addition to the effects of frequency elongation and amplitude decay discussed previously, and all of these effects are concentrated at frequencies greater than about 10 Hz. Generally, an increase in transfer function amplitude should generate larger spectral accelerations at these frequencies. However, the phasing of these frequencies is incoherent such that they destructively interfere with one another. Considering the relative differences for SCH shown in Figure 6.4, it is the phase incoherence effect that further reduces the nonlinear response compared with the LE response at frequencies above 20 Hz. At frequencies 10 and 20 Hz, the linear-elastic and nonlinear results are similar indicating that neither the increase in high frequency amplitudes nor the incoherence in high-frequency phasing significantly influences the spectral ratios in this frequency range. The amplitude and phase of the equivalent transfer functions for the CC site are shown in Figure 6.7. Large amplitudes and incoherent phases at high frequencies are clearly observed, and it is the phase incoherence effect further reduces the nonlinear response relative to the EQL response at high frequencies. However, in this case the increase in high frequency amplitudes results in less under prediction for the spectral accelerations between 3 and 17 Hz.

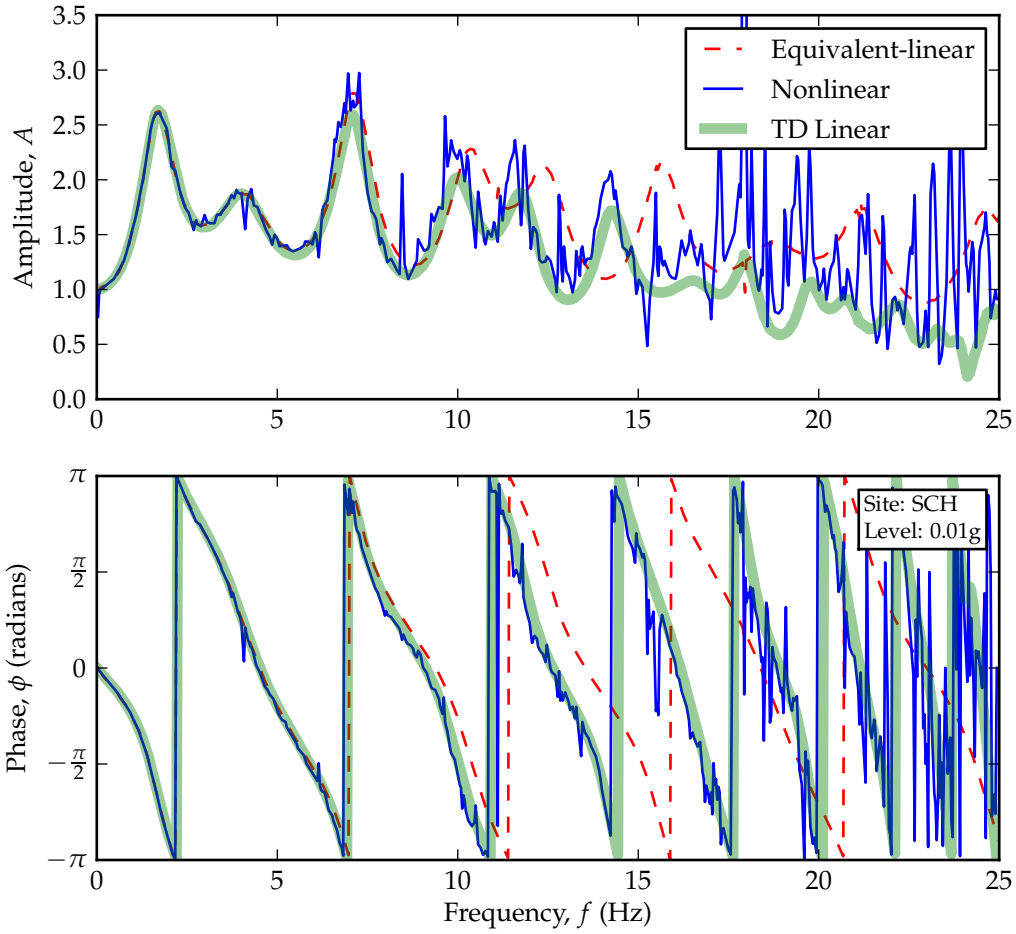

Figure 6.6: Amplitude and phase of the transfer functions computed by the EQL and nonlinear methods for the SCH site (input PGA of 0.01 g).

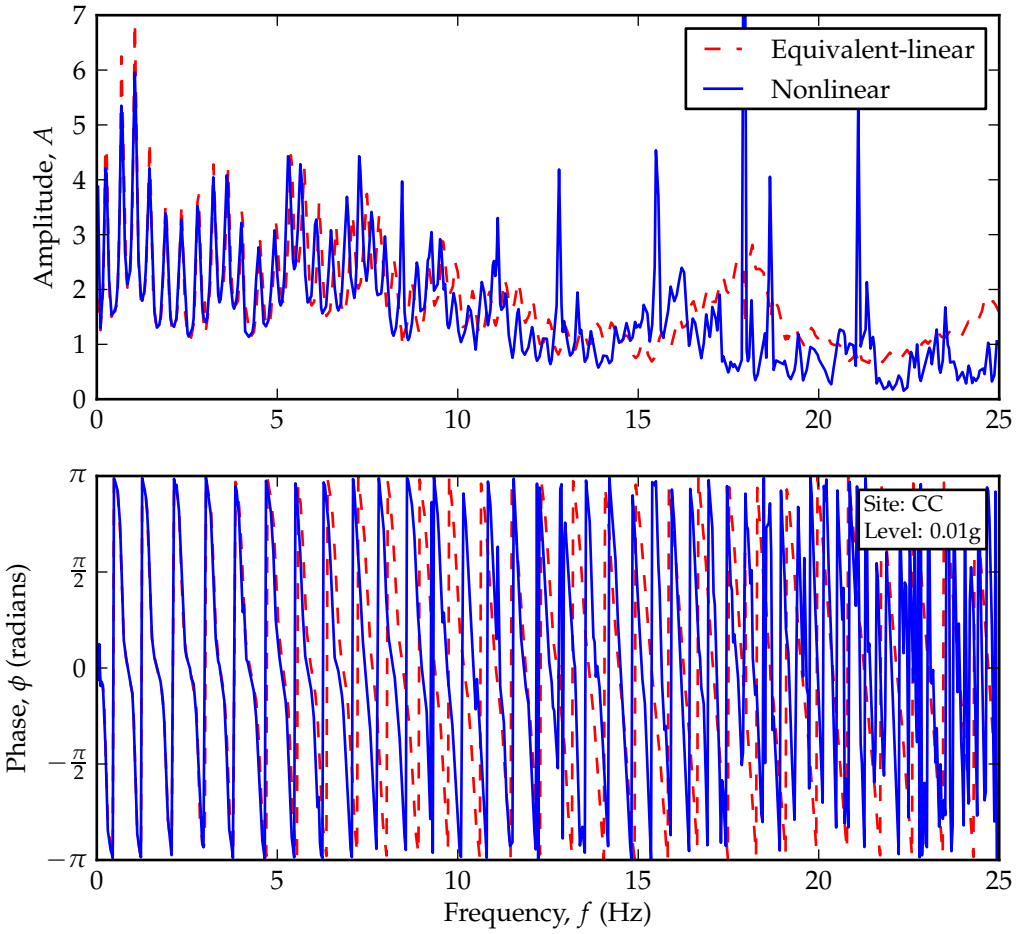

Figure 6.7: Amplitude and phase of the transfer functions computed by the EQL and nonlinear methods for the CC site (input PGA of 0.01 g).

6.4 Analyses for Moderate- to High-Intensity Input Motions

The previous section showed that the time variation of soil properties in nonlinear analysis causes an increase in the high-frequency amplitudes of motion, but at the same time causes these high-frequency motions to be incoherent in phase. This section further investigates the results from nonlinear analysis, and its comparison with EQL analysis, at higher input intensities of 0.13 g and 0.40 g.

Figure 6.8 shows the spectral ratios and relative differences between nonlinear and EQL analysis for the SCH site and the 0.13 g input intensity. The nonlinear and EQL analyses provide similar results at frequencies below 10 Hz, with the spectral ratios within 6% of one another. However, the nonlinear analysis now predicts larger spectral ratios than EQL analysis at frequencies between 10 and 25 Hz. This result can be explained by the equivalent transfer functions shown in Figure 6.9, which shows that the nonlinear analysis amplifies significantly the motions at frequencies greater than 10 Hz. Despite these large amplitudes at high frequencies, the spectral ratios at frequencies above 25 Hz from nonlinear analysis are still more than 10% smaller than those from EQL analysis (Figure 6.8). This reduction is caused by the phase incoherence that is introduced by the time varying properties, which in this case now extends down to about 10 Hz (Figure 6.9). Finally, the spectral ratios from nonlinear analysis are about 5% smaller than those from EQL analysis for frequencies from about 1 to 5 Hz (Figure 6.8). This difference most likely results from EQL analysis using constant strain-compatible softened properties throughout the time series, while the softened properties in nonlinear analysis vary within the time series based on the induced strains at any one time.

To further illustrate the influence of phase incoherence on the computed site response, a hybrid transfer function is created by combining the transfer function amplitude

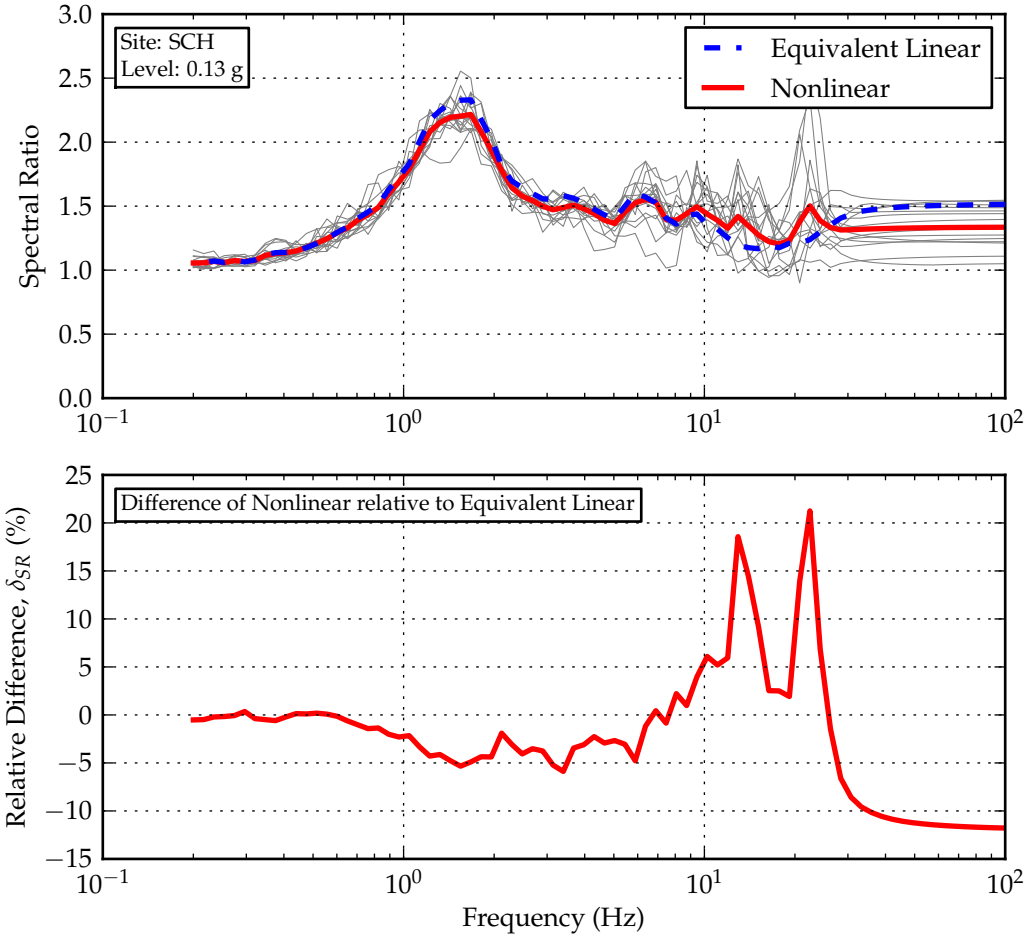

Figure 6.8: The spectral ratio and relative difference for the SCH site computed with nonlinear and EQL methods using the spectrally-matched ground motions (input PGA of 0.13 g).

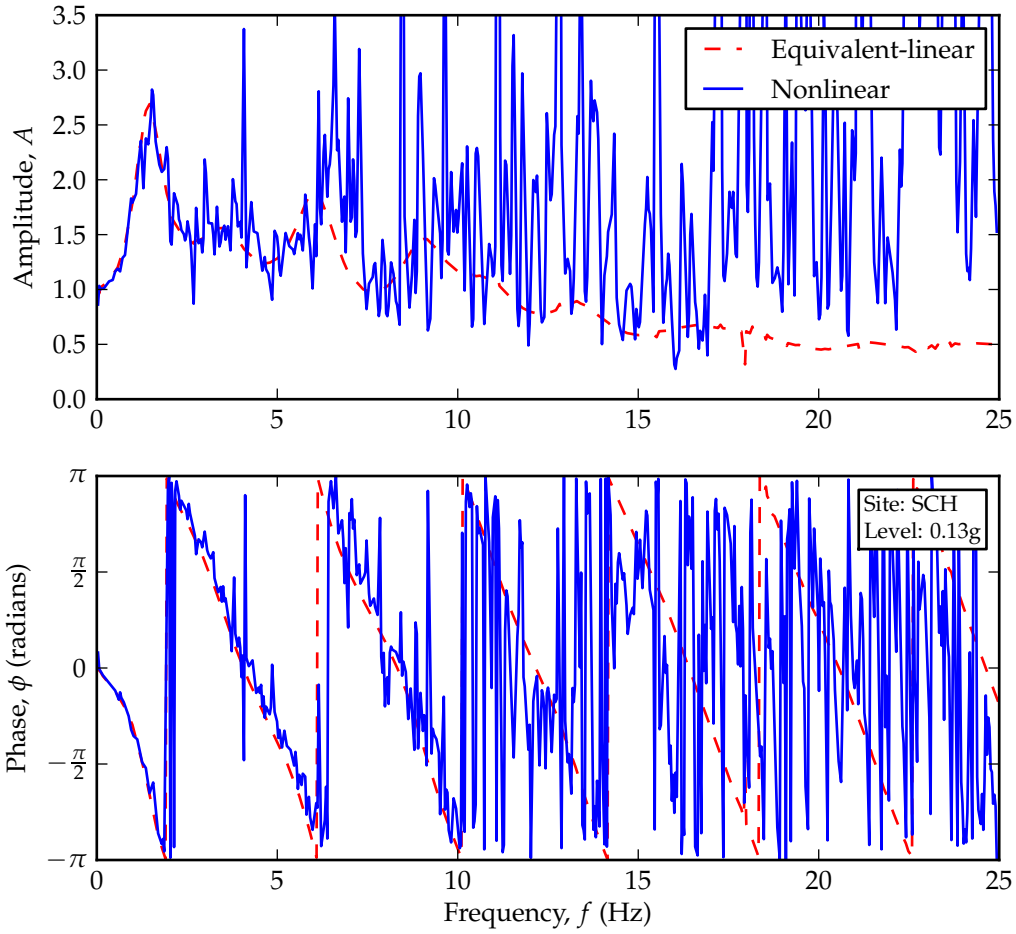

Figure 6.9: Amplitude and phase of the transfer functions computed by the EQL and nonlinear methods for SCH (input PGA of 0.13 g).

inferred from the nonlinear analysis with a smooth phase relationship derived from the EQL analysis. A new surface motion and associated response spectrum is computed by applying this hybrid transfer function to the original input motion. Figure 6.10 shows the surface response spectra predicted for the SCH site and the `KOZANI-KOZ-L` input motion using nonlinear analysis and using the hybrid transfer function. Smoothing the phase incoherence via the hybrid transfer function increases the spectral acceleration at frequencies below 25 Hz by more than 10%, but it does not affect the lower frequencies. Thus, it is the phase incoherence that causes the nonlinear analysis to predict smaller spectral accelerations at very high frequencies.

The site response predictions for the SCH site and an input motion intensity of 0.40 g are shown in Figure 6.11. The trends previously observed at high frequencies are magnified. The nonlinear analysis predicts spectral ratios almost 20% smaller than EQL analyses at frequencies above 25 Hz, and predicts spectral ratios 30 to 60% larger than EQL analysis at frequencies between 5 and 25 Hz. Close to the site frequency (1.1 Hz), the nonlinear analysis predicts a spectral ratio about 15% smaller than EQL analysis. This difference is again caused by the continuously varying softened properties in nonlinear analysis, but may also be influenced by the divergence in the MKZ damping curves and the damping curves used in the EQL analysis at large strains (Figure 3.3). This difference could be reduced by fitting the MKZ model parameters over the strain level experienced by the site for this input intensity. Interestingly, the maximum shear strains induced by nonlinear and EQL analyses are similar for all the input intensities investigated (Figure 6.12).

The nonlinear and EQL site response predictions for the CC site for input intensities of 0.13 g and 0.40 g are shown in Figure 6.13. At an input intensity of 0.13 g, the nonlinear analysis predicts spectral ratios about 5 to 10% smaller than EQL analysis at frequencies above 20 Hz. At frequencies between 5 and 20 Hz, the nonlinear analysis predicts spectral ratios between 10 and 20% larger than the EQL analysis. Outside

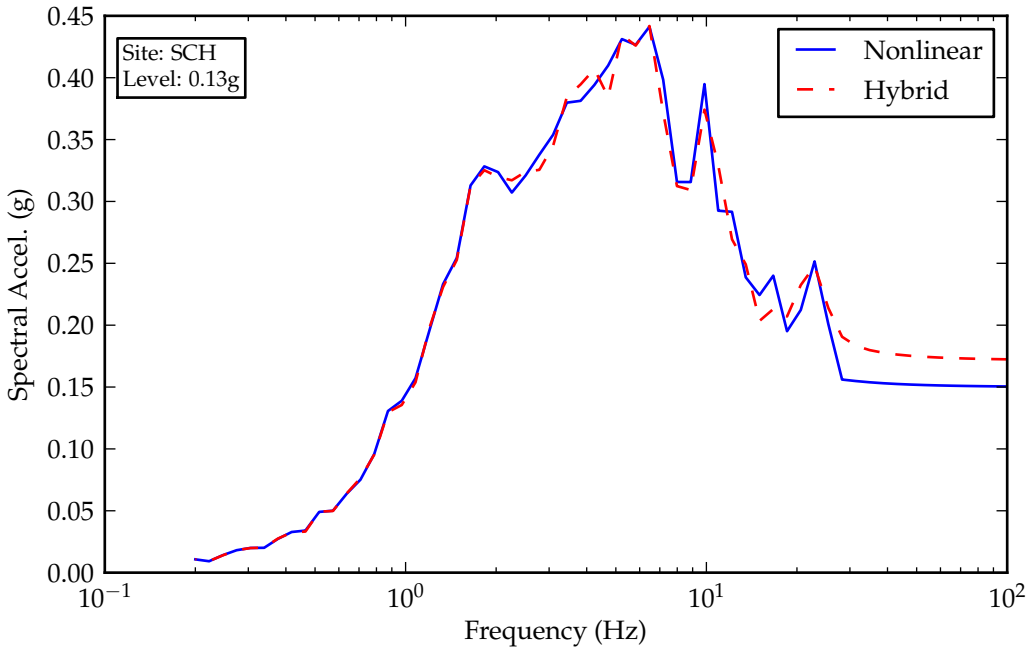

Figure 6.10: The effect of smooth phase on the surface response spectrum for the SCH site.

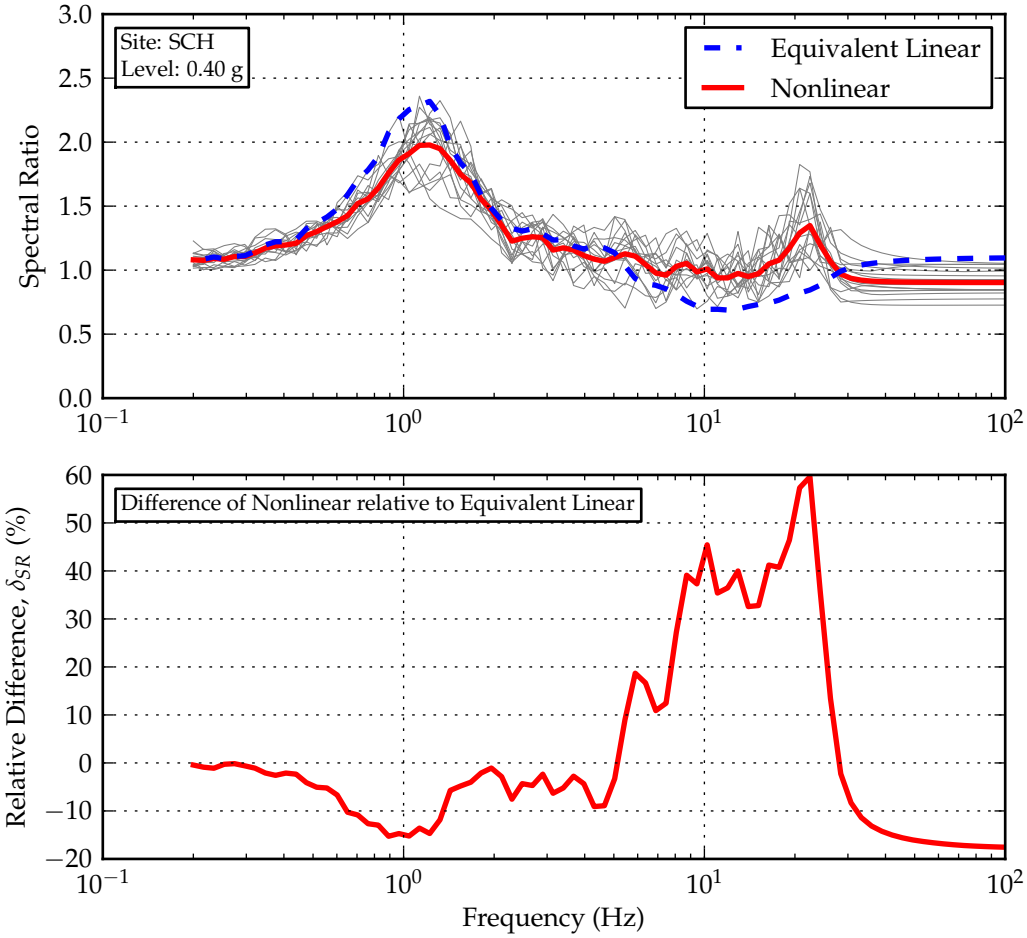

Figure 6.11: The spectral ratio and relative difference for the SCH site computed with nonlinear and EQL methods using the spectrally-matched ground motions (input PGA of 0.40 g).

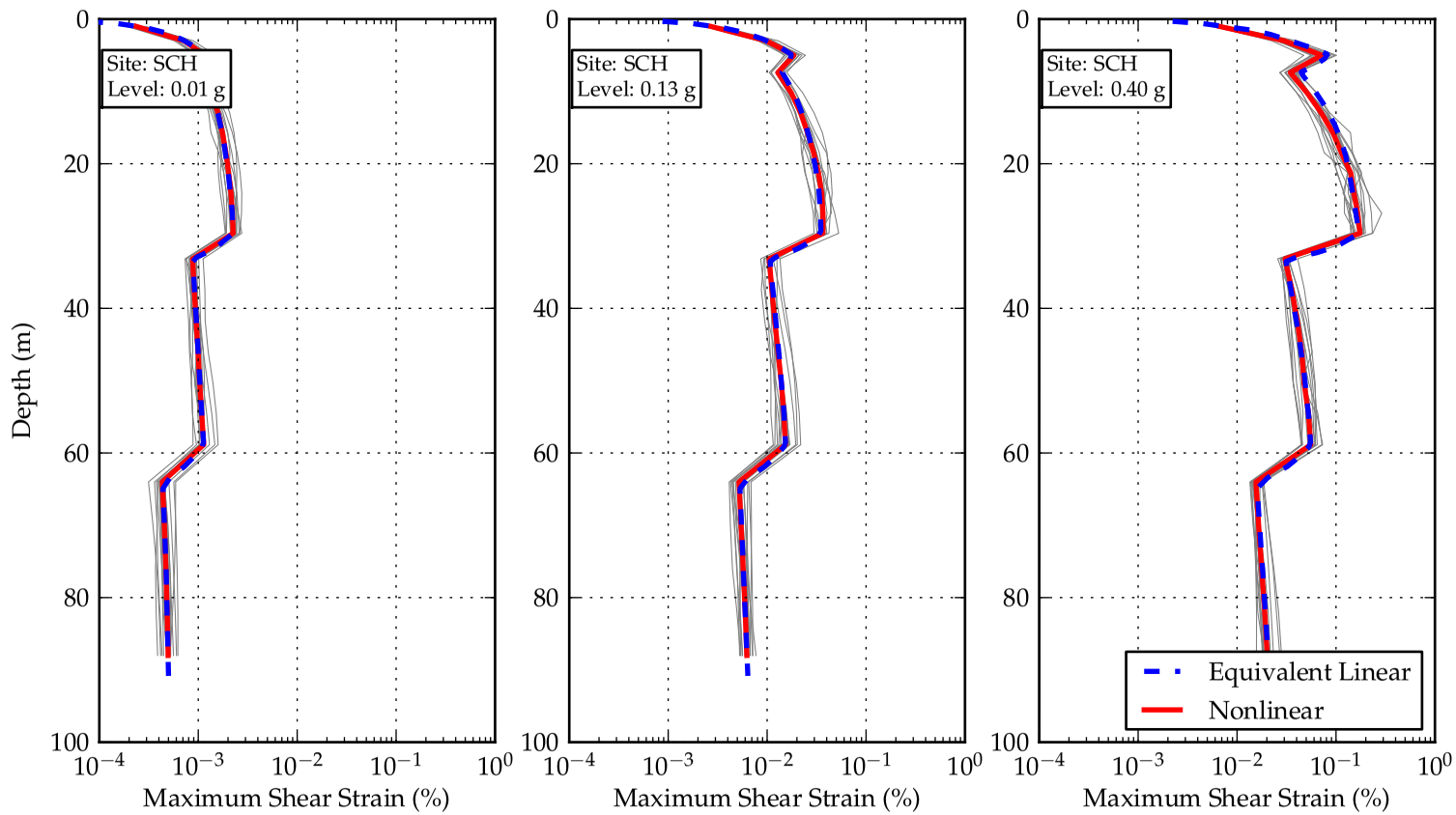

Figure 6.12: The maximum strain profile for the SCH site computed with the nonlinear and EQL methods.

of this frequency range, the nonlinear analysis predicts spectral ratios within 10% of the EQL analysis. As the intensity level increases, the nonlinear analysis predicts even larger spectral ratios between 5 and 20 Hz with relative differences exceeding 60%. The difference in this frequency range is influenced also by over-damping in the EQL at large strain levels. The relative difference for the spectral ratios outside of this frequency range are similar to those for an input intensity of 0.13 g.

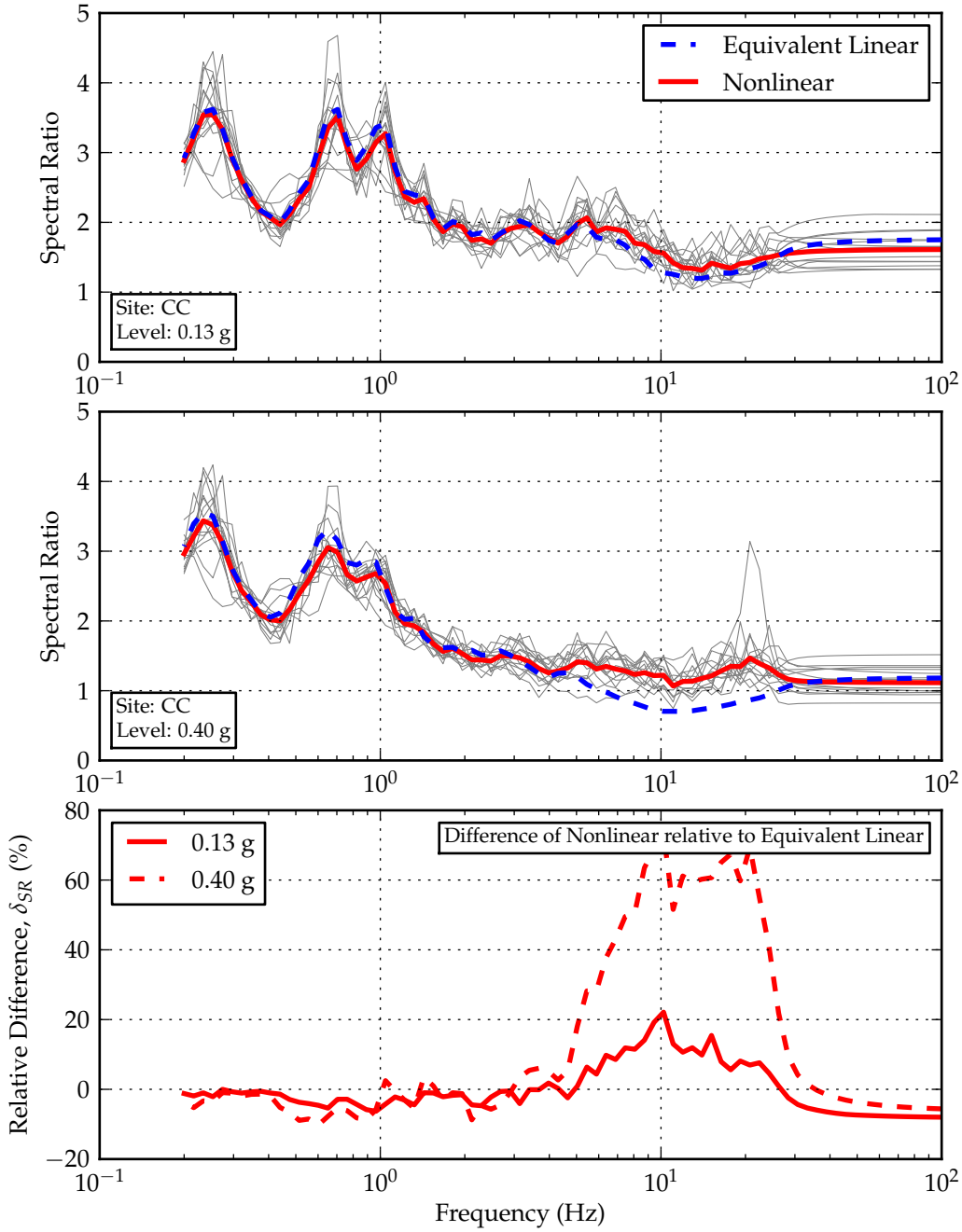

Figure 6.13: The spectral ratio and relative difference for the CC site computed with nonlinear and EQL methods using the spectrally-matched ground motions.

6.5 Summary

The comparisons between nonlinear and EQL analysis for different input intensities and the two site considered are summarized in Figure 6.14. At frequencies above 25 Hz, the nonlinear method consistently predicts smaller spectral ratios and spectral acceleration than EQL analysis due to the phase incoherence introduced at high frequencies. This effect generally increases with input intensity, and may be as larger as 15 to 20%. At frequencies between about 5 and 20 Hz, the nonlinear method predicts smaller spectral ratios than EQL analyses at very low-input intensities due to numerical errors associated with the time stepping method used to solve the dynamic equations of motions. At larger input intensities (greater than about 0.1 g), the nonlinear method predicts larger spectral ratios than EQL analysis in this frequency range (5 and 25 Hz). This difference is caused by two things: high-frequency amplification in nonlinear analysis caused by instantaneous changes in stiffness upon load reversal, and over-damping of high frequencies in EQL analysis at larger strains. At frequencies above 5 Hz, nonlinear analysis generally predicts smaller spectral ratios than EQL analysis and this difference may be as large as 10 to 15% at the site frequency at larger intensities. This difference is caused by the continuously-varying softened properties used in nonlinear analysis.

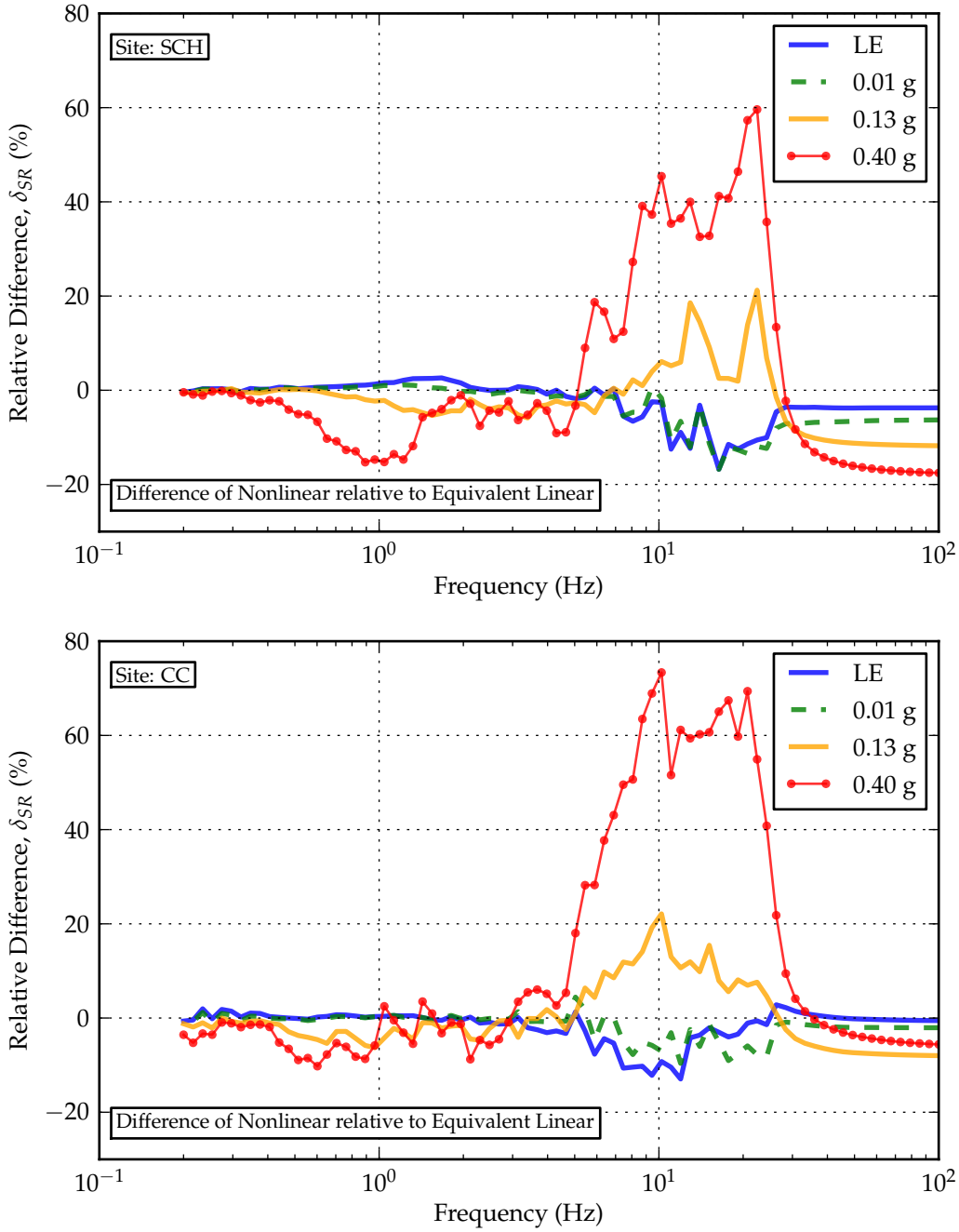

Figure 6.14: The relative difference of the spectral ratio of the SCH and CC sites computed with nonlinear and EQL methods using the spectrally-matched ground motions.

Chapter 7

Conclusion

7.1 Summary

In this report, suites of input ground motions were used to compare relative differences between various site response techniques. Specifically, results from equivalent-linear (EQL) site response analysis using time-series and random-vibration-theory (RVT) approaches were compared, as well as results from equivalent-linear and nonlinear site response approaches.

When compared to the time series approach, the RVT approach may over-predict the spectral ratio at the site frequency by as much as 30%, as well as over predict the maximum strains. The over amplification computed by the RVT approach is a result of the smooth shape of the input Fourier amplitude spectrum used in the RVT analysis. This smooth shape has a greater sensitivity to the site transfer function. The level of over-amplification and associated RVT difference is dependent on the site characteristics, with the difference of the RVT approach increasing with increasing bedrock impedance contrast, and increasing site frequency. The over-prediction of strains is also caused by the smooth input FAS used in the RVT approach, and these larger strains lead to over-damping of high frequencies for larger input intensities.

This study also provided some interesting insights regarding the influence of input motion specification on the results from site response analysis. Three different suites of time series were used in the EQL analysis: stochastically-simulated motions, linearly-scaled motions, and spectrally-matched motions. While each of the suites of input motions predicted responses that peaked at the same frequency, the median spectral ratio at the site frequency was largest for the spectrally-matched motions and smallest for the scaled motions. The differences in the median spectral ratio was due to differences in the motion-to-motion variability within each suite of input motions. The suite of scaled ground motions had the greatest variability and produced the smallest median spectral ratio at the site frequency. The spectral ratio at the site frequency is sensitive to the variability in the suite of input motions because each input motion induces a different level of strain and a different site frequency. The averaging of the individual input motions pulls down the median spectral ratio. The reduced variability in the suite of spectrally matched ground motions produced the most similar results to the RVT approach.

The comparisons between the EQL and nonlinear methods yielded several important findings. For deep sites, it is recommended that the frequency-independent Rayleigh damping formulation proposed by Phillips and Hashash (2009) be used. However, even with this frequency-independent damping, the nonlinear method predicts smaller spectral ratios at high frequencies (above 5 Hz) under small intensities (less than about 0.1 g) due to numerical errors associated with the time stepping algorithm. At larger input intensities, the nonlinear method predicts less amplification than the EQL method at very high frequencies (above 25 Hz), more amplification than the EQL method at high frequencies (5 to 25 Hz for the SCH site), and less amplification than the EQL method at the site frequency. The nonlinear method predicts less amplification at very short frequencies due to the incoherence in the phase introduced by the nonlinear stress-strain response. The greater amplification predicted by the nonlinear method at high

frequencies is a result of high-frequency amplification generated by the instantaneous change in stiffness upon stress reversal in the nonlinear analysis, as well as over-damping of high frequencies in the EQL analysis. The smaller amplification predicted by the nonlinear method close to the site frequency is caused by the continuously changing stiffness modeled in nonlinear analysis.

7.2 Recommendations for Future Work

The comparisons performed in this study were limited to hypothetical events, which only allow for relative comparisons to be made between the different methods of analysis. Future research work should employ data from borehole arrays that provide both the recorded input and surface ground motions. This information would allow for an assessment of the true performance of the site response methods, instead of only providing relative comparisons.

The results of this study indicate that there is a significant difference in the site response predicted RVT approach due to the smooth FAS used as the input motion in RVT analysis. Further work needs to be done to establish a method to correct for this difference in a manner that could be implemented into future site response analyses.

Bibliography

N. Abrahamson and W. Silva. Empirical response spectral attenuation relations for shallow crustal earthquakes. *Seismological Research Letters*, 68:94–127, 1997.

N. A. Abrahamson. Non-stationary spectral matching. *Seismological Review Letters*, 63 (1):30, 1992.

N. A. Abrahamson and W. J. Silva. Empirical ground motion models. Technical report, Brookhaven National Laboratory, Lipton, New York, 1996.

D. M. Boore. Simulation of ground motion using the stochastic method. *Pure and Applied Geophysics*, 160(3-4):635–676, March 2003.

D. M. Boore. SMSIM – fortran programs for simulating ground motions from earthquakes: version 2.3. Open-File Report OFR 96-80-A, U.S. Geological Survey, Menlo Park, California, 2005.

D. M. Boore and G. M. Atkinson. Ground-motion prediction equations for the average horizontal component of PGA, PGV, and 50.01 s and 10.0 s. *Earthquake Spectra*, 24 (1):99–138, Feburary 2008.

D. M. Boore and W. B. Joyner. A note on the use of random vibration theory to predict peak amplitudes of transient signals. *Bulletin of the Seismological Society of America*, 74(5):2035–2039, October 1984.

D. Cartwright and M. Longuet-Higgins. The statistical distribution of the maxima of a random function. *Proceedings of the Royal Society of London. Series A, Mathematical and Physical Sciences*, 237(1209):212–232, 1956.

S. W.-Y. Chang. *Seismic response of deep stiff soil deposits.* PhD thesis, University of California, Berkeley, December 1996.

A. K. Chopra. *Dynamics of Structures: Theory and Applications to Earthquake Engineering.* Prentice Hall, Upper Saddle River, New Jersey, third edition edition, 2007.

M. B. Darendeli. *Development of a new family of normalized modulus reduction and material damping curves.* PhD thesis, The University of Texas, Austin, 2001.

D. A. Gasparini and E. H. Vanmarcke. Simulated earthquake motions compatible with prescribed response spectra. Technical Report R76-4, Massachusetts Institute of Technology, Department of Civil Engineering, Cambridge, Massachusetts, 1976.

J. Gibbs, J. Tinsley, D. Boore, and W. Joyner. Seismic velocities and geological conditions at twelve sites subjected to strong ground motion in the 1994 Northridge, California, earthquake: a revision of OFR 96-740. U.S. Geological Survey Open-File Report 99-446, U.S. Department of the Interior, U.S. Geological Survey, 1999.

J. Hancock. An improved method of matching response spectra of recorded earthquake ground motion using wavelets. *Journal of Earthquake Engineering*, 10(1):67–89, 2006.

Y. M. Hashash. Viscous damping formulation and high frequency motion propagation in nonlinear site response analysis. *Soil Dynamics and Earthquake Engineering*, 22 (7):611–624, September 2002.

Y. M. A. Hashash and D. Park. Nonlinear one-dimensional seismic ground motion

propagation in the mississippi embayment. *Engineering Geology*, 62(1-3):185 – 206, 2001.

I. M. Idriss and J. I. Sun. User's manual for shake91: a computer program for conducting equivalent linear seismic response analyses of horizontally layered soil deposits. Technical report, Center for Geotechnical Modeling, University of California, Davis, 1993.

A. R. Kottke and E. M. Rathje. A semi-automated procedure for selection and scaling of recorded earthquake motions for dynamic analysis. *Earthquake Spectra*, 24(4): 911–932, November 2008a.

A. R. Kottke and E. M. Rathje. Technical manual for Strata. Report 2008/10, Pacific Earthquake Engineering Research (PEER) Center, Berkeley, California, 2008b.

N. Matasović and M. Vucetic. Cyclic characterization of liquefiable sands. *Journal of Geotechnical Engineering*, 119(11):1805–1822, November 1993.

R. K. McGuire, W. J. Silva, and C. J. Costantino. Technical basis for revision of regulatory guidance on design ground motions: Hazard- and risk-consistent ground motion spectra guidelines. Technical Report NUREG/CR-6728, U.S. Nuclear Regulatory Commission, Washington, DC, 2001.

R. K. McGuire, W. J. Silva, and C. J. Costantino. Technical basis for revision of regulatory guidance on design ground motions: Development of hazard- and risk-consistent seismic spectra for two site. Technical Report NUREG/CR-6769, U.S. Nuclear Regulatory Commission, Washington, DC, 2002.

G. Ordónez. User's manual for shake91: a computer program for conducting equivalent linear seismic response analyses of horizontally layered soil deposits. Technical report, GeoMotions, 2002.

C. Phillips and Y. M. Hashash. Damping formulation for nonlinear 1d site response analysis. *Soil Dynamics and Earthquake Engineering*, 29(7):1143–1158, July 2009.

E. M. Rathje and A. R. Kottke. Procedure for random vibration theory based seismic site response analyses. Geotechnical Engineering Report GR08-09, The University of Texas at Austin, Austin, TX, 2008.

J. Rayleigh and R. Lindsay. *The theory of sound*. Dover Publications, New York, 1st american edition, 1945.

C. Real, A. Shakal, and B. Tucker. Overview of the Turkey Flat ground motion prediction experiment. In *Proc. SMIP06 Seminar on Utilization of Strong-Motion Data*, pages 117–136, 2006.

C. R. Real. Turkey flat, USA site effects test area – report 2: Site characterization. TR 88-2, California Division of Mines and Geology, 1988.

P. B. Schnabel, J. Lysmer, and H. B. Seed. SHAKE: A computer program for earthquake response analysis of horizontally layered site. Report UCB/EERC-72/12, Earthquake Engineering Research Center, University of California, Berkeley, California, 1972.

W. Silva, N. Abrahamson, G. Toro, and C. Costantino. Description and validation of the stochastic ground motion model. Report 770573, Brookhaven National Laboratory, Upton, New York, 1996.

J. P. Stewart, A. O.-L. Kwok, Y. M. Hashash, N. Matasovic, R. Pyke, Z. Wang, and Z. Yang. Benchmarking of nonlinear geotechnical ground response analysis procedures. Report 2008/04, Pacific Earthquake Engineering Research (PEER) Center, Berkeley, California, 2008.

UniStar Nuclear Services. Calvert Cliffs nuclear power plant unit 3, combined license application, part 2: Final safety analysis report, rev. 6, 2007.

Regulatory Guide 1.208: A performance-based approach to define the site-specific earthquake ground motion. U.S. Nuclear Regulatory Commission, Washington, DC, 2007.

Appendix A

Input Files

A.1 SMSIM Parameter File

```
!Title
 Sample data file **** NOT FOR A PARTICULAR APPLICATION **
!rho, beta, prtitn, radpat, fs:
    2.8 3.6 0.71 0.55 2.0
!spectral shape: source number, pf_a, pd_a, pf_b, pd_a
! where source number means:
!  1 = 1-corner (S = 1/(1+(f/fc)**pf_a)**pd_a)
!  2 = Joyner (BSSA 74, 1167--1188)
!  3 = Atkinson (BSSA 83, 1778--1798; see also Atkinson & Boore,
   BSSA 85,
!      17--30)
!  4 = Atkinson & Silva (BSSA 87, 97--113)
!  5 = Haddon 1996 (approximate spectra in Fig. 10 of
!          Haddon's paper in BSSA 86, 1300--1313;
!          see also Atkinson & Boore, BSSA 78, 917--934)
!  6 = AB98-California (Atkinson & Boore BSSA 78, 917--934)
!  7 = Boatwright & Choy (this is the functional form used by
!                         Boore & Atkinson, BSSA 79, p. 1761)
!  8 = Joyner (his ENA two-corner model, done for the SSHAC
   elicitation
!      workshop)
!  9 = Atkinson & Silva (BSSA 90, 255--274)
! 10 = Atkinson (2005 model),
! 11 = Generalized two corner model
!      (S = [1/(1+(f/fa)**pf_a)**pd_a]*[1/(1+(f/fb)**pf_b)**pd_b
   ])
```

```
! pf_a, pd_a, pf_b, pd_a are used for source numbers 1 and 11,
   usually
! subject to the constraint pf_a*pd_a + pf_b*pd_b = 2 for an
   omega-squared
! spectrum. The usual single-corner frequency model uses
! pf_a=2.0,pd_a=1.0; the Butterworth filter shape is given by
! pf_a=4.0,pd_a=0.5.  pf_b and pd_b are only used by source 11,
   but dummy
! values must be included for all sources.
     1 2.0 1.0 0.0 0.0
!spectral scaling: stressc, dlsdm, fbdfa, amagc, c1_fa, c2_fa,
   amagc4fa
! (stress=stressc*10.0**(dlsdm*(amag-amagc))
! (fbdfa, amagc for Joyner model, usually 4.0, 7.0)
! c1_fa, c2_fa are the coefficients relating log fa to M in
! source 11, as given by the equation log fa = c1_fa + c2_fa*(M-
   amagc4fa).
! fb for source 11 is given such that the high-frequency spectral
    level
! equals that for a single corner frequency model with a stress
   parameter
! given by stress=stressc*10.0**(dlsdm*(amag-amagc).
! See Tables 2 and 3 in Boore (2003) for various source
   descriptions
! (Note: the parameters in the line below are not used for most
   of the
! sources, for which the spectrum is determined by fixed
   relations between
! corner frequency and seismic moment, but placeholders are still
    needed)
    80.0 0.0 4.0 7.0  0.0 0.0 0.0
!gsprd: r_ref, nsegs, (rlow(i), a_s, b_s, m_s(i)) (Usually set
! r_ref = 1.0 km)
    1.0
    3
      1.0 -1.0 0.0 6.5
     70.0  0.0 0.0 6.5
    130.0 -0.5 0.0 6.5
!q: fr1, Qr1, s1, ft1, ft2, fr2, qr2, s2, c_q
    0.1 275 -2.0 0.2 0.6 1.0 88.0 0.9 3.6
!source duration: weights of 1/fa, 1/fb
    1.0 0.0
!path duration: nknots, (rdur(i), dur(i)), slope of last segment
    4
    0.0 0.0
   10.0 0.0
   70.0 9.6
  130.0 7.8
    0.04
```

```
!site amplification: namps, (famp(i), amp(i))
    5
    0.1   1.0
    1.0   1.5
    2.0   2.0
    5.0   2.5
    10.0  3.0
!site diminution parameters: fm, akappa, dkappadmag, amagkref
    25.0 0.03 0.0 6.0
!low-cut filter parameters: fcut, norder
    0.0 2
!rv params: zup, eps_int (int acc), amp_cutoff (for fup),
   osc_crrctn(1=b&j;2=l&p)
    10.0 0.00001  0.001 1
!window params: idxwnd(0=box,1=exp), tapr(<1), eps_w, eta_w,
   f_tb2te, f_te_xtnd
    1 0.05 0.2 0.05 2.0 1.0
!timing stuff: dur_fctr, dt, tshift, seed, nsims, iran_type (0=
   normal;1=uniform)
    1.3  0.005 20.0 640.0 640 0
```

Appendix B

Scaled Time Series

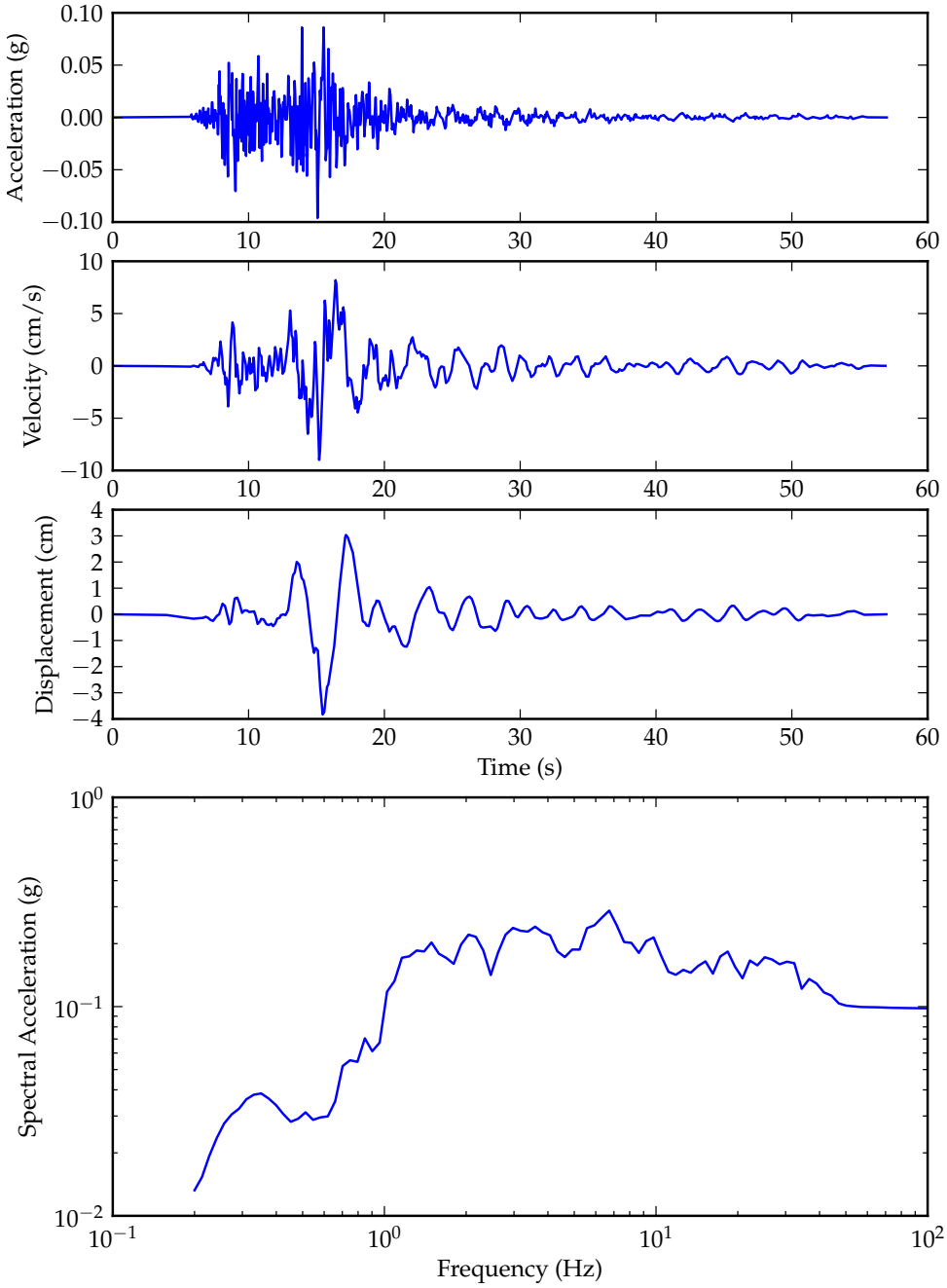

Figure B.1: The `CHICHI06-TCU076-E` time series scaled by 0.79.

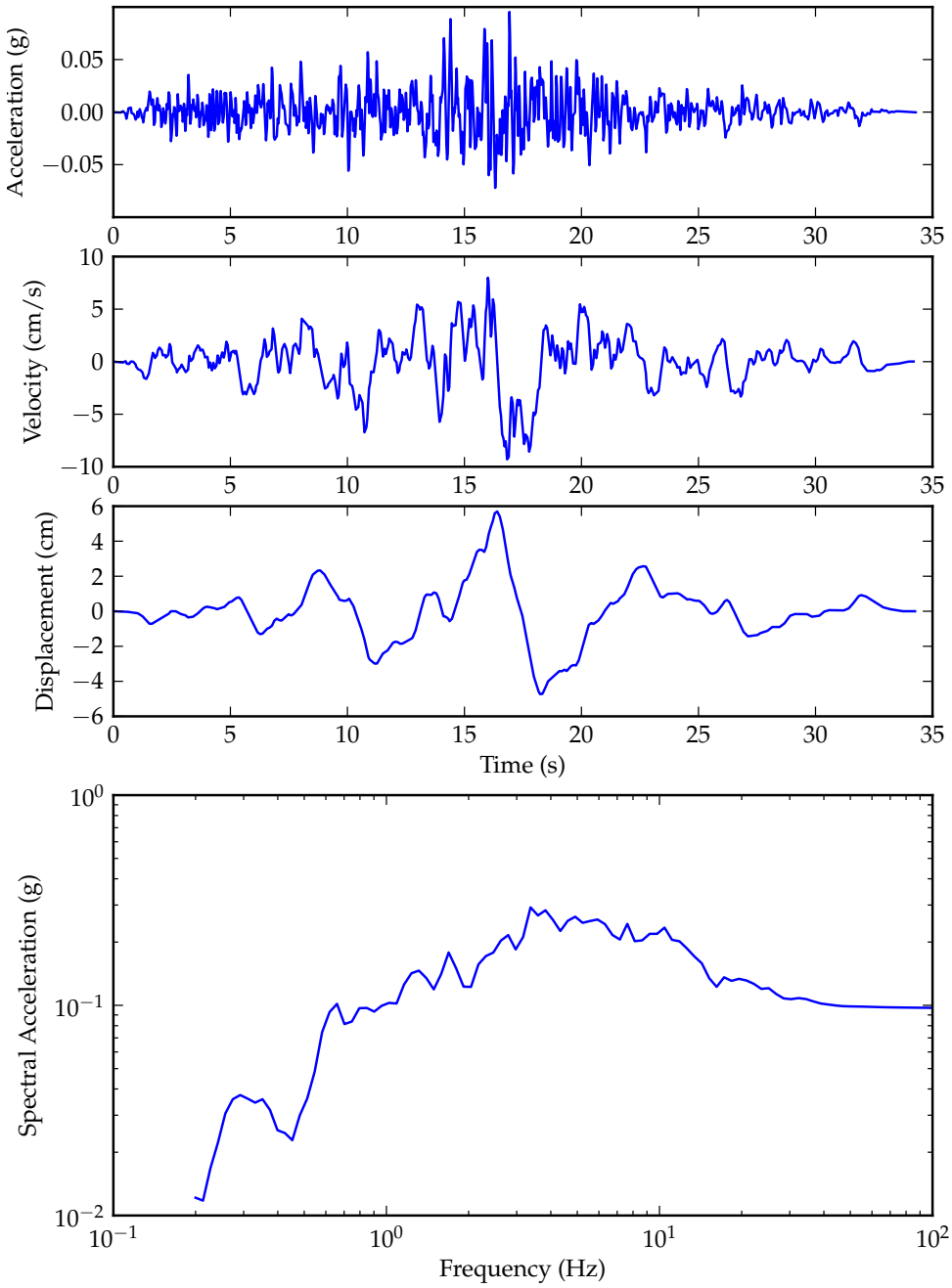

Figure B.2: The `ITALY-A-AUL270` time series scaled by 1.55.

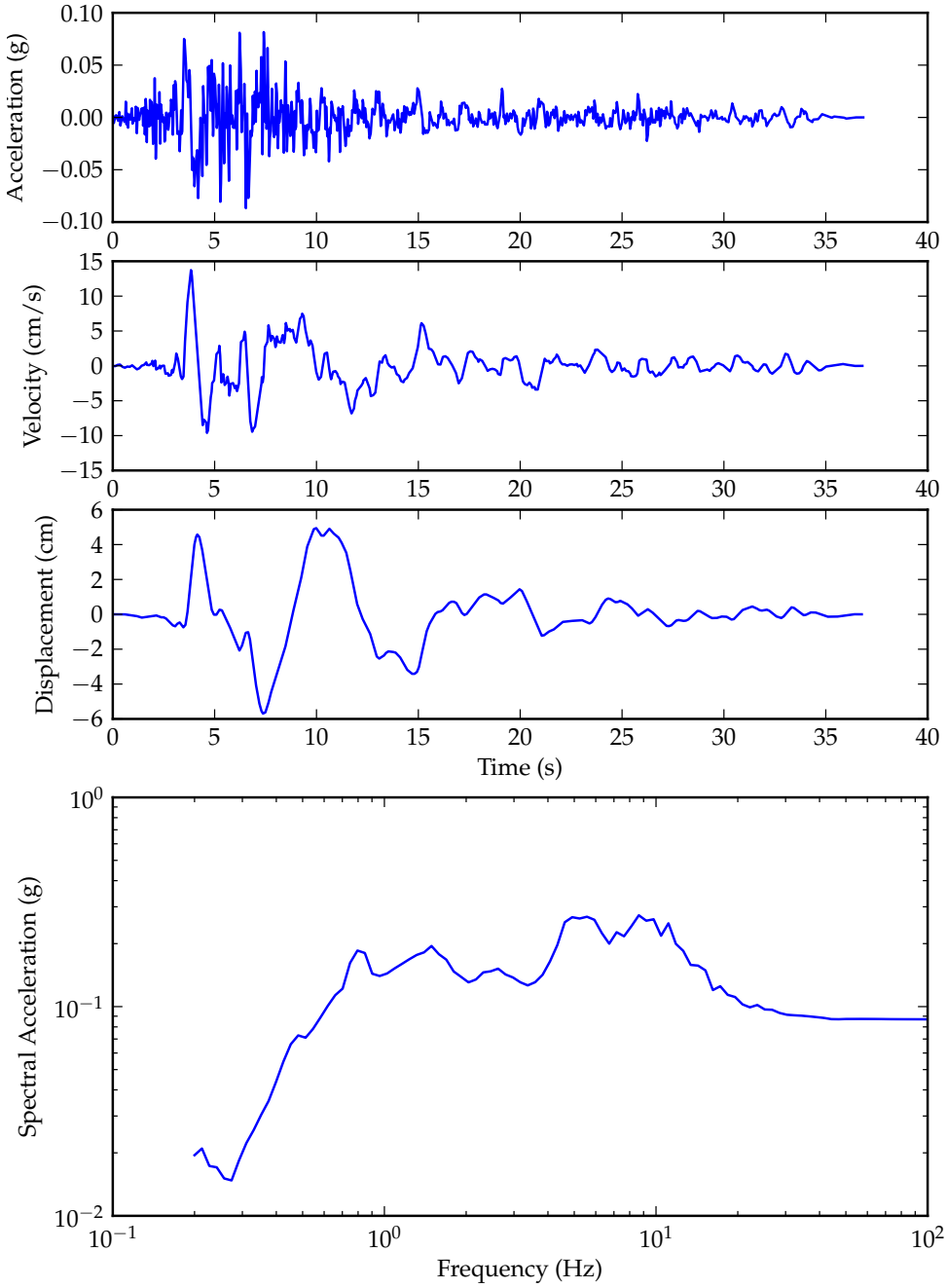

Figure B.3: The `ITALY-A-BAG00` time series scaled by 0.62.

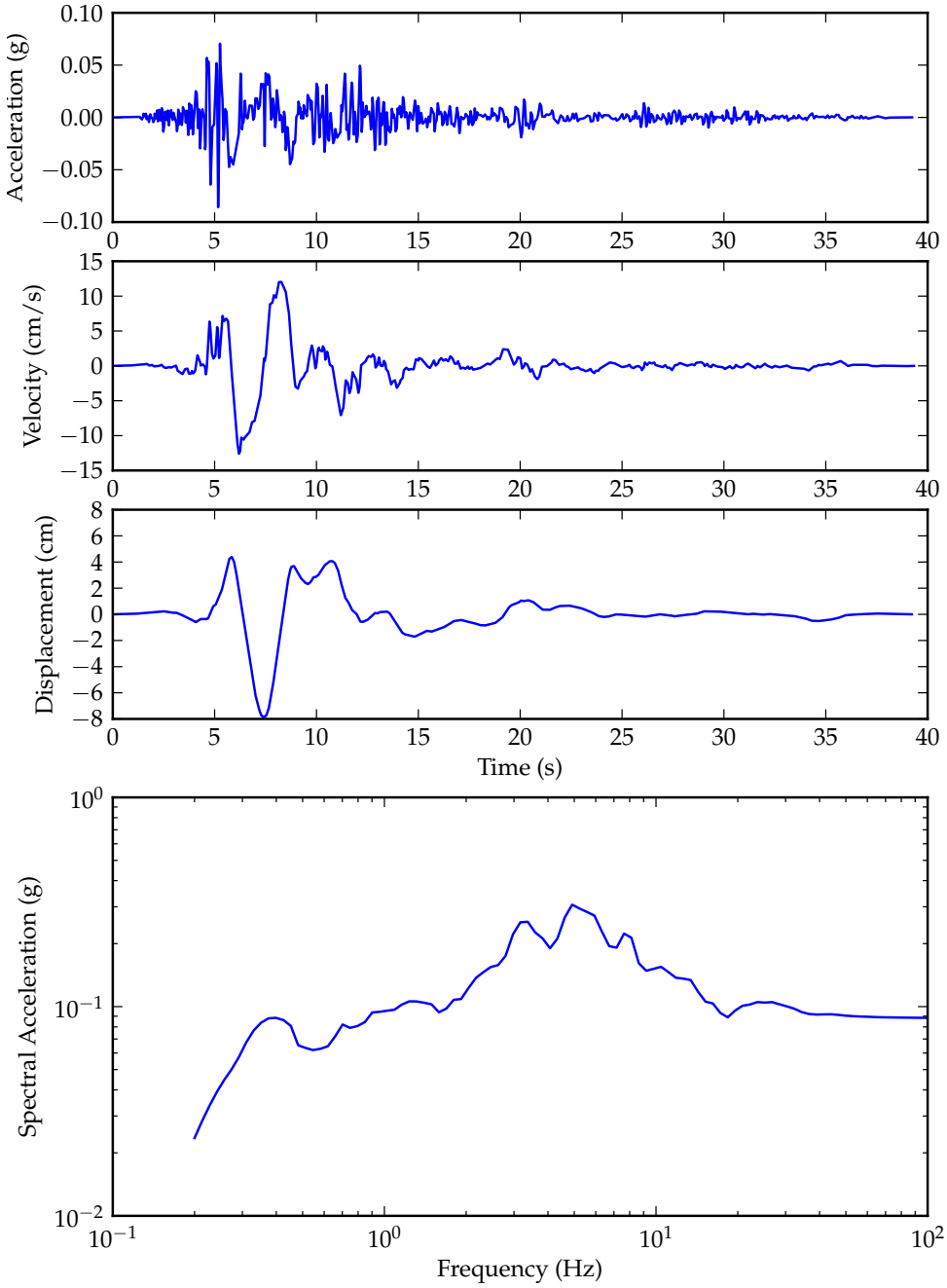

Figure B.4: The `ITALY-A-STU270` time series scaled by 0.25.

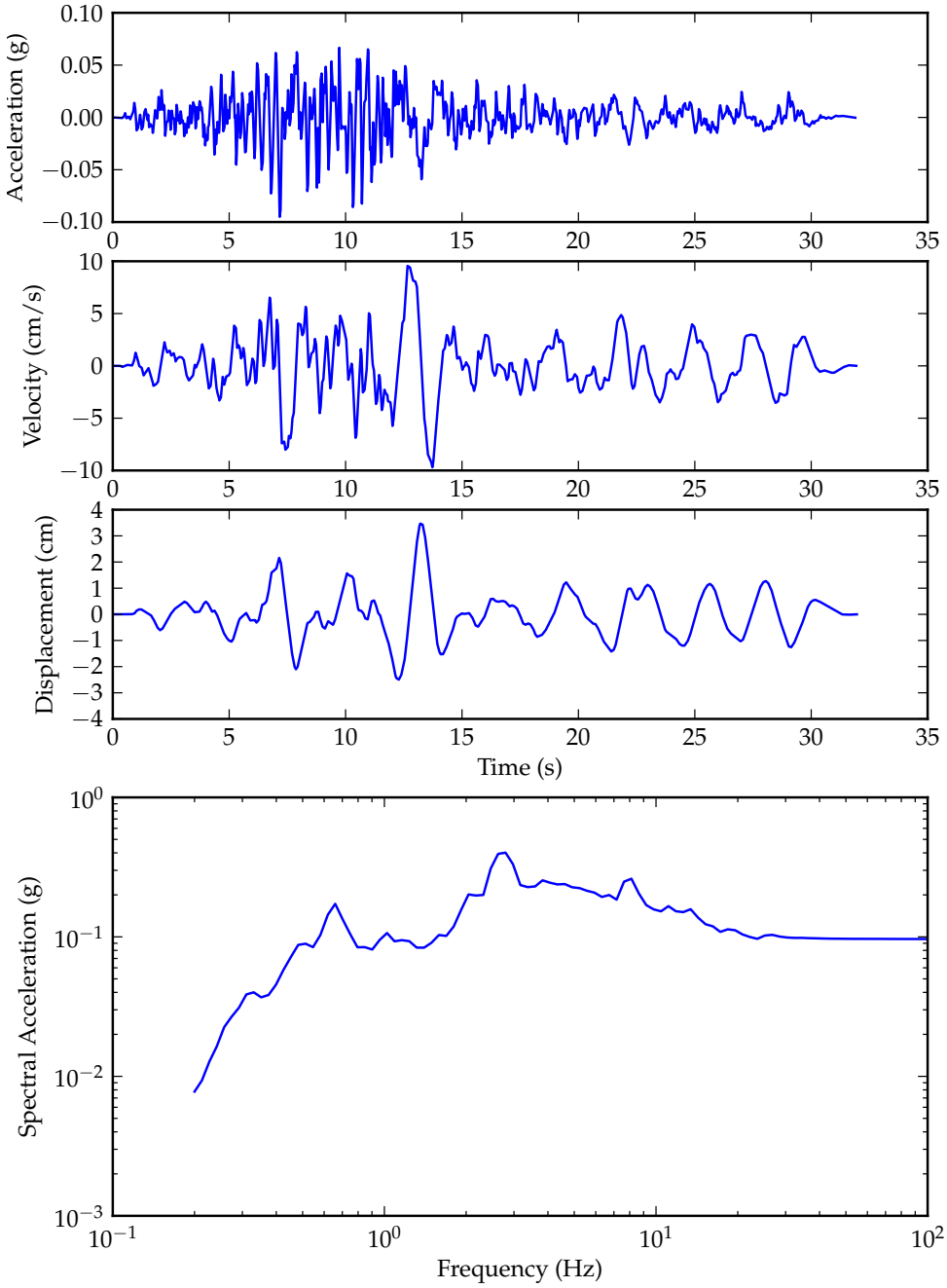

Figure B.5: The `ITALY-B-AUL270` time series scaled by 4.19.

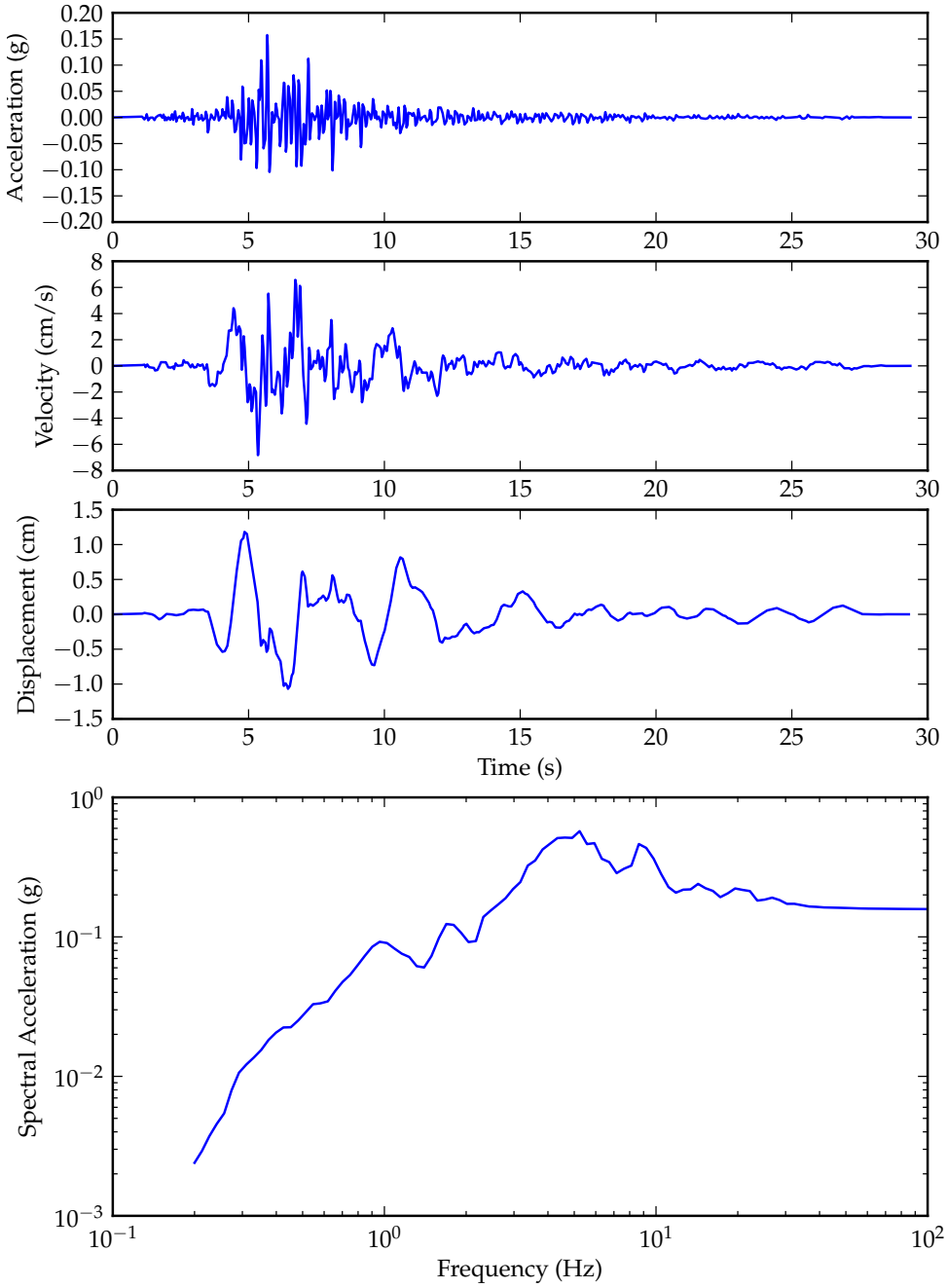

Figure B.6: The `KOZANI-KOZ--L` time series scaled by 0.73.

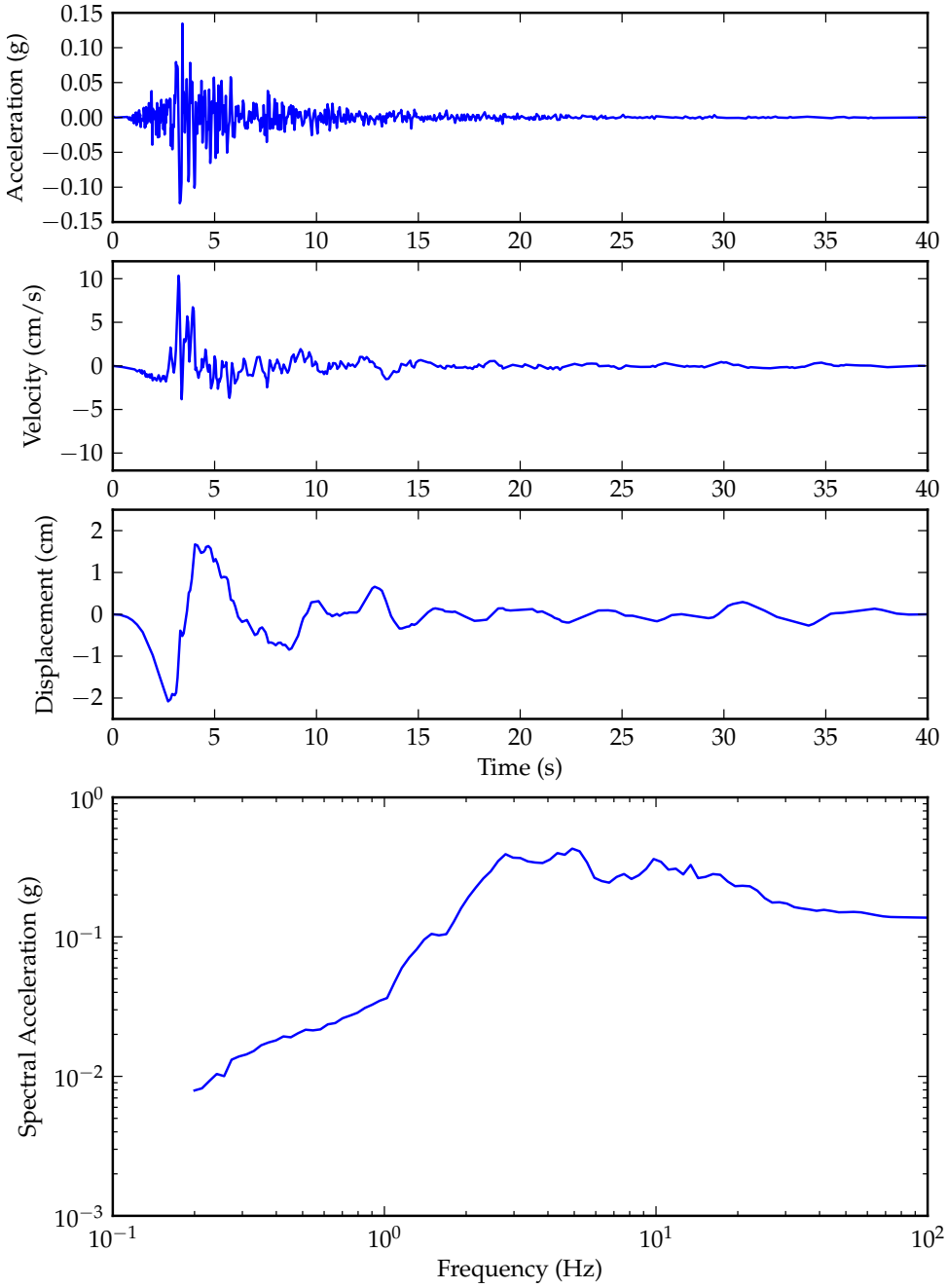

Figure B.7: The `LOMAP-G01000` time series scaled by 0.33.

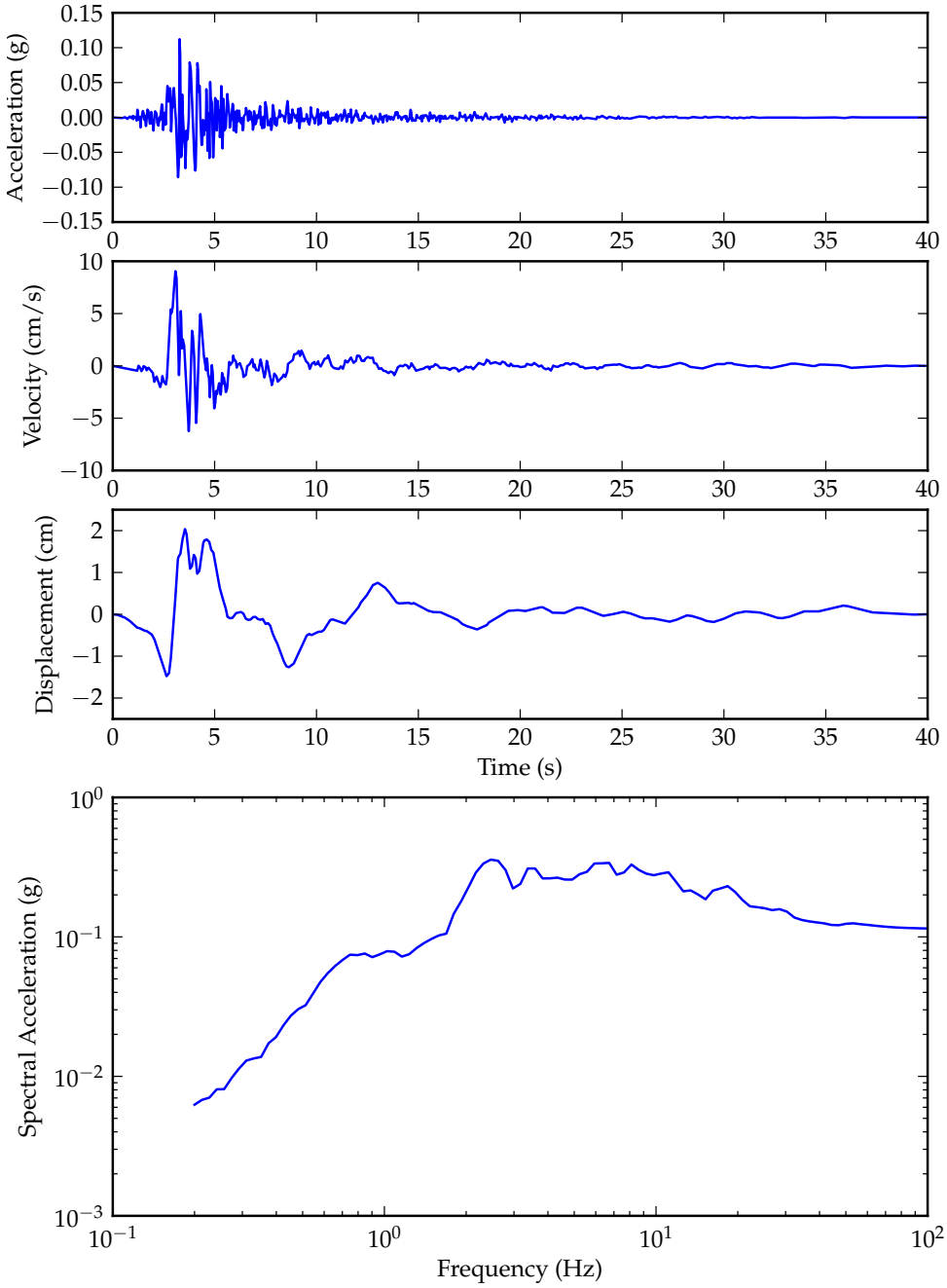

Figure B.8: The `LOMAP-GIL067` time series scaled by 0.32.

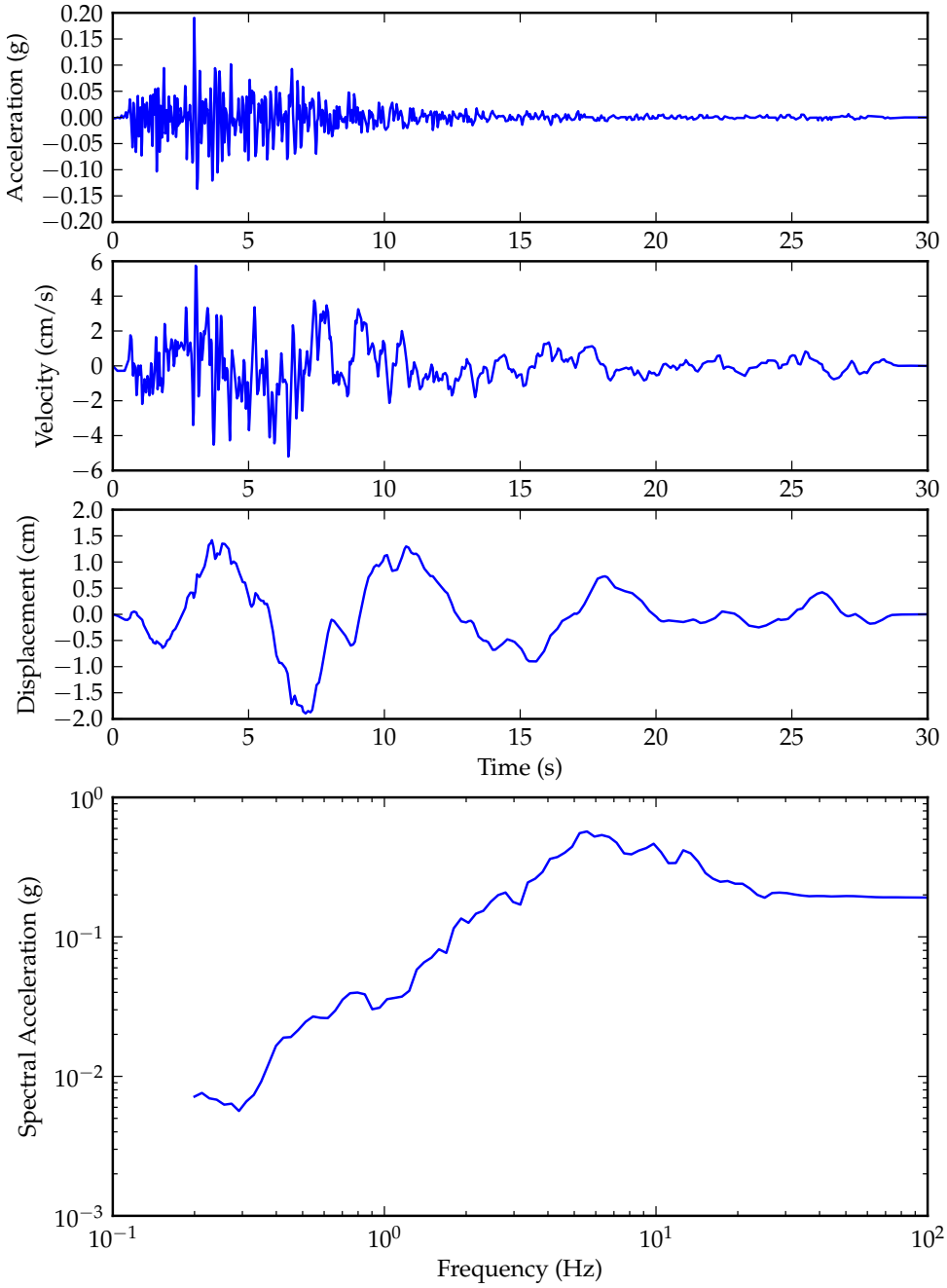

Figure B.9: The `MORGAN-GIL337` time series scaled by 2.01.

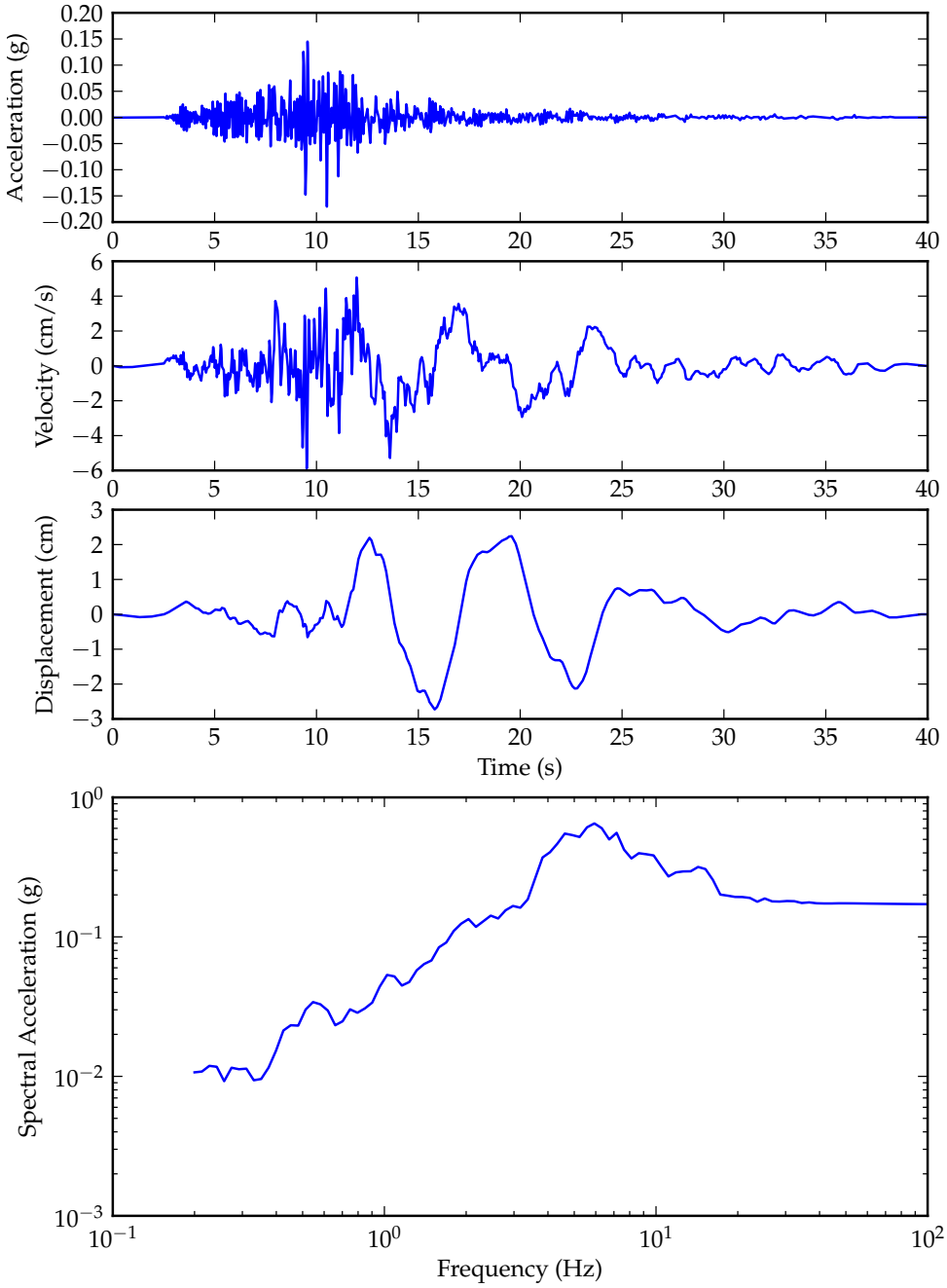

Figure B.10: The `NORTHR-H12180` time series scaled by 0.66.

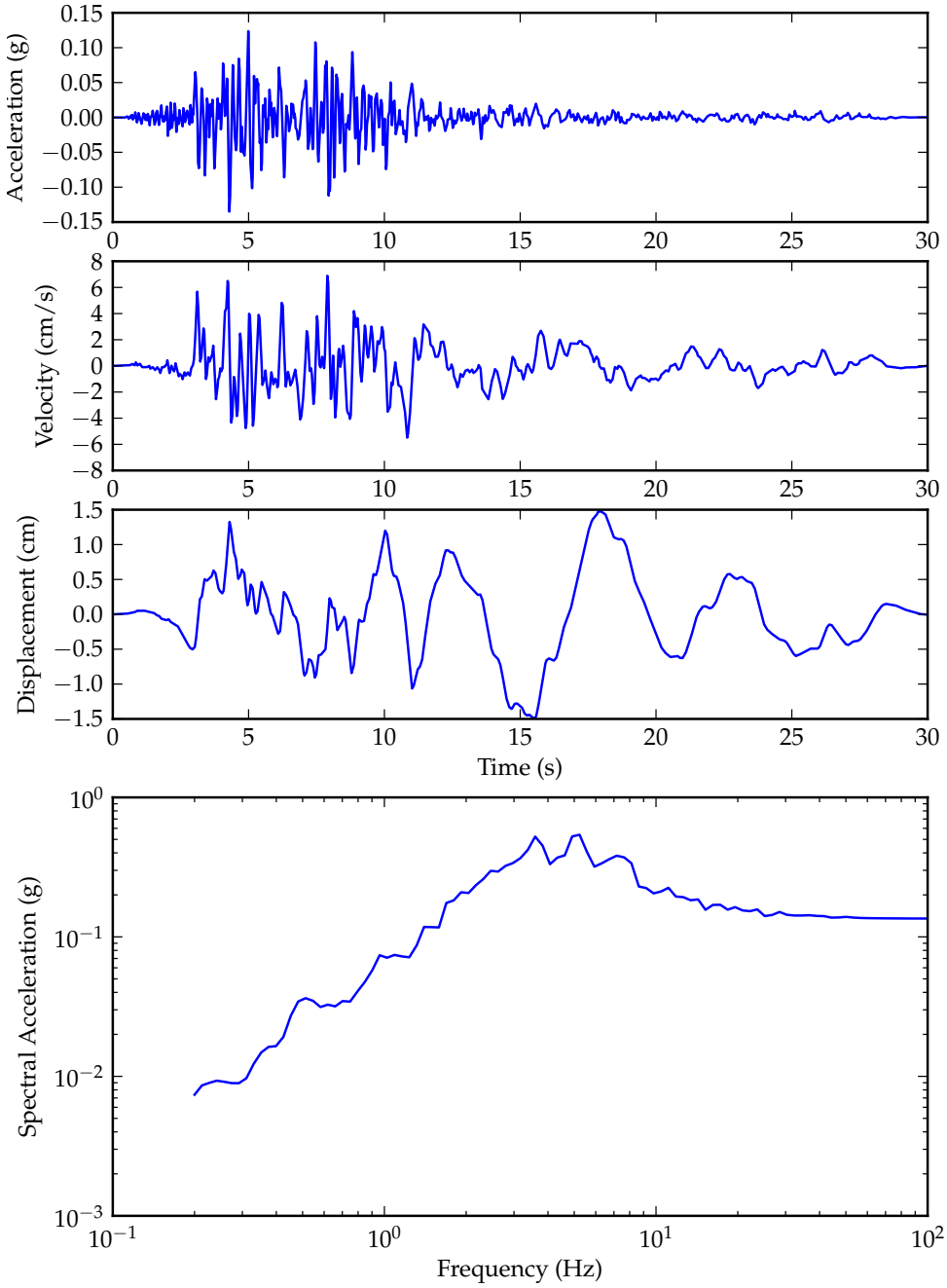

Figure B.11: The NORTHR-HOW330 time series scaled by 0.83.

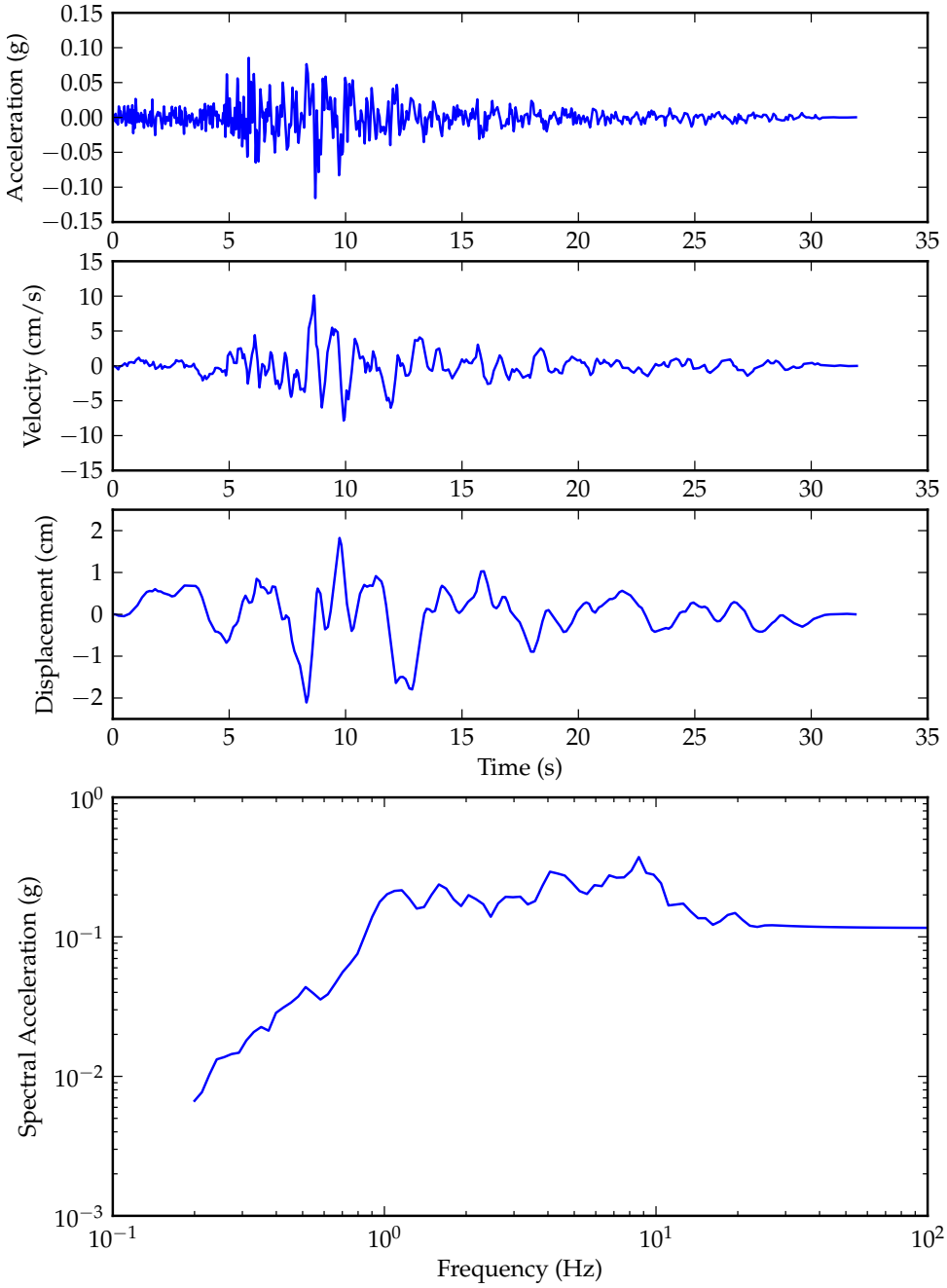

Figure B.12: The `NORTHR-LV1000` time series scaled by 1.30.

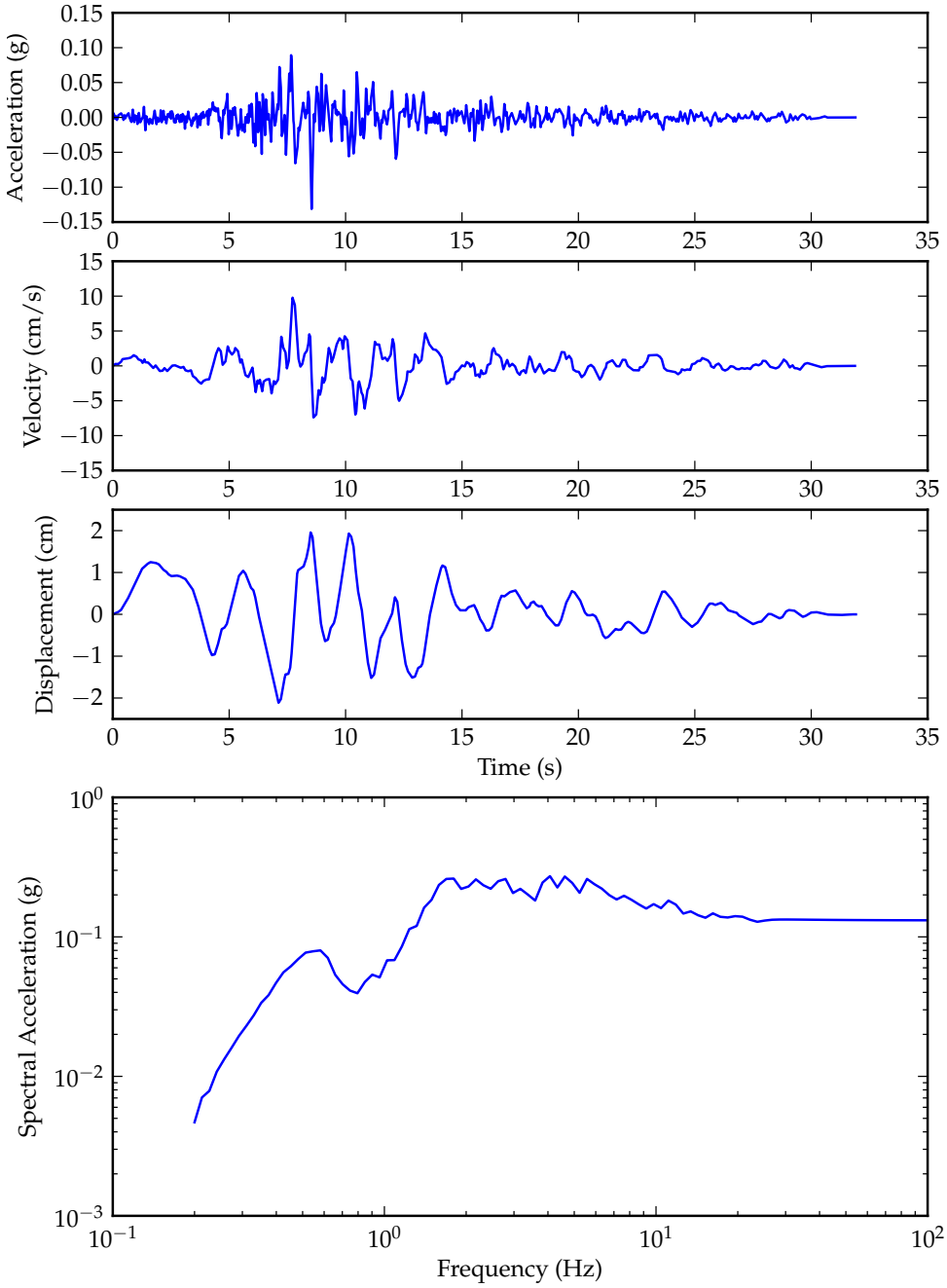

Figure B.13: The `NORTHR-LV3090` time series scaled by 1.24.

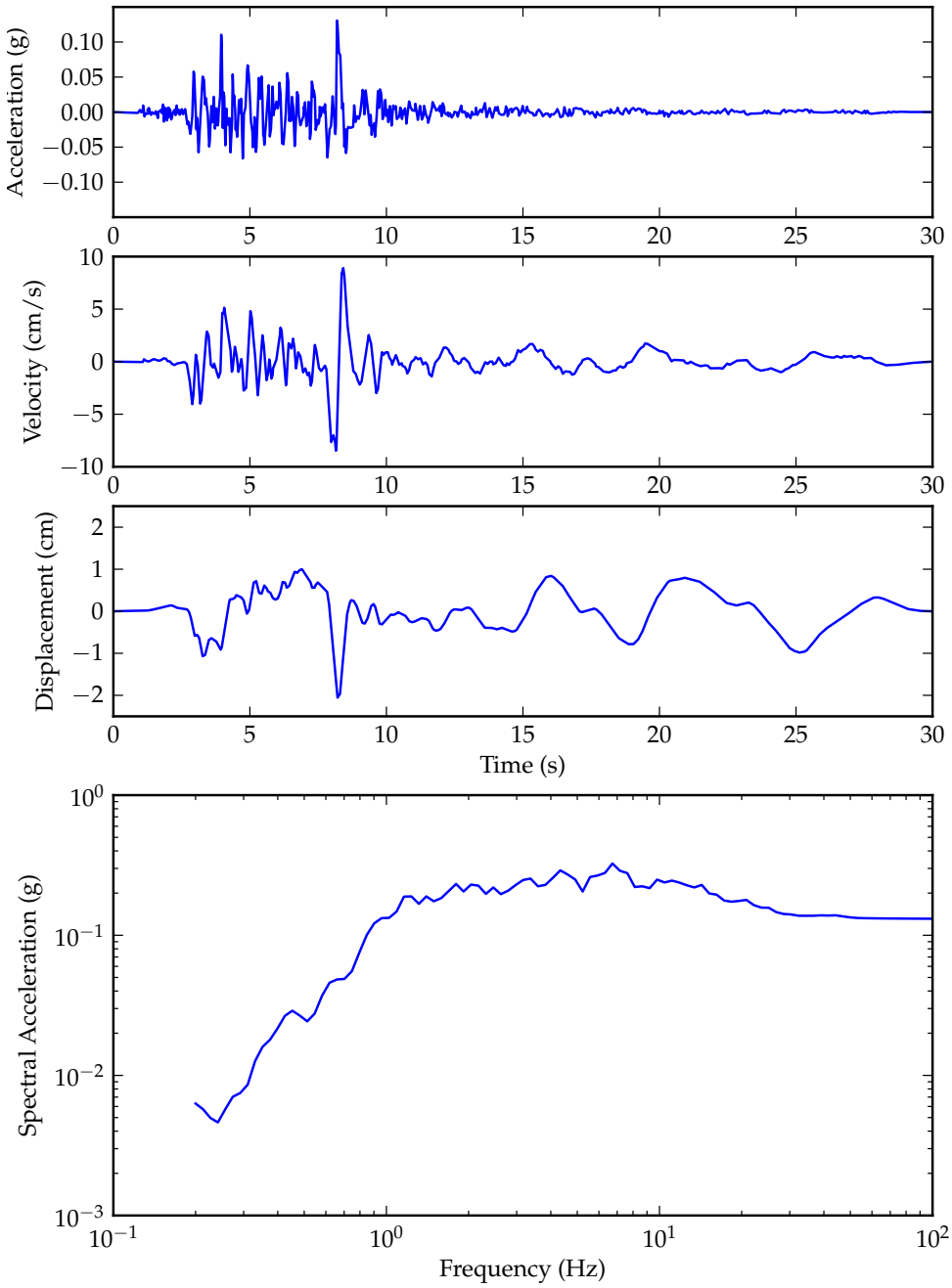

Figure B.14: The `NORTHR-WON185` time series scaled by 0.76.

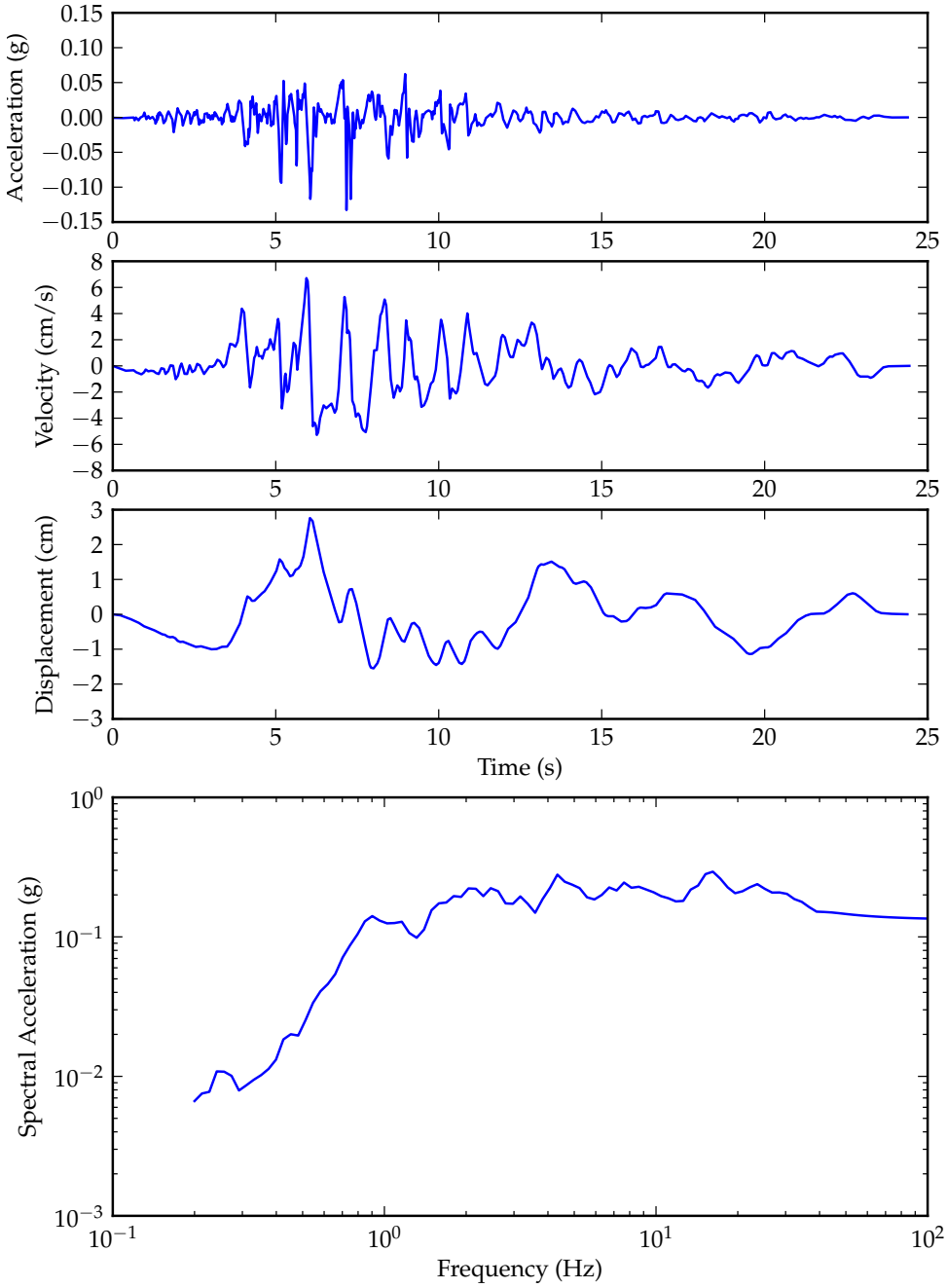

Figure B.15: The `VICT-CPE045` time series scaled by 0.21.

Appendix C

Spectrally-Matched Time Series

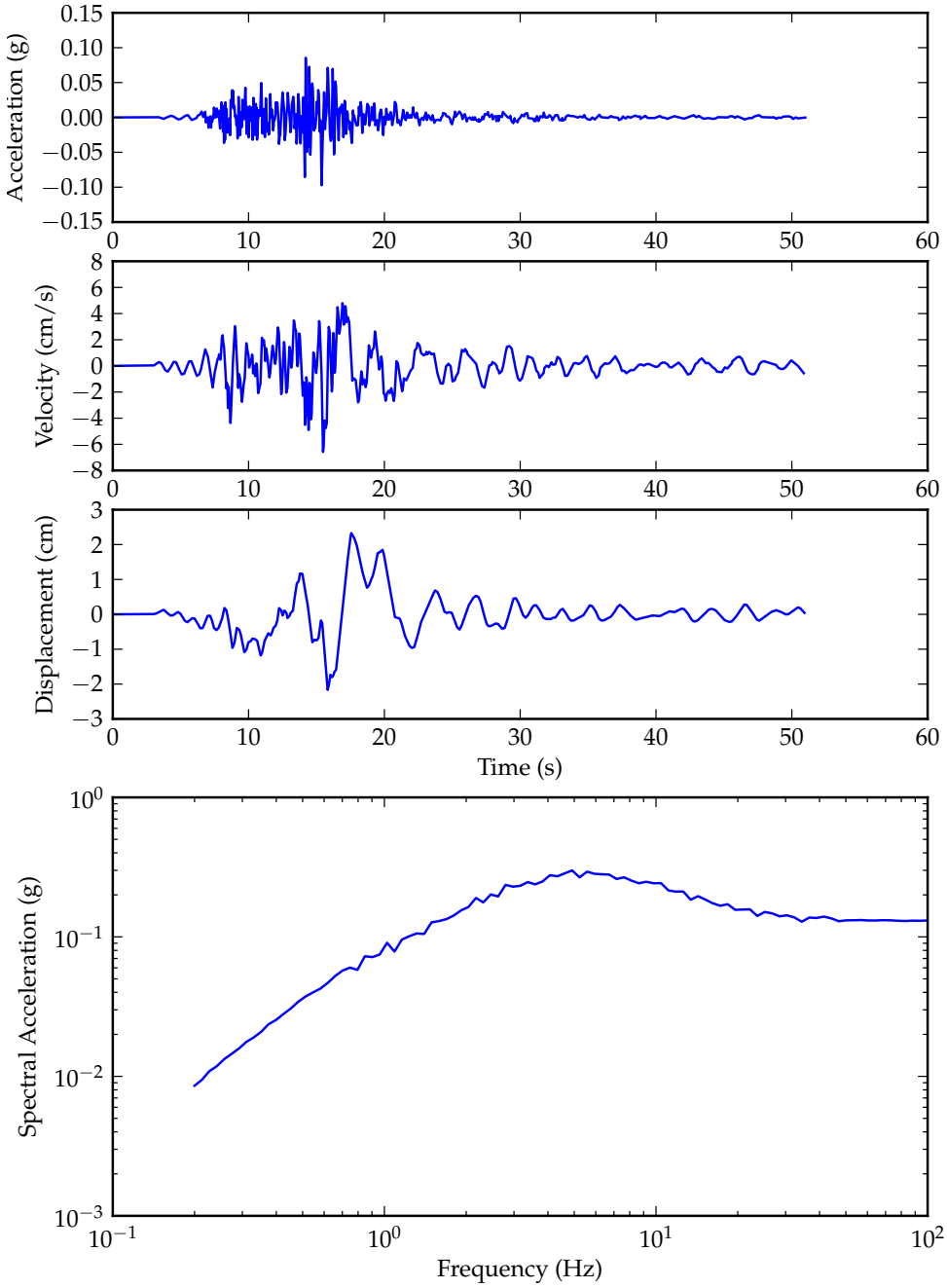

Figure C.1: The spectrally-matched `CHICHI06-TCU076-E` time series.

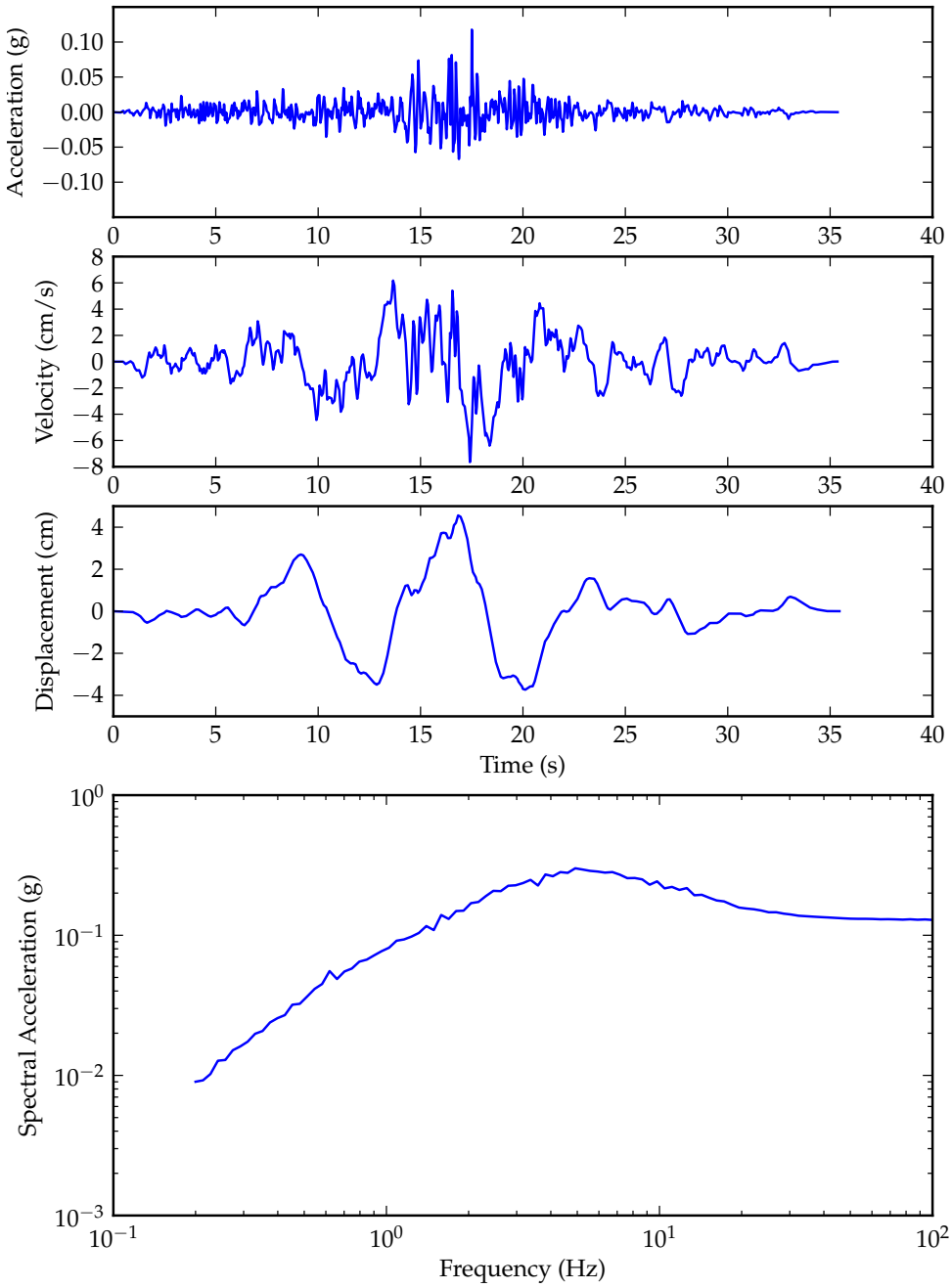

Figure C.2: The spectrally-matched `ITALY-A-AUL270` time series.

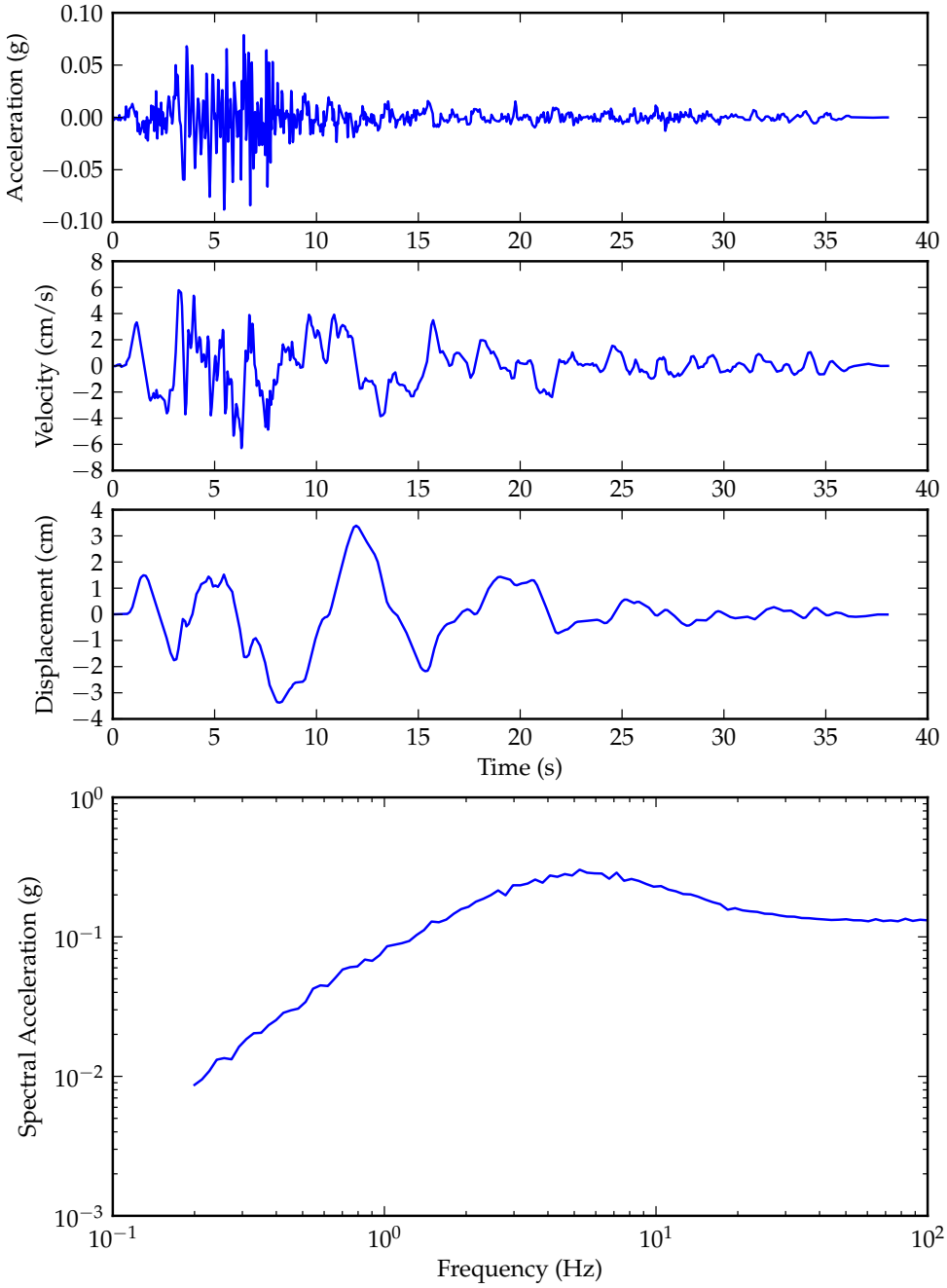

Figure C.3: The spectrally-matched `ITALY-A-BAG000` time series.

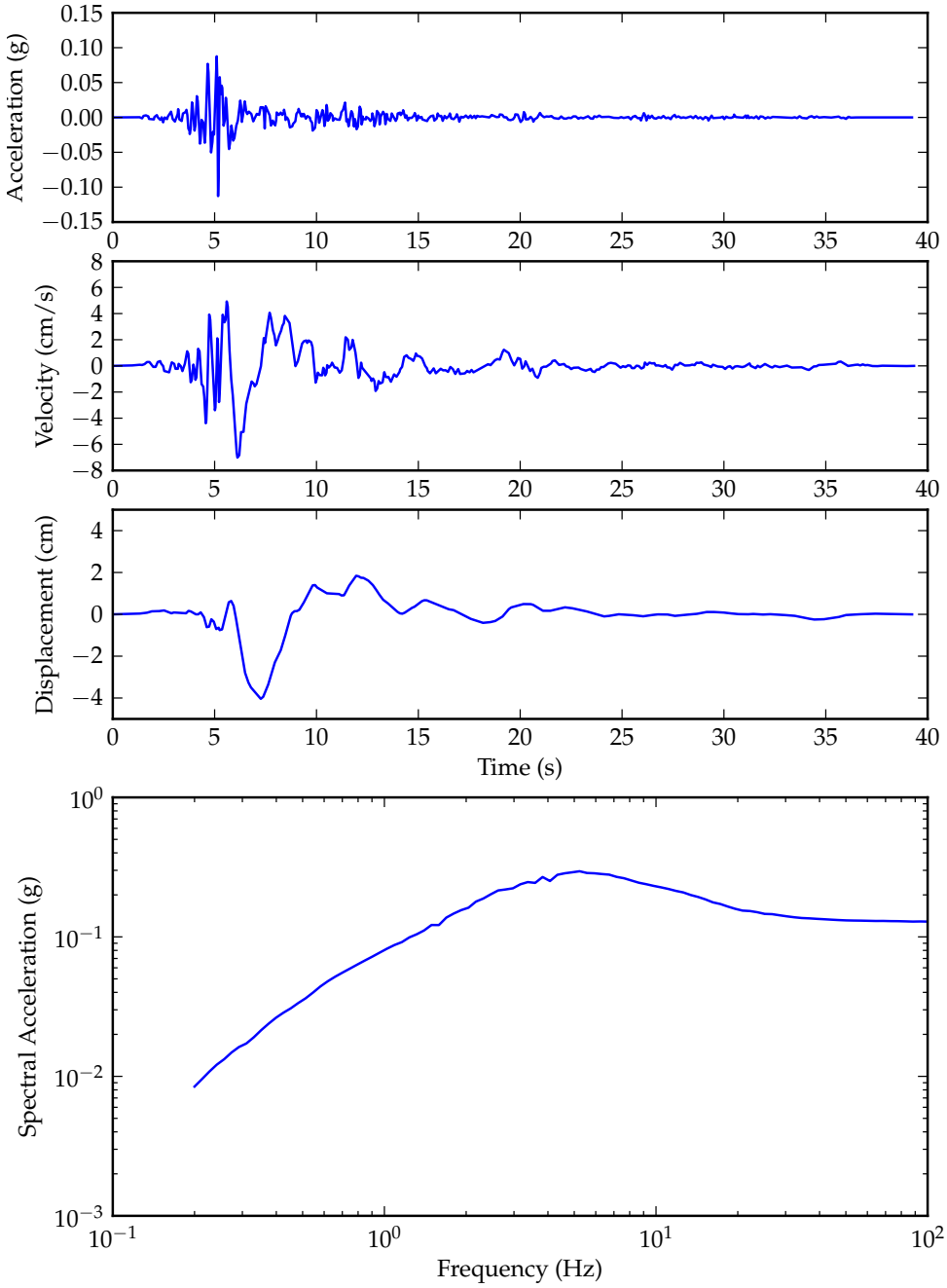

Figure C.4: The spectrally-matched `ITALY-A-STU270` time series.

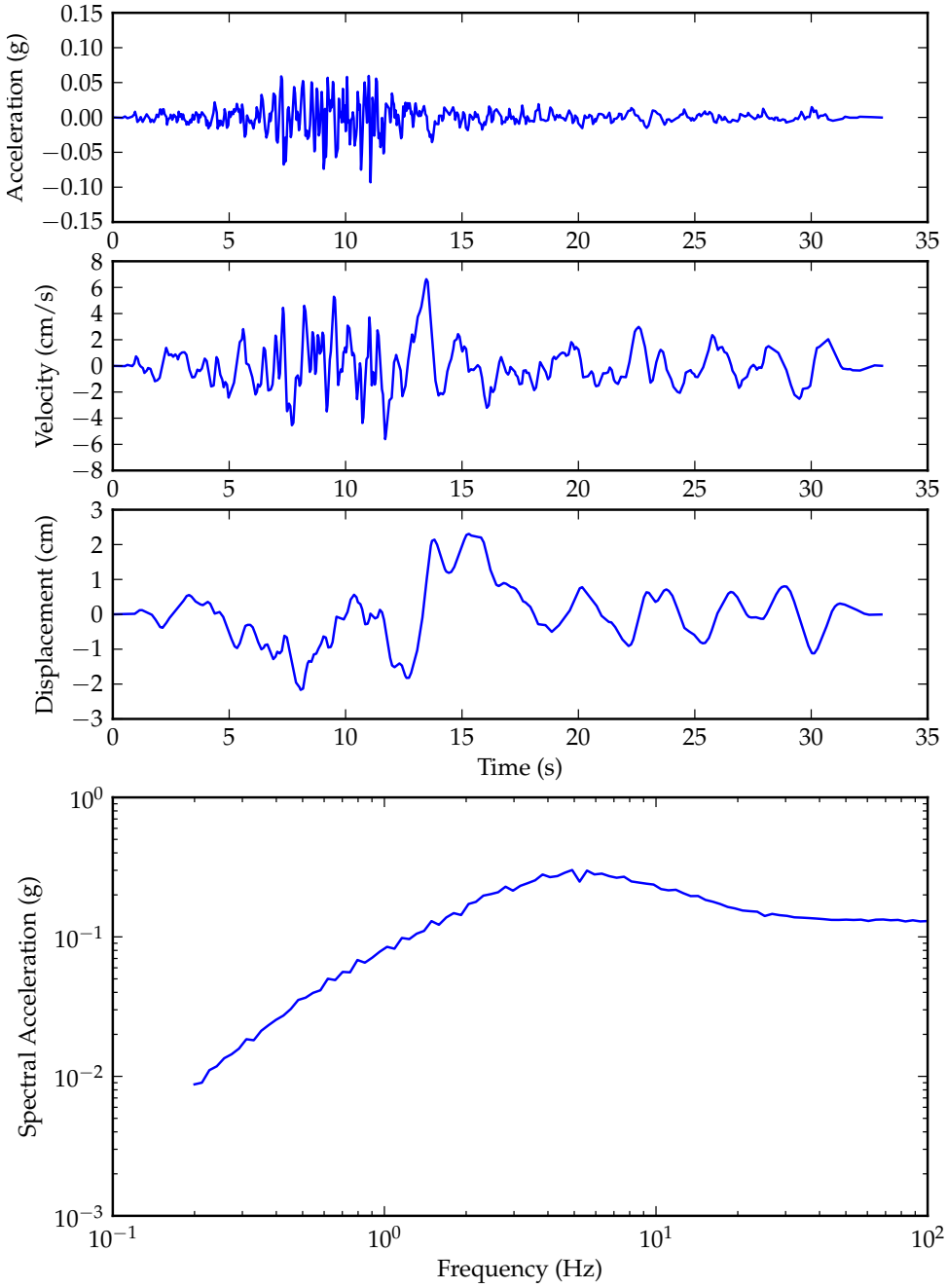

Figure C.5: The spectrally-matched `ITALY-B-AUL270` time series.

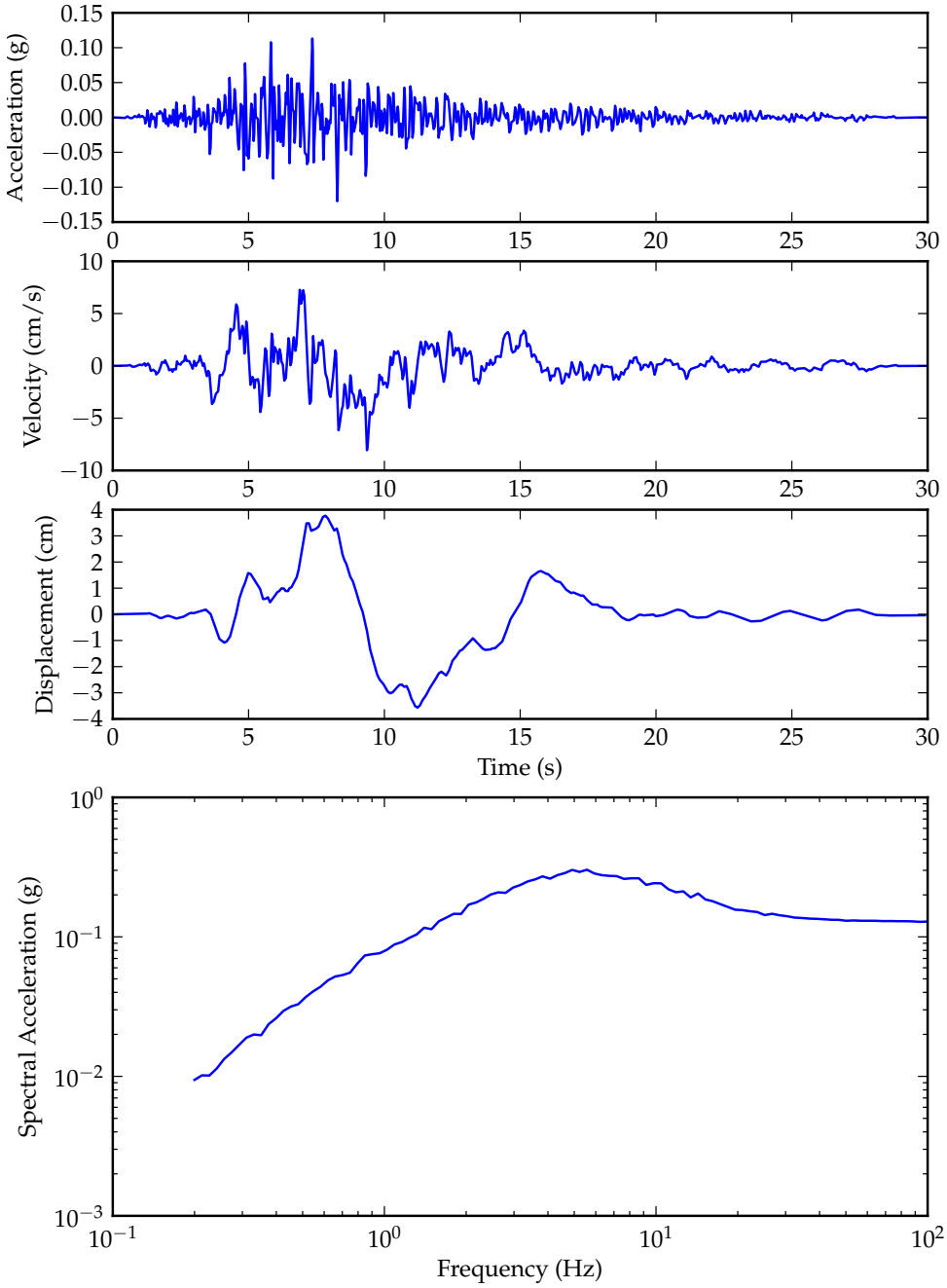

Figure C.6: The spectrally-matched `KOZANI-KOZ--L` time series.

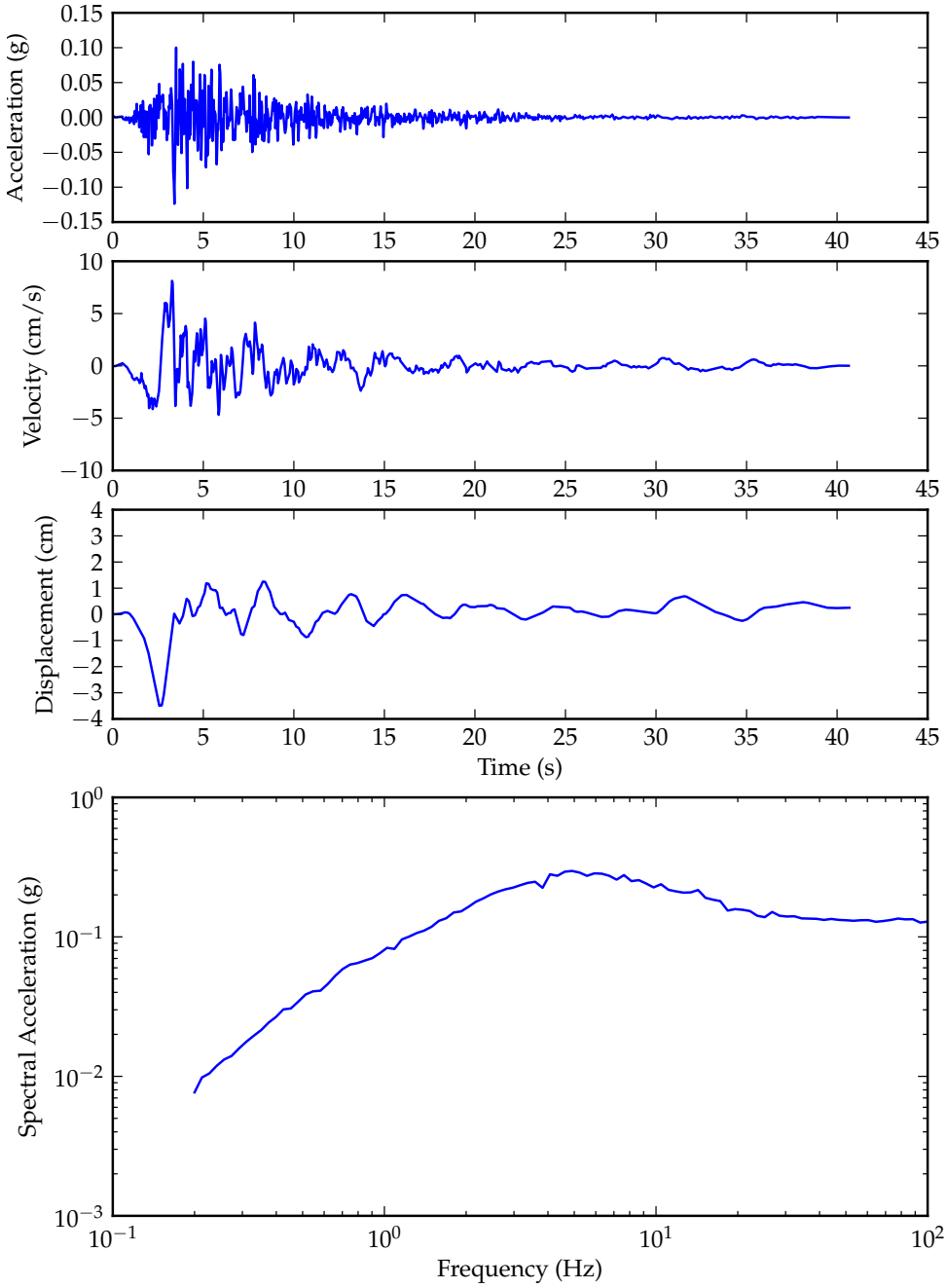

Figure C.7: The spectrally-matched `LOMAP-G01000` time series.

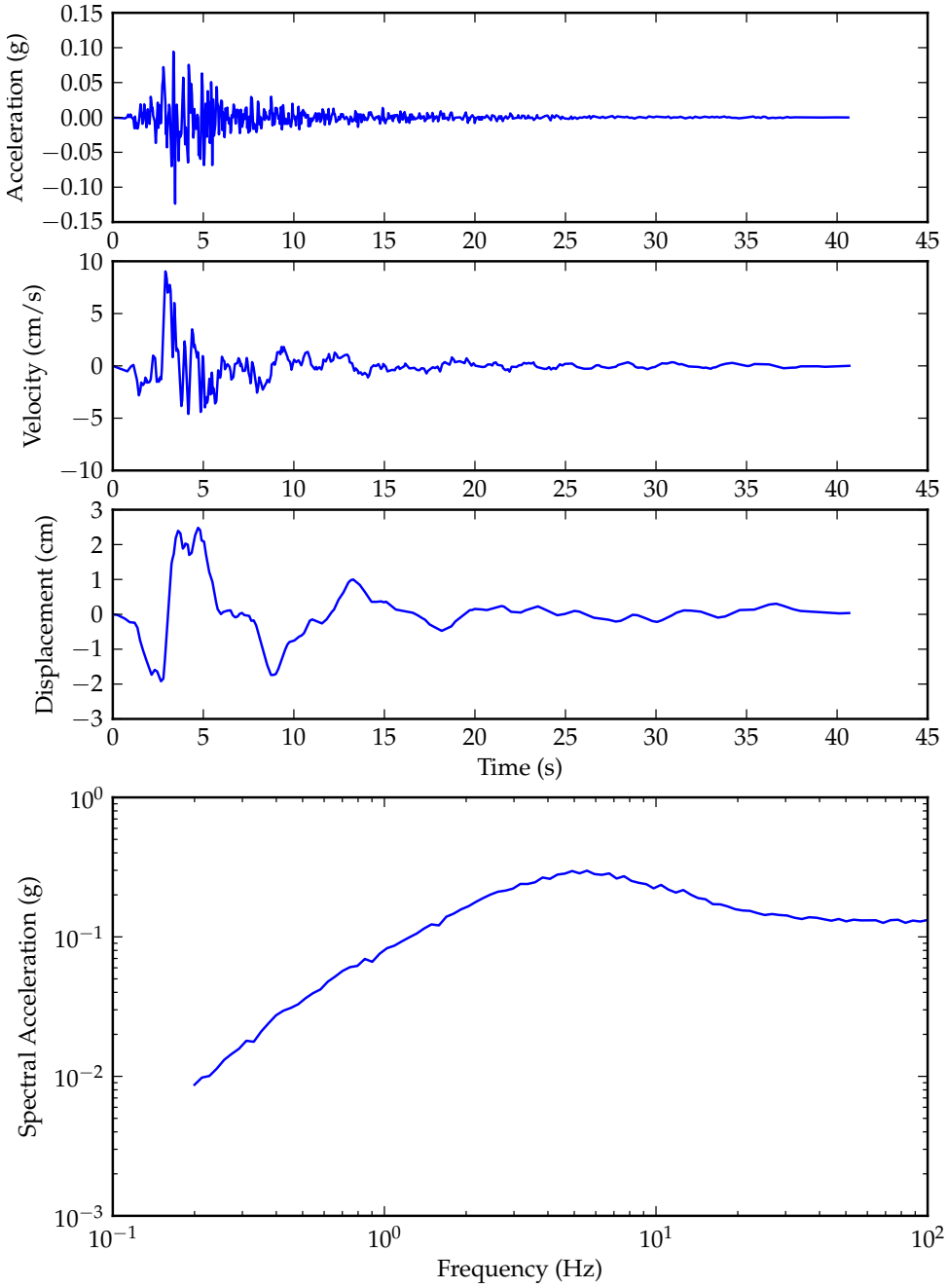

Figure C.8: The spectrally-matched `LOMAP-GIL067` time series.

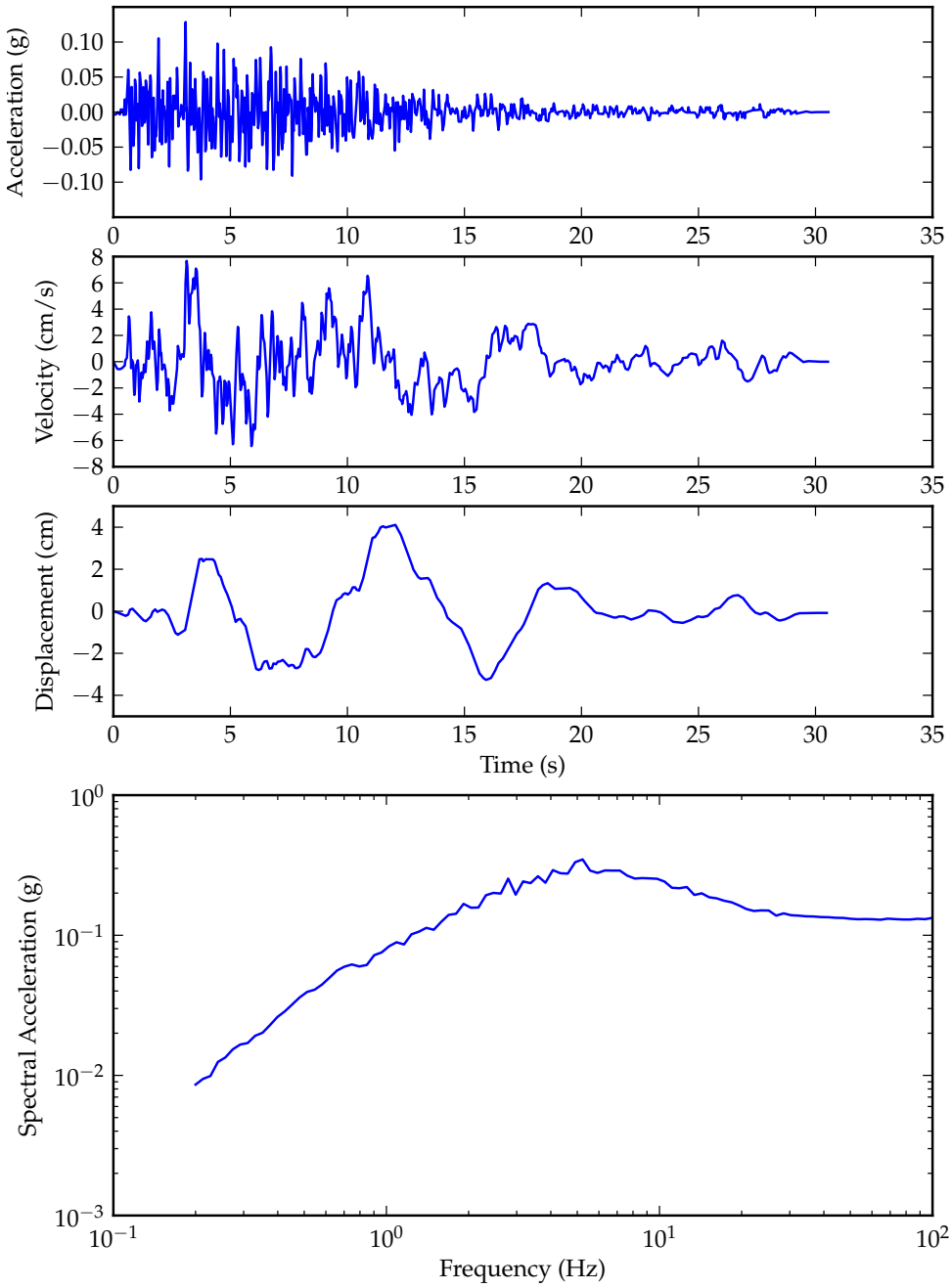

Figure C.9: The spectrally-matched `MORGAN-GIL337` time series.

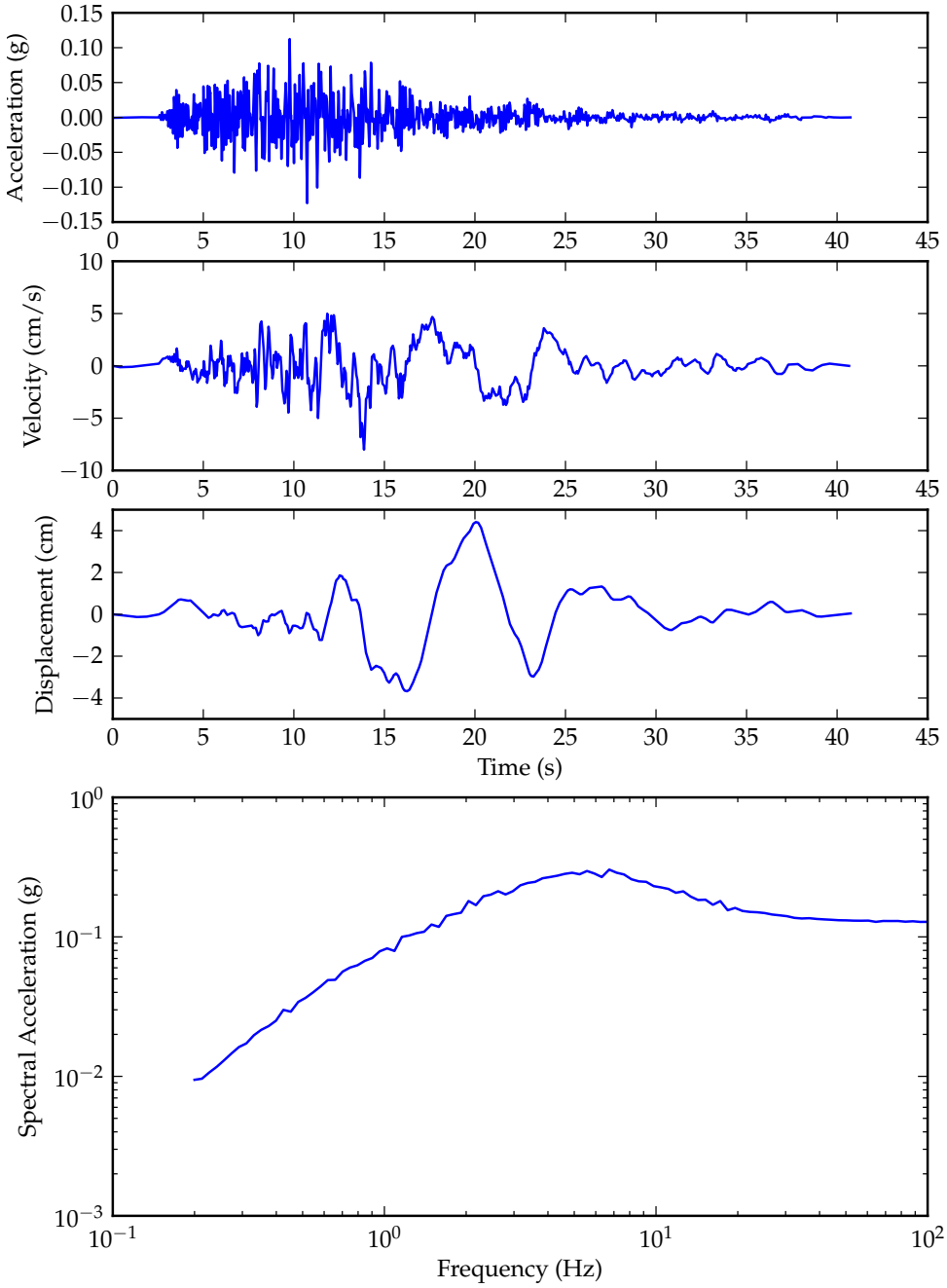

Figure C.10: The spectrally-matched `NORTHR-H12180` time series.

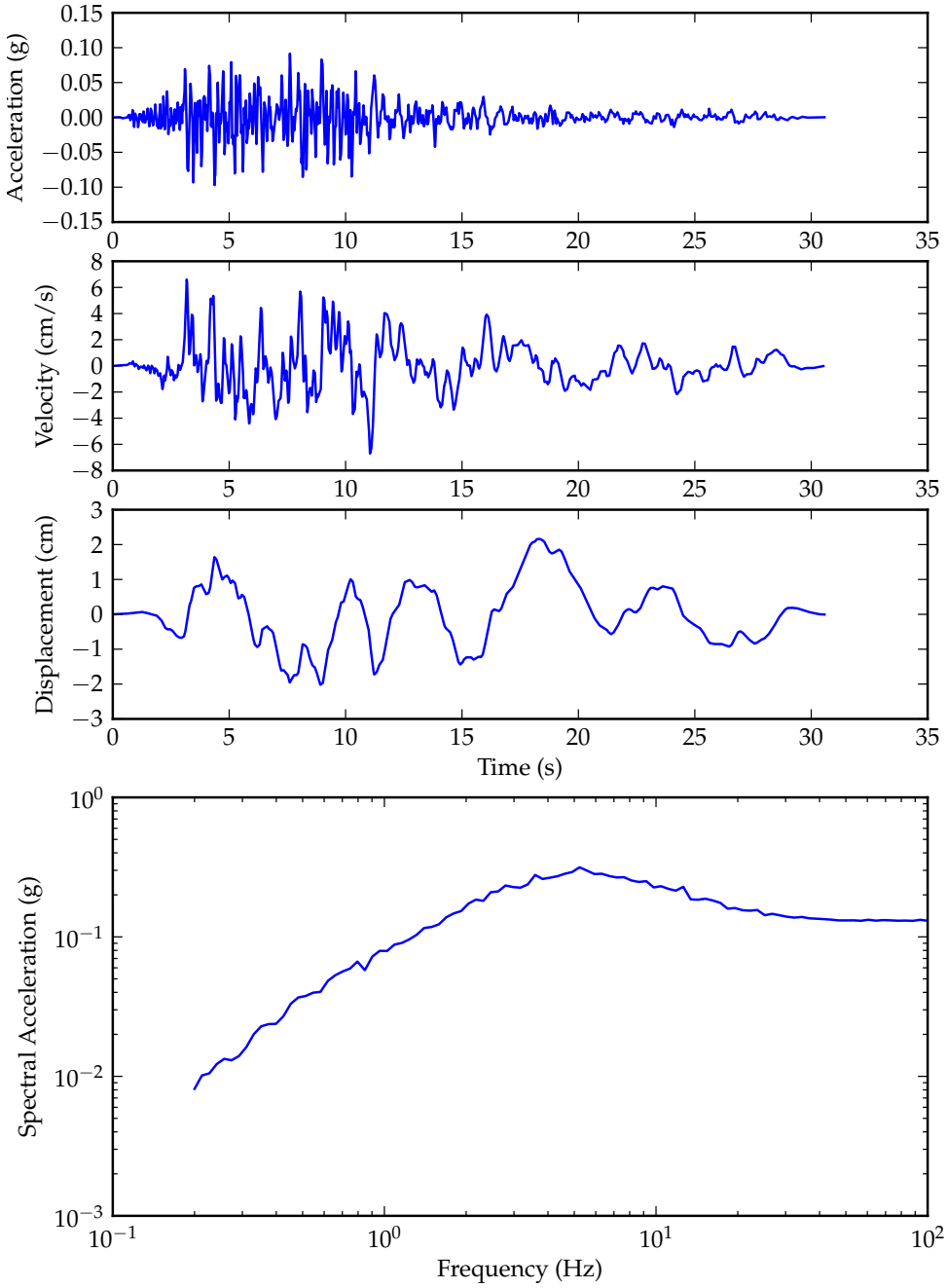

Figure C.11: The spectrally-matched `NORTHR-HOW330` time series.

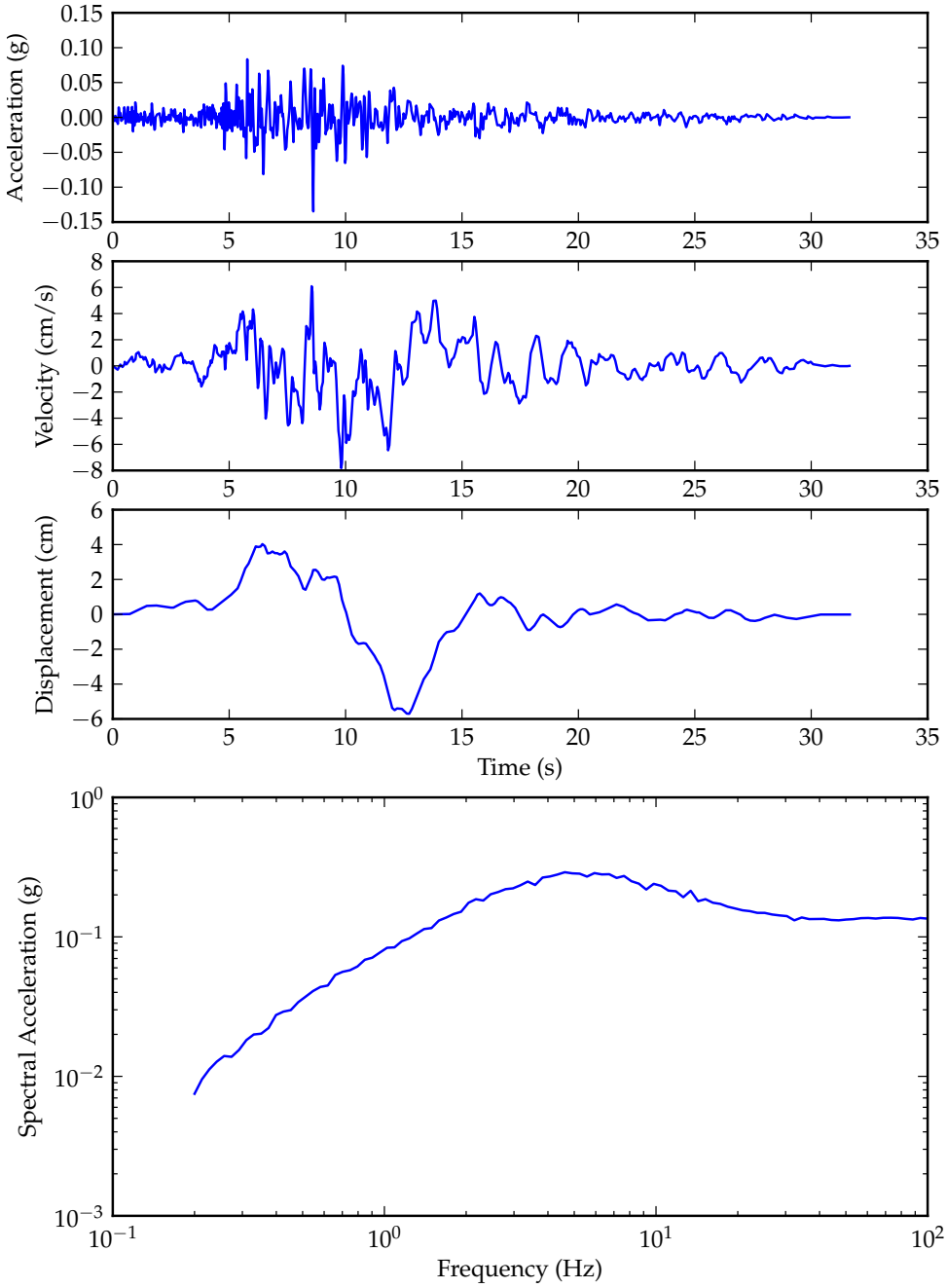

Figure C.12: The spectrally-matched `NORTHR-LV1000` time series.

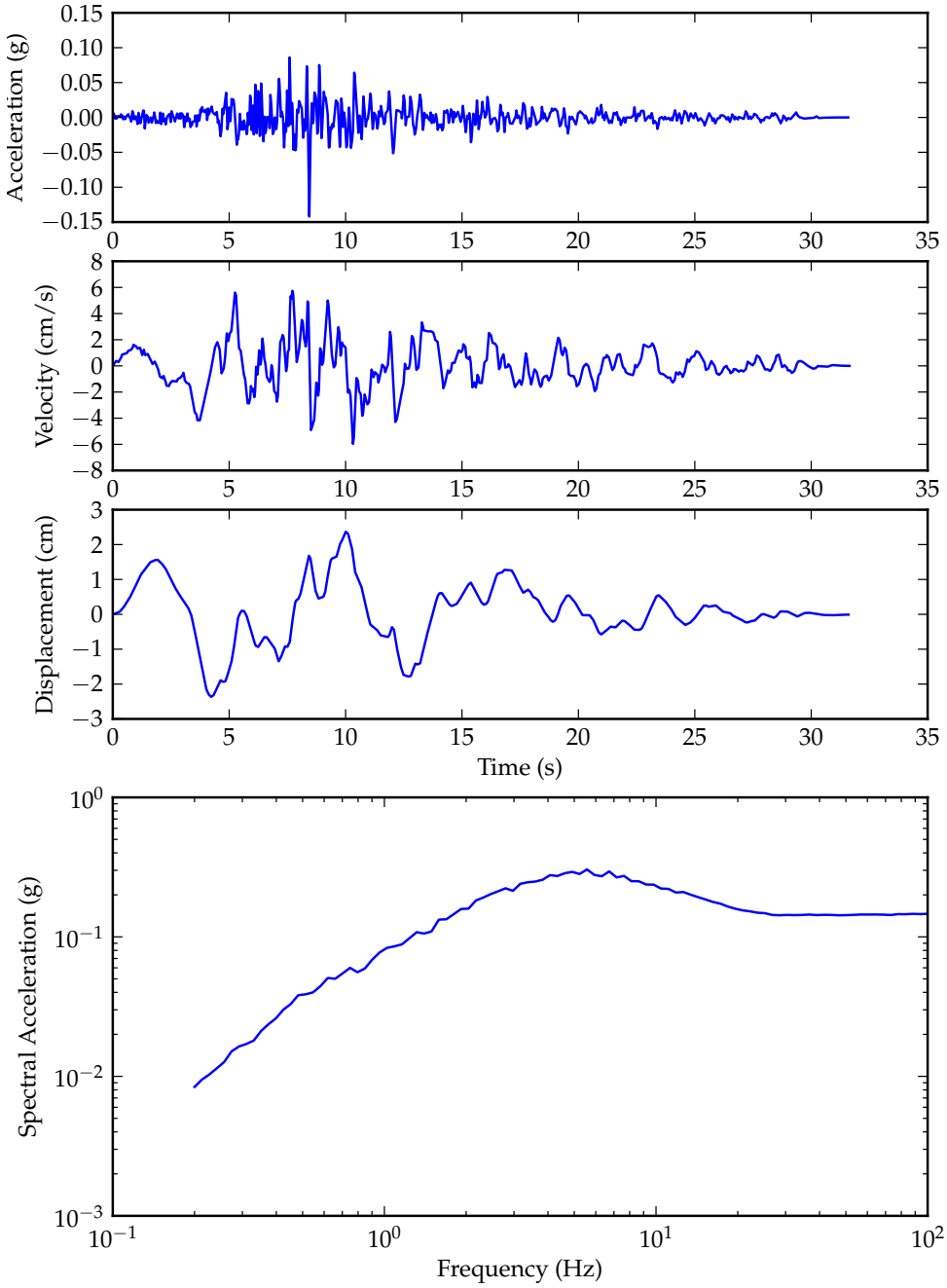

Figure C.13: The spectrally-matched `NORTHR-LV3090` time series.

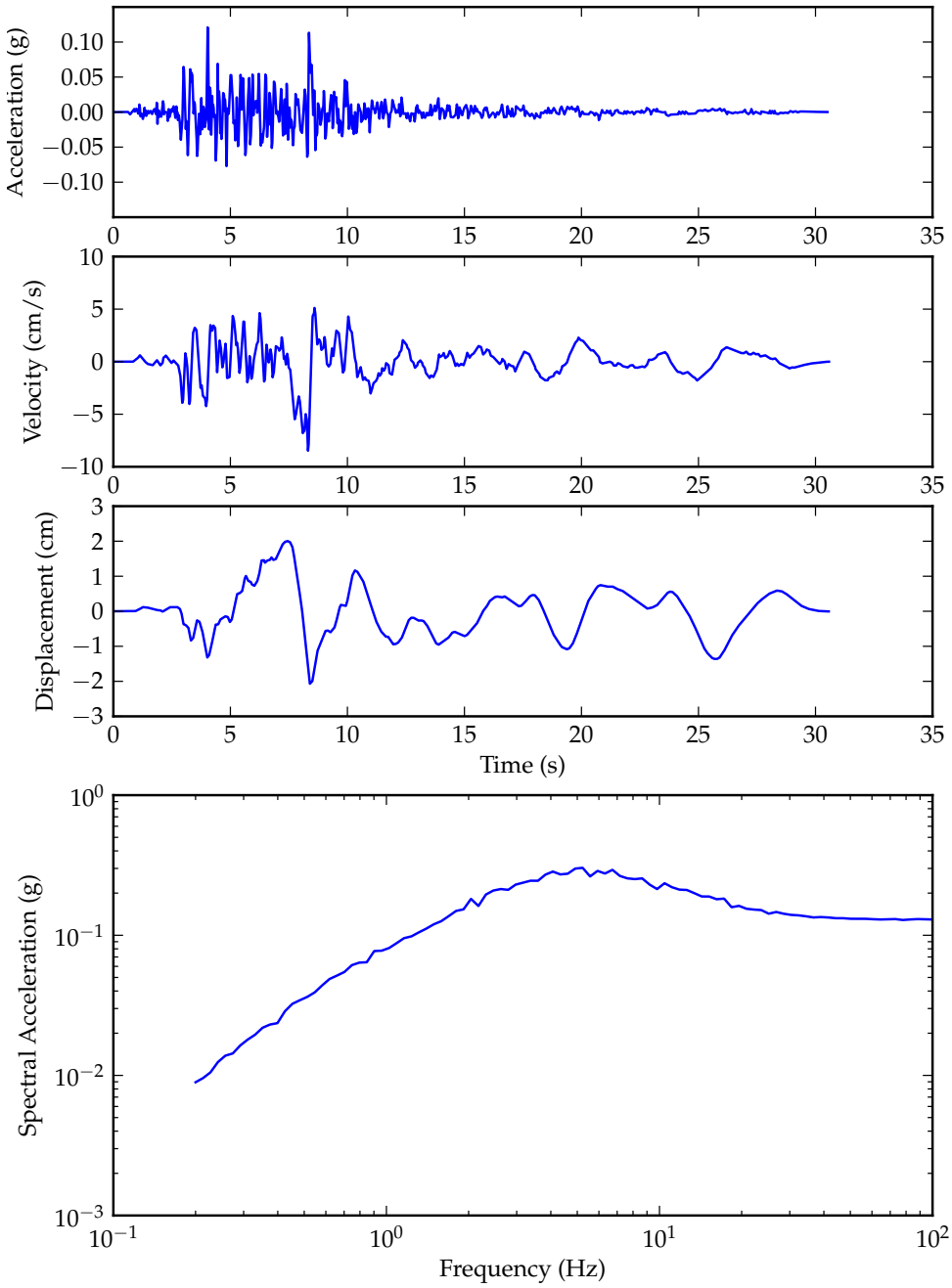

Figure C.14: The spectrally-matched `NORTHR-WON185` time series.

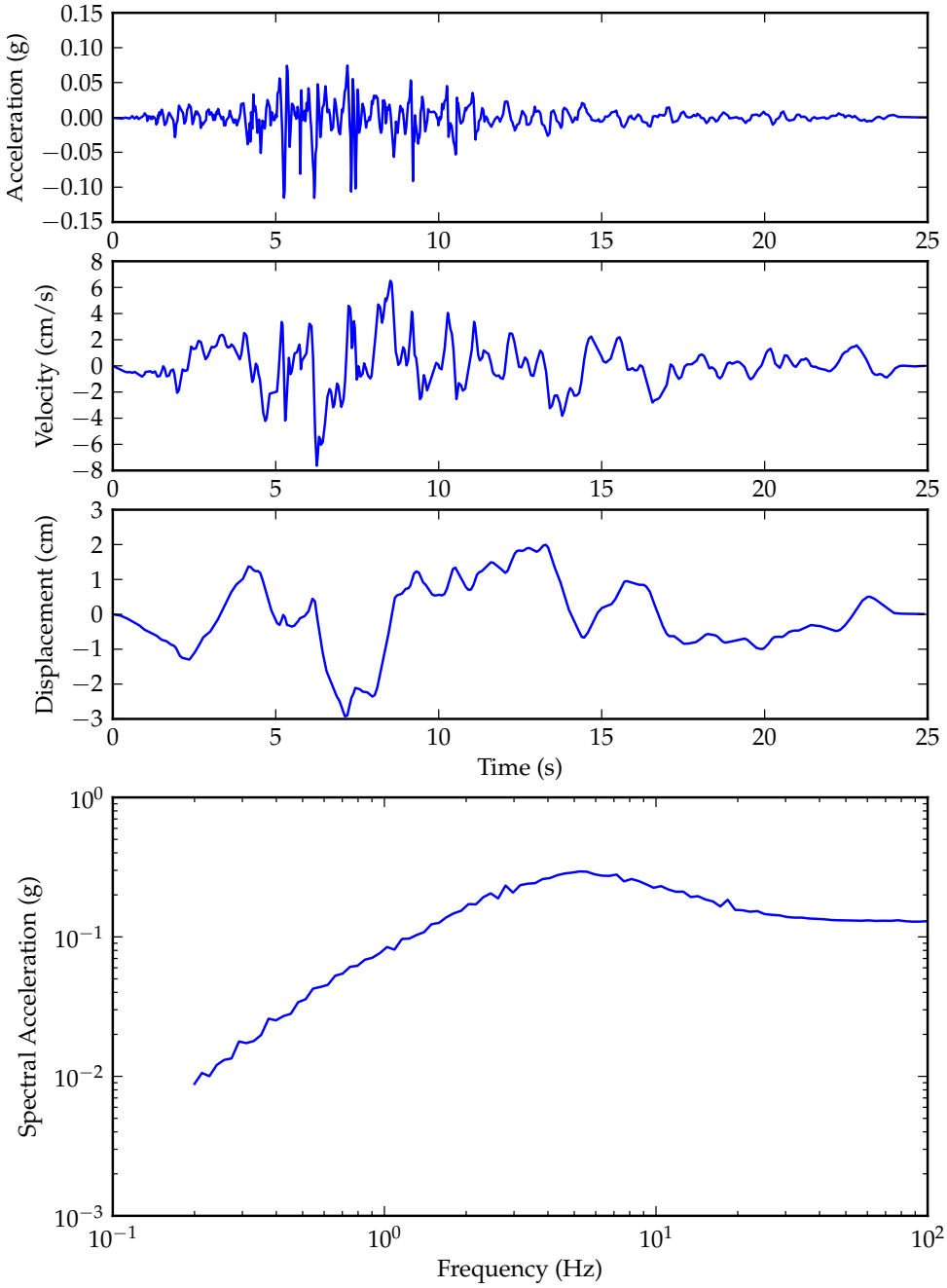

Figure C.15: The spectrally-matched `VICT-CPE045` time series.